Toward Understanding the Origin of Mass-Independent Fractionation in Sulfur Allotropes and in Ozone

Igor Gayday
Marquette University

TOWARD UNDERSTANDING THE ORIGIN OF MASS-INDEPENDENT FRACTIONATION IN SULFUR ALLOTROPES AND IN OZONE

by

Igor Gayday, M.S.

A Dissertation submitted to the Faculty of the Graduate School,
Marquette University,
in Partial Fulfillment of the Requirements for
the Degree of Doctor of Philosophy

Milwaukee, Wisconsin

May 2021

ABSTRACT
TOWARD UNDERSTANDING THE ORIGIN OF MASS-INDEPENDENT FRACTIONATION IN SULFUR ALLOTROPES AND IN OZONE

Igor Gayday, M.S.

Marquette University, 2021

Mysterious isotope effects, found in atmospheric ozone, cannot be explained by the standard mass-dependent statistical model. Similar mass-dependent isotope effects were also uncovered in sulfur deposits older than 2 billion years. In an effort to pinpoint possible reasons of these isotope effects, we build a theoretical description of the recombination reactions in sulfur allotropes and in ozone. No potential energy surface exists for the sulfur allotropes, so electronic structure calculations are also required. Ab initio calculation of two dimensionally reduced (2D and 3D) models of the potential energy surface for the tetrasulfur molecule at CCSD(T)-F12 and MRCI levels of theory are considered here. The 2D model is used to calculate the vibrational states energies up to 2000 cm^{-1}. Normal mode analysis indicates that the two considered modes in S_4 represent a significant mixture of conventional bending and stretching motions. Analysis of the bound vibrational state properties in ozone reveals that the ratio between the number of states in asymmetric and symmetric ozone molecules deviates noticeably from the statistical factor of 2, but in different directions for the singly- and doubly-substituted molecules. However, in the upper part of the spectrum both singly- and doubly-substituted species behave in the same way, which can be a factor contributing to the isotope effects in ozone. Rotation-vibration coupling and its implications for the isotope effects have been studied in detail for ozone isotopomers for both bound states and scattering resonances, using uncoupled, partially coupled and fully coupled approached. We found that the effects of rovibrational coupling are minor for low values of J, but become more significant for large values of J. However, these effects are rather uniform for both symmetric and asymmetric ozone isotopomers, therefore we conclude that the Coriolis coupling does not seem to favor the formation of asymmetric ozone molecules and cannot be responsible for symmetry-driven mass-independent fractionation of oxygen isotopes. A general program for calculation of energies and lifetimes of bound rotational-vibrational states and scattering resonances for ABA/AAB-type systems is developed (SpectrumSDT). The data calculated by this program can be useful for spectroscopic analysis and prediction of reaction rates.

ACKNOWLEDGMENTS

Igor Gayday, M.S.

First and foremost, I would like to thank my advisor, Dr. Dmitri Babikov, for all his help, mentoring and expertise that guided me throughout this research.

I would like to acknowledge the sources of financial support that I received in my years at Marquette, which include Dr. Babikov's grants, MolSSI Investment Fellowship, Arthur J. Schmitt Fellowship, MGS Endowed Summer Fellowship and Bournique Award. I acknowledge National Energy Research Scientific Computing Center (NERSC) for providing computational resources for this research.

I acknowledge the help of my co-authors: Dr. Dmitri Babikov, Dr. Alexander Teplukhin, Dr. Brian Kendrick, and (to be Dr.) Elizaveta Grushnikova.

I thank my committee members: Dr. Dmitri Babikov, Dr. Scott Reid, Dr. Qadir Timerghazin, and Dr. Chae Yi for taking their time to review this dissertation and making suggestions to improve it.

I express my gratitude to Dr. Dmitri Babikov, Dr. Qadir Timerghazin and Dr. Anne Clough for taking their time to write recommendation letters for me.

Furthermore, Dr. Qadir Timerghazin and Dr. Kirk Peterson are acknowledged for their advices on ab initio methods for calculation of the PES of S_4. Dr. Richard Dawes is acknowledged for sharing the PES of O_3. Dr. Jacek Kłos is acknowledged for sharing the PES of SO_2. Dr. Jose Roman is acknowledged for his advices regarding SLEPc library. Dr. Bill Poirier is acknowledged for his advices regarding the choice of benchmark systems for SpectrumSDT.

I thank my past and present group members: Dr. Alexander Teplukhin, Dr. Alexander Semenov, Bikramaditya Mandal, Elizaveta Grushnikova, Dulat Bostan, and Carolin Joy for fruitful discussions and fun time together.

Finally, my thanks to Marquette University as a whole and Chemistry Department in particular for all their help and support.

TABLE OF CONTENTS

LIST OF TABLES

LIST OF FIGURES

CHAPTER 1. INTRODUCTION

1.1. The Role of Sulfur in Atmospheric Chemistry

Sulfur is a naturally abundant element, most commonly found in its elemental, solid form in meteorites and rock deposits. In the Earth's atmosphere sulfur is mainly represented by sulfur dioxide, which constitutes just a tiny fraction of atmosphere's composition, about 2.5×10^{-6} %. Although nowadays concentration of sulfur in the atmosphere is quite low, it was not always the case. Geological records indicate that during the Archean eon (4.0 to 2.5 billion years ago) concentration of sulfur vapors, released in the atmosphere from volcanic activity, was substantially higher. Together with negligible presence of free oxygen in the atmosphere,[1] this allowed for a chain of sulfur polymerization reactions (Eqs. (1)-(4)), which played an important role in the chemistry of early atmosphere and life.

$$S + S \rightarrow S_2 \quad (1)$$

$$S + S_2 \rightarrow S_3 \quad (2)$$

$$S_2 + S_2 \rightarrow S_4 \quad (3)$$

$$S_4 + S_4 \rightarrow S_8 \quad (4)$$

The four stable isotopes of sulfur alongside with their natural abundances are shown in Figure 1. About 95% of sulfur isotopes are sulfur-32. The other isotopes are relatively rare and constitute less than 5% in total.[2]

1.2. Isotope Fractionation in Sulfur

One feature of particular interest observed in sulfur species is its anomalous isotope fractionation for which no explanation was found yet. Before we can discuss that, we have to introduce several concepts.

First of all, it is important to understand, that the reaction rate of a specific reaction depends on isotopic composition of its reagents. Isotopic composition defines mass, which affects kinetic energy, density of states, tunneling probability and other quantities. Moreover, an isotopic substitution distorts symmetry of a molecule, which can change probabilities of some quantum state-to-state transitions. The dependence of a reaction rate on isotopic composition of reagents is called *kinetic isotope effect*, or just *isotope effect*, for brevity.

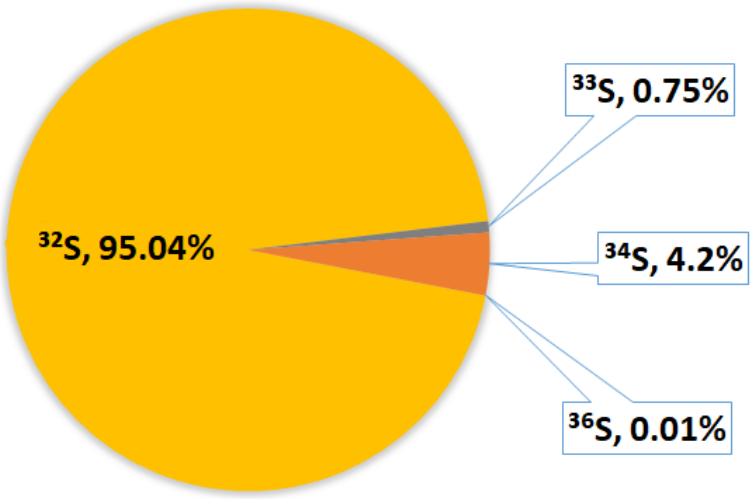

Figure 1. Natural abundances of sulfur isotopes.

The existence of the isotope effect leads to another closely related phenomenon – isotope fractionation. To understand what isotope fractionation is, let us consider the reaction in Eq. (1), as shown in Figure 2.

In the upper part of the figure, we see a schematic representation of the natural abundances of two sulfur isotopes: ^{34}S and ^{32}S (let us not worry about other sulfur isotopes for now). There is a certain ratio between the concentrations of different isotopes in nature (see Figure 1), let us define it as a *reference isotope ratio*:

$$f_R^{34} = \frac{[^{34}S]}{[^{32}S]} \tag{5}$$

Both isotopes can react with ^{32}S, forming either $^{34}S^{32}S$ or $^{32}S^{32}S$. Due to the isotope effect, formation reaction of the isotopically substituted product $^{34}S^{32}S$ occurs with a somewhat higher probability, which leads to an increased abundance of ^{34}S among

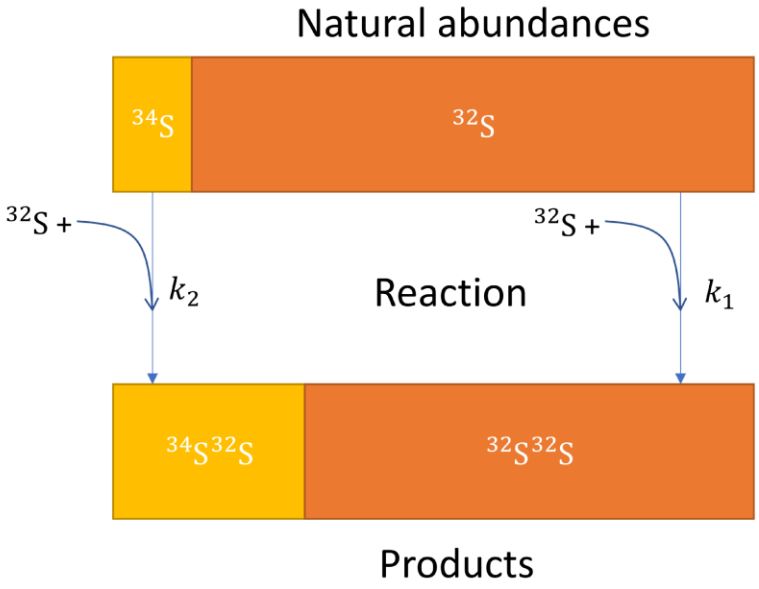

Figure 2. A schematic representation of isotope fractionation. ^{34}S and ^{32}S react with ^{32}S with different rates (k_2 and k_1), which leads to an increased fraction of rare isotope on the products side.

the products, relative to its natural abundance, as shown in the lower part of Figure 2. In a manner similar to Eq. (5), let us define *sample isotope ratio* as:

$$f_S^{34} = \frac{1[^{34}S^{32}S] + 0[^{32}S^{32}S]}{1[^{34}S^{32}S] + 2[^{32}S^{32}S]} = \frac{[^{34}S^{32}S]}{[^{34}S^{32}S] + 2[^{32}S^{32}S]} \quad (6)$$

The numerator of Eq. (6) counts the number of ^{34}S atoms among the products: one per the $^{34}S^{32}S$ molecule and zero per the $^{32}S^{32}S$ molecule. In a similar way, the denominator counts the number of ^{32}S atoms. Eq. (6) has the same meaning as Eq. (5) – it shows relative abundance of ^{34}S atom, but on the product side of the reaction (lower part of Figure 2).

Note that the definition given in Eq. (6) is specific for the reaction considered in this example and assumes the sample under consideration contains only products of this reaction, but the concept is not bound by it and can be defined for arbitrary samples in a similar way.

Isotope fractionation is a measure of deviation between the natural abundance of a certain isotope and its abundance in a *specific sample* of *certain product*. For sulfur-34 it is defined as:

$$\delta^{34} = \frac{f_S^{34}}{f_R^{34}} - 1 \quad (7)$$

where f_S^{34} term is sample-specific and can be defined in the same way as in the example above. Replacing all instances of ^{34}S in the Eqs. (5) and (7) with either ^{33}S or ^{36}S would give us analogous definitions for δ^{33} and δ^{36} respectively. In all cases fractionation is defined for one of the rare isotopes relative to the most abundant isotope.

Positive fractionations are usually referred to as *enrichments*. Negative fractionations are called *depletions*.

1.3. Mass-Dependent and Mass-Independent Fractionations

If a process leads to enrichment with one isotope, it is reasonable to assume that the same process should also work with other isotopes. However, the magnitude of the effect is expected to be different (for example, because the zero-point energy for different isotopologues is not the same, which affects reaction barrier heights). So, what is the predicted relationship between different delta-values? It can be shown[3] that in the statistical equilibrium limit, inevitably achieved on geological timescales, or at high temperature and pressure, in the condensed phase δ^{33} and δ^{36} can be expressed as a function of δ^{34} as:

$$\delta^{x} = (1 + \delta^{34})^{{}^{x}\lambda} - 1 \tag{8}$$

where $x = \{33, 36\}$ labels rare isotopes and ${}^{x}\lambda = \left(\frac{1}{m_{32}} - \frac{1}{m_x}\right) / \left(\frac{1}{m_{32}} - \frac{1}{m_{34}}\right)$ is determined based solely on differences in masses between different isotopes, so this behavior is called *mass-dependent fractionation*.

When δ^{34} is small, Eq. (8) can be very well approximated with a straight line using Tailor series, namely:

$$\delta^{x} \approx {}^{x}\lambda * \delta^{34} \tag{9}$$

where ${}^{33}\lambda \approx 0.516$ and ${}^{36}\lambda \approx 1.890$.

Eq. (9) has been proven to be quite accurate in practice by numerous experimental measurements of enrichments in many different rock samples taken from various locations all around the Earth (see Figure 3, reproduced from Ref. 4).

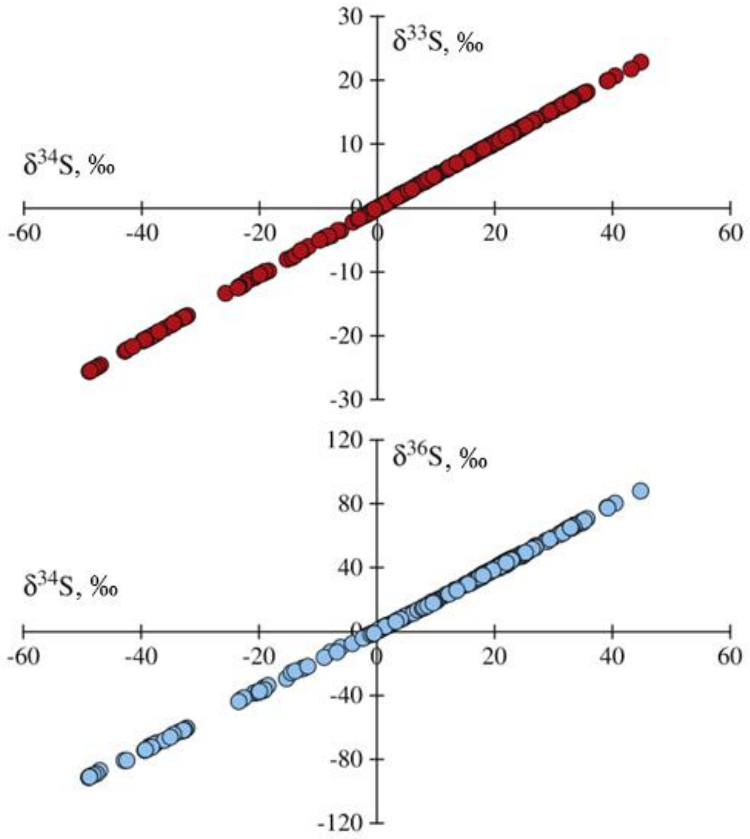

Figure 3. The δ-values computed based on data obtained from rocks younger than 2 Ga. Linear approximation of the data is in a very good agreement with the mass-dependent statistical slopes of $^{33}\lambda \approx 0.516$ and $^{36}\lambda \approx 1.890$. This figure is reproduced from Ref. 4.

Surprisingly, rock samples older than 2.4 Ga showed significant deviation from what seemed to be a well-established behavior[5–7] (see Figure 4, adapted from Ref. 8) for unknown reasons. Since this behavior could not be explained by the mass-based model, it was named *mass-independent fractionation* (MIF of sulfur or S-MIF).

The amount of mass-independent fractionation is measured as amount of deviation from the predicted value:

$$\Delta^x = \delta^x - \overline{\delta^x} \tag{10}$$

where δ^x is the actual (e.g. experimentally measured) enrichment and $\overline{\delta^x}$ is the value of enrichment predicted by Eq. (8).

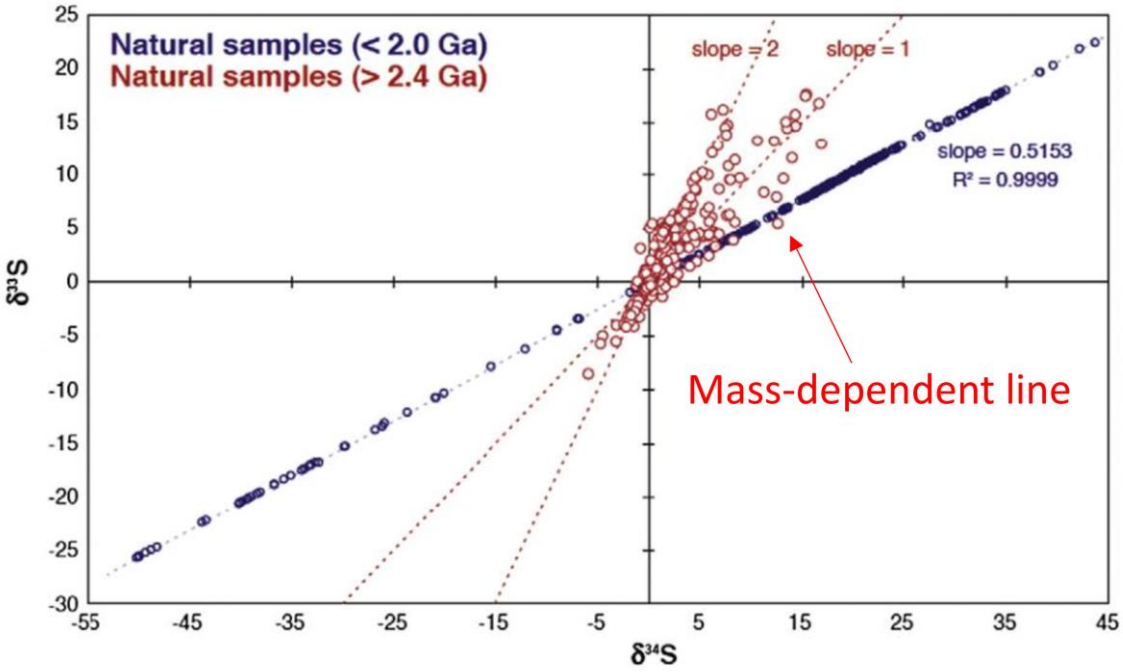

Figure 4. Significant deviation from the mass-dependent behavior was observed in the samples older than 2.4 Ga. This figure is adapted from Ref. 8.

Analysis of the amount of S-MIF in samples of different age, revealed a large spike at approximately 2.4 Ga (see Figure 5, adapted from Ref. 4). The spike marks a significant change in the environmental conditions of the ancient Earth and is generally attributed to rise of oxygen levels and transition from the ancient anoxic atmosphere to an atmosphere much more similar to the one we have nowadays.

S-MIF indicates the importance of gas-phase sulfur chemistry in the anoxic atmosphere of Earth during the Archean eon.[9–11] This discovery offers the geochemists a unique tool for analysis of conditions on Earth just prior to, and during, the great oxygenation event (after which eukaryotic life emerged), based on isotope analysis of the Archean rock record available to us today.[12–14] This knowledge can also serve as a

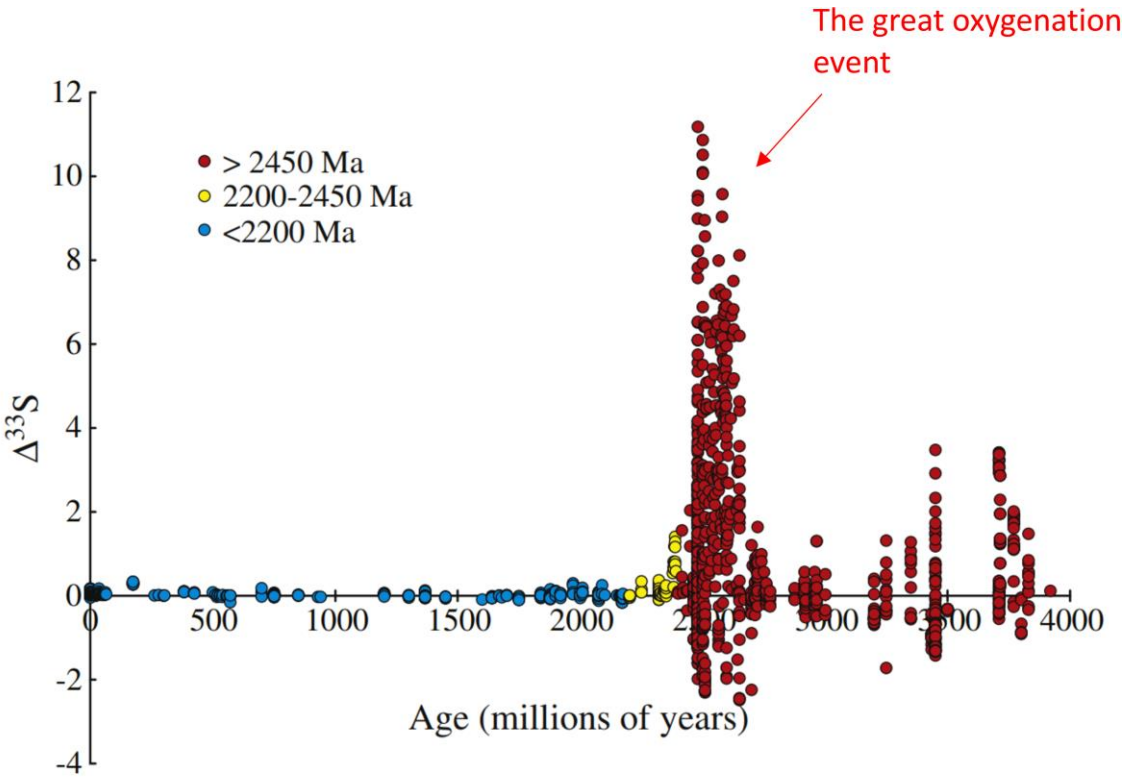

Figure 5. The amount of S-MIF in samples of different age. A sharp spike in S-MIF, which is observed at approximately 2.4 Ga, is attributed to the great oxygenation event. This figure is adapted from Ref. 4.

foundation for understanding or predicting atmospheric conditions on potentially habitable exoplanets that pass through a similar stage of their evolution.

1.4. Sources of S-MIF

The reasons of S-MIF are currently unknown, but several research groups are actively investigating possible contributions from different processes. Primarily, they focus on photochemistry of sulfur compounds,[15–21] gas-phase recombination reactions of sulfur allotropes,[22,23] aerosol formation,[24] surface deposition,[25] and kinetic modelling of the outcome of all these processes acting together.[26–28] Understanding each of these components is a challenge, but physical chemistry has much to offer for an interpretation of SMIF.[2,29]

The idea we want to focus on in this work is to explore the chain of sulfur recombination reactions that are expected to play a significant role in anoxic conditions. In short, in the oxygen-rich atmosphere, such as we have today, photolytically produced sulfur atoms and diatomic molecules, S_2, are quickly oxidized to sulfates, removed from the gas phase by rainout and dissolved in the ocean. But in anoxic conditions of the early Earth, sulfur recombination reactions are likely to proceed all the way up to formation and surface deposition of the elemental sulfur – S_8. In particular, it was demonstrated recently[22] that one step of this polymerization hierarchy,

$$S_2 + S_2 \xrightarrow{+bath\ gas} S_4 \qquad (11)$$

may, indeed, be responsible for the generation of large S-MIF.

It was hypothesized that the mechanism of S-MIF is similar to that of the famous mass-independent fractionation of the oxygen isotopes, happening during recombination reactions that form ozone in the stratosphere of today's Earth:[30,31]

$$O + O_2 \xrightarrow{+bath\ gas} O_3 \qquad (12)$$

1.5. Isotope Effects in Ozone

In 1981 mass-independent fractionations of ozone,[32,33] similar to those observed in sulfur, were discovered in the atmosphere of Earth by Mauersberger.[34] In 1983 Thiemens and Heidenreich managed to reproduce the observed effect in laboratory experiments and showed that it is mass-independent (same for ^{17}O and ^{18}O),[35] and, later on, Mauersberger and coworkers proved decisively that the ozone recombination reaction (Eq. (12)) alone is responsible for the O-MIF.[36]

Let us look at the ozone recombination reaction in more details. One can consider several different variations of it, when a single isotopic substitution with ^{18}O is introduced. Asymmetric ozone $^{16}O^{16}O^{18}O$ can be formed in two distinguishable pathways, called *A* and *B*:

$$^{16}O + {}^{16}O^{18}O \xrightarrow{A} {}^{16}O^{16}O^{18}O \xleftarrow{B} {}^{16}O^{16}O + {}^{18}O \qquad (13)$$

For the symmetric ozone molecule $^{16}O^{18}O^{16}O$ both options are indistinguishable and called *S*:

$$^{16}O + {}^{18}O^{16}O \xrightarrow{S} {}^{16}O^{18}O^{16}O \xleftarrow{S} {}^{16}O^{18}O + {}^{16}O \qquad (14)$$

Similar labels can also be introduced for the doubly-substituted case:

$$^{18}O + {}^{18}O^{16}O \xrightarrow{A} {}^{18}O^{18}O^{16}O \xleftarrow{B} {}^{18}O^{18}O + {}^{16}O \qquad (15)$$

$$^{18}O + {}^{16}O^{18}O \xrightarrow{S} {}^{18}O^{16}O^{18}O \xleftarrow{S} {}^{18}O^{16}O + {}^{18}O \qquad (16)$$

The reactions 13-16 can be written with ^{17}O in place of ^{18}O too, since oxygen has three stable isotopes: ^{16}O, ^{17}O and ^{18}O with the corresponding abundances of 99.76%, 0.04% and 0.2%.[37]

Note that the zero-point energy of reagents is different in pathways *A* and *B* since masses of $^{16}O^{18}O$ and $^{16}O^{16}O$ are different. Heavier species have lower zero-point energy, so in the singly-substituted case dissociation channel *A* opens earlier than *B*, while it is vice versa for the doubly-substituted case. The energy difference between channels *A* and *B* is referred to as ΔZPE.

The experiments conducted by Janssen et al.[38] in early 2000s allowed to measure reaction rates for each pathway separately, which revealed a strong correlation between the reaction rates and the amount of ΔZPE, as shown in Figure 6 (reproduced from Ref. 39). One can see that the reactions going through the lower pathways (*A* for the singly-substituted, and *B* for the doubly-substituted) are substantially faster than those going through the upper pathways. The correlation between the relative reaction rate coefficients and the amount of ΔZPE between the pathways *A* and *B* (taken with the positive sign for the lower pathways and the negative sign for the upper pathways) is called ζ-effect or ΔZPE-effect.

Numerically, ζ-effect is measured as a reaction rate coefficient of a faster pathway relative to a slower pathway, which, essentially, represents dissimilarity between the two pathways:

$$\zeta = \frac{\kappa_{fast}}{\kappa_{slow}} \tag{17}$$

where κ_{fast} corresponds to the reaction rate constant of pathway *A* in the singly-substituted case and pathway *B* in the doubly-substituted case, and κ_{slow} is the reaction rate constant of the other pathway.Experimentally measured values of ζ-effect are

approximately equal to $\zeta = 1.55$ and $\zeta = 1.63$ for the singly- and doubly-substituted ozone molecules respectively.[38]

Another effect that one can notice in Figure 6 is the deviation of reaction rate constants of the symmetric ozone species from the trend set up by the asymmetric ozone reaction rate constants dependency on ΔZPE. This effect is called η-effect.[30,40–42]

Quantitatively, η-effect is defined as amount of difference between the linear prediction set up by the ΔZPE-trend and the actual reaction rate constants:

$$\eta = \frac{(\kappa_{fast} + \kappa_{slow})/2}{\kappa_{sym}} \tag{18}$$

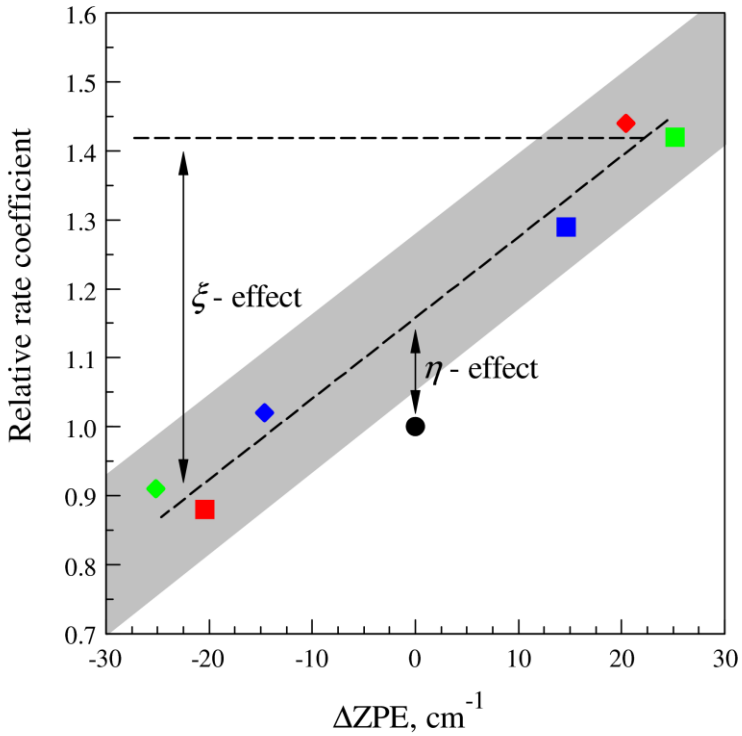

Figure 6. Isotope effects in ozone. Squares and rhombs mark pathways *A* and *B*, respectively. Green color corresponds to the $^{16}O^{16}O^{18}O$ molecule, red to the $^{18}O^{18}O^{16}O$ molecule, and blue to the $^{16}O^{16}O^{17}O$ molecule. Horizontal axis shows the value of ΔZPE for the other pathway relative to the considered one. Vertical axis shows reaction rate coefficients relative to the unsubstituted ozone reaction rate coefficient. All symmetric ozone species are represented by the black dot. This figure is reproduced from Ref. 39.

where the meaning of κ_{fast} and κ_{slow} is the same as in Eq. (17) and κ_{sym} is the reaction rate constant for the symmetric ozone species. The reaction rate constants for all varieties of symmetric ozone, including unsubstituted, singly-, doubly- and even triply-substituted species, are all very similar and are represented by a single black dot in Figure 6.

Experimentally measured values of η-effect are nearly identical in both singly- and doubly-substituted case and are approximately equal to η = 1.16.[38,43]

The experimental values of ζ-effect and η-effect have never been reproduced with adequate precision in theoretical calculations, despite many attempts made by different research groups. Although satisfactory explanation of the effects does not exist, some useful insights can be gained from the existing studies.[44] In particular, it was shown that purely classical trajectories cannot explain the effects,[41,45,46] so the origin has to be quantum mechanical.

Several existing quantum mechanical studies of ozone[47–50] conclude that ZPE difference between pathways *A* and *B* and properties of scattering resonances, especially Feshbach resonances,[51] could be the key to the explanation. Another possible source could be in the process of stabilization of metastable ozone species by collision with a bath-gas.[52,53] Nevertheless, the origin of the effects remains a mystery and the search continues.

1.6. Objectives and the Structure of This Dissertation

The ultimate goal of this work is to investigate possible sources of S-MIF and O-MIF and estimate magnitudes of their contributions to the overall effect. Each chapter is focused on a particular aspect of this global problem. The content of this document is structured as follows:

Chapter 2 is dedicated to the electronic structure calculations for tetrasulfur (S_4). First, the simplest possible model is considered at low energies in the vicinity of the isomerization pathway. Two degrees of freedom are included in this model: S_2–S_2 distance R and the gearing motion angle α. The double-bond lengths are fixed, and all atoms are restricted to a single plane. Potential energy surface calculations are carried out at the CCSD(T)-F12a/VTZ-F12[54,55] level of theory for a 2D-grid of points, and the PES is built using bi-cubic spline interpolation. The global PES up to the dissociation limit of $S_4 \rightarrow S_2 + S_2$ is explored using the multi-reference configuration interaction (MRCI) method.[56–58] In these calculations a new degree of freedom, the second bending angle, is incorporated, which is important for the configurations outside of the isomerization pathway, at higher energies.

In Chapter 3, the focus is on the calculation of the vibrational states of S_4 using the computed 2D PES. We conducted accurate quantum calculations of vibrational states of S_4 in the energy range up to 2000 cm^{-1} above the C_{2v} minimum, which is well above the D_{2h} transition state energy. These calculations were done using a custom computer code written in Fortran, which I developed from scratch. The calculations on the 3D PES will be a subject of a future work.

In Chapter 4, we develop general theory of coupled rotation-vibration calculations in APH coordinates, derive analytical the matrix element expressions where possible, and provide practical advices about possible implementations of this theory. The developed theory is further applied to ozone isotopomers to study possible sources of the isotope effects in Chapters 5-8. The theoretical framework developed in this chapter is general

and can be applied to any three-atomic systems. Application to systems other than ozone is considered in Chapter 9.

In Chapter 5, we present the results of accurate calculations of *bound vibrational* states up to the dissociation threshold for without overall rotation ($J = 0$) in singly- and doubly-substituted ozone molecules, to figure out whether the ratio between the number of purely vibrational states in asymmetric and symmetric molecules is different from statistical expectations. Analysis of these spectra suggests that the ratio between the number of states in asymmetric and symmetric ozone molecules may be a factor contributing to the η-effect during the stabilization of the metastable ozone species.

In Chapter 6, we investigate the effect of *rotation-vibration coupling* on spectra of bound states in singly- and doubly-substituted ozone molecules with excitations up to $J = 5$ and both inversion parities. The roles of the asymmetric-top rotor term and the Coriolis coupling term are determined individually, and it is found that they both affect these splittings, but in the opposite directions. Thus, the two effects partially cancel out, and the residual splittings are relatively small. Splittings between the states of different parities are calculated and analyzed. Analytical extrapolation of the splittings and their effect on larger values of J is discussed. The computed spectra are used to estimate consequences of rotation-vibration coupling in bound states for the isotope effects in ozone.

In Chapter 7, we study the role of rotation-vibration coupling for *scattering resonances* above the dissociation threshold for all values of the total angular momentum J from 0 to 4. To make these calculations numerically affordable, a new approach is developed, which employs one vibrational basis set optimized for a typical rotational excitation to run coupled rotation-vibration calculations at several desired values of J. In

order to quantify the effect of Coriolis coupling, new data are contrasted with those computed using the symmetric-top rotor approximation, where the rotation-vibration coupling terms are neglected. Implications of rovibrational coupling in the resonance spectra of ozone for the isotope effects are discussed.

In Chapter 8, we devise a new method of partial coupling that allows to approximately take into account the effects of rotation-vibrational coupling for large values of J. The partially coupled approach enables the calculations of scattering resonances above dissociation threshold for *large values of total angular momentum, J* = 24 and 28, which permits to quantify the role of Coriolis effect at room temperature. Once again we study the implications of rovibrational coupling in this regime to the isotope effects in ozone molecules.

In Chapter 9, we generalize the program that we developed for ozone (SpectrumSDT) and make it applicable to other three-atomic systems. SpectrumSDT is capable of calculations of energies and lifetimes of bound rotational-vibrational states below and scattering resonances above the dissociation threshold on a global potential energy surface of a triatomic system, which may include stable molecules, weekly-bound van-der-Waals complexes, and unbound atom + diatom scattering systems. All options considered in Chapters 5-8 for ozone are generalized and can be used for other systems. A benchmark calculation of sulfur dioxide (SO_2) is considered.

In Chapter 10 an overall summary of the work and future plans are laid out.

CHAPTER 2. ELECTRONIC STRUCTURE CALCULATIONS FOR TETRASULFUR

In this chapter we consider ab initio calculation of potential energy surface (PES) for tetrasulfur in reduced dimensionality (2D and 3D), using different methods. The 2D PES is further used in Chapter 3 to compute and analyze vibrational states of tetrasulfur.

As it was suggested in the work of Babikov et al.,[22] the sulfur recombination reaction (11) is one of the possible candidates for a major source of S-MIF contribution. Before we can study this reaction, we need to have a global potential energy surface (PES) for it. As of present, no accurate potential energy surfaces for sulfur allotropes exist beyond S_2, so the first step we need to undertake is to compute one. We will start with an overview of the existing electronic structure calculations for S_4, which will serve as a useful benchmark for our own PES.

2.1. Overview of the Existing Electronic Structure Calculations for the Sulfur Species

For S_2, calculations by Francisco and coworkers at CCSD(T)[59,60] level of theory with large basis sets and extrapolation to the complete basis set (CBS) limit gave the double-bond length, vibrational and rotational constants, and dissociation energy,[61,62] all in an excellent agreement with experimental spectroscopic and thermochemical data. Calculations at the multi-reference configuration interaction (MRCI) level gave very similar results for S_2,[23,63] but also permitted to construct its potential energy curve up to the dissociation limit. Such diatomic potentials were employed[64] in classical trajectory simulations of recombination reaction

$$S + S \xrightarrow{+bath\ gas} S_2 \qquad (19)$$

and in a more recent study,[23] where all ro-vibrational states of S_2 (bound states up to the dissociation threshold and scattering resonances above it) were accurately computed and used in a quantum mechanical model for the reaction (3), to explore a possible source of S-MIF. In both cases argon was considered as bath gas, but it should be emphasized that interaction of Ar with the sulfur atoms in S_2 was introduced in a pairwise-additive fashion, which is a computationally cheap and approximate method.

For S_3, both CCSD(T) and MRCI calculations of electronic structure were carried out to determine its geometry and energetics,[62,63] and it was found that their results agree well. MRCI method was further used to compute one-dimensional slices through the PES of S_3 (for the ground and excited electronic states, to provide some insights into its photochemistry),[63] whereas CCSD(T) method was employed to construct a simplified PES for the chaperon mechanism of recombination (in a bath of argon):[65]

$$S + S_2 \xrightarrow{+bath\ gas} S_3 \qquad (20)$$

Again, it should be stressed that a pairwise-additive description of interaction was employed, with separately computed three-body interaction terms added, and four-body interaction neglected. No accurate global PES was constructed.

For S_4, an emphasis was on identification of the lowest energy conformer. It was demonstrated recently, based on CCSD(T) calculations with large basis sets and the CBS extrapolation, that the global minimum of the singlet PES of S_4 corresponds to an isosceles trapezoidal C_{2v} structure,[66] rather than to several other existing isomers.[67] The structure and energetics of S_4 predicted at CCSD(T) and MRCI levels[66] are in an excellent agreement with experimental data.

The same computational study[66] reported a transition state, where S_4 has rectangular D_{2h} shape, just 790 cm^{-1} above the minimum energy point. It was suggested that this low-energy transition state connects two energetically equivalent C_{2v} structures, as indicated in Figure 7.

The process of isomerization between the two C_{2v} wells was in a focus of another study,[68] where classical trajectory simulations, with gradients computed on-the-fly using DFT method, were launched to predict vibrational frequencies of S_4. It was concluded that interconversion between the two isomers should occur readily at the room temperature, but careful reading of the paper reveals that the barrier height in the DFT calculations was lower, almost by a factor of 2, compared to the accurate benchmark CCSD(T) calculations of Ref. 66. Moreover, it is hard to justify the use of the classical trajectory method for a description of a process where four vibrational modes (out of six in S_4) must remain at their zero-point energy level, and the two other modes may only receive one quantum of excitation. At such conditions, quantum dynamics calculations of

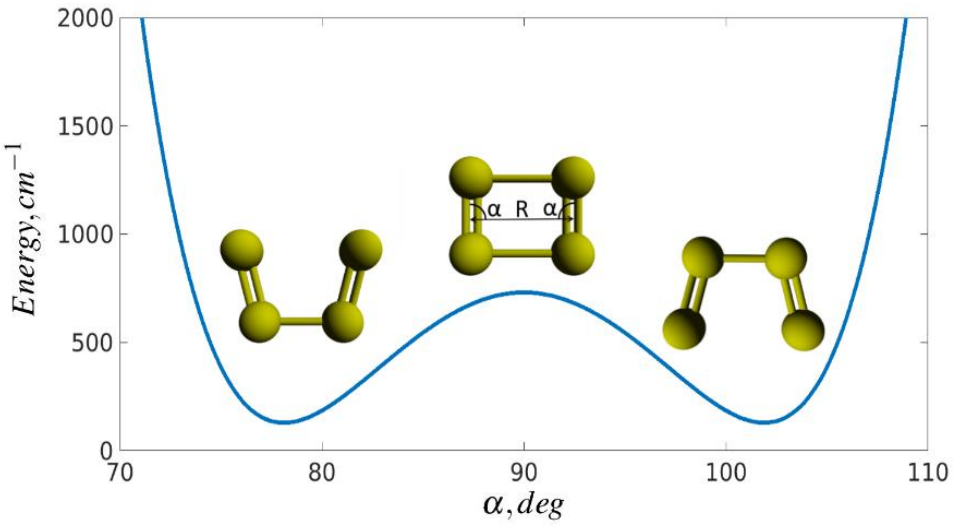

Figure 7. The two energetically equivalent minima and the transition state of the tetra-sulfur. The dimer-dimer distance R and the bending angle α are the two degrees of freedom varied in this work to compute a dimensionally-reduced PES of S_4.

vibrational motion are indispensable, but those would require a PES, which was not constructed in Ref. 68.

2.2. Benchmarking of the *Ab Initio* Methods

In this section we compare the results of several ab initio method and basis sets, and decide which method is the most appropriate for calculation of the PES.

Before computing the actual PES, we tested several levels of electronic structure theory by optimizing the C_{2v} and the D_{2h} geometries of S_4. Following the benchmark study of Ref. 66 by Francisco and coworkers, we repeated their CCSD(T) calculations with gradually increasing size of the basis set: aV(T+d)Z, aV(Q+d)Z and aV(5+d)Z. In addition, we carried out calculations at the CCSD(T)-F12a/VTZ-F12[54,55] level of theory, since it is known that the explicitly correlated methods generally provide faster convergence towards the CBS limit. The "*a*" version of the method was chosen according to a general recommendation on the MOLPRO's website. All calculations were done using MOLPRO[69,70] suit of electronic structure programs.

Tables 1 and 2 summarize optimized geometric parameters of the C_{2v} and the D_{2h} structures of S_4, including the lengths of the double bonds S=S, the length of the single bond S−S, the bending angle α, and the diatomic-diatomic distance R (introduced above and in Figure 7).

The first two rows of each table indicate that our CCSD(T) results are nearly identical to those of Francisco and coworkers (given in brackets for comparison). Comparison of the third and fourth rows of each table indicates that the results of the explicitly-correlated F12 method with a relatively small basis set VTZ, are close to the standard coupled-cluster results, obtained with a very large basis set aV(5+d)Z. Moreover, our F12 calculations were a factor of seven faster than the CCSD(T)/aV(5+d)Z calculations, which is another argument in favor of the explicitly-correlated approach.

Comparison with experimental data,[71,72] available for the minimum energy point (C_{2v}), indicates that our predictions obtained with the F12 method are off by just 0.005

Table 1. Geometric parameters of the equilibrium point of S_4 (C_{2v}).

Method	S=S (Bohr)	S-S (Bohr)	α (deg)	R (Bohr)
CCSD(T)/aV(T+d)Z	3.6188 (3.6188)	4.0857 (4.0862)	104.25 (104.25)	4.9765 (4.9769)
CCSD(T)/aV(Q+d)Z	3.6024 (3.6026)	4.0391 (4.0389)	104.65 (104.64)	4.9502 (4.9494)
CCSD(T)/aV(5+d)Z	3.5955	4.0310	104.55	4.9343
CCSD(T)-F12a/VTZ-F12	3.5949	4.0491	104.24	4.9336
Experiment[71]	3.5899	4.1070	103.98	4.9742
Experiment emp.[72]	3.5876	4.0726	104.22	4.9538

Table 2. Geometric parameters of the transition state of S_4 (D_{2h}).

Method	S=S (Bohr)	S-S (Bohr)	α (deg)	R (Bohr)
CCSD(T)/aV(T+d)Z	3.5944 (3.6128)	4.8393 (4.8583)	89.96 (90.00)	4.8366 (4.8583)
CCSD(T)/aV(Q+d)Z	3.5772 (3.5773)	4.8102 (4.8027)	89.88 (90.00)	4.8024 (4.8027)
CCSD(T)/aV(5+d)Z	3.5714	4.7926	89.88	4.7851
CCSD(T)-F12a/VTZ-F12	3.5710	4.7956	89.97	4.7939

(0.007) Bohr for the double-bond length, by 0.058 (0.024) Bohr for the single-bond length, and by 0.26 (0.02) degree for the bending angle, where the numbers in the brackets correspond to deviations from the empirically corrected experimental data.

Finally, comparison of the double-bond length S=S in Table 1 and Table 2 indicates that, by going from the C_{2v} to the D_{2h} geometry, it changes by just 0.024 Bohr, according to our F12 calculations (in fact, exactly the same change is predicted at the CCSD(T)/aV(5+d)Z level of theory).

Energies of critical points on the PES of S_4, relative to the minimum energy point (C_{2v}), computed using same four levels of the electronic structure theory are presented in Table 3. The second column of Table 3 gives energy of the transition state point in D_{2h} geometry, third column gives dissociation energy of S_4 computed as energy of isolated S_2 (in a triplet state) multiplied by two. These two columns, again, emphasize nearly perfect agreement of our results with the benchmark data of Francisco and coworkers (given in brackets for comparison) at the CCSD(T) level, except small differences by few wavenumbers in the case of the largest basis set.

Table 3. The relative energies of the critical points on the PES of S_4 (cm^{-1}).

Method	S_4 (D_{2h})	$2\times S_2$ (triplet)[a]	S_2+S_2 (singlet)	$2\times S_2$ (singlet)	S_2+S_2 (quintet)[a]
CCSD(T)/aV(T+d)Z	613.65 (613.65)	7082.45 (7082.45)	19361.90	19361.76	7082.45
CCSD(T)/aV(Q+d)Z	748.69 (748.69)	7896.90 (7896.71)	19993.77	19993.63	7896.89
CCSD(T)/aV(5+d)Z	766.89 (768.82)	8236.04 (8232.28)	20269.29	20269.43	8236.03
CCSD(T)-F12a/VTZ-F12	690.46	8853.45	20546.95	20546.79	8853.46

[a] The unrestricted open-shell version of the coupled-cluster was used for non-singlet systems.

Comparing results obtained with different methods one can see that transition state energy predicted by our F12 calculations with relatively small basis set is closer to result of CCSD(T)/aV(Q+d)Z (see Table 3). Namely, at the CCSD(T)-F12a/VTZ-F12 level of theory transition state energy is 690.46 cm^{-1}, which is 100 cm^{-1} below the value derived by Francisco and coworkers in the CBS limit based on two-point extrapolation. This seems to be acceptable, taking into account much lower cost of our calculations and the goal of covering large range of molecular shapes on the PES. Dissociation energy of S_4 (derived as $2\times S_2$, column 3 of Table 3) from our F12 calculations is 8853.45 cm^{-1}, which is closer to prediction of CCSD(T)/aV(5+d)Z. It exceeds the CBS limit of dissociation energy from Francisco and coworkers by only 269 cm^{-1}. This, again, attests for good accuracy of the explicitly-correlated approach, even when used with small basis set. The double-bond length in calculations for one individual S_2 is r = 3.5788 Bohr, at the UCCSD(T)-F12a/VTZ-F12[73–75] level of theory. Note that this value differs from the double-bond lengths in the equilibrium C_{2v} structure by 0.016 Bohr only (see Table 1).

However, one has to realize that although the data for an isolated S_2 are useful for thermochemical predictions, they are useless for construction of the global PES up to dissociation limit, where bond breakage should be described by calculations for S_2+S_2 super-molecule, in the overall singlet state. Thus, for the 2D-PES (discussed in the next section) dissociation energy for $S_4 \longrightarrow S_2 + S_2$ is found to be 20553.67 cm^{-1}, which overshoots the actual value by a factor of almost three. In fact, this failure is to be expected since it is well known that coupled-cluster theory, which is a single-reference approach, cannot be used to describe bond-breaking.

In order to investigate what this high-energy dissociation limit corresponds to, we carried out several additional calculations for super-molecule S_2+S_2 with dimer-dimer distance set to 20 Å, and double bonds allowed to relax. Results are also presented in Table 3, and they, indeed, indicate dissociation energy on the order of 20000 cm^{-1}. Looking at occupancy numbers of orbitals in these calculations we realized that the overall singlet state of the super-molecule is attained by placing each S_2 dimer into a singlet state (with all electrons paired, in contrast to the usual triplet configuration of the ground state of S_2 with two unpaired electrons). Thus, this high-energy dissociation threshold is an artifact of the closed-shell coupled-cluster method.

To solidify this conclusion, we also derived dissociation energy of S_4 as energy of an isolated S_2 in its singlet state, multiplied by two. As expected, results obtained in this way were nearly identical to those for S_2+S_2 super-molecule in the singlet state (see Table 3). Also, we carried out calculations for S_2+S_2 super-molecule in the overall quintet state, in order to restrict each S_2 dimer to its triplet configuration with two unpaired electrons. These calculations give correct prediction of dissociation energy, as one can see from Table 3. Optimized length of double-bonds in the super-molecule at F12 level of theory is 3.6053 Bohr which is only 0.01 Bohr longer than in the C_{2v} minimum of S_4, which, again, supports the frozen-bond approach for construction of the PES.

Our conclusion is that the coupled-cluster PES of singlet S_4 constructed in this work should be restricted to a reasonable vicinity of the equilibrium point and should not be used close to dissociation limit. Thus, we carry out calculations of vibrational states in S_4 up to energy of 2000 cm^{-1}. This is well above the D_{2h} transition state energy but is well below the dissociation limit.

2.3. PES Dimensionality Considerations

In this section we decide which degrees of freedom are to be included in our dimensionally-reduced model of PES.

Construction of a global PES for a tetra-atomic system is a challenging task,[76,77] which requires massive electronic structure calculations and state-of-the-art fitting techniques for the six internal vibrational degrees of freedom.[78–80] It is known, however, that rather useful insights can often be obtained based on a reduction of dimensionality in the problem.[81–84]

First, the data in Table 1 and Table 2 show that the double bond lengths change very little, just by 0.024 Bohr between the C_{2v} and the D_{2h} structures and even less in comparison with the dissociation limit value. Thus, we can neglect this small change and use, for the whole surface, one fixed value of r = 3.5949 Bohr, optimized for the C_{2v} configuration. This eliminates two degrees of freedom.

To make further assumptions, we explored the isomerization path by doing geometry optimizations at several intermediate points between the minimum (C_{2v}) and the transition state (D_{2h}). The results of these optimizations are summarized in Table 4. It shows that the minimum energy path goes through a planar configuration with both bending angles staying nearly equal (the maximum deviation is ~ 2°).

In addition to this we carried out scans along the torsional angle for the same five points (the minimum, the transition state, and the three points in between). The results are

Table 4. Optimized geometry parameters for different values of α_1 along the isomerization pathway, computed at the CCSD(T)-F12a/VTZ-F12 level of theory. See Figure 8 for the definitions of these parameters.

	α_1 = 90.00° (trans. state, D_{2h})	α_1 = 93.56°	α_1 = 97.13°	α_1 = 100.69°	α_1 = 104.24° (minimum, C_{2v})
α_2, degree	90.00	95.12	99.14	102.02	104.24
R, Bohr	4.7939	4.7985	4.8200	4.8623	4.9334
r_1, Bohr	3.5710	3.5737	3.5805	3.5881	3.5949
r_2, Bohr	3.5710	3.5747	3.5819	3.5893	3.5949
β, degree	0.00	0.00	0.00	0.00	0.00

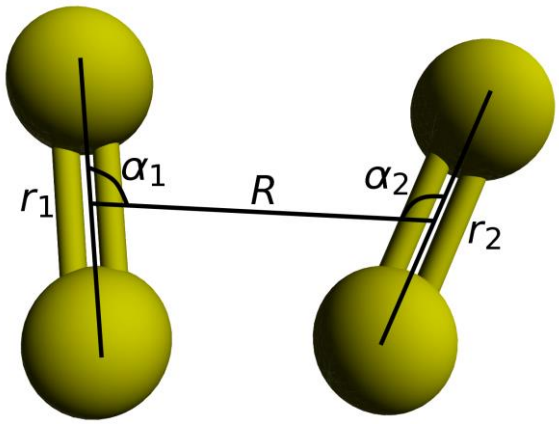

Figure 8. All degrees of freedom in the tetra-sulfur system. r_1 and r_2 are the internuclear distances in each S_2 dimer. R is the distance between the centers of mass of the two dimers. α_1 and α_2 are the bending angles between r_1 and R, and r_2 and R, correspondingly. The last degree of freedom, a torsional angle β (not shown) is defined as angle between the planes formed by segments (r_1,R) and (R,r_2).

summarized in Figure 9. One can see that the minimum energy point always corresponds to 0 degrees torsion (coplanar) and no other minima are observed in the significant energy range above that (about $10kT$ at room temperature). The same conclusion is also supported based on the findings of Ref. 68, where no three-dimensional structures were observed during the well-to-well isomerization process.

Based on these observations, we set the torsional angle equal to 0° and forced the two bending angles to be equal to each other, thus eliminating two more degrees of freedom.

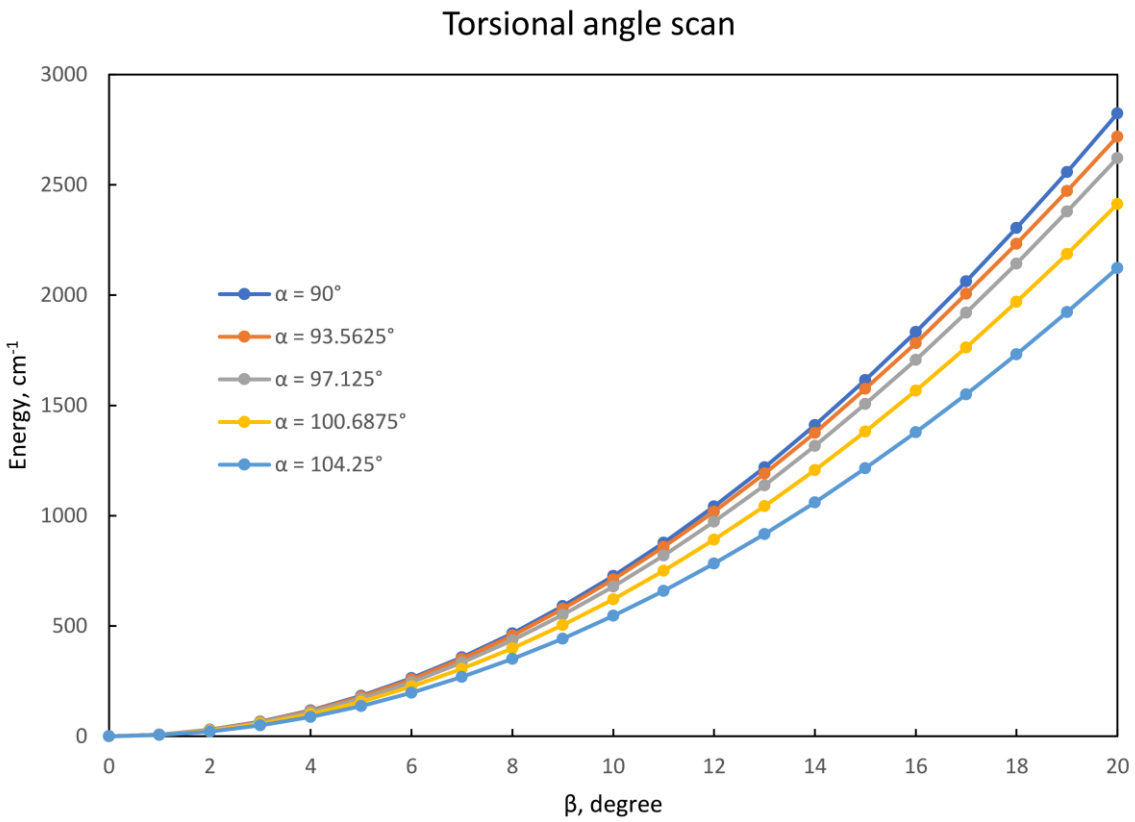

Figure 9. One-dimensional scans along the torsional angle β. Each color corresponds to a specific value of the "gearing" motion angle α. The value of R for each α was preoptimized to make sure that each starting point belongs to the isomerization pathway. The double bonds were frozen at the same values as we used for the PES calculations (r = 3.5949 Bohr).

2.4. Bonding Character in Tetrasulfur

The last question we want to discuss before proceeding to the PES calculations is bonding character (or bond order) in S_4. Qualitatively, this molecule can be represented as a complex of two weakly-perturbed S_2 molecules. Indeed, as one can see from Tables 1 and 2, the lengths of the two double-bonds in S_4 are less than 0.01 Å longer than in the unperturbed S_2 (3.5788 Bohr at UCCSD(T)-F12/VTZ-F12 level of theory). Moreover, the vibrational frequency of the double-bond symmetric stretch mode in S_4 (697.1 cm^{-1}) is only ~4% lower than the vibrational frequency of S_2 (728.8 cm^{-1}, both obtained at the CCSD(T)-F12a/VTZ-F12 level of theory). One can argue that the two unpaired electrons in the antibonding π orbital of one S_2 in a triplet state pair up with the two corresponding electrons of the other S_2, creating two bonds in S_4: one shorter and one longer. Authors of Ref. 66 came out with a similar conclusion and described S_4 as two dimers connected by one single bond (as shown in Figure 7).

However, Ref. 68 gives a picture of S_4 with one double bond in the middle and two single bonds at the terminal atoms. This is contradictory, so we decided to count occupancies of the bonding, antibonding and nonbonding molecular orbitals in S_4.

We found that the two S_2 dimers within S_4 are connected not only by a single bond on one side, but also by a weaker bond on the other side, as shown in the left frame

of Figure 10.This longer bond in S_4 has a bond order of roughly ½ and occurs due to several highly delocalized bonding orbitals in S_4, one of which is presented in the right frame of Figure 10. Thus, the process of isomerization between the two C_{2v} minima should not be described as a simple bending motion. Instead, it corresponds to swapping the shorter (single) bond with the longer bond (of the order of ½). This unusual bonding character has consequences for the vibrational modes in S_4, as will be shown further.

2.5. The Dimensionally Reduced PES (2D)

In this section, we construct the first potential energy surface for S_4, which covers two energetically equivalent C_{2v} isomers and the D_{2h} transition state between them. We use only two degrees of freedom: the distance R between center-of-mass points of the two S_2 moieties within S_4, and the bending angle α, as shown in Figure 7.

Ab initio calculations at the CCSD(T)-F12a/VTZ-F12 level of theory were carried out for S_4 geometries in the ranges $4.0 \leq R \leq 8.0$ Bohr and $90 \leq \alpha \leq 160°$, for 2714 points. Along R, size of the step was 0.05 Bohr for $4.2 \leq R \leq 6.0$ Bohr and was 0.1 Bohr outside

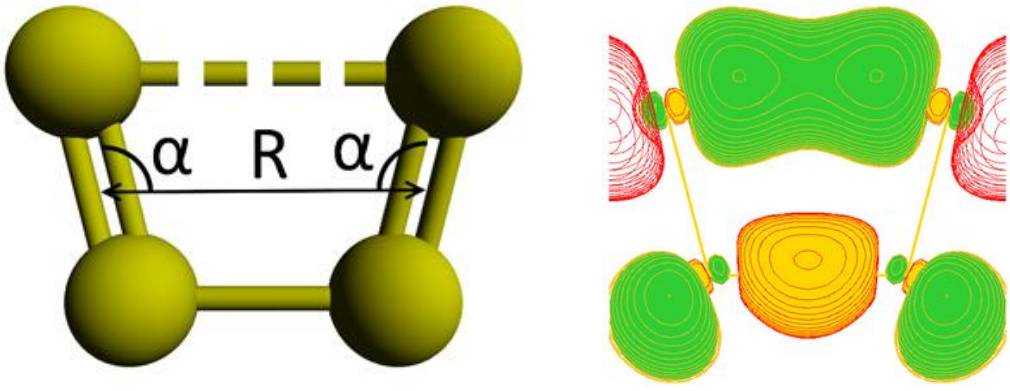

Figure 10. One of the occupied molecular orbitals in S_4. It has bonding character between the two most distant atoms in S_4, and therefore is responsible for formation of a weak bond between them (roughly, an order of ½). The value of the isosurface is 0.05. The two coordinates used for the PES are shown in the left frame. An interpretation of bonding in S_4 is given in the right frame, with the two weakly-perturbed S_2 dimers bonded on both sides.

(59 points total). Along α, size of the step was 1° degree for $90 \leq \alpha \leq 110°$ and was 2° outside (46 points total). A simple reflection through $\alpha = 90°$ was used to obtain the energies for the range $90 \leq \alpha \leq 160°$, since the two C_{2v} minima are energetically equivalent. This gave 5369 data points total, on both sides of the D_{2h} transition state. In order to build a continuous PES, two-dimensional bi-cubic spline interpolation of these data was employed using code written by Wolfgang Schadow.[85]

The PES is presented in Figure 11 as a function of two coordinates, $V(\alpha, R)$, in the energy range below $V = 2000$ cm^{-1}. The two equivalent wells, similar to those observed in other sulfur species,[86–88] are seen on the picture separated by the transition state at $\alpha = 90°$. The minimum is found at $R = 4.9336$ Bohr, the transition state is at $R =$

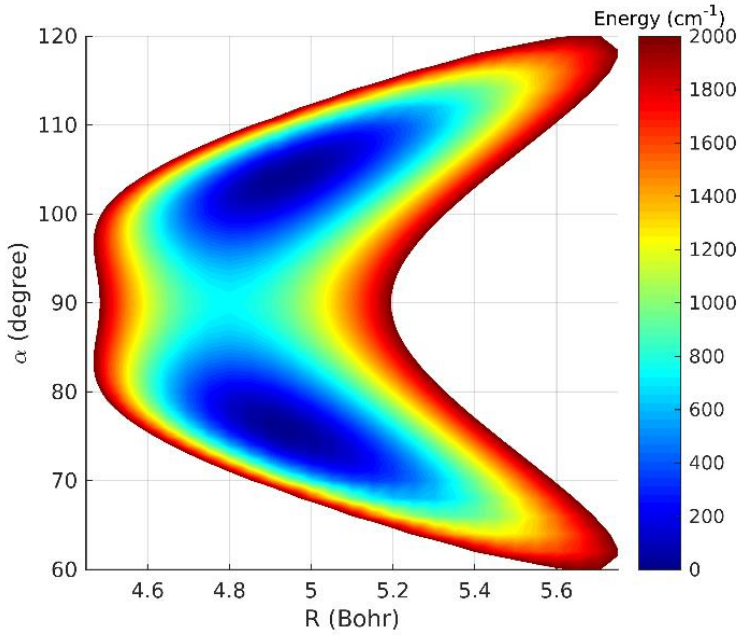

Figure 11. The 2D-PES of S_4 computed at the CCSD(T)-F12a/VTZ-F12 level of theory. The energy range below 2000 cm^{-1} is shown. Deep blue color indicates the two equivalent wells. The narrow transition state between them appears in turquoise. Red color, which encircles these features, corresponds to higher energy.

4.7939 Bohr (according to Table 1 and Table 2). The Fortran source files for this PES are available in the Supplemental Information of Ref. 89.

The PES is clearly anharmonic and exhibits a definite double-well structure. As the dimer-dimer distance *R* is increased, the minimum energy points shift towards more acute trapezoidal structures, further from the rectangular shape. Closer to the energy of 2000 cm^{-1} the PES acquires a very pronounced ε-shape. These properties indicate that prediction of the vibrational spectrum of S_4, based on conventional normal mode analysis at the minimum energy point, is likely to be inaccurate.

The 2D-model of the PES of tetrasulfur, considered in the previous section, is the simplest possible approximation of the tetrasulfur recombination reaction (11). Although it is useful as a first step, it is only suitable for the low-energy isomerization pathway exploration. In order to expand it to higher energies, a few changes are necessary:

1. As the discussion after Table 3 mentions, single reference methods cannot be used to adequately describe bond-breaking processes, so the dissociation limit of our 2D PES overshoots the actual limit by a factor of almost 3. This was not a problem for the purposes of studying the isomerization process and properties of the low-lying states, but for the tetrasulfur recombination reaction (11) we need higher energy parts of the spectrum, so the correct dissociation limit is necessary. One way to obtain correct dissociation energy is to use a multi-reference method, such as Multi-Reference Configuration Interaction (MRCI).[56–58,90] MRCI is a rigorous and powerful but expensive method: calculation of a single point on the PES takes up to 24 hours on a 32-core node.

2. Outside of the plane with the isomerization pathway our geometries are not restricted to 2D, so we need to consider other degrees of freedom. The double-bonds

stretching and torsional motion are fairly harmonic (see Figure 9) and independent as shown in Section 3 below, so they can be approximated with an analytical model. The second bending angle, however, is harder to approximate analytically so in the 3D model we decided to make it independent.

2.6. The Global PES of S_4 (3D)

The three-dimensional PES calculations are ongoing at MRCI+Q/aug-cc-pV(T+d)Z level of theory with full valence active space and Davidson correction using 2-state average, where the convergence criterion for the upper state is reduced for speedup. The PES is divided into two regions with different densities of the points:

1. The "isomerization plane" $\alpha_1 = \alpha_2$ (the 2D PES we considered previously). Since this is an especially important part of the PES, the density of points is higher here.

2. The space outside of the isomerization plane ($\alpha_1 \neq \alpha_2$). The density of points is lower here.

The bending angles are sampled in the range $30° \leq \alpha_1, \alpha_2 \leq 150°$ with a step of 5° in the isomerization plane and 10° outside.

Furthermore, one can take advantage of the fact that the behavior of the PES near the dissociation limit is smooth and does not require as many points as in the covalent well region, so the step size along the *R*-coordinate varies as well. In the isomerization plane the considered values of *R* are $4 \leq R \leq 8$ Bohr with a step size of 0.1 Bohr, $8 \leq R \leq 12$ Bohr with a step size of 0.5 Bohr and $12 \leq R \leq 20$ Bohr with a step size of 1 Bohr. Outside of the isomerization plane the considered values of *R* are $4 \leq R \leq 10$ Bohr with a step size of 0.4 Bohr, as well as 12, 16 and 20 Bohr.

Distribution of points computed so far is presented in Figure 12. Note that because of the symmetry considerations, only the solid symbols in Figure 12 actually need to be computed, the rest can be obtained by symmetry reflections. Indeed, a point with coordinates (α_1, α_2) is indistinguishable from point (α_2, α_1). This symmetry can be viewed as reflection through the isomerization plane. Moreover, another kind of

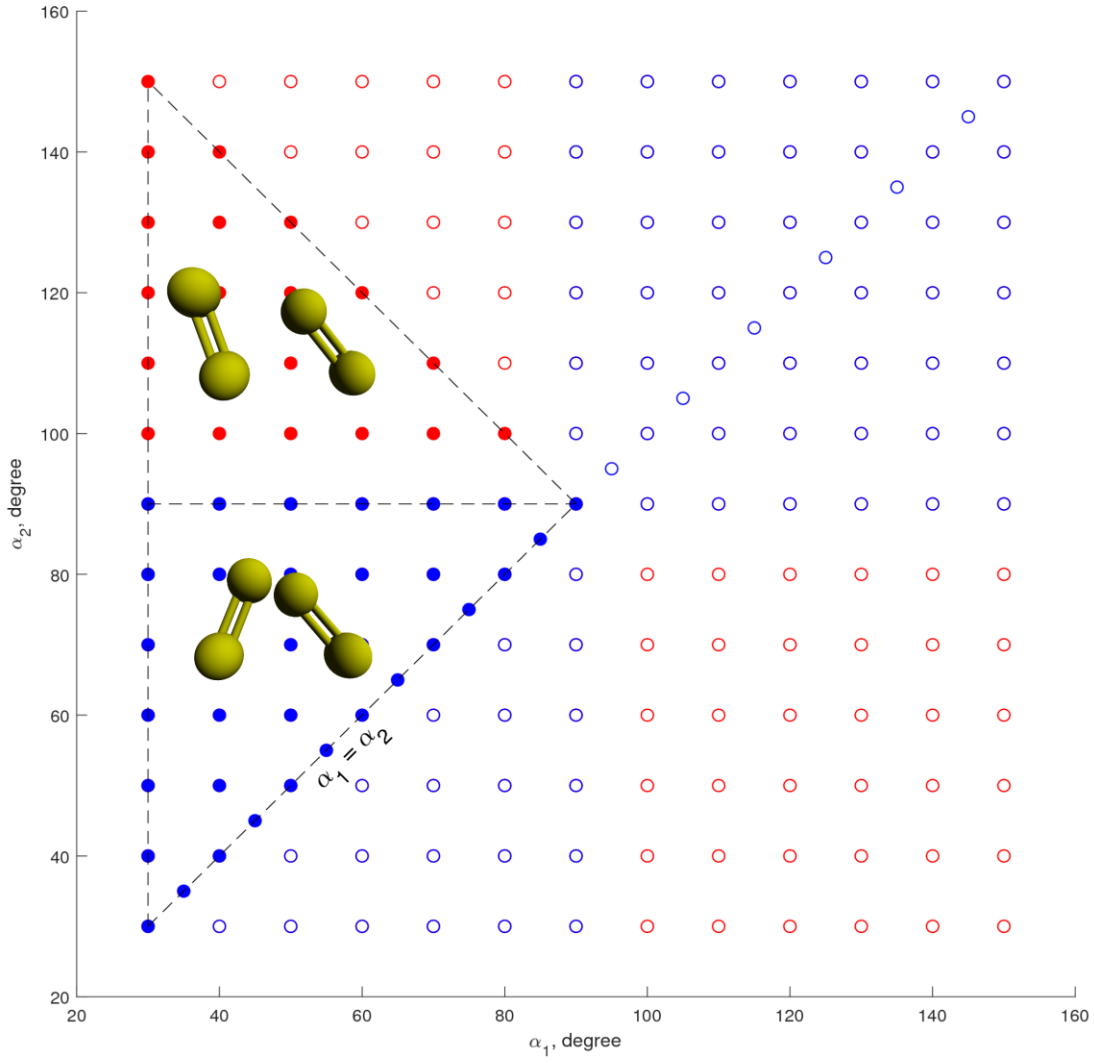

Figure 12. Distribution of points as viewed in the (α_1, α_2) plane for MRCI calculations. The blue circles are conditionally associated with cis-isomer, the red circles are conditionally associated with trans-isomer. Calculation at the hollow symbols are unnecessary since they are identical to one of the solid points.

symmetry tells us that (α_1, α_2) is the same as (180 – α_1, 180 – α_2), which represents inversion through the rectangular (90, 90) configuration.

Figure 13 shows a view of the points distribution along the reaction coordinate *R*. This can be considered as a "side" view of Figure 12. The size of step along *R* was selected based on the analysis of spline interpolation behavior applied to the previously computed 2D surface. The points computed so far (marked blue in Figure 12 and Figure 13) allow one to visualize the isomerization path.

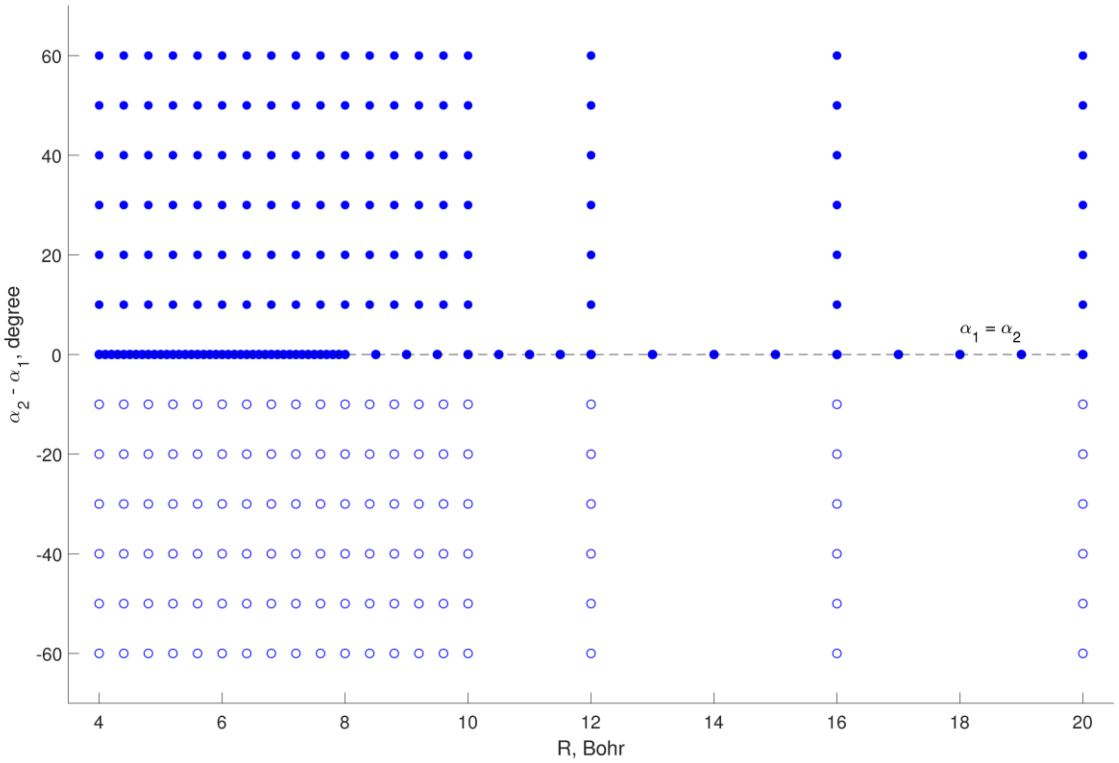

Figure 13. Distribution of points as viewed in the (*R*, α_2) plane for MRCI calculations. The dashed black line represents the isomerization plane ($\alpha_1 = \alpha_2$). The points are denser in the covalent well region (4-10 Bohr) and more rarefied outside. The isomerization plane is an important region, so more points are placed in it.

One-dimensional slices through the isomerization path of the PES are shown in Figure 14. The whole isomerization plane of the PES is shown in Figure 15.

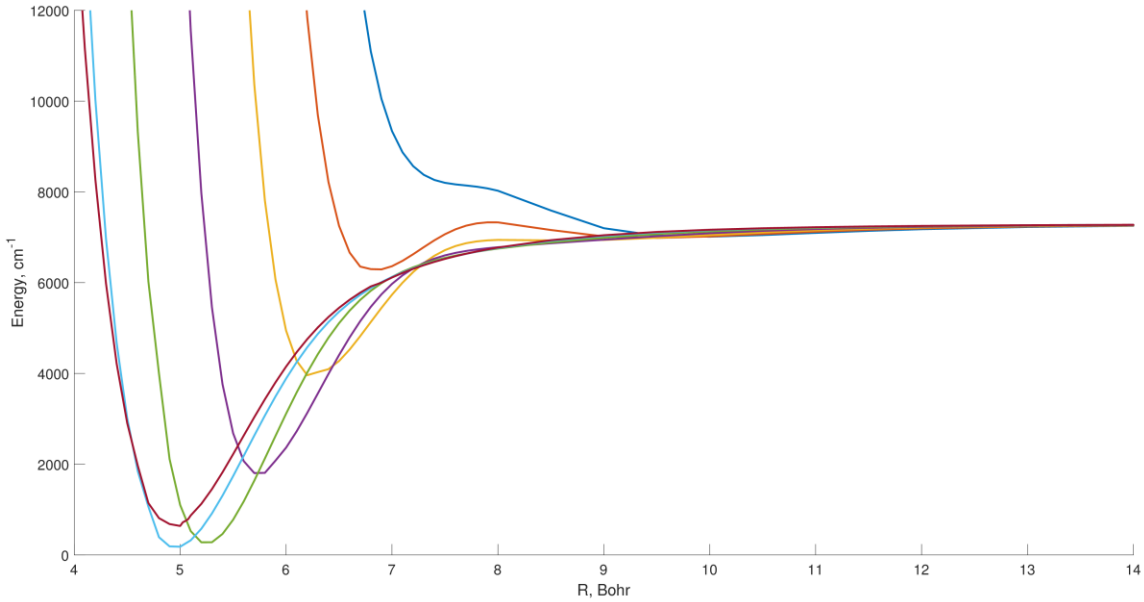

Figure 14. 1D slices through the isomerization plane of the PES.

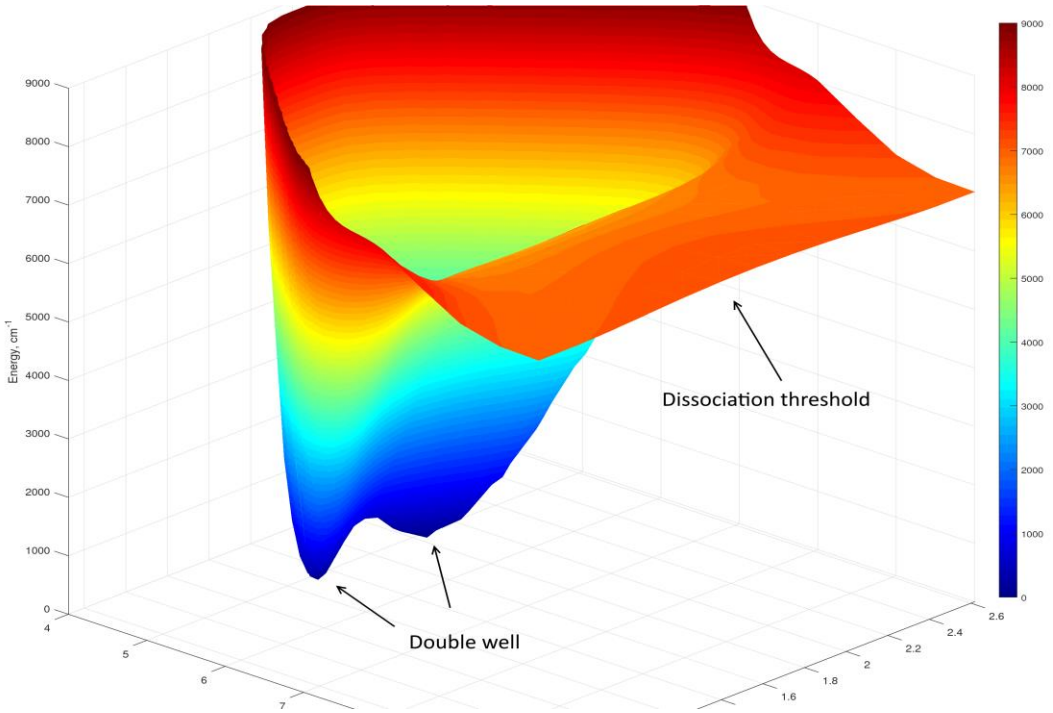

Figure 15. A part of the of the PES 3D PES of S_4 computed at MRCI/aug-cc-pV(T+d)Z level of theory. The colorbar units are in cm^{-1}. The dissociation threshold can be seen clearly.

Another view of the surface in (α_1, α_2)-plane, where *R* is relaxed is given in Figure 16. The diagonal on this figure, where the two angles are equal, is the isomerization plane, which was the focus of the previously computed 2D PES. The global double-well minimum (dark blue) is associated with the cis-isomer of tetrasulfur. In addition to the global minimum, one can see that at the energies close to the dissociation threshold of tetrasulfur, there is a transition state, leading to a pair of secondary wells, corresponding to trans-isomers of tetrasulfur. Analysis of the trans structures and their relevance to the recombination reaction of tetrasulfur is a work in progress and will be reported elsewhere.

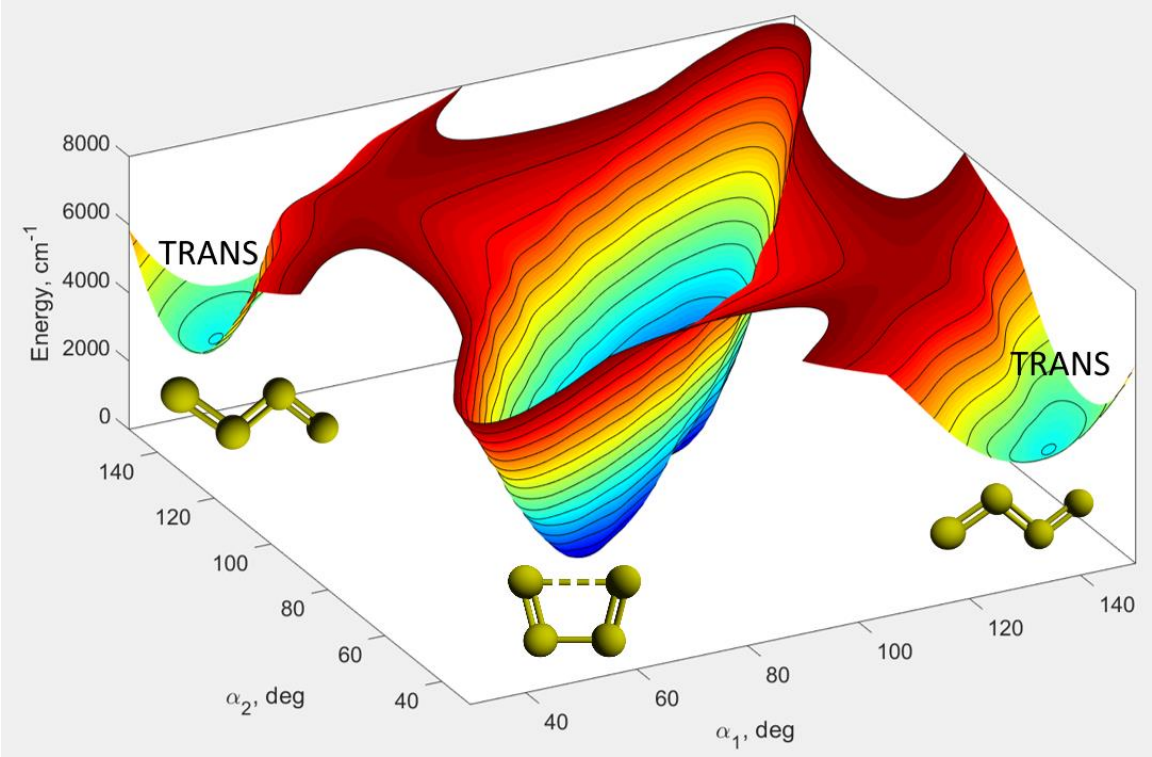

Figure 16. The 3D potential energy surface of S_4 computed at MRCI/aug-cc-pV(T+d)Z level of theory, viewed as a function of the two bending angles α_1 and α_2. The values of *R* at each point are selected to minimize energy.

The obtained results can be used to estimate geometries and energies of the critical points on the global PES. Geometry parameters for the minimum energy point and transition state are presented in Tables 5 and 6. The first row of Table 5 shows the new results obtained at MRCI+Q/aug-cc-pV(T+d)Z level of theory. The numbers in parenthesis show analogous results, computed by Francisco and coworkers[66] at the same level of theory. Small discrepancies in the bending angle are explained by different reference function: the authors of Ref. 66 retained the 50 most important configurations from a preceding CASSCF calculation, whereas we did not exclude any configurations.

The remaining rows summarize the results already presented in Tables 1 and 2 and are included here for the purpose of comparison with MRCI. One can see that the

Table 5. Geometric parameters of the equilibrium point of S_4 (C_{2v}).

Method	S=S (Bohr)	S-S (Bohr)	α (deg)	R (Bohr)
MRCI+Q/aug-cc-pV(T+d)Z	3.6230 (3.6230)	4.1592 (4.0969)	103.89 (105.26)	5.0291 (5.0505)
CCSD(T)/aV(T+d)Z	3.6188 (3.6188)	4.0857 (4.0862)	104.25 (104.25)	4.9765 (4.9769)
CCSD(T)-F12a/VTZ-F12	3.5949	4.0491	104.24	4.9336
Experiment [44]	3.5899	4.1070	103.98	4.9742
Experiment emp.[45]	3.5876	4.0726	104.22	4.9538

Table 6. Geometric parameters of the transition state of S_4 (D_{2h}).

Method	S=S (Bohr)	S-S (Bohr)	α (deg)	R (Bohr)
MRCI+Q/aug-cc-pV(T+d)Z	3.6230[a]	4.9767	90.00	4.9767
CCSD(T)/aV(T+d)Z	3.5944 (3.6128)	4.8393 (4.8583)	89.96 (90.00)	4.8366 (4.8583)
CCSD(T)-F12a/VTZ-F12	3.5710	4.7956	89.97	4.7939

[a)] The length of double-bond is frozen in our calculations

geometries obtained with MRCI are a little further from the experiment as compared to those, obtained with the coupled-cluster methods.

Table 6 shows somewhat scarcer information available for the geometries of the transition state of S_4. The authors of Ref. 66 did not present results of MRCI calculations for the transition state, so only our results are shown. Note, that the value of double-bond length is the same as for the minimum energy point. This is because the double-bond length was frozen in our PES calculation, so this value was not optimized and given for comparison purposes.

The relative energies of the critical points on the PES of S_4 are given in Table 7. One can see the main advantage of MRCI method: the dissociation limit, given in column 3, has a reasonable value now. The computed results are in good agreement with a similar MRCI calculation carried out by Francisco and coworkers[66] (given in parenthesis), as well as with the results of coupled-cluster method with the same basis set.

The coupled-cluster results, extrapolated in Ref. 66, to 8219.2 cm^{-1} and 8390 cm^{-1} at 298 K using DTQ and Q5 extrapolations respectively, are close to the experimentally measured value of 9275 $\pm$ 715 cm^{-1}, which allows to conclude that the MRCI results are reasonable at 0 K for this basis set.

Table 7. The relative energies of the critical points on the PES of S_4 (cm^{-1}).

Method	Isomerization energy	Dissociation energy[b]
MRCI+Q/aV(T+d)Z	637.90	7288.25 (7205)
CCSD(T)/aV(T+d)Z	613.65 (613.65)	7082.45 (7082.45)
CCSD(T)-F12a/VTZ-F12	690.46	8853.45

a) The unrestricted open-shell version of the coupled-cluster was used for non-singlet systems.

b) Computed as 2 x S_2 for coupled cluster methods and S_2 + S_2 supermolecule for MRCI

2.7. Summary

In this chapter, we carried out *ab initio* calculations for the tetra-sulfur molecule, S_4, with a goal to understand its electronic structure in the double-well region of the PES. Two potential energy surfaces were considered. The first one is the simplest possible 2D model, focused on the understanding of the isomerization pathway structure. Two degrees of freedom were taken into account: the dimer-dimer distance *R*, and the gearing motion angle α. Based on careful benchmarking against earlier calculations by other authors, we have chosen the CCSD(T)-F12a/VTZ-F12 level of theory (within the MOLPRO program), as a compromise between accuracy and speed of calculations. To the best of our knowledge, this 2D-PES is the first ever constructed. The Fortran source files for this PES are available in the Supplemental Information of Ref. 89.

One interesting finding of this work is the interpretation of bonding character in S_4. We noticed that the two weakly-perturbed S_2 dimers (within S_4) are connected by *two* bonds on their both sides, forming a trapezoidal structure, which can be viewed as an intermediate between a closed ring with two equal bonds, and an open *cis*-isomer with only one single bond between the two S_2 dimers. The newly identified bond is longer and weaker (the bond order is roughly ½) than the other single bond in S_4, but it has important implications for the vibrational motion of S_4.

The second model of the PES is focused on the global description of the tetrasulfur recombination reaction (11) up to the dissociation threshold. The calculations of the second PES are ongoing at the MRCI/aug-cc-pV(T+d)Z level of theory, which is required to adequately calculate electronic energy in the region of bond dissociation. The

second bending angle is introduced for this surface, which raises the dimensionality to 3D.

This surface will offer a theoretical prediction of the density of states near the dissociation threshold and above it. Using this information one can compute reaction rate constants and equilibrium constants, which allows to estimate the magnitude of isotope fractionations given by Eqs. (7) and (10) in the Introduction.

CHAPTER 3. VIBRATIONAL STATES CALCULATIONS FOR TETRASULFUR

In this chapter we consider calculation and analysis of vibrational states on 2D potential energy surface (PES), constructed in Chapter 2 for tetrasulfur.[89] The computed states are used to compare with the existing data to estimate accuracy of dimensionally-reduced approach and determine further research directions.

3.1. Methodology of Calculation of the Vibrational States

We solve numerically the time-independent Schrodinger equation for the vibrational motion in two dimensions, $\hat{H}\,\psi(\alpha,R) = E\,\psi(\alpha,R)$, where the Hamiltonian operator $\hat{H} = \hat{T} + V(\alpha,R)$ contains the 2D-PES discussed in the last section. The two degrees of freedom are introduced to describe the distance R between the centers of mass of the two S_2 dimers within S_4, and simultaneous symmetric bending of the two dimers, denoted α (the gearing motion). The higher frequency vibration of S_2 dimers is neglected (they are kept rigid), and the motion of all the atoms is restricted to one plane. The overall rotation of S_4 is not included ($J = 0$). Then, a kinetic energy operator is:[91]

$$\hat{T} = \hat{T}_R + \hat{T}_\alpha = -\frac{\hbar^2}{2\mu}\frac{\partial^2}{\partial R^2} - 2\frac{\hbar^2}{2I}\frac{\partial^2}{\partial \alpha^2} \tag{21}$$

Here, the first term describes relative motion of the two dimers. Reduced mass μ, in the case of all equal masses (e.g., the same most abundant isotope ^{32}S), appears to be equal to the mass of one sulfur atom:

$$\mu = \frac{m_{S_2} m_{S_2}}{m_{S_2} + m_{S_2}} = \frac{m_{S_2}}{2} = m_S \tag{22}$$

The second term of the kinetic energy operator describes rotations of the two dimers, each around its center of mass, by the same angle α, all in one plane. The moment of inertia *I* of each diatomic, in the case of equal masses, is given by

$$I = 2m_S\left(\frac{r}{2}\right)^2 = \frac{1}{2}m_S r^2 \tag{23}$$

where r is the bond length of the diatomic moiety. The factor of 2 in Eq. (23) is because there are two atoms in each dimer, while the factor of 2 in front of the second kinetic energy term in Eq. (21) is due to the two simultaneously rotating dimers.

A computational approach we adopted includes the Sequential Diagonalization Truncation (SDT) technique,[92,93] which allows to greatly reduce the size of the Hamiltonian matrix. First, we generate a grid of *N* points along R. For each point *n* on the grid, we make a slice of the PES along coordinate α, named $V_n(\alpha) = V(\alpha, R_n)$, and solve the one-dimensional Schrodinger equation for the motion along this slice:

$$\hat{h}^n\,\phi_k^n(\alpha) = \varepsilon_k^n\,\phi_k^n(\alpha) \tag{24}$$

where $\hat{h}^n = \hat{T}_\alpha + V_n(\alpha)$ is the corresponding 1D Hamiltonian operator. Index *k* labels 1D-solutions within a given slice *n*, which includes the energies ε_k^n and the wave functions $\phi_k^n(\alpha)$.

Some examples of one-dimensional solutions in a slice through the transition state are shown in Figure 17. One can see how the spectrum evolves as it transitions from the double-well behavior to the global single-well behavior. At low energies, the antisymmetric and symmetric states are nearly degenerate. However, above the isomerization barrier (starting from the third quantum of excitation), non-negligible splittings appear and intensify as the states move higher in energy, gradually transforming the spectrum character into that of the classical single-well harmonic oscillator, where symmetric and antisymmetric states alternate. If Ψ_a and Ψ_b are the "solutions" in each well, then the global symmetric and antisymmetric solutions can be thought of as $\frac{1}{\sqrt{2}}(\Psi_a + \Psi_b)$ and $\frac{1}{\sqrt{2}}(\Psi_a - \Psi_b)$, respectively.

Couplings between different values of R are contained in an overlap matrix:

$$O_{kl}^{nm} = \langle \phi_l^m | \phi_k^n \rangle \tag{25}$$

These couplings are taken into account at the second step of the calculations, when the 1D wave functions $\phi_k^n(\alpha)$ from all the slices R_n are collected and used to form

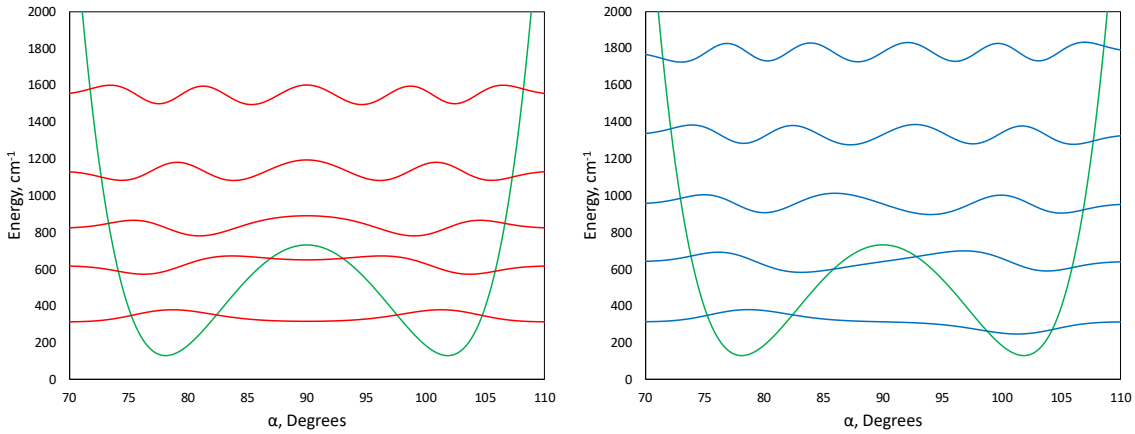

Figure 17. Example of series of 1D solutions in a slice through the transition state. The symmetric and antisymmetric solutions are shown on the left and right frame, respectively. The green line is the potential energy in the slice.

an efficient (locally optimal) basis for representation of the overall 2D Hamiltonian matrix:[93]

$$H_{kl}^{nm} = O_{kl}^{nm} \times T_R^{nm} + \delta_{kl}\,\delta_{nm}\,\varepsilon_k^n \qquad (26)$$

Here, T_R^{nm} is a matrix element of the kinetic energy operator $\hat{T}_R$ in the DVR basis (which is a grid of *N* points R_n) and δ is the Kronecker symbol. A block-structure of the overall Hamiltonian matrix H_{kl}^{nm} was discussed in detail in Ref. 94. It has the same size as O_{kl}^{nm} and is obtained from it by multiplying each its R-blocks with the corresponding matrix element T_R^{nm}, and then adding to each diagonal element the corresponding value of the one-dimensional energy ε_k^n.

Efficient reduction of the Hamiltonian matrix size is achieved by truncating the number of the basis functions $\phi_k(\alpha)$ in each slice, independently, using one global value of cut-off energy. In this work, only the functions with $\varepsilon_k < 8000$ cm^{-1} were included in the basis. Closer to the edges of the grid, where the energies are high and no states with $\varepsilon_k < 8000$ cm^{-1} are present at all, ten lowest energy states were still retained in each slice.

This process is reflected in Figure 18. One can see that at the edges of the grid we have very few basis functions, while in middle of the grid, in the region of deep covalent well, many basis functions are retained. This allows to optimize the size of the Hamiltonian matrix by keeping more solutions only in the regions where higher flexibility is needed.

The resultant Hamiltonian matrix was diagonalized using LAPACK[95] software, to obtain the energies E and the wave functions $\psi(\alpha, R)$ of the 2D-states.

The one-dimensional Schrodinger equation for α (at each value of R) was solved using a VBR of cosine or sine functions.[94] Namely, for the antisymmetric solutions we used:

$$\phi(\alpha) = \sum_{j=1}^{M} a_j \, f_j(\alpha) \tag{27}$$

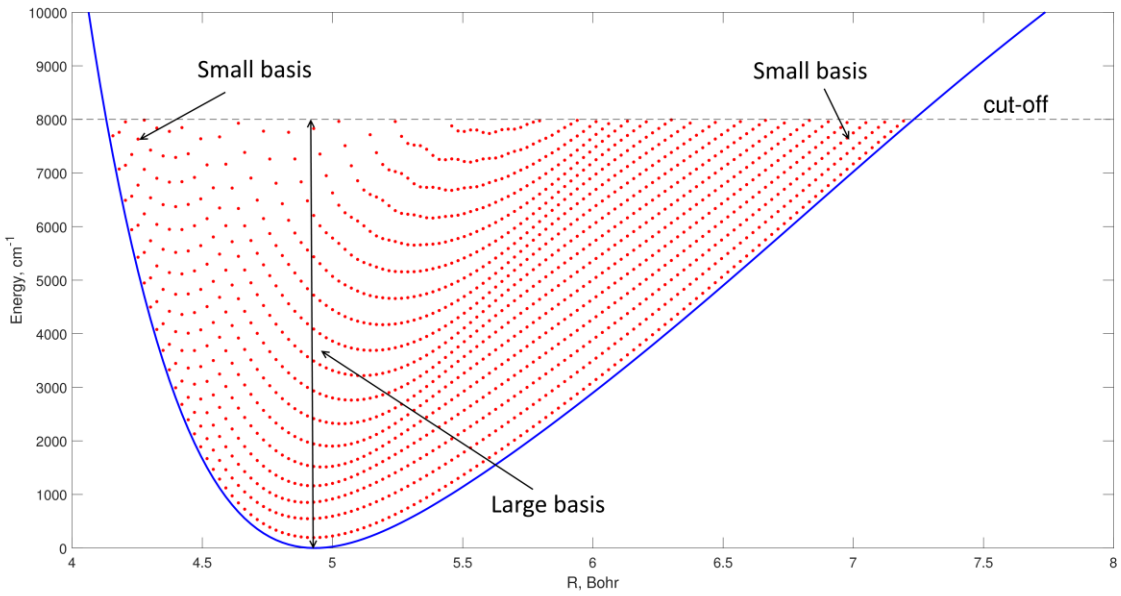

Figure 18. One-dimensional energies computed in each slice along the reaction coordinate *R*. The blue curve represents the minimum energy path along *R*. Red dots show 1D energies for each value of *R* in the grid. Cut-off value of 8000 cm^{-1} is shown with the dashed line.

$$f_j(\alpha) = \frac{1}{\sqrt{\alpha_{max}}} \sin\left\{\frac{\pi j}{\alpha_{max}}\left(\alpha - (90 - \alpha_{max})\right)\right\} \tag{28}$$

Similar definitions are used for the symmetric solutions, except that $\cos\{...\}$ functions are used instead of the $\sin\{...\}$ and the first function of the symmetric basis set is $f_0(\alpha) = 1/\sqrt{2\alpha_{max}}$. The range of α around the symmetry plane is determined by one parameter: $\alpha \in 90° \pm \alpha_{max}$. We set α_{max} = 70°, which gives the overall grid range 20 ≤ α ≤ 160°, same as for the PES. The basis set size *M* is a convergence parameter. In this basis set, elements of the 1D Hamiltonian matrix are given by:

$$h_{ij} = \frac{1}{2\mu}\left(\frac{\pi j}{\alpha_{max}}\right)^2 \delta_{ij} + v_{ij}, \qquad i,j \le M \tag{29}$$

The matrix of the kinetic energy operator is analytic and diagonal, with $h_{00} = 0$. The elements of the potential energy operator $v_{ij} = \langle f_i(\alpha)|V_n(\alpha)|f_j(\alpha)\rangle$ are computed numerically, using a large 1D quadrature of equally spaced points.

Note that the sequential mixed VBR/DVR approach allows us to separate the symmetric and the antisymmetric solutions at the level of 1D, thus reducing the total size of the 2D Hamiltonian matrix by a factor of two. This also provides automatic assignments of symmetry to the numerical solutions.

The elements of the kinetic energy operator for *R* (in the DVR basis) were computed numerically using Fourier transform to compute derivatives. The same result could be obtained analytically:[96,97]

$$T_R^{nn} = \frac{\pi^2}{\mu L^2}\frac{N^2+2}{6} \tag{30}$$

$$T_R^{nm} = (-1)^{n-m}\frac{\pi^2}{\mu L^2}\frac{1}{\sin^2[(n-m)\pi/N]} \tag{31}$$

where L is the length of R grid in Bohr. The difference between the energies obtained with the analytic formula and with the numerical evaluation is of the order of 0.01 cm^{-1}.

The number of points for the 1D quadrature along α was 3038, and the corresponding basis set size M was 40. The number of points along R was 166, and the size of the truncated 2D Hamiltonian matrix was 2059 x 2059.

3.2. Results of Calculation of the Vibrational States of Tetrasulfur (S_4)

We carried out accurate calculations of the vibrational state energies and the wave functions $\psi(\alpha, R)$ on our dimensionally reduced PES of S_4 using a rigorous method described in the last section.

The energies and the assignments of the states in terms of the two vibrational modes, v_1 and v_2, are presented in Table 8. We identified 29 symmetric and 28 antisymmetric states with the energies below 2000 cm^{-1}. Symmetry is defined with respect to a reflection through $\alpha = 90°$.

The assignments of the states were carried out based on the shapes of their wave functions and their energies relative to the other states in a vibrational progression. At low energies either of these two methods can be used to obtain a fairly certain and non-contradictory assignment. Among the 57 states in Table 8, more than half are assigned unambiguously.

However, at high energies both approaches fail to provide a definitive assignment. The vibrational modes start mixing up , making the shapes of the wave functions rather

Table 8. The energies and assignments of the vibrational states on the 2D-PES of the S_4 (cm^{-1}).

State	Symmetric	Antisymmetric	(v_1, v_2)
1	317.63	317.65	(0,0)
2	491.82	492.17	(1,0)
3	658.24	661.18	(2,0)
4	737.91	741.41	(0,1)
5	813.15	827.83	(3,0)
6	886.86	911.81	(1,1)
7	964.76	995.00	(4,0)
8	1023.63*	1076.35	(2,1)
9	1105.87*	1129.98	(0,2)
10	1133.62*	1163.79	(5,0)
11	1185.30*	1251.05	(3,1)
12	1245.09*	1310.70*	(1,2)
13	1305.72*	1335.71*	(6,0)
14	1359.35*	1427.26	(4,1)
15	1392.11*	1484.55*	(7,0)
16	1433.98*	1490.09*	(0,3)
17	1490.82*	1519.45*	(2,2)
18	1536.81*	1603.23	(5,1)
19	1582.66*	1655.94	(8,0)
20	1606.23*	1695.98*	(3,2)
21	1660.86*	1716.27	(1,3)
22	1701.25*	1777.78	(6,1)
23	1750.53*	1822.38	(9,0)
24	1760.22*	1859.03	(0,4)
25	1808.90*	1888.56*	(4,2)
26	1847.91*	1924.57	(2,3)
27	1879.89*	1951.79	(7,1)
28	1933.75*	1988.10	(10,0)
29	1977.01*		(5,2)

complicated, especially beyond the second quanta of excitation in the “gearing” mode, labeled by v_2. In such cases we combined input from both approaches, using energy as the main criterion to narrow down possible choices and then judging by the shape of a wave function. In addition to that, we used antisymmetric states assignments as a guidance for the symmetric states. It turned out that assignments for both symmetries are identical.

We also found that some progressions retain their definitive features even at higher energies, such as the long v_1-progressions with $v_2 = 0$ or $v_2 = 1$ (see Figures 19 and 20), thus allowing a definite assignment.

Other progressions deteriorate faster, thus making the corresponding assignments less certain. These ambiguous assignments are marked by an asterisk in Table 8. In the considered energy range, about 50% of the states are assigned ambiguously, particularly those with more than one quantum of excitation in the second mode.

The primary reason for the ambiguity of state assignments is evolution of the spectrum from the local double-well character at lower energies, where the symmetric and the antisymmetric states are expected to be (nearly) degenerate, to the global character above the isomerization threshold, where the symmetric and the antisymmetric states should alternate in the spectrum.

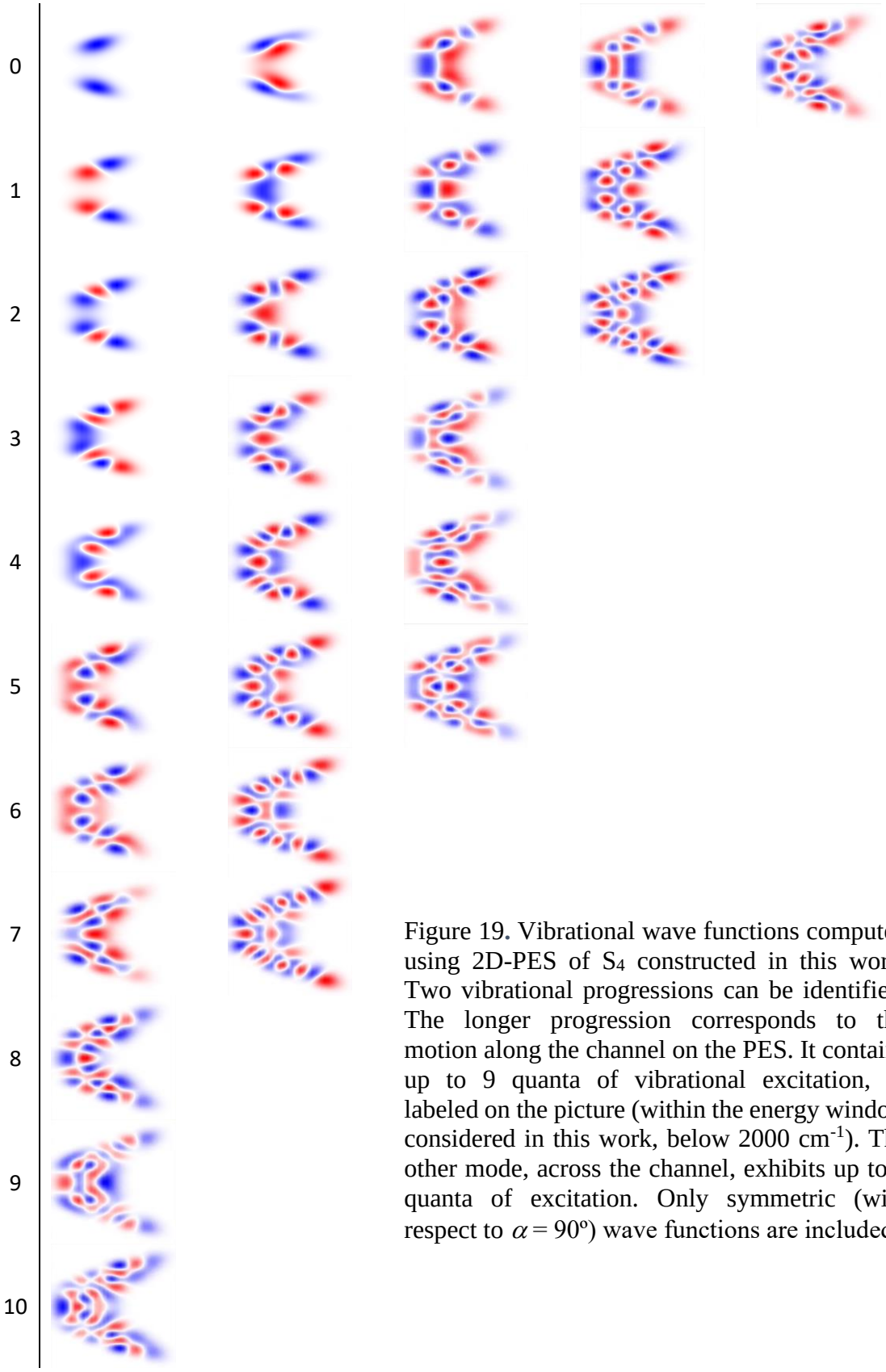

Figure 19. Vibrational wave functions computed using 2D-PES of S_4 constructed in this work. Two vibrational progressions can be identified. The longer progression corresponds to the motion along the channel on the PES. It contains up to 9 quanta of vibrational excitation, as labeled on the picture (within the energy window considered in this work, below 2000 cm^{-1}). The other mode, across the channel, exhibits up to 4 quanta of excitation. Only symmetric (with respect to $\alpha = 90^{o}$) wave functions are included.

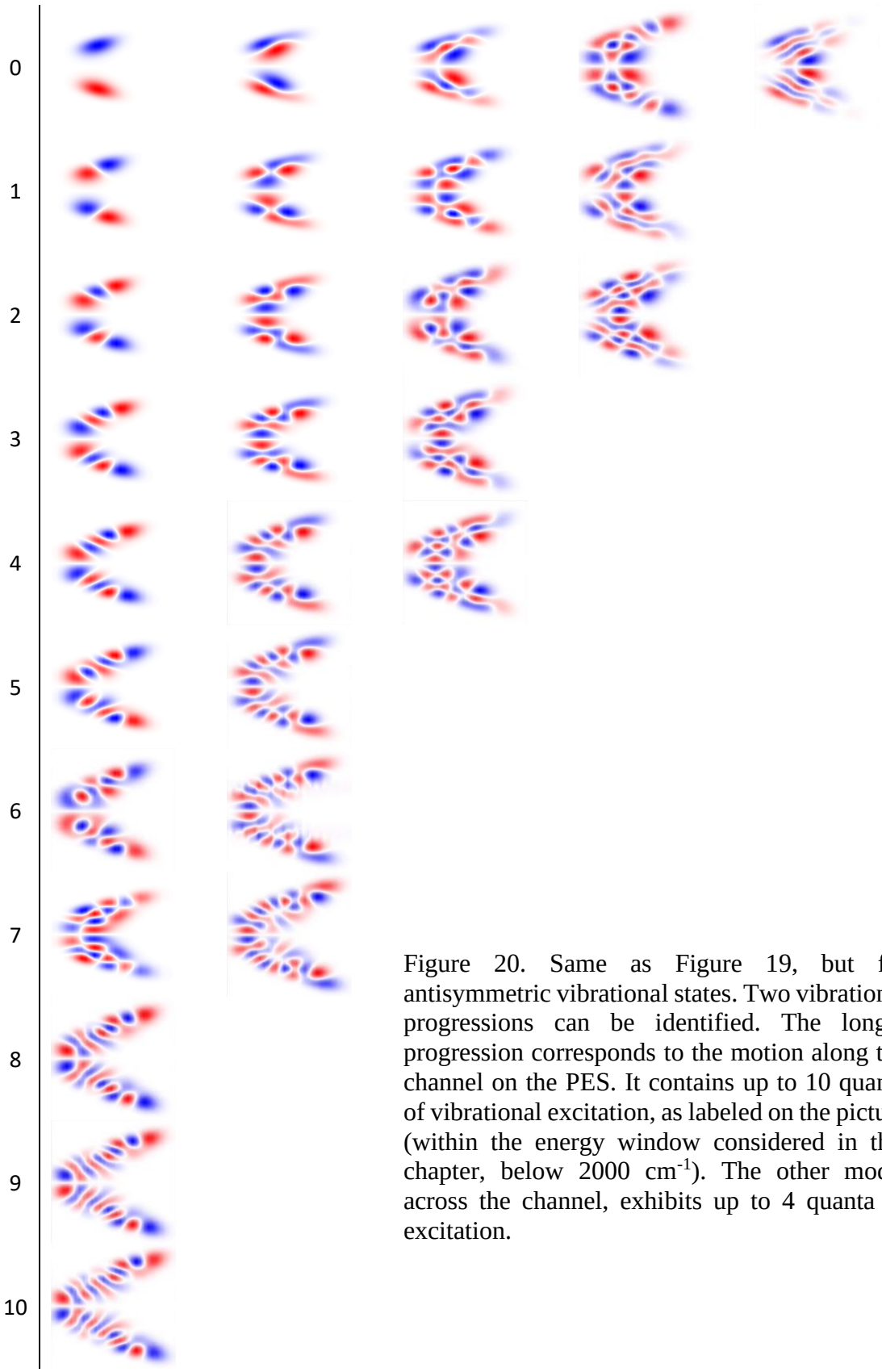

Figure 20. Same as Figure 19, but for antisymmetric vibrational states. Two vibrational progressions can be identified. The longer progression corresponds to the motion along the channel on the PES. It contains up to 10 quanta of vibrational excitation, as labeled on the picture (within the energy window considered in this chapter, below 2000 cm^{-1}). The other mode, across the channel, exhibits up to 4 quanta of excitation.

This is illustrated by Figure 21, where a one-dimensional slice of the PES along α (with fixed $R = 4.7939$ Bohr) is shown, together with the one-dimensional states $\psi(\alpha)$ computed for this slice. The first pair of the symmetric and the antisymmetric states is, indeed, nearly degenerate. The second pair shows a non-negligible splitting, while the third pair of states is already in high energy part of the spectrum, where the symmetric and the antisymmetric states alternate. This fast evolution of the vibrational states character in S_4 manifests in the two-dimensional spectrum reported in Table 8, and leads to irregularities of state energies in several vibrational progressions.

3.3. Fitting of the Vibrational Energies

We found that, overall, it is easier to assign progressions of the antisymmetric states, because their wave functions are required to vanish at $\alpha = 90°$, which results in a more regular and more independent nodal structure in the two wells of the PES. We also

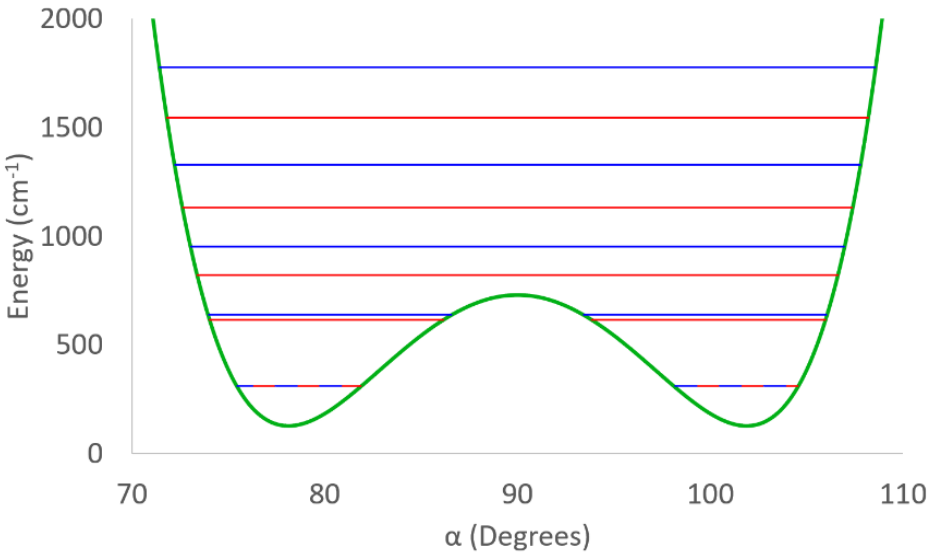

Figure 21. A 1D slice (green) of the PES through the transition state point of S_4 along the bending degree of freedom α, and the spectrum of the 1D states computed for this slice. The energies of the states with the symmetric and the antisymmetric wave functions are shown in red and blue, respectively. One can see a pair of nearly degenerate states in the wells (dashed lines), a pair of split states closer to the barrier top, and a spectrum of non-degenerate states at higher energies.

found that, despite the assignment difficulties at higher energies, the lower part of the spectrum can be fitted with a simple analytic formula, such as Dunham expansion:

$$E_{\text{fit}}(v_1, v_2) = c + \omega_1\left(v_1 + \frac{1}{2}\right) + \omega_2\left(v_2 + \frac{1}{2}\right)$$

$$-\delta_1\left(v_1 + \frac{1}{2}\right)^2 - \delta_2\left(v_2 + \frac{1}{2}\right)^2 - \delta_{12}\left(v_1 + \frac{1}{2}\right)\left(v_2 + \frac{1}{2}\right)$$

Tables 9 and 10 list parameters of this model, for the symmetric and the antisymmetric progressions of the vibrational states fitted separately. In each case, several fits were obtained, with a different number of states included in the fit (which also determines the minimal number of the independent fitting parameters). The simplest fit,

Table 9. Analytic fit parameters for the spectrum of the symmetric vibrational states in S_4 (cm^{-1}).

Fitted States	c	ω_1	ω_2	δ_1	δ_2	δ_{12}	RMSE
3 states	20.4	174.2	420.3	0	0	0	0
below barrier (4)	17.5	182.0	420.3	3.9	0	0	0
6 states	-8.5	194.6	485.2	3.9	26.2	25.2	0
"good" states (8)	-8.4	195.8	484.6	4.1	25.1	27.0	0.92
all states (29)	79.0	148.7	372.5	-2.1	1.6	-1.9	31.9

Table 10. Analytic fit parameters for the spectrum of the antisymmetric vibrational states in S_4 (cm^{-1}).

Fitted States	c	ω_1	ω_2	δ_1	δ_2	δ_{12}	RMSE
3 states	18.5	174.5	423.8	0	0	0	0
below barrier (4)	16.5	180.0	423.8	2.8	0	0	0
6 states	2.3	182.0	460.9	2.7	17.6	4.1	0
"good" states (10)	14.3	169.9	445.8	0.5	14.0	-3.9	1.52
all states (28)	34.2	162.8	415.7	0.2	6.7	-10.2	10.7

based on three states: (0,0), (1,0), and (0,1), permits to determine the frequencies of the normal modes ω_1 and ω_2. Adding the state (2,0) to the set permits to determine the anharmonicity parameter for the first mode, δ_1. Note that these four states cover the energy range below the transition state point. Adding the states (1,1) and (0,2) to the set permits to determine δ_2 for the second mode and the inter-mode anharmonicity (or coupling) parameter δ_{12}. These fits are perfect (zero RMSE), since the number of the states is equal to the number of the fitting parameters.

Adding more states to the set permits to expand the range of coverage but also leads to a larger RMSE. Two such fits are reported in each table. One fit includes only those states that keep the RMSE small: 8 in the symmetric progression (states 1 to 8) and 10 in the antisymmetric progression (states 1 to 7, 9, 10 and 12) in Tables 9 and 10, respectively. The last fit includes all the available states. The RMSE of such global fit exceeds 20 cm^{-1} (for the symmetric states, see Table 9), since a simple Dunham expansion formula cannot reproduce evolution of the spectrum as energy exceeds the transition state point. Note, however, that the antisymmetric states of S_4 exhibit much smaller RMSE, and thus are fitted much better by the Dunham expansion (see Table 10). This is because their wave functions are required to have a node at $\alpha = 90°$, which is the transition state for the isomerization. This forces the vibrational wave function to disappear over the isomerization barrier, minimizes the effect of the isomerization at higher energies and leads to simpler shapes of the wave functions and more regular progressions of energies. This feature may be useful for a spectroscopic characterization of S_4.

Analysis of the data in Tables 9 and 10 indicates, first of all, that the frequencies of the modes are rather sensitive to the number of the states included in the fit. This means that the analytic description developed for the lower states of the spectrum must be adjusted when higher energy states are included, which, again, reflects the transformation of the vibrational spectrum as energy passes through the transition state point. The accurate fits (in the first four lines of Tables 9 and 10) give the frequency of the first mode in the range 174 to 196 cm^{-1}, and the second mode in the range 420 to 485 cm^{-1}, depending on a subset of the fitted states. Second, one sees that the anharmonicity of the second mode is rather large in many fits, up to 25 cm^{-1}, or 5% of the mode's frequency. This very anharmonic higher frequency vibration corresponds to the motion across the elongated "channel" on the PES of S_4. The more harmonic, lower frequency vibrational mode corresponds to the motion along the "channel". Also note that the fitted frequencies and the anharmonicities are somewhat different for the symmetric and the antisymmetric progressions of the vibrational states.

Interestingly, the results of this section indicate that in S_4 the lower frequency mode corresponds to stretching (a vibration along the channel, mostly along R) while the higher frequency mode corresponds to bending (a vibration across the channel, mostly along α), in contrast to a typical behavior. Indeed, in majority of small molecules, bending modes exhibit lower frequencies compared to stretching modes. The unusual behavior of S_4 can be explained by the shape of the PES, which is rather tight for the motion across the channels but is relatively flat for the motion along the channel, as one can see in Figure 11. This property is further analyzed in the next section.

3.4. Normal Mode Analysis

To check validity of the results reported in the previous section, we performed a two-dimensional normal mode analysis of our PES, using spline derivatives to compute the Hessian matrix at the minimum energy point. A diagonalization of the Hessian matrix gave us the frequencies of the normal modes and their components in terms of the two PES variables α and R, or, more precisely, $\Delta\alpha$ and ΔR, defined as deviations from the minimum energy point. The results are presented in Table 11.

Two components of the mode are, basically, projections of the mode's direction vector onto axes α and R (see Figure 11), which helps to understand character of the corresponding vibrations. To facilitate comparison, the components were scaled to have the same value of $\Delta\alpha = 32°$ in each mode, which corresponds to the arc length of 1 Bohr that S atoms swipe during the bending motion. From Table 11 we see that the first mode, indeed, has a significant amount of stretching mixed in, in addition to bending. In fact, the amount of stretch in the first mode is more than it is in the second, over the factor of two!

One can probably say that bending and stretching modes swap in S_4, but it is more accurate to say that neither of the two modes is closer to pure bending or pure stretching, since they both exhibit a significant amount of coupling between α and R. The major difference between these two modes is that bending and stretching motions occur *in*

Table 11. The normal mode analysis for the dimensionally-reduced 2D-PES of S4.

Mode Frequency (cm^{-1})	Deviation $\Delta\alpha$ (Degree)	Deviation ΔR (Bohr)
179.1	32	0.83
469.7	32	–0.37

phase for the first mode, while in the second mode they occur *out of phase*. Namely, for each Bohr of the bending motion of S atoms, the first mode shows 0.83 Bohr of *stretching* of the dimer-dimer distance *R*, while the second mode shows 0.37 Bohr of its *compression*. The second mode brings S atoms closer together and leads to steeper energy increase, that finally translates into higher frequency of vibration.

The values of two normal mode frequencies in Table 11, roughly 179 and 470 cm^{-1}, fall in the ranges predicted by the fits in Tables 9 and 10. The best agreement is observed with the fit based on 6 lowest states. For this case, the normal mode frequencies deviate by 15.5 cm^{-1} from results of the fit of symmetric states, and by just 2.9 and 8.8 cm^{-1} from results of the fit of antisymmetric states.

We also carried out the standard *ab initio* normal mode analysis for S_4, using MOLPRO. Results are presented in Table 12 for the minimum-energy point (C_{2v}), and in Table 13 for the transition state point (D_{2h}).

Two levels of the electronic structure theory were employed. First, in order to compare with similar result of Ref. 66, we used CCSD(T)/aV(T+d)Z level of theory with average atomic masses (atomic weights). Then, we used CCSD(T)-F12a/VTZ-F12 level of theory, which is the method we used to compute our 2D-PES, with the mass of the most abundant sulfur isotope ^{32}S. We see that our CCSD(T) frequencies are in excellent agreement with those of Ref. 66 (given in parenthesis in Tables 12 and 13). We also see

that the F12-frequencies are rather close to those of the standard coupled-cluster method, with differences on the order of few percents.

We should stress that mode assignments in Tables 12 and 13 are qualitative, based on animations of the vibrational motion generated by MOLPRO. The two modes of interest are at 123 and 340 cm^{-1} (using CCSD(T)-F12a/VTZ-F12 theory level). However,

Table 12. *Ab initio* normal mode frequencies (cm^{-1}) for the minimum energy point of S_4.

Mode Assignment	CCSD(T)/aV(T+d)Z	CCSD(T)-F12a/VTZ-F12	Experiment [b]
Symmetric bending [a]	120.4 (118.8)	123.1	} 322
Torsion	210.6 (210.5)	215.0	
Asymmetric bending	326.5 (325.2)	333.5	303
S−S stretching [a]	329.6 (328.7)	339.8	375
S=S asymmetric stretching	640.1 (640.2)	652.6	662
S=S symmetric stretching	681.2 (681.2)	697.1	678

[a)] Assignments are qualitative; these two modes show significant mixing of bending and stretching.

[b)] Summary of several experimental studies.[67]

Table 13. *Ab initio* normal mode frequencies (cm^{-1}) for the transition state of S_4.

Mode	CCSD(T)/aV(T+d)Z	CCSD(T)-F12a/VTZ-F12
Symmetric Bending	109.2i (91.2i)	120.0i
Torsion	232.8 (233.4)	239.0
Asymmetric bending	260.3 (233.5)	280.2
S-S Stretching	274.0 (278.1)	332.7
S=S Asymmetric stretching	319.1 (319.6)	532.7
S=S Symmetric stretching	713.8 (716.7)	732.7

these frequencies are somewhat different from the two frequencies computed using our PES: near 179 and 470 cm^{-1} (see Table 11 above).

Why the *ab initio* normal-mode frequencies are different from those computed using the PES? One source of discrepancy is in local *vs* global behavior. Indeed, the standard *ab initio* normal-mode analysis (such as in MOLPRO) assumes harmonic behavior of the PES and uses information in the closest vicinity of the minimum energy point only. In contrast, the normal-mode analysis we implemented for the PES "sees" much further from the minimum and is expected to give more reliable results, especially in the case of highly anharmonic landscape, such as double-well PES of S_4. Importantly, results of our normal mode analysis (Table 11) agree well with analytic fits (Tables 9 and 10) of accurately computed spectra (Table 8).

Another source of discrepancy is dimensionality of the problem. Our calculations with the PES have limitation imposed by dimensional reduction. We look at two degrees of freedom only, while the actual molecule has six vibrational modes (see Tables 12 and 13), and the *ab initio* normal mode analysis permits to analyze all of them at once (in proximity of the minim energy point, as explained above). Thus, each method has its pros and cons. It would be instructive to estimate what can be gained by expanding our global approach onto more degrees of freedom (say by building a 3D-PES of S_4, rather than 2D-PES), and what coordinate is the most important to add?

For this, we expressed six normal vibration modes in Tables 12 and 13 in terms of their components along six internal vibrational coordinates: two bending angles α_1 and α_2, torsional angle β, dimer-dimer separation R and the two double-bond lengths r_1 and r_2. Note that our 2D-PES is obtained by freezing r_1 and r_2 at their equilibrium values,

keeping all four atoms planar by setting $\beta = 0$, and requesting that $\alpha_1 = \alpha_2$. Results are presented in Table 14. Normalization and units are similar to those in Table 11 (degrees for angle increments, and Bohr for bond-length increments). Increments smaller than 1° and 0.02 a_0 are neglected, for clarity.

These data show clearly that angle β is needed for description of the torsional mode only. Double-bond lengths r_1 and r_2 are most important for S=S stretching modes but have small effect on the other modes. The dimer-dimer separation R is essential for the two modes of interest (symmetric bending and S–S stretching in Table 14) but has no effect on the other modes. However, angles α_1 and α_2 are needed for three modes simultaneously. This observation suggests that adding one more independent coordinate to the PES, $\alpha_2 \neq \alpha_1$, might enable more accurate and consistent description of three normal vibration modes: symmetric bending, asymmetric bending, and single-bond stretching in S_4.

Table 14. *Ab initio* normal modes of S_4 expressed through increments of the internal coordinates.

Mode	$\Delta\alpha_1$	$\Delta\alpha_2$	ΔR	Δr_1	Δr_2	$\Delta\beta$
Symmetric bending [a]	32	32	1.17	0.09	0.09	0
Torsion	0	0	0	0	0	32
Asymmetric bending	–32	32	0	–0.06	0.04	0
S-S stretching [a]	9	9	–1.00	0	0	0
S=S asymmetric stretching	0	0	0	1.00	–1.00	0
S=S symmetric stretching	0	0	0	1.00	1.00	0

[a)] Assignments are qualitative; these two modes show significant mixing of bending and stretching.

Finally, comparing Table 14 vs Table 11, we see that the two modes in Table 11 (computed from the PES) are qualitatively-similar to the 1st and 4th modes in Table 14 (predicted by full-dimensional analysis). In each case the modes are described by superposition of $\Delta\alpha$ and ΔR, with lower frequency mode characterized by *in phase* combination, and higher frequency mode characterized by *out of phase* combination of $\Delta\alpha$ and ΔR. We conclude that these two modes include a fair amount of coupling between stretching and bending motions. Assignment of one mode as symmetric bending and the other as S−S stretching, as in Tables 11-13, is not particularly accurate (used here for historic reasons only).

Experimental data on vibration frequencies of S_4 are sparse and rather inconclusive due to presence of multiple sulfur allotropes and isomers, which causes difficulty of band assignments.[67] Absorption spectra in solid argon matrix[98] contain one frequency of C_{2v} isomer, at 662 cm^{-1}, which most likely corresponds to asymmetric stretching of the double-bonds in S_4. The other study of Raman spectra in hot vapor,[99] in addition to symmetric stretching of the double-bonds at 678 cm^{-1}, reports two lower frequencies at 375 and 303 cm^{-1} that probably correspond to S−S stretching and asymmetric bending of S_4. One more frequency at 322 cm^{-1} was assigned as a combination of symmetric bending and torsional motion in S_4. These data are summarized in the last column of Table 12.

So, it appears that experimental frequency at 375 cm^{-1} is almost in the middle between predictions of the *ab initio* normal mode analysis (~340 cm^{-1}, see Table 12) and the fitted spectrum of the 2D-PES (~420 cm^{-1}, see Tables 9 and 10). Based on these data

it seems impossible to say what method of frequency prediction is in better agreement with experiment.

3.5. Summary

The vibrational states are computed on the 2D PES, discussed in Chapter 2, using an accurate numerical solution of the time-independent Schrodinger equation. The states are assigned quantum numbers, based on the shapes of the vibrational wave functions and positions in the energy spectrum. Two progressions of the vibrational states are identified. The long progression of easily assignable states that develop nodes along the "channels" on the PES corresponds to the lower frequency, ~180 cm^{-1}. The other (shorter) progression of states that develops nodes across the "channels" is characterized by higher frequency, ~ 420 cm^{-1} and is much harder to assign due to the effect of the double-well nature of the PES.

Normal mode analysis indicates that the two modes in S_4, indeed, represent a significant mixture of the bending and the stretching motions of the trapezoidal shape of this molecule. When the bending angle is increased, the lower frequency mode corresponds to *stretching* of the distance between the two S_2 dimers, while the higher frequency mode corresponds to *compression* of the distance between them.

Our results are in a qualitative agreement with earlier *ab initio* studies of the normal modes in S_4, and with rather limited experimental data. The advantage of our approach is in the global description of the vibrations, using the PES in a broad range of coordinates, which covers both wells and the transition state between them, and considers all this information at the same time (in contrast to the conventional normal mode analysis, which is performed locally, either at a minimum or at a transition state point).

Our calculations show that the transition state point in S_4 is reached by only one quantum of excitation of the second mode, or two quanta of the first mode (in addition to the zero-point energy), which means that the spectrum is highly anharmonic and all the vibrational states, even the ground state, are highly delocalized over the PES. In this situation the conventional normal mode analysis is not expected to give an accurate prediction of the vibrational spectrum.

The considered degrees of freedom, R and α, allow us to investigate the isomerization process at the simplest level possible. Despite the simplicity of our model, the obtained results are in qualitative agreement with the experiments and lay the groundwork for future improvements that will provide more precise results. Those improvements will include expansion of the PES onto more degrees of freedom and extension towards the dissociation limit. To the best of our knowledge, our calculations are the first variational calculations of the vibrational states of tetrasulfur.

Calculations of a global 3D PES, using MRCI method are in progress. With little changes, needed to take into account another degree of freedom, the framework described in this chapter can be used to calculate the energies and lifetimes of the vibrational states of tetrasulfur on this global surface up to the dissociation limit. These data can be utilized to compute reaction rates and equilibrium constants and estimate the magnitude of the isotope effects given by Eqs. (7) and (10) in Introduction, which allows one to understand the role of tetrasulfur recombination reaction in S-MIF.

Interestingly, in the ozone molecule that has been under intense investigation in the Babikov's group in recent years, similar isotope effects are observed. The ozone

molecule is also 3D, so practice with the calculations of the vibrational states of ozone can serve as a good starting point for the 3D calculations in tetrasulfur.

The 2D PES, used for calculations of vibrational states in this chapter, is available in the Supplemental Information of Ref. 89.

CHAPTER 4. GENERAL THEORY OF COUPLED ROTATION-VIBRATION CALCULATIONS IN APH COORDINATES

In this chapter we formulate theoretical concepts necessary to perform calculations of coupled rotation-vibration states in Adiabatically adjusting Principal axis Hyperspherical (APH) coordinates, and derive the necessary equations and matrix element expressions. The formulated theory is further used in Chapters 5-7 to perform calculations of rovibrational states in ozone and investigate various properties of bound states and scattering resonances in an effort to detect a robust and mass-independent trend that could be responsible for the experimentally observed isotope effects in ozone. In Chapter 9 this theory serves as a foundation for development of a general-purpose software package (SpectrumSDT), able to perform calculations of coupled rovibrational energies and lifetimes of bound states and scattering resonances for arbitrary triatomic systems (subject to the limitations outlined in Chapter 9).

4.1. Adiabatically Adjusting Principal Axis Hyperspherical (APH) Coordinates

The present theory is formulated in Adiabatically adjusting Principal axis Hyperspherical (APH) coordinates, which are designed specifically for (and restricted to) triatomic systems.[79,100–105]

In APH coordinates, the vibrational motion is described through three coordinates: ρ, θ and φ. Qualitatively ρ serves as a measure of the overall size of the bounding triangle for the system (the "breathing" motion); θ changes in the range from 0 to $\pi/2$ and corresponds to translation from equilateral triangle at $\theta = 0$ to a linear molecule at $\theta = \pi/2$ (the "bending" motion); φ changes in the range from 0 to 2π and is responsible for isomerization, such that $\varphi = \pi/3$, π and $5\pi/3$ correspond to AAB, ABA and BAA arrangements respectively, as shown in Figure 22 (adapted from Ref. 106). See

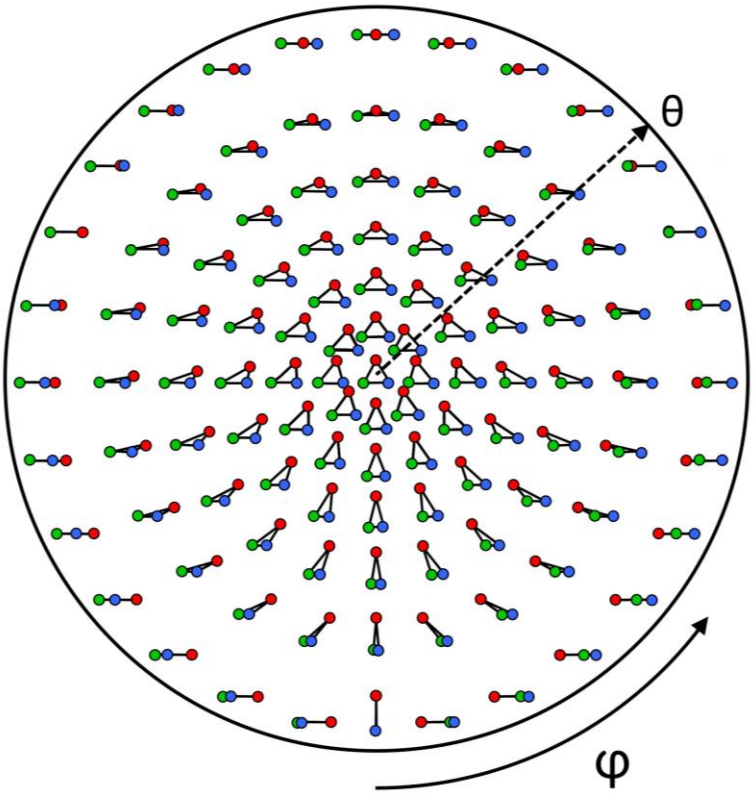

Figure 22. Visualization of molecular arrangements corresponding to different values of (θ, φ) and a fixed value of ρ in APH coordinates. The value of θ increases radially outward from the center (where $\theta = 0$) to the rim (where $\theta = \pi/2$). φ is an angle in the range $[0; 2\pi]$ measured from the bottom of the circle. Symmetric obtuse ABA configuration corresponds to $\varphi = \pi$. The value of ρ defines overall size of the triangle formed by the three atoms. This figure is adapted from Ref. 106.

also Ref. 101 for an interactive visualization tool of the motion along φ and Ref. 102 for 3D representation of APH coordinates on the example of ozone.

In contrast to more traditional coordinate systems, such as Jacobi coordinates, APH coordinates provide a number of advantages. First of all, APH coordinates have a somewhat simpler form of the Hamiltonian operator and thus are more efficient numerically. Second, they fully exploit the symmetry of the ozone molecule and allow the treatment of all isotopomers on equal footing, covering all wells on the global PES with the same grids and/or basis sets. Finally, APH coordinates facilitate isotopomer assignment of the computed states.

The rotational motion is described through the usual Euler angles: α, β and γ.

4.2. Definitions and General Considerations

The full rotation-vibration Hamiltonian operator in APH coordinates can be written as a sum of the following terms:[93]

$$\hat{H} = \hat{T}_\rho + \hat{T}_\theta + \hat{T}_\varphi + V_{\text{pes}} + V_{\text{ext}} + \hat{T}_{\text{sym}} + \hat{T}_{\text{asym}} + \hat{T}_{\text{cor}} \tag{32}$$

where the first three operators are associated with the kinetic energy along each vibrational degree of freedom, $V_{\text{pes}}(\rho, \theta, \varphi)$ describes the electronic potential energy surface of the molecule under consideration, and V_{ext} is an extra potential-like term. All these operators affect vibrational degrees of freedom only and the corresponding expressions are given by:[93]

$$\hat{T}_\rho = -\frac{\hbar^2}{2\mu}\frac{\partial^2}{\partial\rho^2} \tag{33}$$

$$\hat{T}_\theta = -\frac{2\hbar^2}{\mu\rho^2}\frac{\partial^2}{\partial\theta^2} \tag{34}$$

$$\hat{T}_{\varphi} = -\frac{2\hbar^2}{\mu\rho^2 \sin^2\theta}\frac{\partial^2}{\partial\varphi^2} \tag{35}$$

$$V_{\text{ext}} = -\frac{\hbar^2}{2\mu\rho^2}\left(\frac{1}{4} + \frac{4}{\sin^2 2\theta}\right) \tag{36}$$

where μ is the three-body reduced mass, given by:

$$\mu = \sqrt{\frac{m_1 m_2 m_3}{m_1 + m_2 + m_3}} \tag{37}$$

where m_1, m_2 and m_3 are masses of individual atoms.

The remaining operators ($\hat{T}_{\text{sym}}$, $\hat{T}_{\text{asym}}$ and $\hat{T}_{\text{cor}}$) affect both vibrational and rotational degrees of freedom and their expressions are given by:[94,107]

$$\hat{T}_{\text{sym}} = \frac{A+B}{2}\hat{J}^2 + \left(C - \frac{A+B}{2}\right)\hat{J}_z^2 \tag{38}$$

$$\hat{T}_{\text{asym}} = \frac{A-B}{2}\left(\hat{J}_x^2 - \hat{J}_y^2\right) \tag{39}$$

$$\hat{T}_{\text{cor}} = 4B\,cos\,\theta\left(i\hbar\frac{\partial}{\partial\varphi}\right)\hat{J}_y \tag{40}$$

where the rotational constants A, B and C are given by:

$$A^{-1} = \mu\rho^2(1 + sin\,\theta) \tag{41}$$

$$B^{-1} = 2\mu\rho^2 \sin^2\theta \tag{42}$$

$$C^{-1} = \mu\rho^2(1 - sin\,\theta) \tag{43}$$

and operators $\hat{J}_x$, $\hat{J}_y$ and $\hat{J}_z$ are given by:

$$\hat{J}_x = -i\hbar\left[-\frac{\cos(\gamma)}{\sin(\beta)}\frac{\partial}{\partial\alpha} + \sin(\gamma)\frac{\partial}{\partial\beta} + \cot(\beta)\cos(\gamma)\frac{\partial}{\partial\gamma}\right] \tag{44}$$

$$\hat{J}_y = -i\hbar\left[\frac{\sin(\gamma)}{\sin(\beta)}\frac{\partial}{\partial\alpha} + \cos(\gamma)\frac{\partial}{\partial\beta} - \cot(\beta)\sin(\gamma)\frac{\partial}{\partial\gamma}\right] \tag{45}$$

$$\hat{J}_z = -i\hbar \frac{\partial}{\partial \gamma} \tag{46}$$

The volume element for computing matrix elements of this operator is given by:

$$d^6v = d\rho\ d\theta\ d\varphi\ d\alpha \sin(\beta)\, d\beta\ d\gamma \tag{47}$$

The full-dimensional ro-vibrational wave functions F^k, which includes both vibrational and rotational degrees of freedom (6D overall), can be represented by an expansion over the rotational components $\widetilde{D}_\Lambda(\alpha,\beta,\gamma)$, where the vibrational components $\Psi_\Lambda^k(\rho,\theta,\varphi)$ play the role of expansion coefficients, namely:

$$F^k(\rho,\theta,\varphi,\alpha,\beta,\gamma) = \sum_{\Lambda=0,1}^{J} \Psi_\Lambda^k(\rho,\theta,\varphi)\widetilde{D}_\Lambda(\alpha,\beta,\gamma) \tag{48}$$

$$\widehat{H}F^k(\rho,\theta,\varphi,\alpha,\beta,\gamma) = \varepsilon^k F^k(\rho,\theta,\varphi,\alpha,\beta,\gamma) \tag{49}$$

where *J* is the total angular momentum quantum number and Λ is a quantum number corresponding to projection of total angular momentum onto body-fixed *z*-axis.

The rotational basis functions $\widetilde{D}_\Lambda(\alpha,\beta,\gamma)$ are taken in the form of the modified normalized Wigner *D*-functions of two parities ($p = 0$ and $p = 1$):

$$\widetilde{D}_{\Lambda M}^{Jp} = \sqrt{\frac{2J+1}{16\pi^2(1+\delta_{\Lambda 0})}}\left[D_{\Lambda M}^J(\alpha,\beta,\gamma) + (-1)^{J+\Lambda+p} D_{-\Lambda M}^J(\alpha,\beta,\gamma)\right] \tag{50}$$

where δ is a regular Kronecker delta function.

The values of $p = 0$ and $p = 1$ generate two possible superpositions: one "in phase" and one "out of phase", except that in the case of $\Lambda = 0$ only the in-phase superposition is possible. For even values of *J* the term with $\Lambda = 0$ contributes only to $p = 0$, while for odd values of *J* the term with $\Lambda = 0$ contributes only to $p = 1$. This defines the starting value of Λ in Eq. (48), which is 0 if $J + p$ is even or 1 otherwise. Note

that with the definition of Eq. (50) both $+\Lambda$ and $-\Lambda$ are taken into account simultaneously, in pairs, therefore only non-negative values of Λ are considered on the modified Wigner function $\widetilde{D}^{Jp}_{\Lambda M}$. The total number of different functions $\widetilde{D}^{Jp}_{\Lambda M}$ still stays the same as for regular Wigner functions, due to the extra parity index.

The regular Wigner functions used in Eq. (50) are defined as:

$$D^{J}_{\Lambda M}(\alpha,\beta,\gamma) = e^{iM\alpha} d^{J}_{\Lambda M}(\beta) e^{i\Lambda\gamma} \tag{51}$$

where $d^{J}_{\Lambda M}(\beta)$ term is given by:

$$\begin{aligned} & d^{J}_{\Lambda M}(\beta) \\ & = [(J+\Lambda)!\,(J-\Lambda)!\,(J+M)!\,(J-M)!]^{1/2} \\ & \times \sum_{\kappa} \frac{(-1)^{\kappa}}{(J-M-\kappa)!\,(J+\Lambda-\kappa)!\,(\kappa+M-\Lambda)!\,\kappa!} \\ & \times \left(\cos\left(\frac{\beta}{2}\right)\right)^{2J+\Lambda-M-2\kappa} \left(-\sin\left(\frac{\beta}{2}\right)\right)^{M-\Lambda+2\kappa} \end{aligned} \tag{52}$$

where Λ and M are the quantum numbers for projections of the total angular momentum onto body-fixed and space-fixed z-axes. In contrast to the modified Wigner function of Eq. (50), the values of Λ in regular Wigner function of Eqs. (51) and (52) run from $-J$ to J, same as M.

Different values of J, M and p are not coupled with each other and the corresponding calculations can be carried out independently. Since the values of J, M and p stay constant within each calculation, their indexes are assumed implicit and are omitted further in the text, for clarity. Furthermore, in this formulation of theory, the exact value of M has no effect on the result, therefore all calculated states are $(2J+1)$-degenerate.

The Hamiltonian matrix elements in a general basis of Eq. (48) can be written as:

$$\langle \Psi_\Lambda \widetilde{D}_\Lambda | \hat{H} | \Psi_{\Lambda'} \widetilde{D}_{\Lambda'} \rangle = \langle \Psi_\Lambda | \hat{T}_\rho + \hat{T}_\theta + \hat{T}_\varphi + \mathrm{V_{pes}} + \mathrm{V_{ext}} | \Psi_{\Lambda'} \rangle \langle \widetilde{D}_\Lambda | \widetilde{D}_{\Lambda'} \rangle + \langle \Psi_\Lambda \widetilde{D}_\Lambda | \hat{T}_{\mathrm{sym}} + \hat{T}_{\mathrm{asym}} + \hat{T}_{\mathrm{cor}} | \Psi_{\Lambda'} \widetilde{D}_{\Lambda'} \rangle \quad (53)$$

The first five terms of the Hamiltonian operator (Eq. (32)) only affect the vibrational degrees of freedom, therefore the integration over the rotational degrees of freedom ($\langle \widetilde{D}_\Lambda | \widetilde{D}_{\Lambda'} \rangle$) can be factored out. The same cannot be done for the remaining terms, where both vibrational and rotational degrees of freedom have to considered together.

4.3. Derivation of the Matrix Elements in General Vibrational Basis

In this section we consider derivation of the matrix elements for the terms that affect rotational motion: $\hat{T}_{\mathrm{sym}}$, $\hat{T}_{\mathrm{asym}}$ and $\hat{T}_{\mathrm{cor}}$, in terms of general vibrational basis functions Ψ_Λ of Eq. (53).

4.3.1. Derivation of the Symmetric Top Rotor Matrix Elements

Using the definition of Eq. (38), one can write the matrix element expression for $\hat{T}_{\mathrm{sym}}$ as:

$$\langle \Psi_\Lambda \widetilde{D}_\Lambda | \hat{T}_{\mathrm{sym}} | \Psi_{\Lambda'} \widetilde{D}_{\Lambda'} \rangle = \langle \Psi_\Lambda | \frac{A+B}{2} | \Psi_{\Lambda'} \rangle \langle \widetilde{D}_\Lambda | \hat{J}^2 | \widetilde{D}_{\Lambda'} \rangle + \langle \Psi_\Lambda | C - \frac{A+B}{2} | \Psi_{\Lambda'} \rangle \langle \widetilde{D}_\Lambda | \hat{J}_z^2 | \widetilde{D}_{\Lambda'} \rangle \quad (54)$$

This case is simple, since the modified Wigner functions $\widetilde{D}_\Lambda$ of Eq. (50) are eigenfunctions of both $\hat{J}^2$ and $\hat{J}_z^2$ with the following eigenvalues:[108]

$$\langle \widetilde{D}_\Lambda | \hat{J}^2 | \widetilde{D}_{\Lambda'} \rangle = \hbar^2 J(J+1) \tilde{\delta}_{\Lambda\Lambda'} \quad (55)$$

$$\langle \widetilde{D}_\Lambda | \hat{J}_z^2 | \widetilde{D}_{\Lambda'} \rangle = \hbar^2 \Lambda^2 \tilde{\delta}_{\Lambda\Lambda'} \quad (56)$$

where a modified Kronecker delta function is introduced:

$$\tilde{\delta}_{\Lambda\Lambda'} = \begin{cases} \delta_{\Lambda\Lambda'} & \text{if } \Lambda, \Lambda' \neq 0 \\ \delta_{(-1)^{J+p},1} & \text{if } \Lambda, \Lambda' = 0 \end{cases} \tag{57}$$

Plugging Eqs. (55) and (56) into Eq. (54), one obtains:

$$\langle \Psi_\Lambda \widetilde{D}_\Lambda | \hat{T}_{\text{sym}} | \Psi_{\Lambda'} \widetilde{D}_{\Lambda'} \rangle$$

$$= \hbar^2 \tilde{\delta}_{\Lambda\Lambda'} \left(J(J+1) \langle \Psi_\Lambda | \frac{A+B}{2} | \Psi_{\Lambda'} \rangle + \Lambda^2 \langle \Psi_\Lambda | C - \frac{A+B}{2} | \Psi_{\Lambda'} \rangle \right) \tag{58}$$

Because of the $\tilde{\delta}_{\Lambda\Lambda'}$ term, the symmetric-top rotor term ($\hat{T}_{\text{sym}}$) contributes only to the diagonal Λ-blocks of the Hamiltonian matrix. In a schematic representation of its rotational block structure, shown in Figure 23 the blocks affected by $\hat{T}_{\text{sym}}$ are marked with "S".

4.3.2. Derivation of the Asymmetric Top Rotor Matrix Elements

Next, let us consider the matrix element expression for the asymmetric top rotor operator $\hat{T}_{\text{asym}}$. Using the definition of Eq. (39), one can write:,

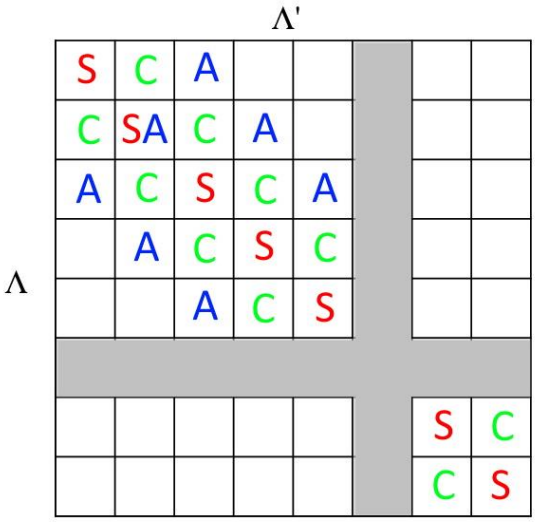

Figure 23. Rotational block structure of the Hamiltonian matrix. Letters S, A and C indicate contributions from symmetric-top rotor, asymmetric-top rotor and Coriolis coupling terms, given in Eqs. (38)-(40), respectively. Other blocks of the matrix are zero. Individual blocks are labelled by values of Λ and Λ′ from a given pair of basis functions $\widetilde{D}_\Lambda$, given by Eq. (50).

$$\langle \Psi_\Lambda \widetilde{D}_\Lambda | \hat{T}_{\text{asym}} | \Psi_{\Lambda'} \widetilde{D}_{\Lambda'} \rangle = \langle \Psi_\Lambda | \frac{A-B}{2} | \Psi_{\Lambda'} \rangle \langle \widetilde{D}_\Lambda | \hat{J}_x^2 - \hat{J}_y^2 | \widetilde{D}_{\Lambda'} \rangle \tag{59}$$

The rotational basis functions $\widetilde{D}_\Lambda$ are not eigenfunctions of $\hat{J}_x^2$ or $\hat{J}_y^2$, therefore let us consider derivation of the last term of Eq. (88) separately.

The following integral can be rewritten in terms of raising and lowering operators:

$$\langle \widetilde{D}_\Lambda | \hat{J}_x^2 - \hat{J}_y^2 | \widetilde{D}_{\Lambda'} \rangle = \frac{1}{2} \left(\langle \widetilde{D}_\Lambda | \hat{J}_+^2 | \widetilde{D}_{\Lambda'} \rangle + \langle \widetilde{D}_\Lambda | \hat{J}_-^2 | \widetilde{D}_{\Lambda'} \rangle \right) \tag{60}$$

where raising and lowering operators, $\hat{J}_+$ and $\hat{J}_-$, are defined as:[100]

$$\hat{J}_+ = \hat{J}_x - i\hat{J}_y \tag{61}$$

$$\hat{J}_- = \hat{J}_x + i\hat{J}_y \tag{62}$$

Or, the other way around:

$$\hat{J}_x = \frac{\hat{J}_+ + \hat{J}_-}{2} \tag{63}$$

$$\hat{J}_y = \frac{\hat{J}_- - \hat{J}_+}{2i} \tag{64}$$

Application of $\hat{J}_\pm$ to a regular Wigner function D_Λ of Eq. (51) is given by:[103]

$$\hat{J}_\pm D_\Lambda = \hbar \lambda_\pm(J, \Lambda) D_{\Lambda \pm 1} \tag{65}$$

where functions $\lambda_\pm(J, \Lambda)$ are given by:

$$\lambda_\pm(J, \Lambda) = \sqrt{(J \pm \Lambda + 1)(J \mp \Lambda)} \tag{66}$$

The functions $\lambda_\pm(J, K)$ have the following useful properties (easily verifiable directly from their definitions):

$$\lambda_+(J, -\Lambda) = \lambda_+(J, \Lambda - 1) \tag{67}$$

$$\lambda_-(J, -\Lambda) = \lambda_-(J, \Lambda + 1) \tag{68}$$

$$\lambda_-(J, \Lambda) = \lambda_+(J, \Lambda - 1) \tag{69}$$

Using Eq. (65), the first term of Eq. (60) can be written as:

$$\langle \widetilde{D}_{\Lambda} | \hat{J}_{+}^{2} | \widetilde{D}_{\Lambda'} \rangle$$

$$= \frac{2J+1}{16\pi^2 \sqrt{(1+\delta_{\Lambda 0})(1+\delta_{\Lambda' 0})}}$$

$$\times \langle D_{\Lambda} + (-1)^{J+\Lambda+p} D_{-\Lambda} | \hat{J}_{+}^{2} | D_{\Lambda'} + (-1)^{J+\Lambda'+p} D_{-\Lambda'} \rangle$$

$$= \frac{2J+1}{16\pi^2 \sqrt{(1+\delta_{\Lambda 0})(1+\delta_{\Lambda' 0})}} \big(\hbar^2 \lambda_{+}(J,\Lambda') \lambda_{+}(J,\Lambda'+1) \langle D_{\Lambda} | D_{\Lambda'+2} \rangle$$

$$+ (-1)^{J+\Lambda+p} \hbar^2 \lambda_{+}(J,\Lambda') \lambda_{+}(J,\Lambda'+1) \langle D_{-\Lambda} | D_{\Lambda'+2} \rangle$$

$$+ (-1)^{J+\Lambda'+p} \hbar^2 \lambda_{+}(J,-\Lambda') \lambda_{+}(J,-\Lambda'+1) \langle D_{\Lambda} | D_{-\Lambda'+2} \rangle$$

$$+ (-1)^{J+\Lambda+p} (-1)^{J+\Lambda'+p} \hbar^2 \lambda_{+}(J,-\Lambda') \lambda_{+}(J,-\Lambda'+1) \langle D_{-\Lambda} | D_{-\Lambda'+2} \rangle \big) \quad (70)$$

Normalization of regular Wigner functions is given by:

$$\langle D_{\Lambda} | D_{\Lambda'} \rangle = \frac{8\pi^2}{2J+1} \delta_{\Lambda,\Lambda'} \quad (71)$$

Plugging Eq. (71) into Eq. (70) one obtains:

$$\langle \widetilde{D}_{\Lambda} | \hat{J}_{+}^{2} | \widetilde{D}_{\Lambda'} \rangle$$

$$= \frac{\hbar^2}{2\sqrt{(1+\delta_{\Lambda 0})(1+\delta_{\Lambda' 0})}} \big(\lambda_{+}(J,\Lambda') \lambda_{+}(J,\Lambda'+1) \delta_{\Lambda,\Lambda'+2}$$

$$+ (-1)^{J+\Lambda+p} \lambda_{+}(J,\Lambda') \lambda_{+}(J,\Lambda'+1) \delta_{-\Lambda,\Lambda'+2}$$

$$+ (-1)^{J+\Lambda'+p} \lambda_{+}(J,-\Lambda') \lambda_{+}(J,-\Lambda'+1) \delta_{\Lambda,-\Lambda'+2}$$

$$+ (-1)^{J+\Lambda+p} (-1)^{J+\Lambda'+p} \lambda_{+}(J,-\Lambda') \lambda_{+}(J,-\Lambda'+1) \delta_{-\Lambda,-\Lambda'+2} \big) \quad (72)$$

The second term of the sum is 0, since $\delta_{-\Lambda,\Lambda'+2} = 0$ for all $\Lambda, \Lambda' \geq 0$. In the fourth term, $(-1)^{J+\Lambda+p}(-1)^{J+\Lambda'+p} = 1$ for all Λ, Λ' such that $\delta_{-\Lambda,-\Lambda'+2} \neq 0$ (i.e. Λ and Λ' have to be of the same parity). Plugging these results back into Eq. (72) and using Eq. (67), we obtain the final expression for the first term of Eq. (60):

$$\langle \widetilde{D}_{\Lambda} | \hat{J}_{+}^{2} | \widetilde{D}_{\Lambda'} \rangle$$

$$= \frac{\hbar^2}{2\sqrt{(1+\delta_{\Lambda 0})(1+\delta_{\Lambda' 0})}} \big(\lambda_{+}(J,\Lambda') \lambda_{+}(J,\Lambda'+1) \delta_{\Lambda,\Lambda'+2}$$

$$+ (-1)^{J+\Lambda'+p} \lambda_{+}(J,\Lambda'-1) \lambda_{+}(J,\Lambda'-2) \delta_{\Lambda,2-\Lambda'}$$

$$+ \lambda_{+}(J,\Lambda'-1) \lambda_{+}(J,\Lambda'-2) \delta_{\Lambda,\Lambda'-2} \big) \tag{73}$$

In a very similar way one can derive an expression for the second term of Eq. (60) (this time using Eq. (68)):

$$\langle \widetilde{D}_{\Lambda} | \hat{J}_{-}^{2} | \widetilde{D}_{\Lambda'} \rangle$$

$$= \frac{\hbar^2}{2\sqrt{(1+\delta_{\Lambda 0})(1+\delta_{\Lambda' 0})}} \big(\lambda_{-}(J,\Lambda') \lambda_{-}(J,\Lambda'-1) \delta_{\Lambda,\Lambda'-2}$$

$$+ (-1)^{J+\Lambda+p} \lambda_{-}(J,\Lambda') \lambda_{-}(J,\Lambda'-1) \delta_{\Lambda,2-\Lambda'}$$

$$+ \lambda_{-}(J,\Lambda'+1) \lambda_{-}(J,\Lambda'+2) \delta_{\Lambda,\Lambda'+2} \big) \tag{74}$$

Using Eq. (69), Eq. (74) can be rewritten in terms of λ_{+} as:

$$\langle \widetilde{D}_{\Lambda} | \hat{J}_{-}^{2} | \widetilde{D}_{\Lambda'} \rangle$$

$$= \frac{\hbar^2}{2\sqrt{(1+\delta_{\Lambda 0})(1+\delta_{\Lambda' 0})}} (\lambda_{+}(J,\Lambda'-1) \lambda_{+}(J,\Lambda'-2) \delta_{\Lambda,\Lambda'-2}$$

$$+ (-1)^{J+\Lambda+p} \lambda_{+}(J,\Lambda'-1) \lambda_{+}(J,\Lambda'-2) \delta_{\Lambda,2-\Lambda'}$$

$$+ \lambda_{+}(J,\Lambda') \lambda_{+}(J,\Lambda'+1) \delta_{\Lambda,\Lambda'+2}) \tag{75}$$

Substitution of Eqs. (73) and (75) back into Eq. (60) gives:

$$\langle \widetilde{D}_{\Lambda} | \hat{J}_x^2 - \hat{J}_y^2 | \widetilde{D}_{\Lambda'} \rangle$$

$$= \frac{\hbar^2}{4\sqrt{(1+\delta_{\Lambda 0})(1+\delta_{\Lambda' 0})}} \big(2\lambda_+(J,\Lambda')\lambda_+(J,\Lambda'+1)\delta_{\Lambda,\Lambda'+2}$$

$$+ \big((-1)^{J+\Lambda'+p} + (-1)^{J+\Lambda+p} \big) \lambda_+(J,\Lambda'-1)\lambda_+(J,\Lambda'-2)\delta_{\Lambda,2-\Lambda'}$$

$$+ 2\lambda_+(J,\Lambda'-1)\lambda_+(J,\Lambda'-2)\delta_{\Lambda,\Lambda'-2} \big) \tag{76}$$

For any Λ, Λ' such that $\delta_{\Lambda,2-\Lambda'} \neq 0$ $(-1)^{J+\Lambda'+p} + (-1)^{J+\Lambda+p} = 2(-1)^{J+\Lambda+p}$ (since, again, Λ and Λ' have to be of the same parity), therefore Eq. (76) can be simplified to:

$$\langle \widetilde{D}_{\Lambda} | \hat{J}_x^2 - \hat{J}_y^2 | \widetilde{D}_{\Lambda'} \rangle = \frac{\hbar^2}{2} U_{\Lambda\Lambda'} \tag{77}$$

where $U_{\Lambda\Lambda'}$ is defined as:

$$U_{\Lambda\Lambda'}$$

$$= \frac{1}{\sqrt{(1+\delta_{\Lambda 0})(1+\delta_{\Lambda' 0})}} \big(\lambda_+(J,\Lambda)\lambda_+(J,\Lambda+1)\delta_{\Lambda,\Lambda'-2}$$

$$+ \lambda_+(J,\Lambda')\lambda_+(J,\Lambda'+1)\delta_{\Lambda,\Lambda'+2}$$

$$+ (-1)^{J+\Lambda+p}\lambda_+(J,\Lambda'-1)\lambda_+(J,\Lambda'-2)\delta_{\Lambda,2-\Lambda'} \big) \tag{78}$$

The first two terms of Eq. (78) make equal contributions to the second upper and lower off-diagonal Λ-blocks, respectively. The last term affects blocks (0, 2), (1, 1) and (2, 0). Because of the last term, the values of blocks (0, 2) and (2, 0) can either be

doubled (if $J + p$ is even) or nullified (if $J + p$ is odd). Contributions of $U_{\Lambda\Lambda'}$ to different Λ-blocks of the Hamiltonian matrix are shown schematically in Figure 24.

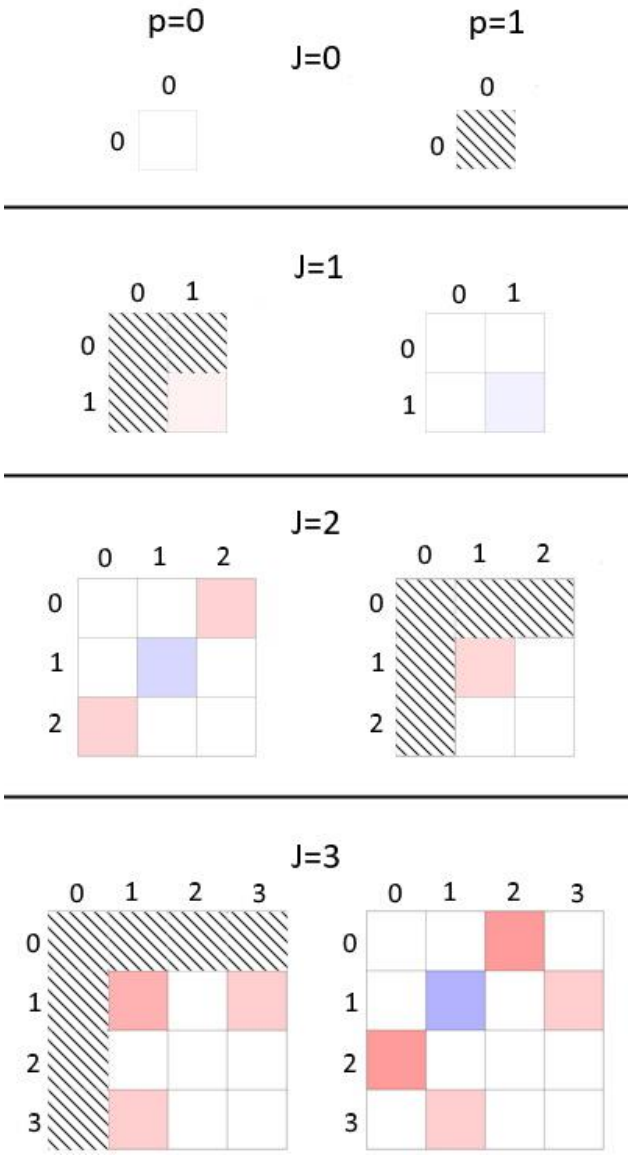

Figure 24. Block structure of the matrix $U_{\Lambda\Lambda'}$ for the rotational states from $J = 0$ to $J = 3$ (intuitive extrapolation to larger values of J is relatively straightforward). The two parities are shown separately: $p = 0$ in the left column and $p = 1$ in the right column. The blocks are labelled by the values of Λ and Λ'. Color indicates magnitudes of matrix elements, with red means positive, blue negative, and white zero. When $J + p$ is odd, all states corresponding to $\Lambda = 0$ or $\Lambda' = 0$ do not exist and the corresponding blocks of the Hamiltonian matrix are excluded (hatched).

Finally, plugging Eq. (77) into Eq. (59) one obtains an expression for the matrix elements of asymmetric top rotor:

$$\langle \Psi_\Lambda \widetilde{D}_\Lambda \big| \hat{T}_{\text{asym}} \big| \Psi_{\Lambda'} \widetilde{D}_{\Lambda'} \rangle = \frac{\hbar^2}{4} U_{\Lambda\Lambda'} \langle \Psi_\Lambda | A - B | \Psi_{\Lambda'} \rangle \tag{79}$$

Contributions of the asymmetric top rotor term are marked with "A" in Figure 23.

4.3.3. Derivation of the Coriolis Coupling Matrix Elements

Using the definition of Eq. (40), one can write the expression for the matrix elements of the Coriolis coupling operator $\hat{T}_{\text{cor}}$ as:

$$\langle \Psi_\Lambda \widetilde{D}_\Lambda \big| \hat{T}_{\text{cor}} \big| \Psi_{\Lambda'} \widetilde{D}_{\Lambda'} \rangle = \langle \Psi_\Lambda | 4B \cos\theta \frac{d}{d\varphi} | \Psi_{\Lambda'} \rangle \langle \widetilde{D}_\Lambda \big| i\hbar \hat{J}_y \big| \widetilde{D}_{\Lambda'} \rangle \tag{80}$$

Once again the modified Wigner functions $\widetilde{D}_\Lambda$ are not eigenfunctions of $\hat{J}_y$, therefore let us consider the last term of Eq. (80) separately. Using Eq. (64), this integral can be expressed through $\hat{J}_+$ and $\hat{J}_-$ as:

$$\langle \widetilde{D}_\Lambda \big| i\hbar \hat{J}_y \big| \widetilde{D}_{\Lambda'} \rangle = \frac{\hbar}{2} \left(\langle \widetilde{D}_\Lambda \big| \hat{J}_- \big| \widetilde{D}_{\Lambda'} \rangle - \langle \widetilde{D}_\Lambda \big| \hat{J}_+ \big| \widetilde{D}_{\Lambda'} \rangle \right) \tag{81}$$

Following the footsteps of the derivation in the previous section (compare with Eqs. (73) and (75)), one can show that

$$\begin{aligned} &\langle \widetilde{D}_\Lambda \big| \hat{J}_+ \big| \widetilde{D}_{\Lambda'} \rangle \\ &= \frac{\hbar}{2\sqrt{(1+\delta_{\Lambda 0})(1+\delta_{\Lambda' 0})}} \big(\lambda_+(J,\Lambda') \delta_{\Lambda,\Lambda'+1} \\ &+ (-1)^{J+\Lambda'+p} \lambda_+(J,\Lambda'-1) \delta_{\Lambda,1-\Lambda'} - \lambda_+(J,\Lambda'-1) \delta_{\Lambda,\Lambda'-1} \big) \end{aligned} \tag{82}$$

and

$$\langle \widetilde{D}_{\Lambda} | \hat{J}_{-} | \widetilde{D}_{\Lambda'} \rangle$$

$$= \frac{\hbar}{2\sqrt{(1+\delta_{\Lambda 0})(1+\delta_{\Lambda' 0})}} \big(\lambda_{+}(J, \Lambda' - 1) \delta_{\Lambda, \Lambda' - 1}$$

$$+ (-1)^{J+\Lambda+p} \lambda_{+}(J, \Lambda' - 1) \delta_{\Lambda, 1-\Lambda'} - \lambda_{+}(J, \Lambda') \delta_{\Lambda, \Lambda'+1} \big) \tag{83}$$

This time the parity of the two Λ values is required to be different, therefore $(-1)^{J+\Lambda+p}(-1)^{J+\Lambda'+p} = -1$, which changes the sign of the last terms in Eqs. (110) and (94).

Plugging Eqs. (110) and (94) back into Eq. (81), one obtains:

$$\langle \widetilde{D}_{\Lambda} | i\hbar \hat{J}_{y} | \widetilde{D}_{\Lambda'} \rangle = \frac{\hbar^2}{2} W_{\Lambda\Lambda'} \tag{84}$$

where $W_{\Lambda\Lambda'}$ is defined as:

$$W_{\Lambda\Lambda'}$$

$$= \frac{1}{\sqrt{(1+\delta_{\Lambda 0})(1+\delta_{\Lambda' 0})}} \big(\lambda_{+}(J, \Lambda) \delta_{\Lambda, \Lambda' - 1} - \lambda_{+}(J, \Lambda') \delta_{\Lambda, \Lambda'+1}$$

$$+ (-1)^{J+\Lambda+p} \lambda_{+}(J, \Lambda' - 1) \delta_{\Lambda, 1-\Lambda'} \big) \tag{85}$$

Similar to the case of $U_{\Lambda\Lambda'}$ in Eq. (78), the first two terms of Eq. (96) make equal contributions to the first upper and lower off-diagonal Λ-blocks, respectively. The last term affects the blocks (0, 1) and (1, 0) and either doubles or nullifies them, depending on

parity of $J + p$. Contributions of $W_{\Lambda\Lambda'}$ to different Λ-blocks of the Hamiltonian matrix are shown schematically in Figure 25.

Finally, plugging Eq. (96) into Eq. (80), one obtains a matrix element expression for Coriolis term:

$$\langle \Psi_\Lambda \widetilde{D}_\Lambda \left| \hat{T}_{\text{cor}} \right| \Psi_{\Lambda'} \widetilde{D}_{\Lambda'} \rangle = 2\hbar^2 W_{\Lambda\Lambda'} \langle \Psi_\Lambda | B \cos\theta \frac{d}{d\varphi} | \Psi_{\Lambda'} \rangle \tag{86}$$

Contributions of the Coriolis term are marked with "C" in Figure 23.

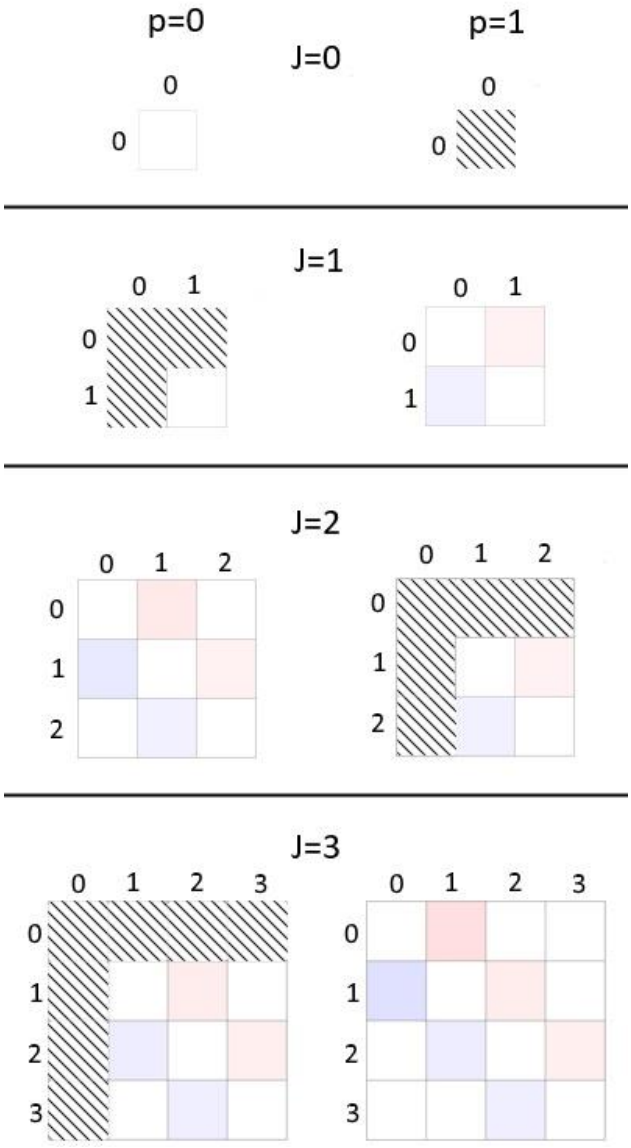

Figure 25. Same as in Figure 24, but for the matrix $W_{\Lambda\Lambda'}$.

4.4. Derivation of the Matrix Elements in Specific Vibrational Basis

So far the matrix element expressions have been derived for the case of an entirely general vibrational basis function $\Psi_\Lambda(\rho,\theta,\varphi)$. In order to derive more specific expressions, one has to consider more specific basis functions. In this work we use a product of DVR (discrete variable representation) functions for ρ ($h_n(\rho)$) and locally optimized functions of the hyper-angles $\mathrm{X}^j_{\Lambda n}(\theta,\varphi)$, i.e.

$$\Psi_\Lambda(\rho,\theta,\varphi) = h_n(\rho)\mathrm{X}^j_{\Lambda n}(\theta,\varphi) \tag{87}$$

where $h_n(\rho)$ is given by:

$$h_n(\rho_i) = \begin{cases} \dfrac{1}{\sqrt{\Delta\rho}}, \rho_i = \rho_n \\ 0, \rho_i \neq \rho_n \end{cases} \tag{88}$$

where $\Delta\rho$ is the step size in ρ-grid. Note that index j on functions $\mathrm{X}^j_{\Lambda n}(\theta,\varphi)$ is different from uppercase J (total angular momentum quantum number).

In the case of ρ, the placement of points is actually optimized based on the shape of the PES in a way that puts more points in the region of deep covalent well and fewer points in the shallow van der Waals interaction (asymptotic) region, which reduces the number of points necessary for the targeted accuracy. Even though the spacing between points is not equidistant, one can still work with it as if it were equidistant by using a mapping procedure. The details of this can be found elsewhere.[96]

Plugging Eq. (87) into Eqs. (58), (79) and (86) one obtains the following expressions:

$$\begin{aligned} \langle h_n \mathrm{X}^j_{\Lambda n}\widetilde{D}_\Lambda|\hat{T}_{\mathrm{sym}}|h_{n'}\mathrm{X}^{j'}_{\Lambda' n'}\widetilde{D}_{\Lambda'}\rangle &= \langle h_n \mathrm{X}^j_{\Lambda n}|V^\Lambda_{\mathrm{rot}}|h_{n'}\mathrm{X}^{j'}_{\Lambda n'}\rangle\,\tilde{\delta}_{\Lambda\Lambda'} \\ &= \langle \mathrm{X}^j_{\Lambda n}|V^{\Lambda n}_{\mathrm{rot}}|\mathrm{X}^{j'}_{\Lambda n}\rangle\,\delta_{nn'}\tilde{\delta}_{\Lambda\Lambda'} \end{aligned} \tag{89}$$

$$\langle h_n \mathrm{X}^{j}_{\Lambda n} \widetilde{D}_{\Lambda} | \hat{T}_{\mathrm{asym}} | h_{n'} \mathrm{X}^{j'}_{\Lambda' n'} \widetilde{D}_{\Lambda'} \rangle = \frac{\hbar^2}{4} U_{\Lambda\Lambda'} \delta_{nn'} \langle \mathrm{X}^{j}_{\Lambda n} | A_n - B_n | \mathrm{X}^{j'}_{\Lambda' n} \rangle \tag{90}$$

$$\langle h_n \mathrm{X}^{j}_{\Lambda n} \widetilde{D}_{\Lambda} | \hat{T}_{cor} | h_{n'} \mathrm{X}^{j'}_{\Lambda' n'} \widetilde{D}_{\Lambda'} \rangle \quad = 2\hbar^2 W_{\Lambda\Lambda'} \delta_{nn'} \langle \mathrm{X}^{j}_{\Lambda n} | B_n \cos\theta \frac{d}{d\varphi} | \mathrm{X}^{j'}_{\Lambda' n} \rangle \tag{91}$$

where the modified Kronecker delta functions $\tilde{\delta}_{\Lambda\Lambda'}$ are given by Eq. (57) and the expression for the rotational potential was introduced:

$$V^{\Lambda}_{\mathrm{rot}}(\rho, \theta) = \hbar^2 \left(J(J+1) \frac{A+B}{2} + \Lambda^2 \left(C - \frac{A+B}{2} \right) \right) \tag{92}$$

Here and later in the chapter, index n is used to signify that ρ is restricted to $\rho = \rho_n$, e.g. $A_n = A_n(\theta) = A(\rho_n, \theta)$, $V^{\Lambda n}_{\mathrm{rot}} = V^{\Lambda}_{\mathrm{rot}}(\rho_n, \theta)$. In a similar way, index l is used when $\theta = \theta_l$, etc.

Using the definition of Eq. (87) and the results of Eqs. (89)-(91), the matrix elements of the Hamiltonian operator of Eq. (53) can be written as:

$$\begin{aligned}
&\langle h_n \mathrm{X}^{j}_{\Lambda n} \widetilde{D}_{\Lambda} | \hat{H} | h_{n'} \mathrm{X}^{j'}_{\Lambda' n'} \widetilde{D}_{\Lambda'} \rangle \\
&\qquad = \langle h_n \mathrm{X}^{j}_{\Lambda n} \widetilde{D}_{\Lambda} | \hat{T}_{\rho} | h_{n'} \mathrm{X}^{j'}_{\Lambda' n'} \widetilde{D}_{\Lambda'} \rangle \\
&\qquad + \langle h_n \mathrm{X}^{j}_{\Lambda n} \widetilde{D}_{\Lambda} | \hat{T}_{\theta} + \hat{T}_{\varphi} + V_{\mathrm{pes}} + V_{\mathrm{ext}} + \hat{T}_{\mathrm{sym}} | h_{n'} \mathrm{X}^{j'}_{\Lambda' n'} \widetilde{D}_{\Lambda'} \rangle \\
&\qquad + \langle h_n \mathrm{X}^{j}_{\Lambda n} \widetilde{D}_{\Lambda} | \hat{T}_{\mathrm{asym}} + \hat{T}_{\mathrm{cor}} | h_{n'} \mathrm{X}^{j'}_{\Lambda' n'} \widetilde{D}_{\Lambda'} \rangle \\
&\qquad = \langle h_n | \hat{T}_{\rho} | h_{n'} \rangle \langle \mathrm{X}^{j}_{\Lambda n} | \mathrm{X}^{j'}_{\Lambda n'} \rangle \tilde{\delta}_{\Lambda\Lambda'} \\
&\qquad + \langle \mathrm{X}^{j}_{\Lambda n} | \hat{T}^{n}_{\theta} + \hat{T}^{n}_{\varphi} + V^{n}_{\mathrm{pes}} + V^{n}_{\mathrm{ext}} + V^{\Lambda n}_{\mathrm{rot}} | \mathrm{X}^{j'}_{\Lambda n} \rangle \delta_{nn'} \tilde{\delta}_{\Lambda\Lambda'} \\
&\qquad + \langle h_n \mathrm{X}^{j}_{\Lambda n} \widetilde{D}_{\Lambda} | \hat{T}_{\mathrm{asym}} + \hat{T}_{\mathrm{cor}} | h_{n'} \mathrm{X}^{j'}_{\Lambda' n'} \widetilde{D}_{\Lambda'} \rangle
\end{aligned} \tag{93}$$

The structure of the Hamiltonian matrix in Eq. (93) can be greatly simplified if the hyper-angle basis functions $\mathrm{X}^{j}_{\Lambda n}(\theta, \varphi)$ are chosen to be the eigenfunctions of the corresponding 2D Hamiltonian:

$$\widehat{H}_{\mathrm{2D}}^{\Lambda n} = \hat{T}_{\theta}^{n} + \hat{T}_{\varphi}^{n} + V_{\mathrm{pes}}^{n} + V_{\mathrm{ext}}^{n} + V_{\mathrm{rot}}^{\Lambda n} \tag{94}$$

i.e.:

$$\widehat{H}_{\mathrm{2D}}^{\Lambda n}\mathrm{X}_{\Lambda n}^{j}(\theta,\varphi) = \varepsilon_{\Lambda n}^{j}\mathrm{X}_{\Lambda n}^{j}(\theta,\varphi) \tag{95}$$

Note that for each ρ_n this operator includes the rotational potential $V_{\mathrm{rot}}^{\Lambda n}$ of a symmetric top rotor, just like in Eq. (92), but with $\rho = \rho_n$.

Using Eqs. (90), (91) and (95), Eq. (93) transforms into the following final expression for the rovibrational Hamiltonian matrix element:

$$\begin{aligned}\langle h_n \mathrm{X}_{\Lambda n}^{j}\widetilde{D}_{\Lambda}\big|\widehat{H}\big|h_{n'}\mathrm{X}_{\Lambda' n'}^{j'}\widetilde{D}_{\Lambda'}\rangle \;&= \tilde{\delta}_{\Lambda\Lambda'}\langle h_n\big|\hat{T}_{\rho}\big|h_{n'}\rangle\,\langle \mathrm{X}_{\Lambda n}^{j}|\mathrm{X}_{\Lambda n'}^{j'}\rangle \\ &+ \tilde{\delta}_{\Lambda\Lambda'}\delta_{nn'}\delta_{jj'}\varepsilon_{\Lambda n}^{j} \\ &+ \frac{\hbar^2}{4}U_{\Lambda\Lambda'}\delta_{nn'}\,\langle \mathrm{X}_{\Lambda n}^{j}|A_n - B_n|\mathrm{X}_{\Lambda' n}^{j'}\rangle \\ &+ 2\hbar^2 W_{\Lambda\Lambda'}\delta_{nn'}\,\langle \mathrm{X}_{\Lambda n}^{j}|B_n\cos\theta\,\frac{d}{d\varphi}|\mathrm{X}_{\Lambda' n}^{j'}\rangle\end{aligned} \tag{96}$$

where the factor of $\delta_{jj'}$ appears due to orthonormal properties of each set of $\mathrm{X}_{\Lambda n}^{j}$ for given values of Λ and n. Note that the same simplification cannot be done for the first term of Eq. (96), since the values of n on the basis functions there are different.

4.5. Sequential Diagonalization Truncation (SDT)

In this section we consider Sequential Diagonalization Truncation (SDT) approach to derive specific expressions for the hyper-angle basis functions $\mathrm{X}_{\Lambda n}^{j}(\theta,\varphi)$ of Eq. (96) in terms of underlying basis functions.

In order to determine a suitable set of 2D functions $\mathrm{X}_{\Lambda n}^{j}(\theta,\varphi)$, the hierarchy of expansions is continued. Namely, for each point n of ρ-grid and for each Λ the following expansion is constructed:

$$\mathrm{X}^{j}_{\Lambda n}(\theta,\varphi)=\sum_{l}^{L}\sum_{i}^{S_{\Lambda nl}} b^{j}_{\Lambda nli}\, g_l(\theta)\Phi^{i}_{\Lambda nl}(\varphi) \tag{97}$$

where $\Phi^{i}_{\Lambda nl}(\varphi)$ is a locally-optimal basis set of functions for the hyper-angle φ, and $g_l(\theta)$ is a set of DVR basis functions for the hyper-angle θ, defined, in a way similar to Eq. (88), as:

$$g_l(\theta_i)=\begin{cases}\dfrac{1}{\sqrt{\Delta\theta}}, \theta_i=\theta_l\\ 0, \theta_i\neq\theta_l\end{cases} \tag{98}$$

where $\Delta\theta$ is the step size in θ-grid. Here and later in the text index l is used to signify that θ is restricted to $\theta=\theta_l$.

The matrix elements of $\widehat{H}^{\Lambda n}_{\mathrm{2D}}$ (Eq. (94)) in this basis of Eq. (97) are given by:

$$\begin{aligned}\langle g_l\Phi^{i}_{\Lambda nl}|\widehat{H}^{\Lambda n}_{\mathrm{2D}}|g_{l'}\Phi^{i'}_{\Lambda nl'}\rangle &= \langle g_l|\hat{T}^{n}_{\theta}|g_{l'}\rangle\langle\Phi^{i}_{\Lambda nl}|\Phi^{i'}_{\Lambda nl'}\rangle\\ &+\langle\Phi^{i}_{\Lambda nl}|\hat{T}^{nl}_{\varphi}+V^{nl}_{\mathrm{pes}}+V^{nl}_{\mathrm{ext}}+V^{\Lambda nl}_{\mathrm{rot}}|\Phi^{i'}_{\Lambda nl}\rangle\delta_{ll'}\end{aligned} \tag{99}$$

Once again, $g_l(\theta)$ is non-zero only at $\theta=\theta_l$, so one can set $\theta=\theta_l$ in the operator $\hat{T}^{n}_{\varphi}$ and in the functions V^{n}_{pes}, V^{n}_{ext} and $V^{\Lambda n}_{\mathrm{rot}}$, by introducing in Eq. (99) their versions labelled by l.

Looking at Eq. (99), one can see that the structure of this matrix is simplified by choosing $\Phi^{i}_{\Lambda nl}(\varphi)$ to be the eigenfunctions of the 1D operator in hyper-angle φ:

$$\widehat{H}^{\Lambda nl}_{\mathrm{1D}}=\hat{T}^{nl}_{\varphi}+V^{nl}_{\mathrm{pes}}+V^{nl}_{\mathrm{ext}}+V^{\Lambda nl}_{\mathrm{rot}} \tag{100}$$

i.e.:

$$\widehat{H}^{\Lambda nl}_{\mathrm{1D}}\Phi^{i}_{\Lambda nl}(\varphi)=\varepsilon^{i}_{\Lambda nl}\Phi^{i}_{\Lambda nl}(\varphi) \tag{101}$$

Each of the sets of $\Phi^{i}_{\Lambda nl}(\varphi)$ is orthonormal, therefore Eq. (99) transforms to:

$$\langle g_l\Phi^{i}_{\Lambda nl}|\widehat{H}^{\Lambda n}_{\mathrm{2D}}|g_{l'}\Phi^{i'}_{\Lambda nl'}\rangle=\langle g_l|\hat{T}^{n}_{\theta}|g_{l'}\rangle\langle\Phi^{i}_{\Lambda nl}|\Phi^{i'}_{\Lambda nl'}\rangle+\varepsilon^{i}_{\Lambda nl}\delta_{ii'}\delta_{ll'} \tag{102}$$

Finally, the locally optimal sets of 1D functions $\Phi^i_{\Lambda nl}(\varphi)$ are expanded in a variational basis representation (VBR) basis set for hyper-angle φ:

$$\Phi^i_{\Lambda nl}(\varphi) = \sum_m^M a^i_{\Lambda nlm} f_m(\varphi) \tag{103}$$

The elementary VBR basis functions in Eq. (103) are represented by a set of normalized cosine (vibrational symmetry A_1, labelled by "+" for symmetric) or sine (vibrational symmetry B_1, labelled by "–" for antisymmetric) functions:

$$f_m^+(\varphi) = \frac{1}{\sqrt{\pi(\delta_{m0}+1)}} \cos(m\varphi)\,, m = 0 \ldots M-1 \tag{104}$$

$$f_m^-(\varphi) = \frac{1}{\sqrt{\pi}} \sin(m\varphi)\ m = 1 \ldots M \tag{105}$$

In contexts where vibrational symmetry of $f_m(\varphi)$ does not matter (i.e. both symmetries are treated in the same way), we make the symmetry label implicit, for clarity of notation.

The matrix elements of $\widehat{H}^{\Lambda nl}_{1\mathrm{D}}$ (Eq. (100)) in the basis of Eq. (103) are given by:

$$\langle f_m | \widehat{H}^{\Lambda nl}_{1\mathrm{D}} | f_{m'} \rangle = -m^2 \delta_{mm'} + \langle f_m | V^{nl}_{\mathrm{pes}} | f_{m'} \rangle + \left(V^{nl}_{\mathrm{ext}} + V^{\Lambda nl}_{\mathrm{rot}}\right)\delta_{mm'} \tag{106}$$

Practical implementation of this approach proceeds in the reverse order, starting from 1D and going to 6D. The first step is the calculation of eigenvalues $\varepsilon^i_{\Lambda nl}$ and eigenvectors $a^i_{\Lambda nlm}$ for each of the $\Lambda \times n \times l$ one-dimensional operators $\widehat{H}^{\Lambda nl}_{1\mathrm{D}}$, by diagonalization of the corresponding matrices given by Eq. (106). Before proceeding to the next step, this set of 1D solutions is truncated based on their energy, to keep only the solutions with $\varepsilon^i_{\Lambda nl} < E_{\mathrm{cut}}$, where E_{cut} is a convergence parameter that depends on the system and the energy span of the spectrum. The retained solutions represent the locally optimal 1D-basis sets $\Phi^i_{\Lambda nl}(\varphi)$ for Eq. (97).

The second step is the calculation of eigenvalues $\varepsilon_{\Lambda n}^{j}$ and eigenvectors $b_{\Lambda nli}^{j}$ for each of the $\Lambda \times n$ two-dimensional operators $\widehat{H}_{\mathrm{2D}}^{\Lambda n}$, by diagonalization of the corresponding matrices given by Eq. (99). Again, before proceeding to the next step, this set of 2D solutions is truncated using the same energy criterion $\varepsilon_{\Lambda n}^{j} < E_{\mathrm{cut}}$ to determine the locally-optimized 2D-basis sets $\mathrm{X}_{\Lambda n}^{j}(\theta, \varphi)$ for Eq. (87). It should be emphasized that this method adjusts basis sets locally to the shape of the PES, but also takes into account the level of rotational excitation of the system (determined by the values of J and Λ), since the rotational potential $V_{\mathrm{rot}}^{\Lambda nl}$ is introduced at the very beginning, in Eq. (100).

At the final third step a set of three-dimensional vibrational eigenvectors $c_{\Lambda nj}^{k}$ is obtained by diagonalizing the Hamiltonian matrix of Eq. (96), which also takes into account the rotational-vibrational couplings (the asymmetric top rotor terms and the Coriolis coupling terms, including the effect of parity p). This gives the spectrum of coupled rotational-vibrational eigenstates of the system, ε^{k}, and the overall 6D ro-vibrational wave function, expressed by combination of Eqs. (103), (97), (87) and (48), as follows:

$$F^{k}(\rho, \theta, \phi, \alpha, \beta, \gamma) = \sum_{\Lambda=0,1}^{J} \sum_{n}^{N} \sum_{j}^{S_{\Lambda n}} \sum_{l}^{L} \sum_{i}^{S_{\Lambda nl}} \sum_{m}^{M} c_{\Lambda nj}^{k} b_{\Lambda nli}^{j} a_{\Lambda nlm}^{i} h_{n}(\rho) g_{l}(\theta) f_{m}(\varphi) \widetilde{D}_{\Lambda}(\alpha, \beta, \gamma) \quad (107)$$

Such sequential addition of the vibrational degrees of freedom, with truncation of solutions between the steps, is known as the Sequential Diagonalization Truncation (SDT) method.[109,110] SDT approach allows to significantly reduce the size of the Hamiltonian matrix in comparison to brute-force applications of multi-dimensional basis sets, represented by a direct-product of generic DVR or VBR functions.[111]

4.6. Practical Considerations for Evaluation of the Matrix Elements

In this section we follow the steps of SDT, outlined in the previous sections, and provide more practical guidelines and explicit analytic expressions for evaluation of matrix elements in terms of expansion coefficients over the elementary basis functions of Eq. (107): $c^{k}_{\Lambda nj}$, $b^{j}_{\Lambda nli}$ and $a^{i}_{\Lambda nlm}$. Such explicit analytical expressions provide a good practical way of evaluating the matrix elements, since the right-hand side only involves easily programmable operations such as addition or multiplication.

As outlined in the previous section, practical implementations of the present methodology start from 1D problem and work their way up to 6D, step by step. First, consider evaluation of the 1D matrix elements, given by Eq. (106). The first term is the kinetic energy element for φ, which is already analytical in the basis of functions $f_m(\varphi)$ and represents a simple operation of addition of $-m^2$ to the diagonal of $\widehat{H}^{\Lambda nl}_{\mathrm{1D}}$ matrix. The second term, $\langle f_m|V^{nl}_{\mathrm{pes}}|f_{m'}\rangle$, does not have an analytical expression and the corresponding integral is evaluated numerically, using a large 1D quadrature in φ. The last term in this formula is just a constant energy shift of each individual 1D problem, since V^{nl}_{ext} and $V^{\Lambda nl}_{\mathrm{rot}}$ moieties are reduced to just scalar numbers (see Eqs. (36), (41)-(43) and (92)). Therefore, $\widehat{H}^{\Lambda nl}_{\mathrm{1D}}$ matrix can be readily built and diagonalized, which provides us with optimized 1D basis functions $\Phi^{i}_{\Lambda nl}(\varphi)$ of Eq. (103), their expansion coefficients over the VBR functions ($a^{i}_{\Lambda nlm}$) and energies ($\varepsilon^{i}_{\Lambda nl}$).

Next one needs to evaluate the matrix elements for 2D problem, given by Eq. (102). The first term there is the kinetic energy matrix element for θ. Since the points along θ are equidistant, one can use an analytical expression to evaluate the kinetic energy matrix elements, using parameters of the θ-grid only, as follows:[96]

$$\langle g_l|\hat{T}_\theta^n|g_{l'}\rangle = \begin{cases} \dfrac{\pi^2}{(\theta_{max}-\theta_{min})^2}\dfrac{L^2+2}{6} \text{ if } l = l' \\ (-1)^{l-l'}\dfrac{\pi^2}{(\theta_{max}-\theta_{min})^2}\dfrac{1}{\sin^2\left(\dfrac{(l-l')\pi}{L}\right)} \text{ if } l \neq l' \end{cases} \quad (108)$$

where L is the total number of points in θ-grid and $\theta_{max} - \theta_{min}$ is the physical length of the grid.

The next term of Eq. (102) can be expressed via the expansion coefficients $a^i_{\Lambda nlm}$, readily available from the previous diagonalization step, as:

$$\begin{aligned} &\langle \Phi^i_{\Lambda nl}|\Phi^{i'}_{\Lambda nl'}\rangle \\ &= \langle \sum_m^M a^i_{\Lambda nlm} f_m \,|\, \sum_{m'}^M a^{i'}_{\Lambda nl'm'} f_{m'}\rangle = \sum_m^M \sum_{m'}^M a^i_{\Lambda nlm} a^{i'}_{\Lambda nl'm'} \langle f_m|f_{m'}\rangle \\ &= \sum_m^M a^i_{\Lambda nlm} a^{i'}_{\Lambda nl'm} \end{aligned} \quad (109)$$

The last term is just addition of the energies $\varepsilon^i_{\Lambda nl}$ to the diagonal of matrix $\widehat{H}^{\Lambda n}_{\mathrm{2D}}$. This concludes the construction of $\widehat{H}^{\Lambda n}_{\mathrm{2D}}$ matrix, diagonalization of which gives us 2D basis functions $\mathrm{X}^j_{\Lambda n}(\theta, \varphi)$ of Eq. (97), their expansion coefficients over 1D functions ($b^j_{\Lambda nli}$) and energies $\varepsilon^j_{\Lambda n}$.

Next, one needs to evaluate the final matrix element expression of the overall Hamiltonian matrix $\widehat{H}$, given by Eq. (96). The first term in Eq. (96) is the kinetic energy matrix element for ρ. Unlike the kinetic energy matrix element for θ, this term cannot be evaluated analytically, since the placement of grid points is not equidistant. Therefore, the following expression is evaluated numerically:[93,96]

$$\langle h_n|\hat{T}_\rho|h_{n'}\rangle = -\frac{\hbar^2}{2\mu}\langle h_n|\frac{\partial^2}{\partial\rho^2}|h_{n'}\rangle = -\frac{\hbar^2}{2\mu}\left(\frac{1}{\sqrt{J_\rho}}\frac{\partial}{\partial\rho}\frac{1}{J_\rho}\frac{\partial}{\partial\rho}\frac{h_{n'}}{\sqrt{J_\rho}}\right)_n \tag{110}$$

where J_ρ is ρ-grid Jacobian, obtained during optimized grid generation as discussed in Ref. 93, and n subscript denotes operation of taking n-th element of the resulting vector. Individual derivatives in Eq. (110) can be evaluated, using, for example, discrete Fourier transform.

The second term of Eq. (96) can be expressed through the expansion coefficients of 1D and 2D basis functions by invoking Eqs. (97), (109) and orthonormal properties of $g_l(\theta)$ as:

$$\begin{aligned}
&\langle \mathrm{X}^{j}_{\Lambda n}|\mathrm{X}^{j'}_{\Lambda n'}\rangle \\
&= \langle \sum_{l}^{L}\sum_{i}^{S_{\Lambda n l}} b^{j}_{\Lambda n l i} g_l \Phi^{i}_{\Lambda n l} \,|\, \sum_{l'}^{L}\sum_{i'}^{S_{\Lambda n' l'}} b^{j'}_{\Lambda n' l' i'} g_{l'} \Phi^{i'}_{\Lambda n' l'}\rangle \\
&= \sum_{l}^{L}\sum_{i}^{S_{\Lambda n l}}\sum_{l'}^{L}\sum_{i'}^{S_{\Lambda n l}} b^{j}_{\Lambda n l i} b^{j'}_{\Lambda n' l' i'} \langle g_l|g_{l'}\rangle \langle \Phi^{i}_{\Lambda n l}|\Phi^{i'}_{\Lambda n' l'}\rangle \\
&= \sum_{l}^{L}\sum_{m}^{M}\left(\sum_{i}^{S_{\Lambda n l}} b^{j}_{\Lambda n l i} a^{i}_{\Lambda n l m}\right)\left(\sum_{i'}^{S_{\Lambda n' l}} b^{j'}_{\Lambda n' l i'} a^{i'}_{\Lambda n' l m}\right)
\end{aligned} \tag{111}$$

The third term of Eq. (96) is simply the energy of 2D basis functions $\varepsilon^{j}_{\Lambda n}$, added to the diagonal of the Hamiltonian matrix $\hat{H}$.

The fourth term of Eq. (96) is the asymmetric top rotor term. The value of matrix $U_{\Lambda\Lambda'}$ depends on J and Λ only, and is straightforward to evaluate, using the definition of Eq. (78). The corresponding vibrational term can be evaluated analytically, similar to Eq. (111), as:

$$\langle \mathrm{X}^{j}_{\Lambda n}|A_n - B_n|\mathrm{X}^{j'}_{\Lambda' n}\rangle$$

$$= \langle \sum_{l}^{L}\sum_{i}^{S_{\Lambda n l}} b^{j}_{\Lambda n l i} g_l \Phi^{i}_{\Lambda n l}\,|A_n - B_n|\sum_{l'}^{L}\sum_{i'}^{S_{\Lambda' n l'}} b^{j'}_{\Lambda' n l' i'} g_{l'} \Phi^{i'}_{\Lambda' n l'}\rangle$$

$$= \sum_{l}^{L}(A_{nl} - B_{nl})\sum_{m}^{M}\left(\sum_{i}^{S_{\Lambda n l}} b^{j}_{\Lambda n l i} a^{i}_{\Lambda n l m}\right)\left(\sum_{i'}^{S_{\Lambda' n l}} b^{j'}_{\Lambda' n l i'} a^{i'}_{\Lambda' n l m}\right) \tag{112}$$

The final term of Eq. (96) is the Coriolis coupling term. Once again, the value of matrix $W_{\Lambda\Lambda'}$ depends on J and Λ only, and is straightforward to evaluate, using the definition of Eq. (85). The corresponding vibrational term can be evaluated analytically:

$$\langle \mathrm{X}^{j}_{\Lambda n}|B_n \cos\theta \frac{d}{d\varphi}|\mathrm{X}^{j'}_{\Lambda' n}\rangle$$

$$= \langle \sum_{l}^{L}\sum_{i}^{S_{\Lambda n l}}\sum_{m}^{M} b^{j}_{\Lambda n l i} a^{i}_{\Lambda n l m} g_l f_m\,|B_n \cos\theta \frac{d}{d\varphi}|\sum_{l'}^{L}\sum_{i'}^{S_{\Lambda' n l'}}\sum_{m'}^{M} b^{j'}_{\Lambda' n l' i'} a^{i'}_{\Lambda' n l' m'} g_{l'} f_{m'}\rangle$$

$$= \sum_{l,i,m}\sum_{l',i',m'} b^{j}_{\Lambda n l i} a^{i}_{\Lambda n l m} b^{j'}_{\Lambda' n l' i'} a^{i'}_{\Lambda' n l' m'} \langle g_l|B_n \cos\theta|g_{l'}\rangle \langle f_m|\frac{d}{d\varphi}|f_{m'}\rangle \tag{113}$$

Let us take a closer look at evaluation of $\langle f_m|\frac{d}{d\varphi}|f_{m'}\rangle$ term. The values of $\langle f_m|\frac{d}{d\varphi}|f_{m'}\rangle$ depend on the mutual symmetry of two functions and two cases are possible:

$$\langle f^{\pm}_{m}|\frac{d}{d\varphi}|f^{\pm}_{m'}\rangle = \mp m\langle f^{\pm}_{m}|f^{\mp}_{m'}\rangle = 0 \tag{114}$$

$$\langle f^{\pm}_{m}|\frac{d}{d\varphi}|f^{\mp}_{m'}\rangle = \pm m\langle f^{\pm}_{m}|f^{\pm}_{m'}\rangle = \pm m\delta_{mm'} \tag{115}$$

As one can see, the integral is non-zero only when the functions of different symmetries are combined. The absence of the Coriolis coupling between the functions f_m of the same symmetry (together with the other features of the Hamiltonian matrix

structure, discussed in section 4.3) makes it possible to separate the Hamiltonian matrix into 2 submatrices and diagonalize them separately, as shown in Figure 26, which presents a "zoom in" on the Hamiltonian matrix structure previously shown in Figure 23. The inner structure of each block in Figure 23 is shown as 2x2 subblocks group here. Individual subblocks are labelled by combinations of vibrational symmetries of the basis functions $f_m(\varphi)$. As one can see, symmetric and asymmetric top rotor terms only couple the same symmetries, whereas the Coriolis coupling term only couples the opposite symmetries (Eq. (115)).

Rearranging rows and columns and shown in Figure 26 separates the Hamiltonian into two independent submatrices. Each submatrix uses only one symmetry of f_m in a given Λ-block. The symmetry of f_m alternates between successive Λ-blocks and starts with f_m^+ in one submatrix and f_m^- in the other one. Thus, the $\pm$ sign in Eq. (115) can be expressed through the value of Λ and the value of starting symmetry in the $\Lambda = 0$ block as:

	A_1^0	B_1^0	A_1^1	B_1^1	A_1^2	B_1^2	A_1^3	B_1^3
A_1^0	S			C	A			
B_1^0		S	C			A		
A_1^1		C	SA			C	A	
B_1^1	C			SA	C			A
A_1^2	A			C	S			C
B_1^2		A	C			S	C	
A_1^3			A			C	S	
B_1^3				A	C			S

→

	A_1^0	B_1^1	A_1^2	B_1^3	B_1^0	A_1^1	B_1^2	A_1^3
A_1^0	S	C	A					
B_1^1	C	SA	C	A				
A_1^2	A	C	S	C				
B_1^3		A	C	S				
B_1^0					S	C	A	
A_1^1					C	SA	C	A
B_1^2					A	C	S	C
A_1^3						A	C	S

Figure 26. Left-hand side: a more detailed version of the Hamiltonian matrix structure presented in Figure 23. Rows/columns are labelled by vibrational symmetry (A_1 or B_1) and Λ (in superscript). Right-hand side: a possible rearrangement of rows and columns that leads to separation of the overall Hamiltonian into 2 independent blocks.

$$\langle f_m | \frac{d}{d\varphi} | f_{m'} \rangle = (-1)^{\Lambda+s} m \delta_{mm'} \tag{116}$$

where s is the symmetry of the $\Lambda = 0$ block, defined as:

$$s = \begin{cases} 0 \text{ for } f_m^+ \text{ in } \Lambda = 0 \\ 1 \text{ for } f_m^- \text{ in } \Lambda = 0 \end{cases} \tag{117}$$

Plugging Eq. (116) back into Eq. (113) one obtains:

$$\langle \mathrm{X}_{\Lambda n}^{j} | B_n \cos\theta \frac{d}{d\varphi} | \mathrm{X}_{\Lambda' n}^{j'} \rangle$$

$$= (-1)^{\Lambda+s} \sum_{l}^{L} B_{nl} \cos\theta_l \sum_{m}^{M} m \left(\sum_{i}^{S_{\Lambda n l}} b_{\Lambda n l i}^{j} a_{\Lambda n l m}^{i} \right) \left(\sum_{i'}^{S_{\Lambda' n l}} b_{\Lambda' n l i'}^{j'} a_{\Lambda' n l m}^{i'} \right) \tag{118}$$

Inserting the results of Eqs. (111), (112) and (118), to the coupled rotational-vibrational matrix element expression of Eq. (96), one obtains the following easily evaluable expression in terms of the expansion coefficients of 1D and 2D basis functions:

$$\begin{aligned} &\langle h_n \mathrm{X}_{\Lambda n}^{j} \widetilde{D}_{\Lambda} | \widehat{H} | h_{n'} \mathrm{X}_{\Lambda' n'}^{j'} \widetilde{D}_{\Lambda'} \rangle \\ &= \tilde{\delta}_{\Lambda\Lambda'} \left(\langle h_n | \hat{T}_\rho | h_{n'} \rangle \sum_{l}^{L} \sum_{m}^{M} O_{\Lambda n n' l m}^{j} + \delta_{nn'} \delta_{jj'} \varepsilon_{\Lambda n}^{j} \right) \\ &+ \frac{\hbar^2}{4} U_{\Lambda\Lambda'} \delta_{nn'} \sum_{l}^{L} (A_{nl} - B_{nl}) \sum_{m}^{M} O_{\Lambda\Lambda' n l m}^{j} \\ &+ (-1)^{\Lambda+s} 2\hbar^2 W_{\Lambda\Lambda'} \delta_{nn'} \sum_{l}^{L} B_{nl} \cos\theta_l \sum_{m}^{M} m O_{\Lambda\Lambda' n l m}^{j} \end{aligned} \tag{119}$$

where the following replacement was introduced, for conciseness.

$$O_{\Lambda\Lambda' n n' l m}^{j} = \left(\sum_{i}^{S_{\Lambda n l}} b_{\Lambda n l i}^{j} a_{\Lambda n l m}^{i} \right) \left(\sum_{i'}^{S_{\Lambda' n' l}} b_{\Lambda' n' l i'}^{j'} a_{\Lambda' n' l m}^{i'} \right) \tag{120}$$

4.7. Assignment of Rovibrational States

In contrast to the symmetric top rotor approximation (where the overall Hamiltonian does not have couplings between different values of Λ, and thus each wave function can be characterized by one specific value of Λ), the fully coupled ro-vibrational wave functions F^k have a probability distribution over multiple values of Λ. For each Λ this probability is given by the respective term of the outer sum in Eq. (48), so we can write:

$$\langle F^k | F^{k'} \rangle = \sum_{\Lambda=0,1}^{J} p_\Lambda^k = \delta_{kk'} \tag{121}$$

Eq. (121) can be used for assignment of Λ in cases where one term of Eq. (121) is significantly larger than other terms.

Figure 27 presents a map of the PES, which features three energetically equivalent wells. In isotopically-substituted ozone molecules that contain only ^{16}O and ^{18}O, one of these wells corresponds to symmetric isotopomers (such as $^{16}O^{18}O^{16}O$ or $^{18}O^{16}O^{18}O$) and the other two wells correspond to asymmetric isotopomers (such as $^{16}O^{16}O^{18}O$ or $^{18}O^{18}O^{16}O$). Symmetric and asymmetric isotopomers of a given molecule are computed simultaneously in one run on a global PES. In contrast, different isotopologues (singly- vs. doubly-substituted ozone) are computed independently in two separate runs.

Figure 27 also shows how the covalent well corresponding to the symmetric ozone isotopomer can be separated from the asymmetric ones using the value of hyper-angle φ. The wells of asymmetric isotopomers are centered at $\varphi = \pm\pi/3$, whereas the well of the symmetric isotopomer is centered at $\varphi = \pi$. Therefore, it is convenient to

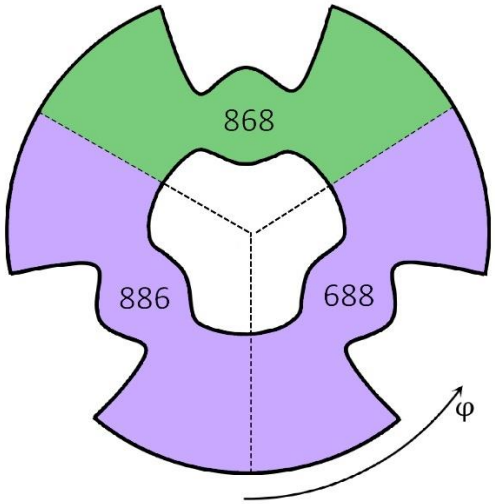

Figure 27. Schematic representation of the PES of ozone in APH coordinates, illustrating differences between symmetric and asymmetric isotopomers. The three covalent wells are labelled as “886”, “688” and “868”, where “6” and “8” stand for ^{16}O and ^{18}O, respectively. Green and violet colors mark the regions of the PES conditionally associated with the symmetric and asymmetric ozone isotopomers, respectively.

define a formal operator, which acts on the basis functions $f_m(\varphi)$ by "cutting out" the part of a wave function that corresponds to the symmetric isotopomer:

$$\hat{P}_{sym} f_m(\varphi) = \begin{cases} f_m(\varphi) \text{ for } \varphi \in \left[\frac{2\pi}{3}, \frac{4\pi}{3}\right] \\ 0 \text{ for } \varphi \notin \left[\frac{2\pi}{3}, \frac{4\pi}{3}\right] \end{cases} \tag{122}$$

With this operator, the probability that a given state F^k is a state of a symmetric molecule is given by $p^k_{sym} = \langle F^k | \hat{P}_{sym} | F^k \rangle$. Since we have only two kinds of isotopomers, either symmetric or asymmetric, the probability that a given state is a state of an asymmetric molecule can be calculated simply as $p^k_{asym} = 1 - p^k_{sym}$. Expressing the value of this integral in terms of expansion coefficients of a wave function, we obtain:

$$\langle F^k | \hat{P}_{sym} | F^k \rangle = \sum_{\Lambda,n,l,j,i,m,j',i',m'} c^{k*}_{\Lambda nj} b^{j}_{\Lambda nli} a^{i}_{\Lambda nlm} c^{k}_{\Lambda nj'} b^{j'}_{\Lambda nli'} a^{i'}_{\Lambda nlm'} \langle f_m | \hat{P}_{sym} | f_{m'} \rangle$$

$$= \sum_{\Lambda,n,l,m,m'} \langle f_m | \hat{P}_{sym} | f_{m'} \rangle \left(\sum_{j}^{S_{\Lambda n}} c^{k*}_{\Lambda nj} \sum_{i}^{S_{\Lambda nl}} b^{j}_{\Lambda nli} a^{i}_{\Lambda nlm} \right) \sum_{j'}^{S_{\Lambda n}} c^{k}_{\Lambda nj'} \sum_{i'}^{S_{\Lambda nl}} b^{j'}_{\Lambda nli'} a^{i'}_{\Lambda nlm'} \tag{123}$$

where * denotes operator of complex conjugation. Here, in contrast to Eq. (109), we cannot eliminate the sum over m', since functions $\hat{P}_{sym} f_m(\varphi)$ are not orthogonal.

In general, the integral $\int_a^b f_m^{\pm} f_{m'}^{\pm} \, d\varphi$, can be calculated analytically for arbitrary limits a and b. In the case of $\langle f_m | \hat{P}_{sym} | f_{m'} \rangle$ in Eq. (123), $a = 2\pi/3$ and $b = 4\pi/3$, which results in the following solutions:

if $m = m' = 0$, then:

$$\langle f_m | \hat{P}_{sym} | f_{m'} \rangle = 1/3 \tag{124}$$

if $m = m' \neq 0$, then:

$$\langle f_m|\hat{P}_{sym}|f_{m'}\rangle = \frac{1}{2\pi}\left(\frac{2\pi}{3} + (-1)^{\Lambda+s}\frac{\sin\left(\frac{2\pi}{3}m\right)}{m}\right) \tag{125}$$

if $m \neq m'$, then:

$$\langle f_m|\hat{P}_{sym}|f_{m'}\rangle$$

$$= -\frac{1}{\pi\sqrt{(\delta_{m0}+1)(\delta_{m'0}+1)}}$$

$$\times\left(\frac{\sin\left(\frac{2\pi}{3}(m-m')\right)}{m-m'} + (-1)^{\Lambda+s}\frac{\sin\left(\frac{2\pi}{3}(m+m')\right)}{m+m'}\right) \tag{126}$$

Eq. (123) can be used for isotopomer assignments in cases when $\langle F^k|\hat{P}_{sym}|F^k\rangle$ evaluates to a number close to 0 or 1, which is always the case for low energies, where tunneling between the covalent wells is negligibly small.

Finally, the states can also be labelled by their overall symmetry. Tables 15 and 16 give a summary of possible symmetries of different components of ro-vibrational wave functions F^k for the case of odd J (on the example of $J = 5$) and even J (on the example of $J = 4$). The first and the second columns show the values of p (parity) and Λ (z-component of J), respectively. The third column shows symmetry of the rotational component $\widetilde{D}^{Jp}_{KM}$ of the total wave function (Eq. (50)), which depends on p and whether the value of Λ is even or odd. The fourth column shows possible symmetries of the vibrational component, defined by symmetry of $f_m(\varphi)$, which can be either A_1

(symmetric, $f_m^+(\varphi)$) or B_1 (antisymmetric, $f_m^-(\varphi)$). Last column gives the rovibrational symmetry of F^k, obtained as a product of rotational and vibrational symmetries.

As discussed in derivation of Eq. (116), the vibrational symmetries of $f_m(\varphi)$ have to alternate and can start with either A_1 or B_1 in $\Lambda = 0$. Since symmetries of the nuclear spin wave function and the ground state electronic wave function of ozone are both A_1,

Table 15. A summary of possible symmetries of different components of ro-vibrational wave functions for the case of $J = 5$ (odd). Green and red colors correspond to allowed and forbidden symmetries, respectively.

Parity	Λ	Γ_{rot}	Γ_{vib}	Γ_{rovib}
$p = 0$	5	B_1	B_1, A_1	A_1, B_1
	4	A_1	A_1, B_1	A_1, B_1
	3	B_1	B_1, A_1	A_1, B_1
	2	A_1	A_1, B_1	A_1, B_1
	1	B_1	B_1, A_1	A_1, B_1
$p = 1$	0	B_2	B_1, A_1	A_2, B_2
	1	A_2	A_1, B_1	A_2, B_2
	2	B_2	B_1, A_1	A_2, B_2
	3	A_2	A_1, B_1	A_2, B_2
	4	B_2	B_1, A_1	A_2, B_2
	5	A_2	A_1, B_1	A_2, B_2

Table 16. Same as Table 15, but for the case of $J = 4$ (even).

Parity	Λ	Γ_{rot}	Γ_{vib}	Γ_{rovib}
$p = 0$	4	A_1	A_1, B_1	A_1, B_1
	3	B_1	B_1, A_1	A_1, B_1
	2	A_1	A_1, B_1	A_1, B_1
	1	B_1	B_1, A_1	A_1, B_1
	0	A_1	A_1, B_1	A_1, B_1
$p = 1$	1	A_2	A_1, B_1	A_2, B_2
	2	B_2	B_1, A_1	A_2, B_2
	3	A_2	A_1, B_1	A_2, B_2
	4	B_2	B_1, A_1	A_2, B_2

the overall symmetry of F^k is the same as the rovibrational symmetry. Note that $\Lambda = 0$ state exists only for even values of $J + p$.

Both ^{16}O and ^{18}O isotopes are bosons, i.e. have zero nuclear spin, therefore the overall wave function in both singly and doubly substituted ozone molecules is required to retain the same sign under permutation of identical particles (Bose-Einstein statistics). Only rovibrational states of symmetries A_1 and A_2 comply with that requirement, therefore they are allowed, while the other two symmetries (B_1 and B_2) are forbidden.

As one can see from Tables 15 and 16, selecting vibrational symmetries A_1 for $p = 0$ and B_1 for $p = 1$ in $\Lambda = 0$ (even when it does not exist) always yields allowed wave functions. Comparing this result with Figure 26, one can see that one of the blocks corresponds to allowed functions only, while the other block corresponds to forbidden functions only. In cases when only allowed functions are of interest, such separation allows one to reduce the necessary calculations twofold by diagonalizing only the allowed half of the Hamiltonian matrix.

4.8. Summary

In this chapter we developed theory for the efficient calculation of coupled rotational-vibrational states in triatomic molecules using APH coordinates and taking into account all terms of the Hamiltonian operator, including the asymmetric-top rotor coupling and the Coriolis coupling. Concise final formulas were derived for the efficient calculations of matrix elements, for construction of the Hamiltonian matrix, for expressing the total ro-vibrational wavefunction, for the assignment of quantum numbers to the computed eigenstates, and finally for the identification of possible isotopomers of the molecule on the global PES (i.e. symmetric vs. asymmetric ozone). Our numerical

approach is distinct from other available methods, since it uses an efficient combination of the VBR and DVR methods (taking advantage of an adaptive grid, which adjusts to the shape of the PES) and significantly reduces the size of the Hamiltonian matrix by constructing and truncating the locally-optimal basis sets at all levels of the calculations.

The methodology developed here can be used for calculations of accurate rotational-vibrational states for any triatomic molecule, not just ozone. The states can be used to quantify the molecule's spectroscopy near the bottom of the well, or to assess its chemical reactivity near the bond-breaking threshold and above it. In particular, it would be important to determine the role of rotational-vibrational couplings in the recombination reaction that forms ozone, focusing on the isotope effect. This is not an easy task, since it would require calculations for different isotopomers and isotopologues of ozone (at least $^{16}O^{18}O^{16}O$, $^{16}O^{16}O^{18}O$, $^{18}O^{16}O^{18}O$ and $^{16}O^{18}O^{18}O$) in a broad range of rotational excitations (up to $J = 50$) and vibrational excitations up to the dissociation threshold (up to 10 quanta in one mode).

CHAPTER 5. PROPERTIES OF PURELY VIBRATIONAL BOUND STATES IN OZONE AS A POSSIBLE SOURCE OF THE ISOTOPE EFFECT

In this chapter the theory outlined in Chapter 4 is applied to calculation of bound vibrational states in ozone, without overall rotation ($J = 0$), with the purpose of investigating possible isotope effects that can come from purely vibrational treatment of bound states only. The ozone molecule has three degrees of freedom, the same number as in our MRCI PES for tetrasulfur (R, α_1, α_2), therefore, in addition to the exploration of the isotope effects in ozone, this chapter has a goal of familiarizing with the 3D calculations of the vibrational states in general.

As it was pointed out in Introduction, mass-independent fractionation of oxygen isotopes in Earth's atmosphere is produced by recombination reaction that forms ozone molecules: $O + O_2 \xrightarrow{+\text{bath gas}} O_3$. One of the isotope effects related to this reaction, called η-effect, makes the rate of this reaction about 16% slower for symmetric ozone molecules, as compared to the asymmetric ones. Here we focus on this effect and investigate how the ratio of between the number of states in asymmetric and symmetric ozone molecules can contribute to it.

5.1. The Expected Ratio Between the Number of States in Asymmetric and Symmetric Ozone Molecules

The number of states in the products has direct bearing on the reaction rate, and it is usually assumed that the number of states in symmetric ozone molecules is a factor of two smaller than in the asymmetric ozone molecules. This difference is rationalized, sometimes, by invoking rotational symmetry numbers for symmetric ozone molecules, but the actual reason for this factor is a doubled phase-space available for vibrations of

asymmetric ozone molecules. One can explain this in simple terms, if one notices that among the three possible isomers of isotopically singly substituted ozone (isotopomers) only one is symmetric, whereas two others are asymmetric and identical. For example, symmetric $^{16}O^{18}O^{16}O$ *vs.* asymmetric $^{16}O^{16}O^{18}O$ and $^{18}O^{16}O^{16}O$, and similar in the case of double substitution.

More rigorous way of looking into this is through the "map" of the potential energy surface (PES) presented in Figure 28 in APH coordinates. This diagram shows three deep covalent wells of O_3 connected to three $O + O_2$ reaction channels, through the regions of weak Van der Waals interaction. One of these wells (in the middle) hosts the symmetric ozone molecule, while the other two wells host the asymmetric ozone molecule. Cleary, two wells can support twice larger number of the vibrational states. In a recent thesis[94] and in another recent paper[39] we carefully worked out what rotational-

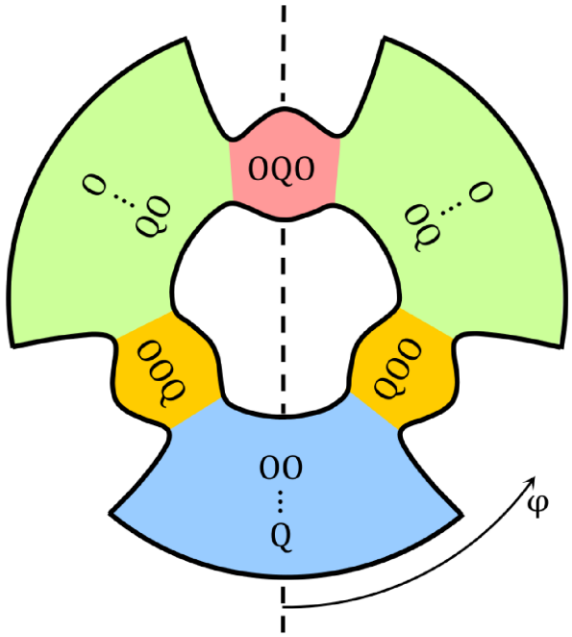

Figure 28. A map of the PES of ozone in APH coordinates. O and Q denote two different oxygen isotopes, such as ^{16}O and ^{18}O. Three potential energy wells (pink, orange) connect through three weak Van der Waals interaction regions (green, blue). Note, that asymmetric ozone molecules occupy two potential wells (orange), whereas symmetric ozone molecules occupy only one (red).

vibrational states are allowed by symmetry and showed that, indeed, their numbers in the symmetric and asymmetric ozone molecules are in the ratio of one to two, roughly. We also showed that this factor of two, by itself, is not responsible for any isotope effects, since it cancels analytically if all features of this reaction are properly taken into account.

But what if this difference is not exactly a factor of two? What if the ratio of the actual number of vibrational states deviates from this statistically-driven expectation? Surprisingly, literature search on this topic reveals that although several accurate PESs exist for ozone,[48,80,112,113] and several calculations of its vibrational spectra have been reported,[93,114–117] no one tried to compare the number of states in symmetric and asymmetric ozone molecules systematically, for both singly- and doubly-substituted cases. Here we report such data, obtained by accurate variational calculations of the vibrational states, and determine the ratio of the corresponding vibrational partition functions for the relevant isotopomers of ozone. Our results indicate a non-negligible deviation from the factor of two and, thus, attest for an appreciable isotope effect. To our best knowledge this property of ozone molecule has never been noticed before.

5.2. Calculation of Bound Vibrational States in Ozone

Calculations reported here were carried out in the entire range of the hyper-angle φ that covers all three wells of Figure 28. This means that the vibrational states of both symmetric and asymmetric ozone isotopomers are computed at once and must be assigned and split into groups afterwards. In order to do these assignments, we computed for each vibrational wave function, four probabilities associated with colored regions of the coordinate space in Figure 28. Two of these probabilities correspond to the regions of deep covalent wells ($\rho < 5$ Bohr), and the other two correspond to the regions of shallow

Van der Waals wells ($5 < \rho < 11$ Bohr). For example, in the case of single isotopic substitution the four probabilities correspond to symmetric ozone $^{16}O^{18}O^{16}O$, asymmetric ozone $^{18}O^{16}O^{16}O$ and $^{16}O^{16}O^{18}O$ (the two wells combined), Van der Waals complex $^{16}O^{16}O\cdots^{18}O$, and Van der Waals complex $^{18}O^{16}O\cdots^{16}O$ (in the two channels combined). These four probabilities are listed for each vibrational state of ozone included in the Tables 17-24. Tables 17-20 report the data for ozone with single ^{18}O, while Tables 21-24 report the data for double substitutions with ^{18}O.

Each table contains 6 columns: state number (counted in each well separately), energy and the four probabilities in each considered region of the PES (see Figure 28). The order of the states is flipped to focus on the upper part of the spectrum (top 20 states in each group). The value of 0 cm^{-1} corresponds to the energy of the lower dissociation channel. The energies are given up to the energy of the upper dissociation channel ($\Delta ZPE \approx 25.14$ cm^{-1} for $^{16}O^{18}O^{16}O$ and 20.38 cm^{-1} for $^{18}O^{16}O^{18}O$). The complete spectrum that includes all bound vibrational states is summarized in Figures 29-32. The full version of Tables 17-24 is available in the Supplemental Information of Ref. 118. All calculations were carried out with SpectrumSDT program.[119]

Our calculations revealed 498 symmetric and 462 antisymmetric vibrational states below the upper dissociation threshold in the singly-substituted case, as well as 509 symmetric and 469 antisymmetric states in case of the doubly-substituted ozone molecule. Note that the vibrational wave functions of singly- and doubly-substituted ozone are either symmetric (symmetry A_1) or antisymmetric (symmetry B_1) with respect to reflection through the dashed line in Figure 28. This assignment is exact, and, in fact, the states of different symmetries are computed in two independent runs with symmetry-

adapted basis sets specified for the hyper-angle φ. The highest-energy bound states from each symmetry are reported separately: A_1 states in the Tables 17, 19, 21 and 23, and B_1 states in the Tables 18, 20, 22 and 24.

In addition, we tried our best to split the vibrational states onto the nearly degenerate pairs (that correspond to the double-well states of asymmetric ozone and the double-channel Van der Waals states) and the remaining non-degenerate states (that correspond to the single-well symmetric ozone and the single-channel Van der Waals states). The non-degenerate states are reported in the Tables 17-18 and 21-22, the nearly degenerate states are reported in the Tables 19-20 and 23-24.

This degeneracy assignment is approximate but is quite certain for the majority of ozone states. A couple of states was considered degenerate if:

- They belong to different vibrational symmetries
- They have similar energies (less than 4 cm^{-1} apart)
- Their wave functions are localized in the same regions of the PES (maximum probability difference per region is less than 0.2)
- They do not belong to the symmetric molecule (symmetric molecule probability is less than 0.2)

Table 17. Top 20 bound non-degenerate states of symmetry A_1 of the singly-substituted symmetric ozone molecule ($^{16}O^{18}O^{16}O$).

#	Energy, cm^{-1}	p_i			
		cov. 686	vdW 6·86	cov. 668	vdW 66·8
315	23.6893763651	0.01	0.77	0.01	0.01
314	23.4766960120	0.00	0.20	0.18	0.11
311	22.8511562110	0.00	0.02	0.75	0.18
309	20.8678885548	0.01	0.12	0.05	0.14
306	14.3202822547	0.00	0.00	0.00	0.98
305	10.2525868971	0.04	0.31	0.01	0.00
303	-2.9729153429	0.33	0.53	0.06	0.01
301	-4.5047713654	0.28	0.39	0.07	0.10
300	-5.1069236816	0.02	0.08	0.02	0.85
298	-9.5383258922	0.23	0.71	0.02	0.02
295	-20.1058808250	0.00	0.01	0.00	0.98
293	-23.4812943829	0.08	0.89	0.02	0.00
292	-28.3331707248	0.00	0.02	0.07	0.90
291	-36.7950620624	0.96	0.03	0.01	0.00
287	-45.4493037559	0.13	0.69	0.13	0.04
286	-48.9005862386	0.02	0.35	0.28	0.35
283	-53.7426924301	0.00	0.18	0.09	0.72
282	-54.7323966658	0.82	0.18	0.00	0.00
280	-60.1136860833	0.40	0.58	0.01	0.01
277	-74.3981136466	0.39	0.57	0.03	0.01

Table 18. Top 20 bound non-degenerate states of symmetry B1 of the singly-substituted symmetric ozone molecule ($^{16}O^{18}O^{16}O$).

#	Energy, cm^{-1}	p_i			
		cov. 686	vdW 6·86	cov. 668	vdW 66·8
316	24.1162464123	0.04	0.55	0.00	0.00
313	23.2583154543	0.04	0.55	0.00	0.00
312	22.9306479449	0.00	0.00	0.98	0.01
310	21.3447095227	0.00	0.01	0.00	0.98
308	20.5965729351	0.73	0.11	0.00	0.00
307	16.6395365468	0.02	0.30	0.00	0.00
304	7.5801311048	0.00	0.00	0.08	0.91
302	-3.2731346615	0.02	0.79	0.07	0.02
299	-5.6652306576	0.06	0.75	0.04	0.01
297	-9.5389686786	0.93	0.06	0.01	0.00
296	-19.2121723993	0.08	0.71	0.07	0.14
294	-20.4161861314	0.02	0.27	0.07	0.65
290	-41.4559043166	0.95	0.04	0.01	0.00
289	-42.0286134158	0.00	0.00	0.18	0.82
288	-43.3204944229	0.04	0.95	0.01	0.00
285	-49.1977625604	0.53	0.23	0.13	0.12
284	-49.3990597687	0.48	0.23	0.14	0.15
281	-55.7157305500	0.21	0.76	0.01	0.02
279	-71.2203480539	0.80	0.19	0.00	0.00
278	-74.2060224992	0.32	0.64	0.03	0.01

Table 19. Top 20 bound nearly-degenerate states of symmetry A_1 of the singly-substituted asymmetric ozone molecule ($^{16}O^{16}O^{18}O$).

#	Energy, cm^{-1}	p_i			
		cov. 686	vdW 6·86	cov. 668	vdW 66·8
322	24.1907605106	0.00	0.20	0.07	0.10
321	23.0040525521	0.00	0.00	0.18	0.73
320	22.4463128046	0.02	0.64	0.00	0.00
319	21.8778962690	0.02	0.38	0.03	0.02
318	20.9747830225	0.03	0.33	0.01	0.04
317	19.6980194234	0.00	0.48	0.02	0.00
316	18.9026783906	0.00	0.71	0.01	0.00
315	18.3871567785	0.02	0.31	0.06	0.01
314	16.9015060508	0.00	0.25	0.03	0.02
313	16.3431688074	0.01	0.34	0.07	0.00
312	16.1325567930	0.00	0.05	0.88	0.00
311	15.7571040215	0.01	0.07	0.09	0.55
310	15.2182593368	0.03	0.30	0.06	0.11
309	13.1760129736	0.06	0.46	0.01	0.00
308	12.0635393430	0.00	0.26	0.01	0.00
307	11.4630593880	0.00	0.56	0.05	0.00
306	8.9697708272	0.00	0.21	0.01	0.00
305	7.8274872728	0.07	0.40	0.05	0.00
304	6.1340194017	0.02	0.42	0.00	0.00
303	5.2911041596	0.00	0.38	0.03	0.04

Table 20. Top 20 bound nearly-degenerate states of symmetry B_1 of the singly-substituted asymmetric ozone molecule ($^{16}O^{16}O^{18}O$).

#	Energy, cm^{-1}	p_i			
		cov. 686	vdW 6·86	cov. 668	vdW 66·8
322	24.4964675184	0.00	0.01	0.01	0.27
321	21.1011477081	0.00	0.03	0.08	0.64
320	22.2043504806	0.02	0.63	0.01	0.02
319	21.5660379021	0.11	0.33	0.01	0.02
318	23.7648627285	0.01	0.43	0.08	0.05
317	19.7732872430	0.02	0.59	0.01	0.01
316	18.8698783968	0.00	0.72	0.01	0.02
315	19.0387022961	0.07	0.24	0.04	0.06
314	16.9550655222	0.03	0.26	0.10	0.13
313	16.1419933317	0.02	0.33	0.15	0.01
312	16.1057595673	0.00	0.07	0.83	0.00
311	17.7895343608	0.02	0.10	0.12	0.49
310	14.2297254128	0.03	0.37	0.03	0.00
309	11.0902028546	0.03	0.57	0.00	0.00
308	12.0761254701	0.00	0.24	0.01	0.00
307	11.4886191115	0.01	0.42	0.05	0.00
306	8.9625884030	0.00	0.21	0.01	0.00
305	8.9313243023	0.03	0.37	0.04	0.01
304	6.3877294142	0.01	0.33	0.02	0.00
303	5.3093598165	0.00	0.30	0.03	0.00

Table 21. Top 20 bound non-degenerate states of symmetry A_1 of the doubly-substituted symmetric ozone molecule ($^{18}O^{16}O^{18}O$).

#	Energy, cm^{-1}	p_i			
		cov. 868	vdW 8·68	cov. 886	vdW 88·6
316	15.7091158552	0.01	0.67	0.07	0.08
314	13.7913145398	0.00	0.07	0.39	0.18
313	9.5340988894	0.91	0.09	0.00	0.00
312	7.9063426862	0.00	0.19	0.22	0.19
311	7.5775495047	0.77	0.22	0.00	0.00
309	1.0985607486	0.00	0.06	0.01	0.70
307	-1.9881012021	0.00	0.13	0.10	0.57
306	-3.3210394465	0.05	0.95	0.00	0.00
305	-3.7732856890	0.00	0.04	0.11	0.23
302	-20.2393314097	0.04	0.83	0.08	0.05
300	-23.7946893281	0.04	0.32	0.14	0.50
299	-24.1766493714	0.70	0.29	0.00	0.01
297	-43.4506875502	0.14	0.82	0.02	0.02
294	-48.0246994592	0.04	0.58	0.02	0.35
293	-52.9770668657	0.00	0.12	0.29	0.59
290	-55.5730392579	0.00	0.26	0.16	0.58
289	-62.3064222046	0.19	0.81	0.00	0.00
286	-67.8430707536	0.00	0.03	0.71	0.26
284	-79.7019302308	0.00	0.00	0.05	0.94
282	-82.4068124950	0.43	0.55	0.01	0.01

Table 22. Top 20 bound non-degenerate states of symmetry B_1 of the doubly-substituted symmetric ozone molecule ($^{18}O^{16}O^{18}O$).

#	Energy, cm^{-1}	p_i			
		cov. 868	vdW 8·68	cov. 886	vdW 88·6
318	17.3092760961	0.00	0.06	0.01	0.32
317	16.1701874115	0.02	0.32	0.05	0.33
315	15.0802428547	0.01	0.24	0.13	0.16
310	7.2861250591	0.00	0.12	0.06	0.66
308	-0.5430607183	0.09	0.73	0.03	0.03
304	-14.2493446449	0.45	0.55	0.00	0.00
303	-19.4785846953	0.06	0.23	0.08	0.64
301	-20.2642971158	0.30	0.43	0.08	0.20
298	-36.5654385547	0.18	0.82	0.00	0.00
296	-46.1993979590	0.31	0.61	0.04	0.05
295	-47.0775801702	0.63	0.22	0.04	0.10
292	-54.3520047142	0.09	0.53	0.18	0.20
291	-55.1144419973	0.13	0.48	0.17	0.21
288	-62.3844735744	0.70	0.30	0.00	0.00
287	-66.7091942498	0.00	0.03	0.38	0.59
285	-73.1052026047	0.00	0.00	0.27	0.73
283	-80.4515967581	0.21	0.79	0.00	0.00
280	-89.7929155192	0.82	0.18	0.00	0.00
279	-102.3537525696	0.65	0.35	0.00	0.00
275	-116.7238105262	0.05	0.95	0.00	0.00

Table 23. Top 20 bound nearly-degenerate states of symmetry A_1 of the doubly-substituted asymmetric ozone molecule ($^{16}O^{18}O^{18}O$).

#	Energy, cm^{-1}	p_i			
		cov. 868	vdW 8·68	cov. 886	vdW 88·6
330	19.4286022286	0.00	0.20	0.03	0.26
329	18.8301101318	0.01	0.59	0.03	0.14
328	18.4260052029	0.01	0.44	0.04	0.10
327	17.6490092060	0.00	0.03	0.02	0.61
326	17.4366493037	0.02	0.78	0.00	0.00
325	15.5242092764	0.03	0.81	0.03	0.04
324	14.6305351162	0.00	0.05	0.04	0.55
323	12.4361381094	0.16	0.70	0.04	0.01
322	12.1614272074	0.01	0.04	0.20	0.33
321	11.4134052468	0.00	0.06	0.34	0.28
320	10.4601473398	0.06	0.94	0.00	0.00
319	8.3481392224	0.00	0.03	0.04	0.23
318	7.9833384500	0.00	0.02	0.70	0.09
317	5.6353311379	0.00	0.13	0.06	0.17
316	5.0382523414	0.00	0.34	0.16	0.15
315	2.7833361700	0.00	0.15	0.03	0.28
314	1.6602756026	0.02	0.71	0.06	0.13
313	-0.7148160202	0.00	0.00	0.00	0.38
312	-2.8138383509	0.00	0.91	0.02	0.03
311	-4.9074134837	0.00	0.05	0.71	0.23

Table 24. Top 20 bound nearly-degenerate states of symmetry B_1 of the doubly-substituted asymmetric ozone molecule ($^{16}O^{18}O^{18}O$).

#	Energy, cm^{-1}	p_i			
		cov. 868	vdW 8·68	cov. 886	vdW 88·6
330	19.8587230969	0.00	0.10	0.03	0.25
329	18.5302046571	0.00	0.69	0.01	0.01
328	19.1313012803	0.02	0.43	0.04	0.05
327	16.7386432580	0.01	0.11	0.03	0.67
326	17.6590148782	0.04	0.78	0.01	0.02
325	15.5765207942	0.01	0.95	0.00	0.01
324	13.9777936356	0.01	0.05	0.13	0.52
323	13.5000523941	0.06	0.69	0.07	0.02
322	12.7161290091	0.00	0.00	0.16	0.46
321	12.1785819135	0.00	0.02	0.45	0.19
320	10.4746994062	0.01	0.97	0.01	0.01
319	10.2259879823	0.00	0.08	0.14	0.32
318	7.9568415081	0.00	0.11	0.88	0.00
317	6.2449342269	0.00	0.23	0.11	0.20
316	4.1080022436	0.01	0.43	0.11	0.20
315	1.5976426166	0.01	0.11	0.06	0.25
314	2.8159763487	0.07	0.63	0.06	0.06
313	-0.9909871890	0.01	0.12	0.03	0.24
312	-2.8224728519	0.00	0.99	0.01	0.01
311	-4.7191900218	0.00	0.01	0.84	0.15

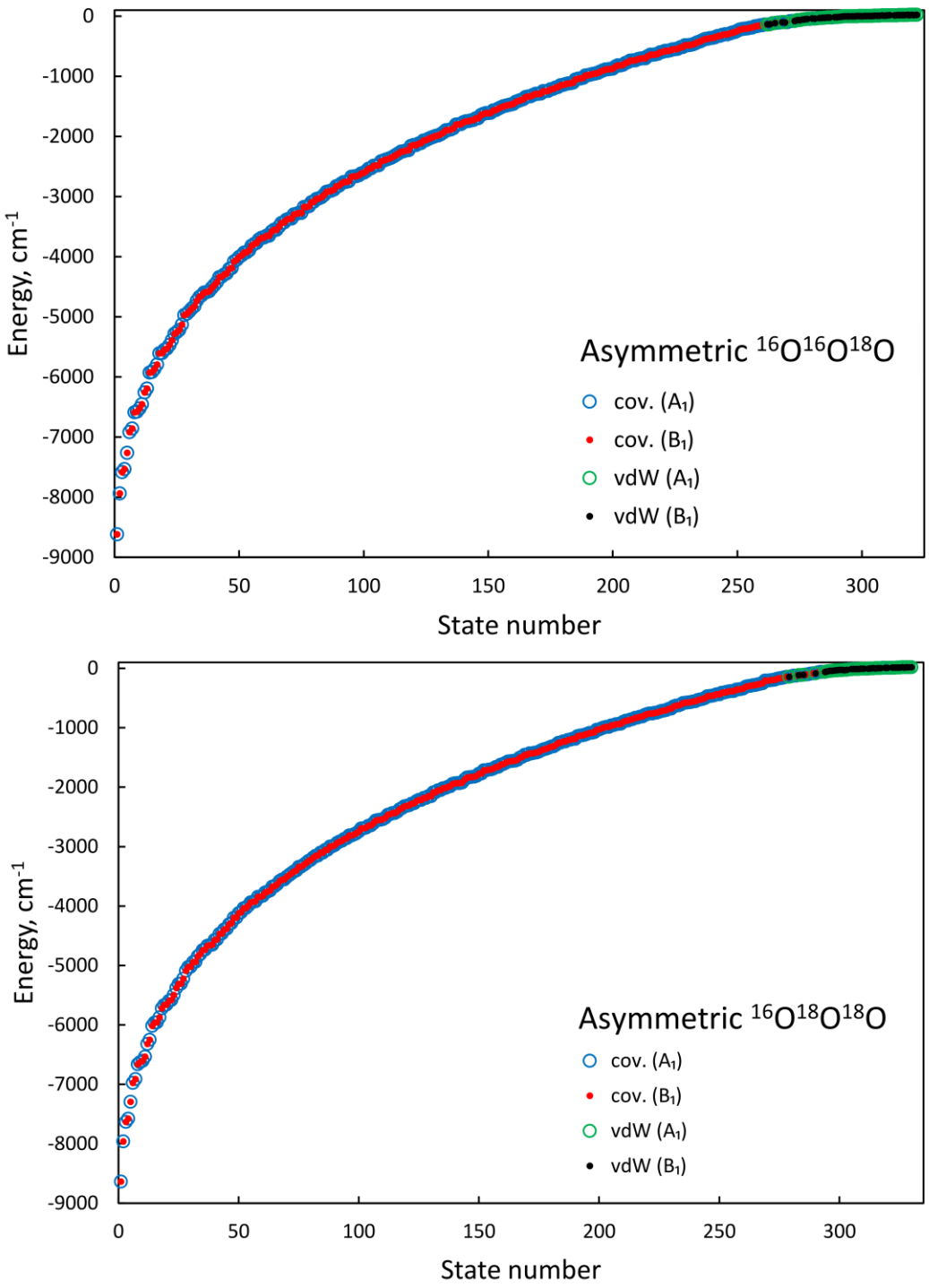

Figure 29. The spectrum of nearly degenerate states for singly- (upper frame) and doubly-substituted (lower frame) ozone molecules in the full energy range. Blue circles and red dots represent the covalently bound vibrational states of two symmetries, A_1 and B_1, respectively. Green circles and black dots mark the Van der Waals states of vibrational symmetries A_1 and B_1, respectively. State numbering is according to the Tables 19-20 and 23-24.

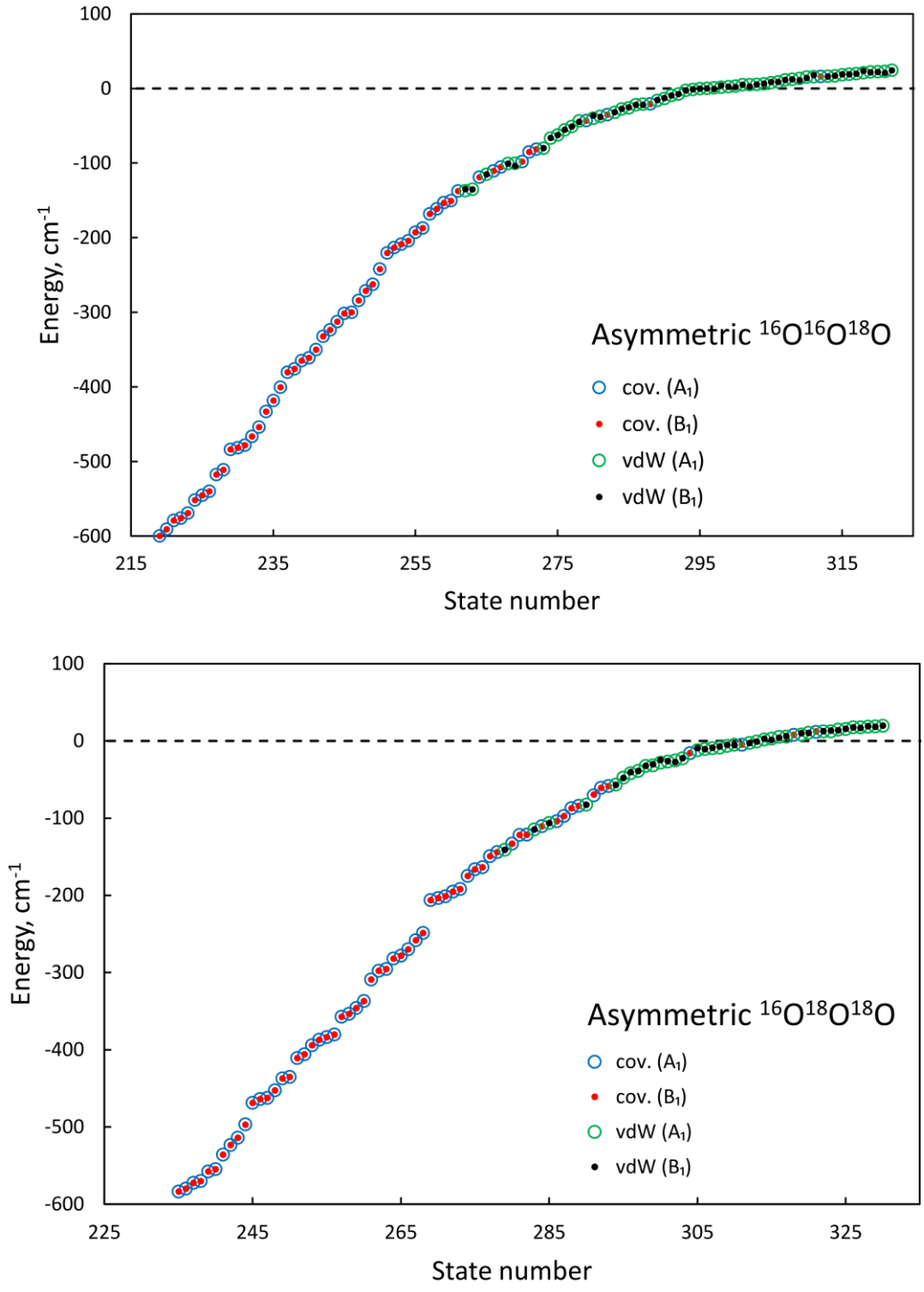

Figure 30. The spectrum of nearly degenerate states for singly- (upper frame) and doubly-substituted (lower frame) asymmetric ozone molecules near the dissociation threshold. Blue circles and red dots represent the covalently bound vibrational states of two symmetries, A_1 and B_1, respectively. Green circles and black dots mark the Van der Waals states of vibrational symmetries A_1 and B_1, respectively. State numbering is according to the Tables 19-20 and 23-24.

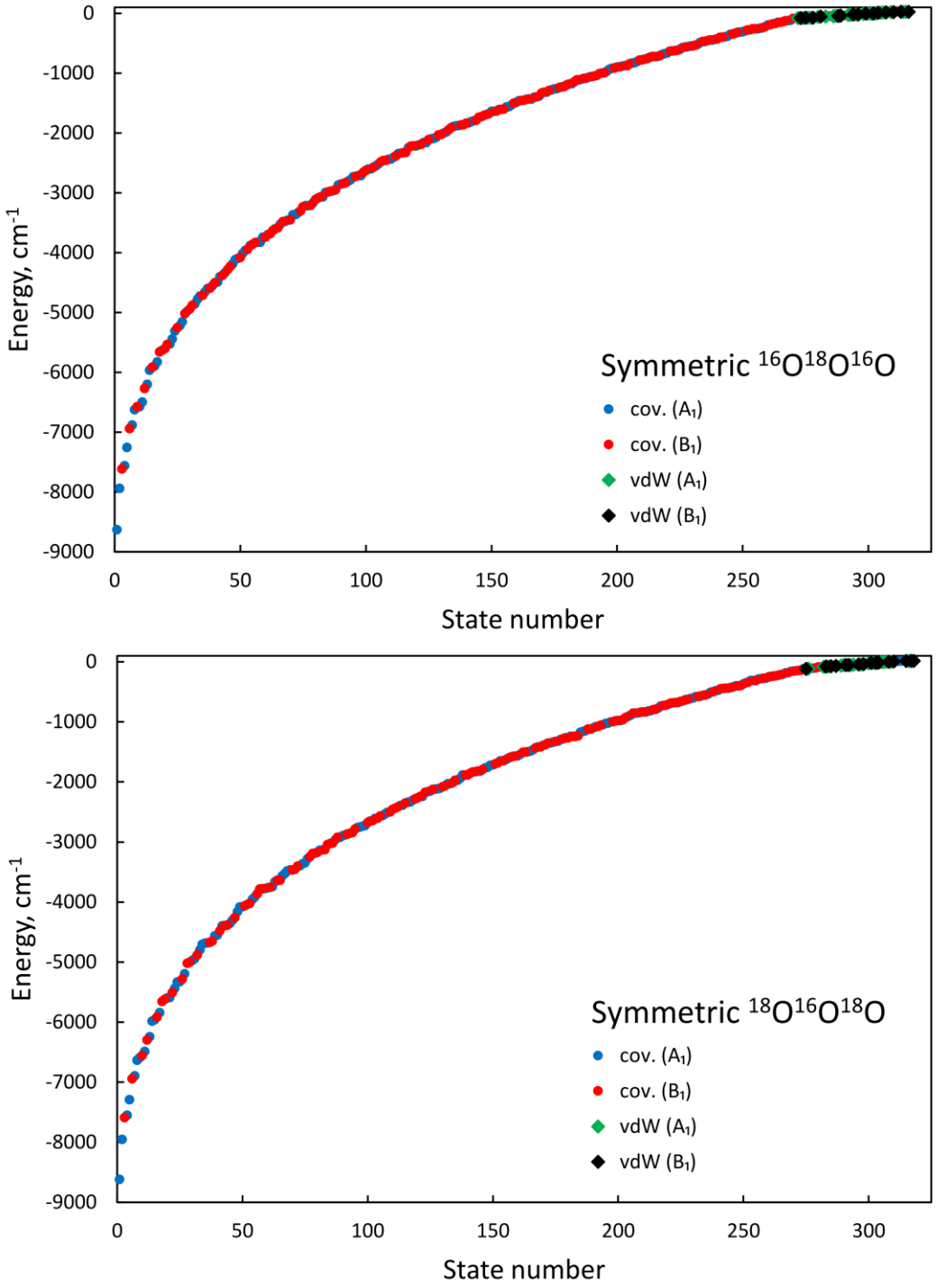

Figure 31. The spectrum of non-degenerate states for singly- (upper frame) and doubly-substituted (lower frame) symmetric ozone molecules in the full energy range. Blue and red dots represent the covalently bound vibrational states of two symmetries, A_1 and B_1, respectively. Green and black diamonds mark the Van der Waals states of vibrational symmetries A_1 and B_1, respectively. State numbering is according to the Tables 17-18 and 21-22.

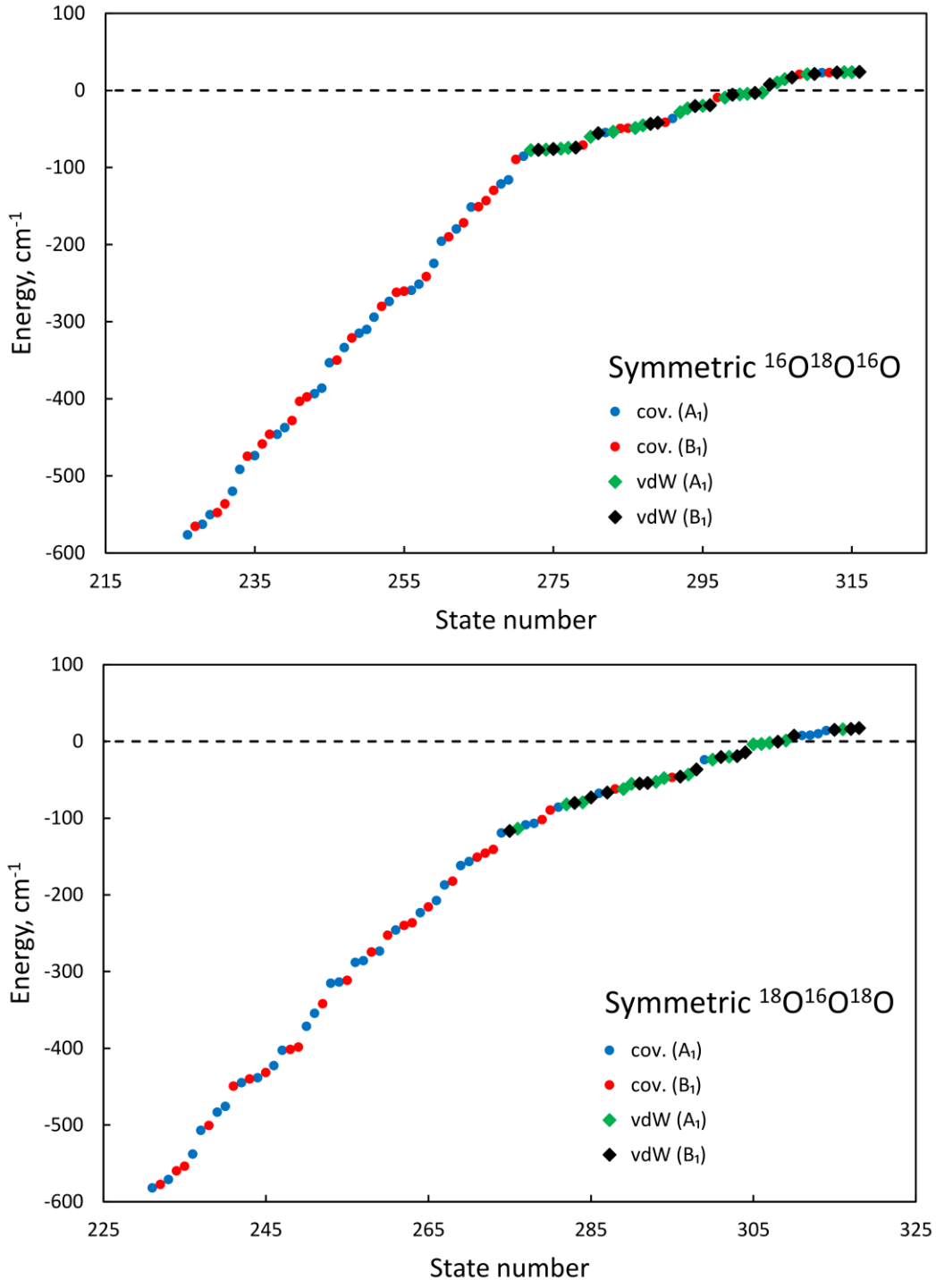

Figure 32. The spectrum of non-degenerate states for singly- (upper frame) and doubly-substituted (lower frame) symmetric ozone molecules near the dissociation threshold. Blue and red dots represent the covalently bound vibrational states of two symmetries, A_1 and B_1, respectively. Green and black diamonds mark the Van der Waals states of vibrational symmetries A_1 and B_1, respectively. State numbering is according to the Tables 17-18 and 21-22.

Figures 29 and 31 show the energies of all bound vibrational states, starting from the ground state. Figures 30 and 32 zoom in on energies of the vibrational states in the upper part of spectrum for the singly- and doubly-substituted ozone. At lower energies, in the asymmetric ozone molecule the states of symmetries A_1 and B_1 are nearly degenerate (see Figure 30), just like in a classic double-well problem, while in the spectrum of symmetric ozone the energies of the states of symmetries A_1 and B_1 alternate (see Figure 32). However, near dissociation threshold, at energies above –130 cm^{-1}, the PES opens up toward dissociation channels and the spectrum is significantly modified. The weakly-bound Van der Waals states dominate in this energy range, but several vibrational states localized in the covalent well are also present. For this reason, the densities of states in both symmetric and asymmetric ozone molecules increase near threshold, as one can see from Figures 30 and 32.

Careful analysis of the computed data reveals that the vibrational states of covalently bound symmetric and asymmetric ozone isotopomers (pink and orange in Figure 28) never mix. However, the weakly-bound states with dominantly Van der Waals character (green in Figure 28) sometimes mix with symmetric (pink) and asymmetric (orange) ozone molecules simultaneously. Such cases, however, are not numerous. They represent exceptions rather than a rule. Overall, one can say that the vibrational states of symmetric and asymmetric ozone molecules are rather independent.

In Figure 33 we present comparison of our computed state energies with those reported by Dawes and coworkers[115] and Poirier and coworkers[117] (available for the singly-substituted ozone only), using the same PES. In our calculations the values of energies converged to 10^{-3} cm^{-1} for the vibrational states with energies below –4800 cm^{-1} (about 50 lowest symmetric and 45 lowest antisymmetric states), to 10^{-2} cm^{-1} in the energy range below –2700 cm^{-1} (about 150 lowest symmetric and 135 lowest antisymmetric states) and to 10^{-1} cm^{-1} at higher energies. Overall, the agreement is better with Poirier,[117] who also reported convergence of his data as 10^{-3} cm^{-1} (for about 100 lower energy states, both symmetries combined). We found that for many states of

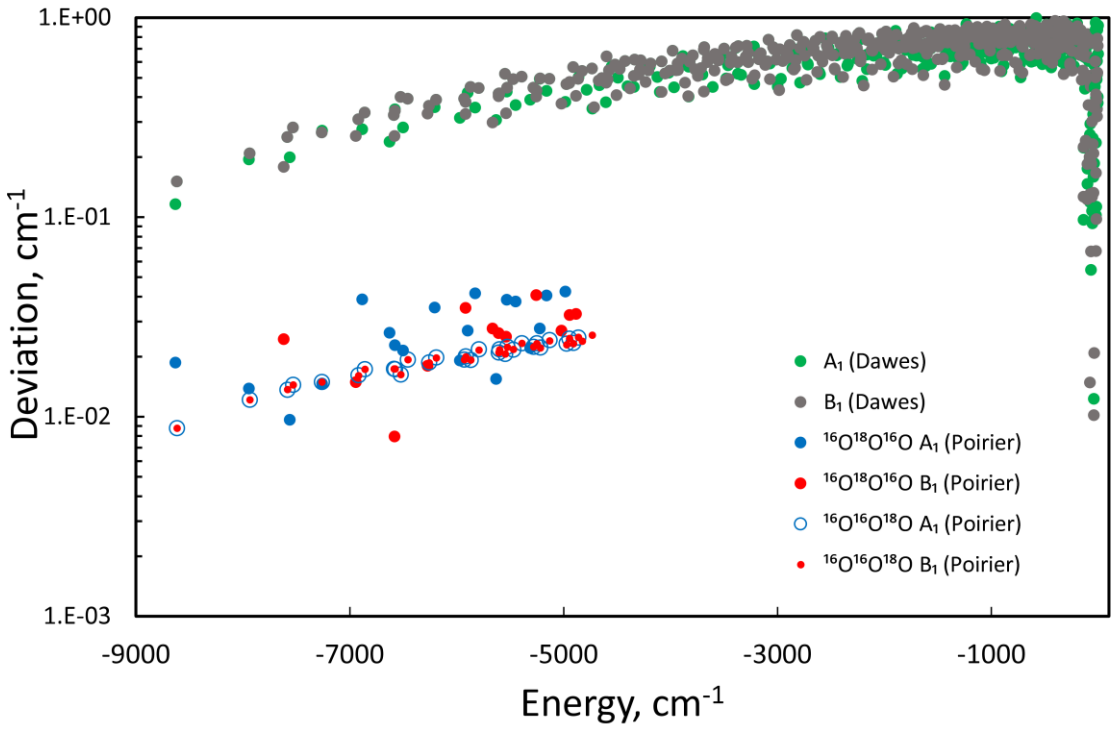

Figure 33. Comparison of the computed state energies (horizontal) with the results of Dawes[115] and Poirier[117]. Vertical axis shows the modulus of deviation. Green and gray circles correspond to vibrational states of symmetries A_1 and B_1 from Ref. 115. Blue and red symbols correspond to Ref. 117 as follows: filled blue and red circles correspond to the vibrational states of symmetries A_1 and B_1, respectively, in the symmetric ozone molecule; empty blue circles and small red dots correspond to symmetries A_1 and B_1 of the asymmetric ozone molecule.

asymmetric ozone $^{18}O^{16}O^{16}O$ our energies deviate from those of Poirier by ~ 10^{-2} cm^{-1}, although some energies deviate less and some deviate more. Interestingly, the differences are systematically larger for symmetric ozone $^{16}O^{18}O^{16}O$. The deviations of our predicted energies from those reported by Dawes[115] are somewhat larger. They form a trend that spans a broad energy range, and, on average, their absolute values are about ~ 0.7 cm^{-1} closer to the dissociation threshold (see Figure 33). Surprisingly, for many Van der Waals states near the threshold agreement is much better (with energy differences ~ 10^{-2} cm^{-1} for several states, see Figure 33). Also, we noticed that, when shifted to the same energy origin, all eigenvalues of Poirier are lower than those of Dawes, and ours are even lower than those of Poirier. Figure 33 gives the absolute values (moduli) of the deviations.

In Figure 34 we present splittings between the nearly degenerate states of symmetries A_1 and B_1 in the asymmetric ozone molecule $^{18}O^{16}O^{16}O$. Some relevant data available from literature are also presented, for comparison. The splittings we obtained for several lower vibrational states are on the order of 10^{-8} cm^{-1}, but they increase roughly exponentially with increasing vibrational excitation. One can wonder if these predictions are reliable at all, since the values of splitting are so small.

We carefully checked all convergence parameters and concluded that the values of those tiny splittings are converged, on average, within 20% of their values. Importantly, Dawes reported that the value of splitting in his calculations was on the order of 10^{-8} cm^{-1} for the ground state,[115] which is quite similar to our results. Moreover,

the values of splittings we found for the Van der Waals states in the upper part of spectrum are also in reasonable agreement with the data of Dawes[115] (see Figure 34).

5.3. Analysis of the Impact of the Bound Vibrational States of Ozone on the η-Effect

Energies of vibrational states of ozone E_i, can be used to compute the following averaged characteristics for the spectra of symmetric and asymmetric ozone molecules:

$$Q_{\text{up}}(\Delta E) = \sum_i p_i \exp\left\{-\frac{E_i - E_0}{\Delta E}\right\} \tag{127}$$

This moiety is very similar to the vibrational partition function where thermal energy is replaced by a continuous positive variable ΔE measured here in the units of

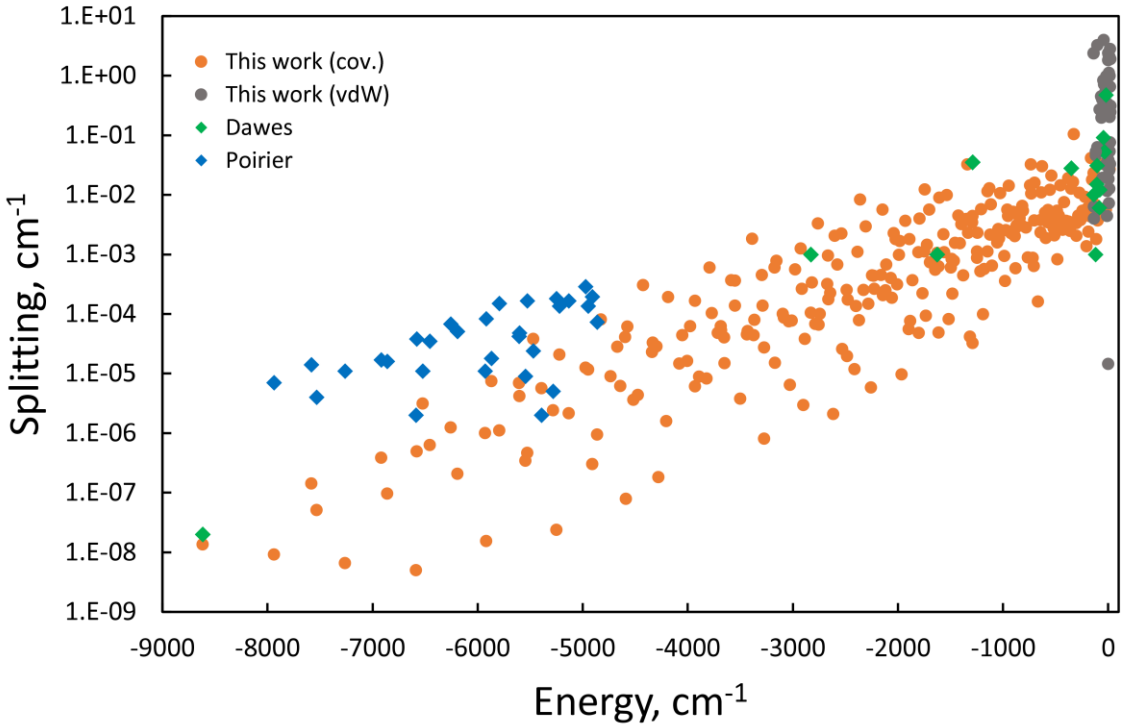

Figure 34. Splittings of the nearly degenerate vibrational states of asymmetric ozone molecule, as a function of state energy. Orange and grey circles correspond to the covalently bound vibrational states and the weekly bound Van der Waals states, respectively, computed in this work. Green and blue diamonds show results available from Refs. 115 and 117, respectively.

wavenumber. Summation is over all states including two vibrational symmetries (A_1 and B_1) but is done differently for symmetric and asymmetric ozone molecules. Namely, when Eq. (127) is used to compute Q_{up}^{sym} and Q_{up}^{asym} the corresponding probabilities are invoked, p_i^{sym} and p_i^{asym}, respectively. These are taken from Tables 17-24 and are introduced to handle those cases when the vibrational wave function is delocalized over both red and orange wells of the PES in Figure 28 (i.e. contributes to both symmetric and asymmetric ozone molecules). The second difference between Q_{up}^{sym} and Q_{up}^{asym} is the origin of their spectra – the ground state energy E_0. For the singly-substituted ozone the ground state of the asymmetric $^{18}O^{16}O^{16}O$ molecule is 14.25 cm^{-1} above the ground state of the symmetric $^{16}O^{18}O^{16}O$ molecule. In the doubly-substituted case the order is reversed: the ground state of the symmetric $^{18}O^{16}O^{18}O$ molecule is 14.49 cm^{-1} above the ground state of the asymmetric $^{16}O^{18}O^{18}O$ molecule.

In Figure 35 we report the ratio of the average number of states in asymmetric and symmetric ozone molecules, computed as $R_{up} = Q_{up}^{asym}/Q_{up}^{sym}$ for both singly- and doubly-substituted ozone, plotted as a function of ΔE in a broad energy range. The expected statistical value of this ratio is 2, but our data agree with this number only if the value of ΔE is small, below 70 cm^{-1}. Note that the vibrational quanta of ozone near the bottom of the well are on the order of 700 cm^{-1}. We see that for ΔE ~ 700 cm^{-1} the value of R_{up} for the singly-substituted ozone is clearly below 2, while for the doubly-substituted ozone it is clearly above 2. For ΔE ~ 7000 cm^{-1}, when the upper vibrational

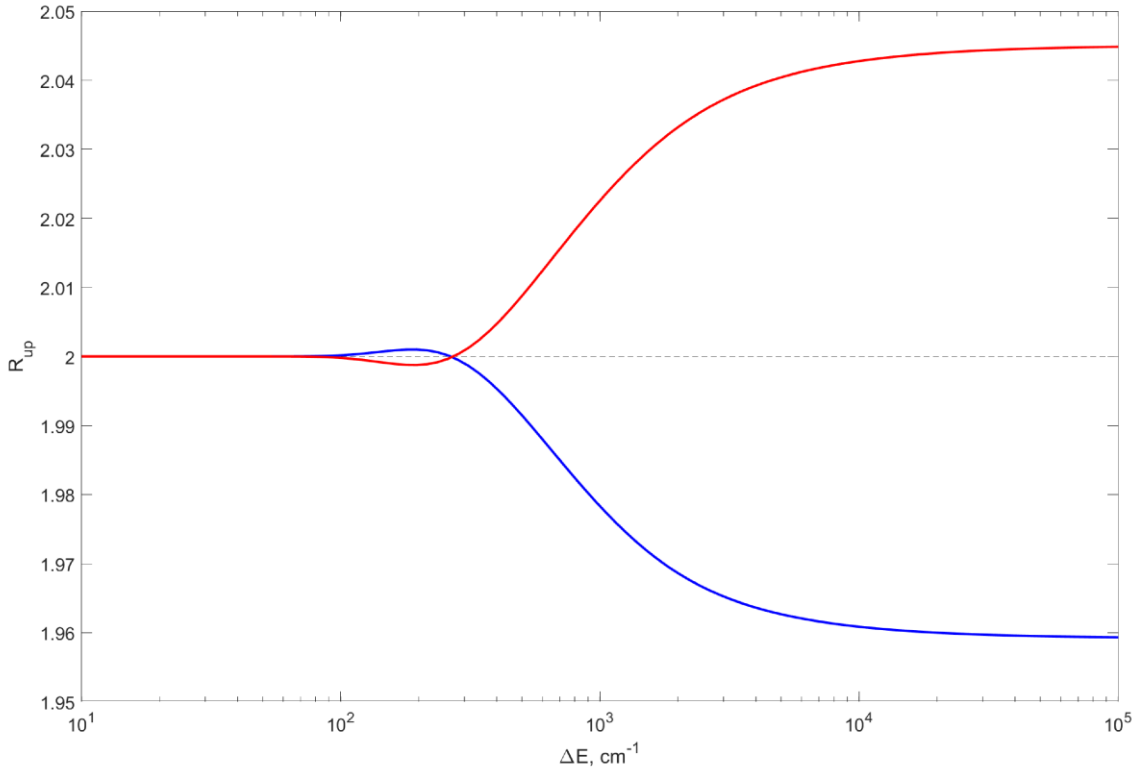

Figure 35. Ratio of the average number of states in asymmetric and symmetric ozone molecules, as defined by Eq. (127). Blue and red curves correspond to singly- and doubly-substituted ozone. Horizontal axis gives the averaging energy window size, ΔE, which in this case is analogous to the thermal energy in the vibrational partition function. The statistical value of two is indicated by dashed line. The deviations of computed data from this reference are obvious in a broad range of energies. Asymptotically they reach ± 0.05.

states near the dissociation threshold start contributing into Q_{up}, the deviations from 2.00 approach ±0.05. Therefore both singly- and doubly-substituted ozone deviate significantly from the expected factor of 2, but these deviations occur in the opposite directions. It is important to emphasize that these effects occur due to the vibrational states of ozone bound in the covalent wells, and thus are robust. Any reasonable calculations of the vibrational states of ozone should be able to reproduce this property.

It is rather clear that Q_{up} of Eq. (127) gives preference to the low-energy states, near the bottom of the covalent well on the PES, just as the usual vibrational partition function. In order to characterize properties of the upper parts of the spectra we tried to compute:

$$Q_{\mathrm{dwn}}(\Delta E) = \sum_i p_i \exp\left\{-\frac{E_i - E^*}{\Delta E}\right\} \qquad (128)$$

where E^* is dissociation threshold and the ΔE is negative. Upper vibrational states, just below the dissociation threshold, are more important for the process of ozone formation, since the scattering resonances above the threshold (the metastable ozone states) are stabilized into the upper bound states by bath gas collisions. The energy transfer process is typically exponential, therefore the sum of Eq. (128) is expected to reflect the total stabilization probability (besides giving the average number of states near the threshold). Thus, ΔE can be thought of as the average amount of transferred energy. The values of threshold energies E^* are defined based on zero-point energies of $^{16}O^{16}O$, $^{16}O^{18}O$ and $^{18}O^{18}O$ in the corresponding dissociation/reaction channels.[47,49] Zero energy always corresponds to the lowest dissociation threshold. Thus, in the case of single substitution, the threshold for asymmetric $^{18}O^{16}O^{16}O$ is 25.14 cm^{-1} above the threshold for the

symmetric $^{16}O^{18}O^{16}O$, which represents zero-point energy change between $^{16}O^{16}O$ and $^{16}O^{18}O$. In the case of double substitution, the order is opposite: the threshold for symmetric $^{18}O^{16}O^{18}O$ is 20.38 cm^{-1} above the threshold for asymmetric $^{16}O^{18}O^{18}O$, which represents zero-point energy change between $^{16}O^{18}O$ and $^{18}O^{18}O$.

In Figure 36 we report the ratio of the average number of states in asymmetric and symmetric ozone molecules, computed as $R_{dnw} = Q_{dwn}^{asym}/Q_{dwn}^{sym}$ using Eq. (128), for both singly- and doubly-substituted ozone and plotted versus $-\Delta E$ in a broad range. The limiting values of R_{dwn} for large ΔE match those of R_{up} in Figure 35, namely 2.00 ±

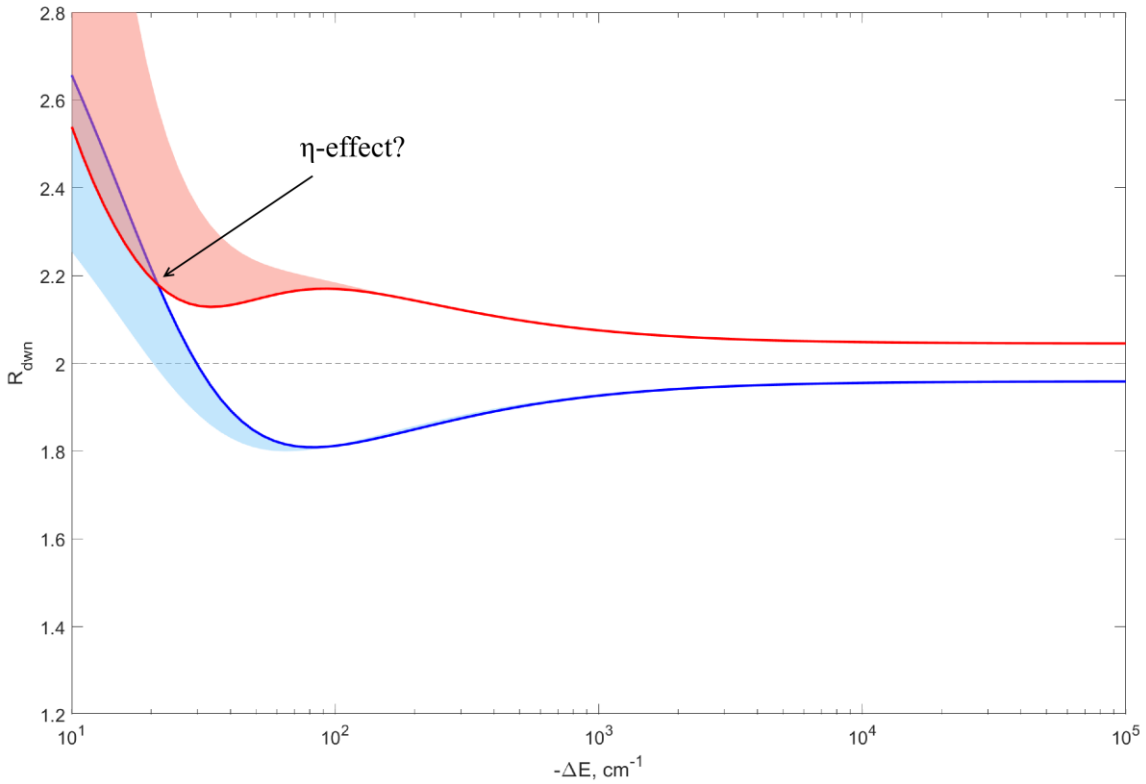

Figure 36. Ratio of the average number of states in asymmetric and symmetric ozone molecules, as defined by Eq. (128). Blue and red curves correspond to singly- and doubly-substituted ozone. Horizontal axis gives the averaging energy window size, $-\Delta E$, which in this case is analogous to the vibrational energy transfer due to bath gas collisions. The statistical value of two is indicated by dashed line. The deviations of computed data from this reference increase at low energies, reaching ±0.20, and then merge near $-\Delta E$~ 20 cm^{-1}, indicating a possible source of η-effect.

0.05, as one might expect, since in the limit of large ΔE they both reflect just the total number of states. What is more interesting is that when the value of ΔE is reduced to about $-\Delta E \sim 100$ cm^{-1}, the values of R_{dwn} for singly- and doubly-substituted molecules split even further apart, reaching 2.00 ± 0.20 (i.e. 20% difference). These numbers indicate a very significant difference between symmetric and asymmetric ozone molecules that has never been noticed before. Unfortunately, this property does not help to explain the η-effect, because our data also indicate that singly- and doubly-substituted molecules behave in the opposite ways, namely, in the singly-substituted case the *symmetric* ozone molecule exhibits more states than expected, whereas in the doubly-substituted case the *asymmetric* ozone molecule exhibits more states than expected.

However, at small values of ΔE the behaviors of two $R_{dwn}(\Delta E)$ dependencies drastically change. We see from Figure 36 that in the energy range $-\Delta E < 20$ cm^{-1} the values of R_{dwn} for singly- and doubly-substituted ozone molecules approach each other, while both exceeding the value of 2.00, substantially. This happens because for small values of ΔE only the very top portion of the spectrum is available, where the ratio of the number of states between asymmetric and symmetric ozone molecules is similar in both singly- and doubly-substituted cases. This holds true only at the top of the spectrum, so, as ΔE increases and more states become available, the main trend, observed in Figure 35, starts to dominate again and the curves return to the same asymptotic values.

Although the behavior of R_{dwn} in the range of small $-\Delta E$ is potentially important for explanation of the η-effect, it should be stated that this phenomenon is not particularly robust with respect to the variations of theory. For example, we tried to alter (artificially) the values of dissociation thresholds, by few wavenumbers, and found that

such modifications may change the low-ΔE behavior of R_{dwn} seen in Figure 36**.** Indeed, the upper part of the spectra contains many delocalized van der Waals states but only a few vibrational states that are localized in the covalent wells of symmetric and asymmetric isotopomers. Thus, addition or removal of just one vibrational state in this energy range may have a significant effect. Such alternation can be caused by small changes of the potential energy surface, or by rotational excitation of the molecule, or by involvement of scattering resonances above the dissociation threshold (not considered here). All we can say is that for the PES at hands, and with the spectra we have accurately computed, the intriguing low-ΔE behavior of R_{dwn} seen in Figure 36 is obtained and is potentially important.

It is also debatable whether the Van der Waals states of ozone are important for the recombination process or not. Even if the Van der Waals complexes of ozone are formed, they are easily destroyed by collisions with bath gas and are hard to stabilize into the main (covalent) well,[120] where the stable ozone molecules are eventually formed. Therefore, it was argued in the past that these states could be neglected. Here, for the exploratory purpose, we tried to include the Van der Waals states into the overall state count, but with the reduced weights of only 10% (which, of course, is rather arbitrary) of their corresponding probabilities, in order to reflect their weak collisional coupling to the rest of the ozone states. With this scaling factor, we counted the Van der Waals states in the average Q_{dwn} by: *a*) Associating with asymmetric ozone molecule the probabilities from the "blue" Van der Waals part of the map in Figure 28; and by *b*) Splitting between symmetric and asymmetric ozone molecules the probabilities from the "green" Van der Waals part of the map. The corresponding results are indicated by shaded areas in Figure

36. We can see that in the range of small $-\Delta E$ < 20 cm^{-1} these areas overlap (pink and blue), again, indicating the same behavior of the singly- and doubly-substituted ozone molecules. Thus, inclusion of the Van der Waals states is unlikely to change conclusions of the previous paragraph.

The unexpected properties of the vibrational states spectra in ozone molecules may help to identify possible source of the mysterious η-effect. One very strange feature of the η-effect is that it has the same direction and magnitude in both singly- and doubly-substituted ozone. In both cases the asymmetric ozone molecules are formed faster. This is incomprehensible, because symmetric and asymmetric isotopomers of ozone behave differently in the singly- and doubly-substituted cases. For example, in the case of single substitution the spectrum of asymmetric ozone is shifted up relative to the spectrum of symmetric ozone by ΔZPE (roughly 10-20 cm^{-1}), while it is just opposite in the case of the double substitution. Moreover, the vibrational partition functions ratios, both R_{up} and R_{dwn}, deviate down from the statistical factor of 2 in the case of single substitution (up to 10%), while it is just opposite in the case of the double substitution (see Figure 35 and Figure 36). These are very robust indications of different behavior of symmetric and asymmetric ozone molecules in the cases of single and double substitutions, yet the experimental η-effect is the same.

One new property reported here, that may contribute to explanation of the η-effect, is behavior of the upper parts of the vibrational spectra, just below the dissociation threshold. It appears that in this energy range the asymmetric ozone molecules contain more than twice as many states than the symmetric ozone molecules, and this property seems to hold for both singly- and doubly-substituted cases. It should be taken into

consideration that the experimental value of energy transfer in ozone[121] is expected to be close to $-\Delta E \sim 20$ cm^{-1}. Thus, the process of ozone formation must be very sensitive to the properties of this narrow part of the vibrational spectrum. Accurate incorporation of this effect into the models of ozone forming recombination reaction requires calculations of the energy-transfer process, and those are numerically demanding, if at all affordable at present time. However, the findings of this work may help to develop a practical approximation for the energy-transfer process that still captures this effect.

5.4. Summary

Accurate calculations of vibrational states in singly- and doubly-substituted ozone molecules are carried out, up to the dissociation threshold. The computed spectrum of the singly-substituted ozone is in a good agreement with the results previously obtained by Dawes and coworkers,[115] and Poirier and coworkers.[117] The spectrum of the doubly-substituted molecule is reported for the first time. The complete dataset used in this chapter is available in the Supplemental Information in Ref. 118.

Analysis of these spectra reveals noticeable deviations from the statistical factor of 2 for the ratio between the number of states in asymmetric and symmetric ozone molecules. It is found that, for the lower energy parts of spectra, the ratio is below 2 in the singly-substituted ozone molecules, but it is above 2 in the doubly-substituted ozone molecules. However, the upper parts of spectra, just below dissociation thresholds, exhibit a different behavior. In this energy range the singly- and doubly-substituted ozone molecules behave similar, with the ratio of states in asymmetric and symmetric ozone molecules being above 2 in both cases. This property may contribute to explanation of the mysterious η-effect (Eq. (18) in Introduction) in the ozone forming reaction, that

favors formation of the asymmetric ozone molecules. Unfortunately, this effect is not particularly robust and may be coincidental.

The above calculations were done in the absence of rotational excitation ($J = 0$). At room temperature many rotational levels in ozone are excited, so it is important to understand the role of rotational excitations on the observed deviations of state ratios from the expected statistical factor of 2. For that, we need to recalculate the spectrum for several typical values of $J > 0$ and repeat the above analysis for the spectra of rotationally excited ozone.

CHAPTER 6. THE ROLE OF ROTATION-VIBRATION COUPLING FOR THE BOUND STATES IN OZONE

In this chapter we use the theory outlined in Chapter 4 to calculate coupled bound rovibrational states in ozone with the values of $J \leq 5$, compare the results with the uncoupled calculations and discuss possible implications of rotation-vibration coupling for the isotope effects in ozone.

In Chapter 5 we found an interesting feature of the near-dissociation bound vibrational spectrum of ozone that can potentially contribute to the η-effect. However, as it was outlined there, the discovered effect is not particularly robust and it does not take into account the resonance spectra above the dissociation threshold, which is expected to be important to the ozone recombination reaction. An extensive study of the properties of such spectra, especially in relation to the isotope effects, has been recently carried out by Teplukhin and Babikov.[39,51,94,122] In their work they were able to reproduce a large portion of ζ-effect, but the η-effect was not reproduced and remained unexplained. This implies that a crucial (for η-effect) feature has not been considered in their model.

It was recently proposed by the group of Rudolf Marcus in a series of recent papers,[41,123] that the Coriolis effect, responsible for the rotation-vibration interaction, occurs more efficiently in the isotopically substituted asymmetric ozone molecules (e.g. $^{16}O^{16}O^{18}O$), compared to the symmetric molecules (e.g. $^{16}O^{18}O^{16}O$). The group of Marcus carried out classical trajectory simulations to gain some insight into the mechanism of this phenomenon but did not find enough evidence for its justification.[123] Interestingly, they concluded with the following statement: "*We speculate that the symmetry effect of Coriolis coupling can appear in quantum mechanical analysis of the model.*"

The Coriolis effect (rotation-vibration coupling) was not taken into account in the work of Teplukhin and Babikov, therefore the goal of this chapter is to test the hypothesis of Marcus and determine if inclusion of rotation-vibration coupling introduces any effects that favor the asymmetric ozone isotopomers more than the symmetric ones consistently in different isotopologues.

Accurate quantum mechanical treatment of coupled rotational-vibrational motion can be a challenging task, even for the smallest molecules such as triatomic, if the range of rotational and vibrational excitations is significant (*e.g.*, up to the dissociation threshold), the atoms are heavy (non-hydrogen). With rotation-vibration interaction terms included, the size of the Hamiltonian matrix is proportional to J (total angular momentum quantum number), and the cost of diagonalization typically grows as J^3, therefore the numerical cost of finding the eigenstates of such Hamiltonian is very significant, often unpractical.

Because of the high computational cost, the symmetric-top rotor approximation remains a popular practical tool for the prediction of ro-vibrational state energies.[93,118,124,125] In this simplified method, the terms in the Hamiltonian operator, responsible for the coupling of rotational and vibrational degrees of freedom, are neglected (assumed to be small), which permits to split the overall Hamiltonian matrix into a number of independent smaller blocks that can be labeled by the value of quantum number Λ, corresponding to projection of the total angular momentum (*J*) onto *z*-axis. Within each block, accurate calculations of the vibrational states can be carried out, and then the overall spectrum of molecule is obtained by collating these individual pieces back together.

The major drawback of this simplified approach is that the resultant spectrum lacks the so-called Λ-doubling.[126,127] Namely, for all values of Λ in the range $1 \leq \Lambda \leq J$, the ro-vibrational states computed in this simplified way are doubly-degenerate, while in nature they are known to exhibit non-zero splittings, the Λ-doubling.[126–128] Importantly, such splittings represent a unique spectroscopic feature of the molecule,[129] and may also play a role in natural phenomena, such as absorption of solar light by atmospheric species.[15,88]

Despite the cost, one can find occasional examples of such nearly exact calculations of the rotational-vibrational spectra in the literature for many molecules, such as H_3^+,[130] HeHF,[131] LiNC,[132] HeN_2^+,[133] H_2O,[134] H_2S[135], SO_2,[126,127] HO_2,[136] and Ar_3,[137] but none of those papers consider calculation of scattering resonances.

For ozone, several accurate quantum calculations of the rovibrational states are available from literature,[47,93,114–116,118] but those are restricted to the ground rotational state ($J = 0$) and one simplest excited rotational state ($J = 1$ of negative parity), where there is only one rotational block in the Hamiltonian matrix and the Coriolis coupling does not occur.

Rotationally excited ozone states were computed in several papers focused on the recombination reaction that forms ozone,[50,51,122,124] for a very broad range of rotational excitations up to $J \sim 50$, but in all those cases the Coriolis coupling terms were neglected to ease calculations. Other systematic studies of the rotationally excited states of ozone were also conducted by Tyuterev and coworkers, using the method of effective Hamiltonian (see Ref. 138 and references therein). Their approach gives valuable interpretation of the experimental spectra, and also permits to validate or even adjust the

potential energy surface (PES) but, due to semi-empirical nature of their Hamiltonian, the method remains accurate only in a limited part of spectrum of given molecule, which restrains its predictive capability.

The first entirely general quantum calculation of the rotational-vibrational states in symmetric and asymmetric ozone molecules $^{16}O^{16}O^{18}O$ and $^{16}O^{18}O^{16}O$ with the Coriolis coupling terms included was published just recently.[117] Both the calculations themselves and the assignment of these states were challenging, so only the lowest 100 ro-vibrational states (for $^{16}O^{16}O^{18}O$ and $^{16}O^{18}O^{16}O$ isotopomers combined) were computed, assigned and reported, up to only $J = 5$. This first step is encouraging, but for the prediction of the formation rate coefficients, we need to push these calculations to much higher energy range and much larger rotational excitation range, for both singly and doubly substituted ozone isotopologues.

In this chapter we start with a relatively simple calculation of coupled rotation-vibration bound states in ozone isotopomers for $J \leq 5$ and analyze the effect of the Λ-coupling terms (asymmetric top rotor and Coriolis) on individual states and spectrum as a whole.

6.1. Overview of the Computed Spectrum

The calculations of coupled rotation-vibration bound states were carried out for four ozone isotopomers: $^{16}O^{18}O^{16}O$, $^{16}O^{16}O^{18}O$, $^{18}O^{16}O^{18}O$ and $^{16}O^{18}O^{18}O$, for $J = 0$ to 5 and both inversion parities (p), using an optimized grid along ρ with 90 DVR functions in the range of 3.4-6.1 Bohr, 130 DVR functions along θ in the range 0.43-1.56 rad and 100 VBR functions of each symmetry. The 3D problem was solved using sequential diagonalization truncation approach (SDT) with the truncation energy set to 6000 cm^{-1}.

Further 20%-perturbations on each of our convergence parameters did not lead to changes in energies greater than 10^{-3} cm^{-1}. All calculations were carried out with SpectrumSDT program.[119]

The masses of oxygen isotopes used in this work are 15.99491461956 u and 17.9991596129 u for ^{16}O and ^{18}O, respectively. The conversion factor from the unified atomic mass unit (u) to kilograms is $1.660538921\times10^{-27}$ kg/u, and from atomic unit of mass to kilograms is 9.10938291×10^{-31} kg/m_e. Thus, the conversion factor from unified atomic mass unit to atomic unit of mass was obtained as a ratio of the above numbers and is equal to 1822.88848477004 m_e/u. The conversion factor from the atomic unit of energy, Hartree (E_h), to wavenumbers used in this work is 219474.6313708 cm^{-1}/E_h. The above constants are taken from Ref. 139.

The potential energy surface of ozone used in this work was constructed by Dawes et al.[112] The computed rovibrational levels where shifted by the values of D_e = 9274.99560025014 cm^{-1} and ZPE of $^{16}O^{18}O$ = 769.370806301787 cm^{-1} to align 0 cm^{-1} with the lower dissociation threshold of $^{16}O^{16}O^{18}O$. The values of D_e and ZPE were computed numerically.

For all ro-vibrational states calculated in this work we computed the values of P_Λ of Eq. (121) and found that the majority of states are still localized in one dominant value of Λ, so this value can still be used to label the ro-vibrational states, just like in the case of the symmetric top rotor approximation. We also saw that when the energies of two states are close to each other, they may display a mixture of several values of Λ, but such cases are relatively rare. Namely, among all the states considered in this chapter (7200 states overall), we found only one pair of energetically close states where the weights of

two largest Λ-components were in the ratio close to 50/50. We also saw two examples when the two largest Λ-components gave the ratio of about 80/20. For all other states, the weight of the second largest value of Λ was below 5%.

The full dataset computed for analysis in this chapter can be found in Supplementary Information of Refs. 107 and 140.

When all terms of the Hamiltonian matrix are included, our results show an excellent agreement with the results of the recent work by Poirier and co-workers.[117] Figure 37 plots the absolute values of the deviations of the state energies computed here relative to those reported in Ref. 117. These data include both symmetric $^{16}O^{18}O^{16}O$ and

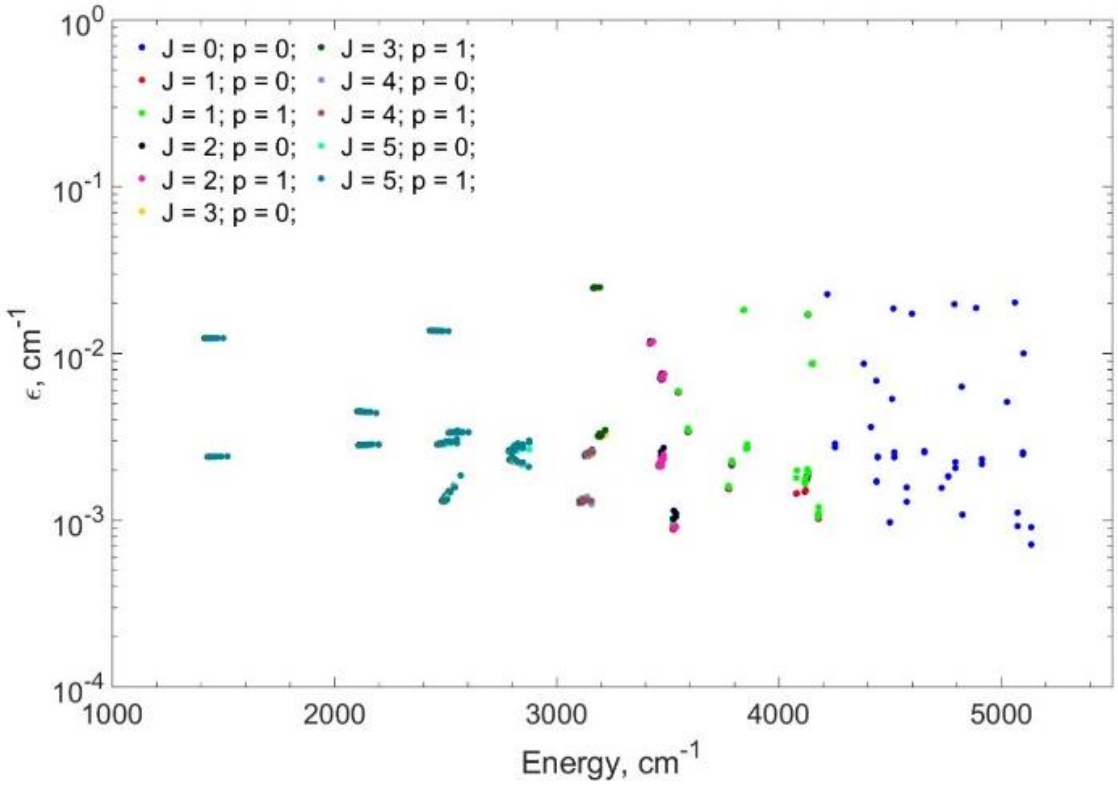

Figure 37. Absolute values of energy differences between the rotational-vibrational states computed here, and the corres`ponding states reported in Ref. 117 for $^{16}O^{18}O^{16}O$ and $^{16}O^{16}O^{18}O$. Individual colors are used for different parities p and different values of angular momentum up to $J = 5$.

asymmetric $^{16}O^{16}O^{18}O$ isotopomers of ozone, combine the results of calculations with $J = 0$ to 5 for about 80 rotational-vibrational states of each parity, per each value of J (about 850 states total). In Figure 37 each combination of (J, p) is shown by its own color. As one can see from the picture, the differences of computed energies are on the order of 10^{-3} cm^{-1} for the majority of states and on the order of 10^{-2} cm^{-1} in the worst case, which matches the target accuracy of Poirier and coworkers. We found that the values of these differences depend on the vibrational character of the states (v_1, v_2, v_3), but are relatively insensitive to the rotational quantum numbers (J, Λ, p).

It should be stressed that the two sets of very similar results presented in Figure 37 (this work *vs.* Poirier and coworkers) were obtained independently by two groups without any communication, using different coordinates (hyper-spherical *vs.* Jacobi), employing two different codes (SpectrumSDT *vs.* ScalIT) and using different computer systems. The excellent agreement at low vibrational energies gave us enough confidence in the theory and the new code we developed to tackle a much more demanding problem – a large range of vibrational excitations.

Namely, for each set of the rotational quantum numbers (J, Λ, p) considered here, we computed 600 vibrational states, 21600 coupled ro-vibrational states total. These new spectra cover roughly 90% of the covalent well of the ozone PES and stop just before the energy where the PES of ozone opens up toward a shallow plateau of the weak van der Waals interaction, followed by the bond breaking and dissociation onto $O + O_2$. Calculations of the vibrational states in the remaining 10% of the energy range are also possible, but this would require a significant expansion of the ρ-grid, which is beyond the scope of this chapter, focused mostly on the rotation-vibrational coupling. Large-

amplitude states near the threshold will be reported elsewhere, together with calculations of scattering resonances above the dissociation threshold.

Figure 41 summarizes the energy progression of these ro-vibrational states for both symmetric $^{16}O^{18}O^{16}O$ and asymmetric $^{16}O^{16}O^{18}O$ ozone up to $J = 5$. We see that these spectra extend up to about 1000 cm^{-1} below the dissociation threshold for all values of J. The states for each value of J are numbered separately. The spectrum of larger values of J is denser due to more values of Λ, available for those J.

For the doubly-substituted ozone isotopomers ($^{18}O^{16}O^{18}O$ and $^{16}O^{18}O^{18}O$) there are no results published in literature to compare with. Therefore, to validate this part of

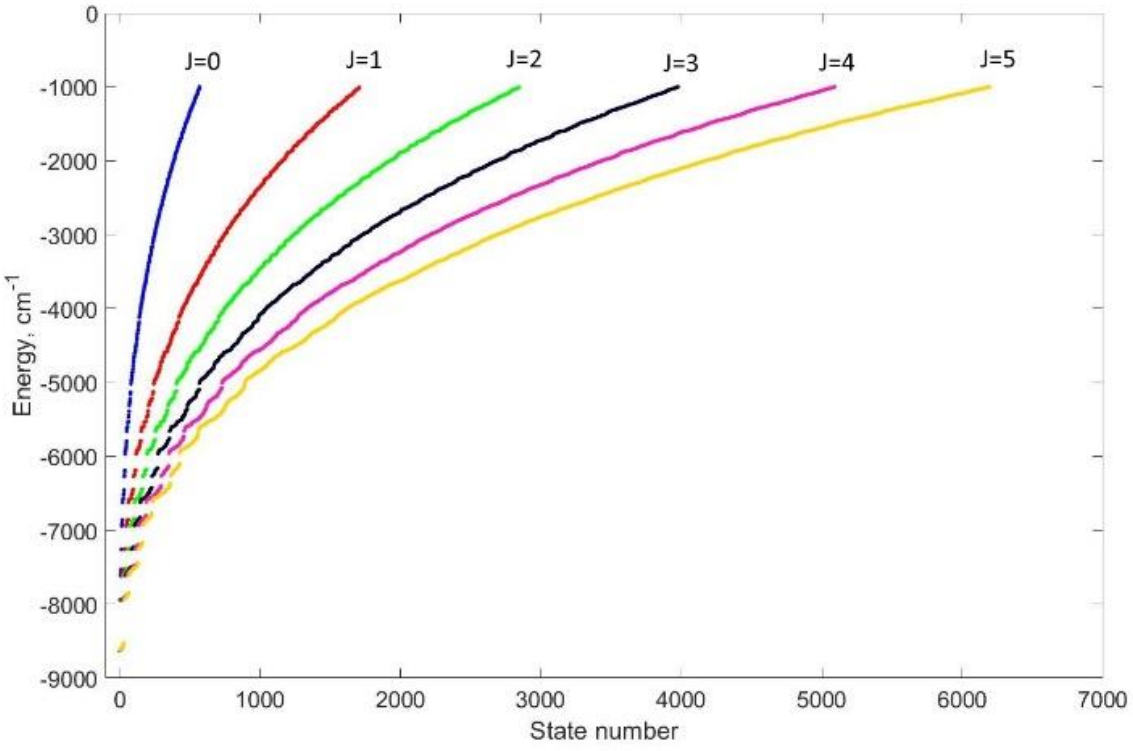

Figure 38. The progressions of energies of coupled ro-vibrational states up to $J = 5$ computed in this work for symmetric $^{16}O^{18}O^{16}O$ and asymmetric $^{16}O^{16}O^{18}O$ combined.

the calculations, we carried out calculations for $J = 3$ again, using a different well-tested code of Kendrick (APH3D).[104]

The code of Kendrick also uses APH coordinates, but it is different in many respects. First of all, it starts with a general Fourier basis $e^{\pm im\varphi}$ for the hyper-angle angle φ, and the vibrational states of two symmetries are projected out only at the 2D level. In contrast, in SpectrumSDT the two symmetries are treated separately from the very beginning, by employing the real-valued basis sets of either $\sin(m\varphi)$ or $\cos(m\varphi)$ functions (Eqs. (104) and (105)). Second, APH3D uses a basis of polynomials for the hyper-angle θ, while here a simple DVR grid is used. Third, APH3D solves the coupled-channel equations for hyper-radius ρ using the method of Numerov, while here we implement one more level of truncation and then build and diagonalize the Hamiltonian matrix for the vibrational 3D problem, using a DVR grid in ρ optimized to the shape of the PES.[93,96] Finally, for the description of rotation APH3D uses the *z*-axis perpendicular to the plane of the molecule and includes the Coriolis terms from the beginning, while in SpectrumSDT the *z*-axis is placed in the molecular plane and the Coriolis couplings are taken into account only at the last step of calculations.

Rotational-vibrational states of both parities ($p = 0$ and $p = 1$) were computed using these two codes for $J = 3$ of the doubly-substituted ozone, both symmetric $^{18}O^{16}O^{18}O$ and asymmetric $^{18}O^{18}O^{16}O$ isotopomers, up to the energy of about 5200 cm^{-1} above the bottom of the well, which is about 4800 cm^{-1} below the dissociation threshold (roughly, 100 vibrational states per each value of Λ). The absolute values of energy differences between the corresponding states computed with the two codes are presented

in Figure 39. As one can see, the majority of the states agree to within 10^{-3} cm^{-1} or better, reaching the difference of about 0.05 cm^{-1} in the worst case at the high energy part of the spectrum. The overall agreement between the results of the two codes allows us to conclude that the ro-vibrational wave functions and their energies, computed with our code are correct.

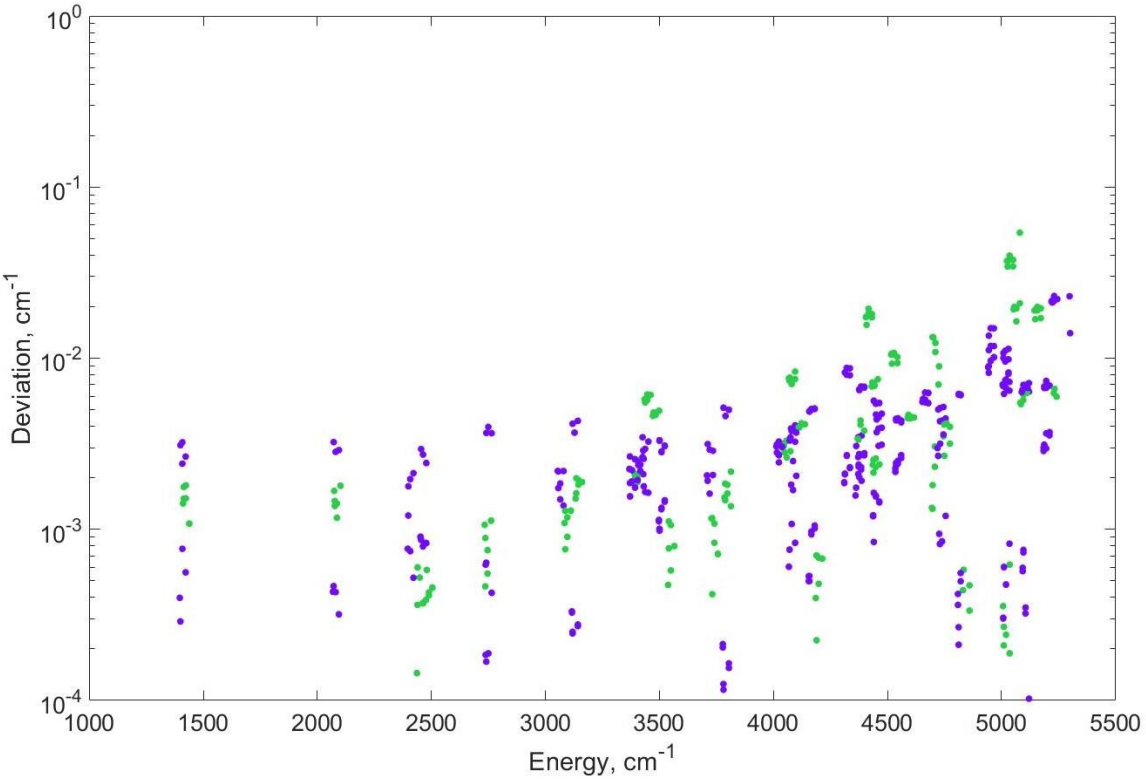

Figure 39. Absolute values of energy difference between the rovibrational states of ozone calculated using SpectrumSDT and the code of Kendrick (APH3D). The states of both values of inversion parity ($p = 0$ and $p = 1$) are shown for the total angular momentum $J = 3$ of doubly substituted ozone molecule. The states of both $^{18}O^{16}O^{18}O$ (green) and $^{18}O^{18}O^{16}O$ (violet) are included. Horizontal axis gives energy relative to the bottom of the well.

6.2. Shifts and Splittings Introduced by Asymmetric Top Rotor and Coriolis Terms

In this section we want to estimate individual and combined effects of both coupling terms (asymmetric top rotor and Coriolis) on uncoupled spectrum of bound states in ozone on example of singly-substituted ozone isotopologue.

To begin with, we carried out calculations of the vibrational-rotational states of ozone in the symmetric-top rotor approximation with only diagonal blocks included ("S" in Figure 23), where both the asymmetric-top rotor terms and the Coriolis couplings were neglected. Then, in one set of intermediate calculations, in order to determine the role of asymmetric top rotor term, we added just the asymmetric-top rotor blocks to the matrix (only the "A" and "S" terms in Figure 23 were included in the Hamiltonian matrix) and we recomputed the vibrational-rotational states. Next, in the second set of intermediate calculations, in order to determine the magnitude of the Coriolis effect alone, we added just the Coriolis coupling blocks to the matrix (only the "C" and "S" terms in Figure 23 were included in the Hamiltonian matrix) and recomputed the vibrational-rotational states again. In the final set of exact calculations, we included all three types of blocks in the Hamiltonian matrix (the "S", "C" and "A" terms in Figure 23).

In Figure 40 we present the shifts of the energies of the ground vibrational state $(v_1, v_2, v_3) = (0,0,0)$ in $^{16}O^{18}O^{16}O$ due to inclusion of the asymmetric-top rotor term for the rotational excitation with $J = 5$. Here we see, first of all, a moderate negative shift by ~ 0.5 cm^{-1} for the $\Lambda = 0$ state (parity is $p = 1$) and then two relatively large shifts of the $\Lambda = 1$ states, but in the opposite directions for two values of parity: positive shift for $p = 1$, and negative shift for $p = 0$. This creates a splitting of ~ 3.5 cm^{-1}. For $\Lambda = 2$ this splitting is reduced to ~ 0.5 cm^{-1}, in which case it is almost exclusively due to the positive shift of the $p = 1$ state, since the $p = 0$ state exhibits only a tiny shift. For $\Lambda = 3$ the shifts of the $p = 0$ and $p = 1$ states are both positive and small, which leads to a tiny

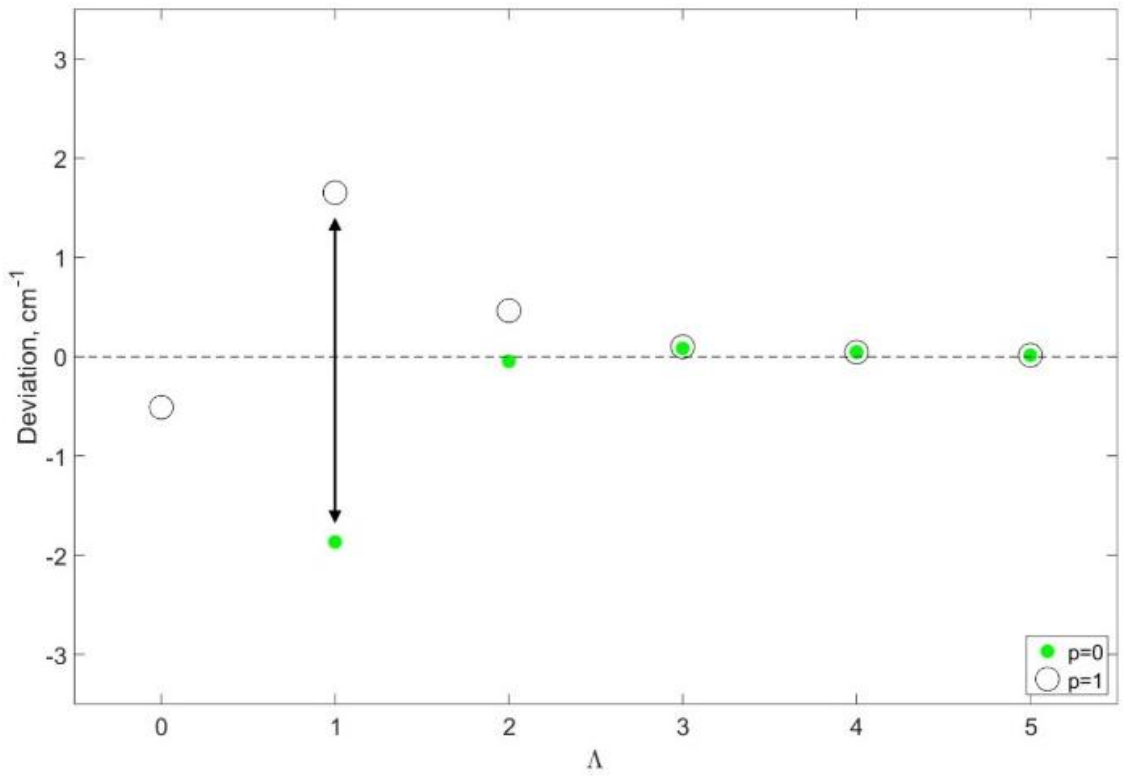

Figure 40. Deviations of the ground vibrational state of $^{16}O^{18}O^{16}O$ from the energies of a symmetric-top rotor due to the asymmetric-top rotor term for $J = 5$. The states of two different parities are denoted by color and symbol type. The magnitude of splitting (Λ-doubling) for $\Lambda = 1$ is indicated by a double arrow.

splitting. For $\Lambda = 4$ and $\Lambda = 5$ the splittings of the ro-vibrational states of the two parities are vanishingly small.

In Figure 41 we present the shifts of energies of the ground vibrational state $(v_1, v_2, v_3) = (0,0,0)$ in $^{16}O^{18}O^{16}O$ due to inclusion of the Coriolis coupling term for the rotational excitation with $J = 5$. We see, first of all, that the Coriolis effect is an order of magnitude larger than the asymmetric-top rotor effect. For example, the shift of the $\Lambda = 0$ state is ~ 5 cm^{-1}. However, since the shifts are negative for *both* $p = 0$ and $p = 1$ parity states, the resultant splittings are of the same order of magnitude as before: close to 4 cm^{-1} for $\Lambda = 1$, about 0.5 cm^{-1} for $\Lambda = 2$, a tiny splitting for $\Lambda = 3$, and vanishingly small splittings for $\Lambda = 4$ and $\Lambda = 5$. Still, the shifts due to the Coriolis term are not small even for $\Lambda = 5$, which is close to negative 1 cm^{-1} for both $p = 0$ and $p = 1$ parity states.

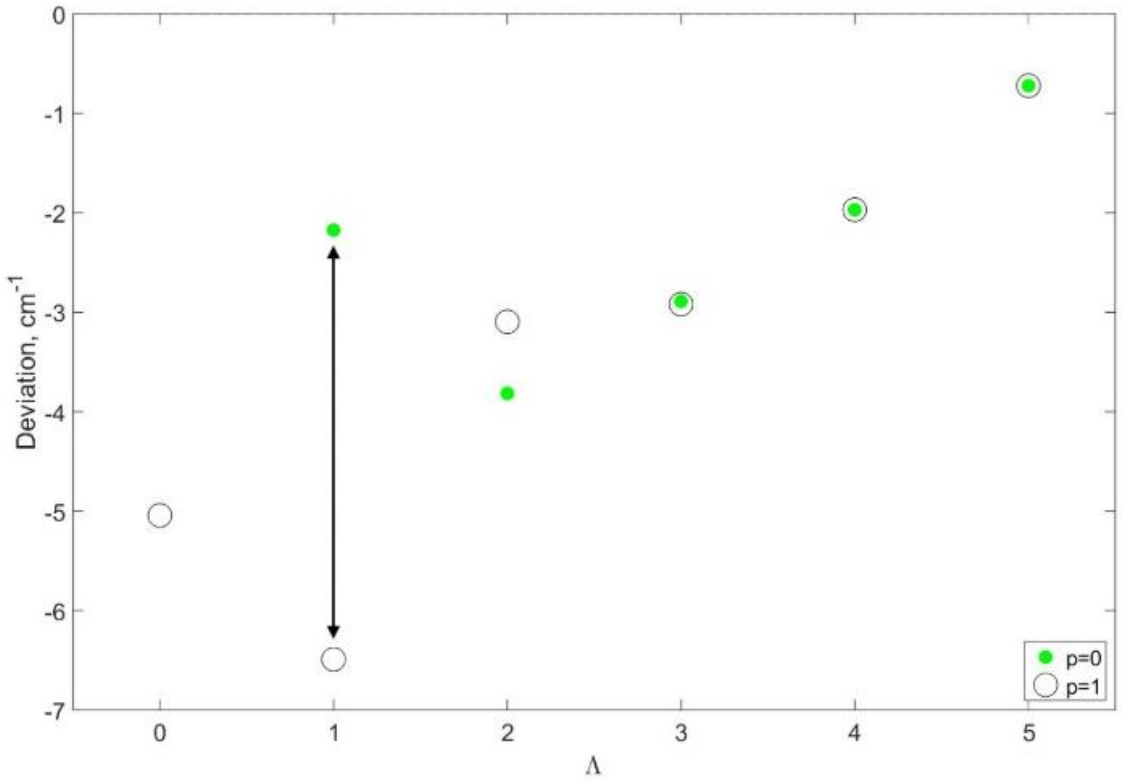

Figure 41. Same as Figure 40, but for the Coriolis term.

In order to understand the features of Figures 40 and 41, it is useful to analyze Eqs. (79) and (86), which provide analytical expressions for the contributions of asymmetric and Coriolis terms respectively. The magnitude of deviation from the energy of the symmetric top rotor is determined by the values of matrix elements of $\hat{T}_{\mathrm{asym}}$ and $\hat{T}_{\mathrm{cor}}$. One can see that, for the asymmetric term, the matrix elements are proportional to $U_{\Lambda\Lambda'}$ and $\frac{A-B}{4}$, while for the Coriolis term they are proportional to $W_{\Lambda\Lambda'}$ and $2B\cos\theta$.

For the equilibrium geometry of ozone, $\frac{A-B}{4} = 0.0138$ cm^{-1} and $2B\cos\theta = 0.489$ cm^{-1}. Thus, the Coriolis coupling term is expected to be more important than the asymmetric top rotor term, at least for the low energy states and small values of J, which is indeed the case, as one can see from Figures 40 and 41. However, the values of $W_{\Lambda\Lambda'}$ grow only as $O(J)$ (Eq. (85)), whereas the values of $U_{\Lambda\Lambda'}$ grow as $O(J^2)$ (Eq. (78)), making the asymmetric-top rotor term more important for the highly excited rotational states (large J). It can also become more important for the excited vibrational states due to larger deviations from the equilibrium geometry.

Looking at the definitions of Eqs. (78) and (85) and Figures 24 and 25, one can see that the matrix elements $U_{\Lambda\Lambda'}$ and $W_{\Lambda\Lambda'}$ have their maximum values at $\Lambda = 0$ and decrease as Λ increases, approaching the limit of $O(J)$ in the case of the asymmetric-top term and $O(\sqrt{J})$ in the case of the Coriolis term, but they never vanish. Because of that, the deviation from the symmetric top rotor limit would be the largest for small values of Λ, decrease as Λ increases, but never reach zero, even when $\Lambda = J$. This is indeed what we see in Figures 40 and 41.

In contrast to the energy shifts, the splittings between the states of the two parities do not depend on the magnitudes of the matrix elements of $\hat{T}_{\mathrm{asym}}$ and $\hat{T}_{\mathrm{cor}}$ directly, but rather on the difference of their magnitudes for the cases of different parities. Looking at Eqs. (78) and (85), one finds that the parity affects two things only. First, it either doubles or nullifies the blocks with $\Lambda = 0$. Second, it changes sign of the diagonal block $\Lambda = \Lambda' = 1$ of the matrix $U_{\Lambda\Lambda'}$ (see Figure 24). This makes the $\Lambda = 1$ case the most susceptible to the splitting (at least for low values of J), since in one parity it is coupled with the $\Lambda = 0$ state, in another parity it is not; in one parity the sign of the diagonal block $\Lambda = \Lambda' = 1$ of $U_{\Lambda\Lambda'}$ is positive, in another parity it is negative (with the same magnitude). The states with other values of Λ experience these effects indirectly, through chain coupling with $\Lambda = 1$, thus their splittings decrease exponentially as Λ increases and eventually vanish. As it was stated earlier, at high values of J the asymmetric top rotor term is expected to take precedence over the Coriolis term. Thus, it is likely that for the high values of J, the splittings for the $\Lambda = 2$ state may become more pronounced than those for $\Lambda = 1$.

In Figure 42 we present the shifts of energies of the ground vibrational state $(v_1, v_2, v_3) = (0,0,0)$ in $^{16}O^{18}O^{16}O$ for the rotational excitation with $J = 5$, due to inclusion of *both* the Coriolis coupling term and the asymmetric-top rotor term. Most importantly, this figure indicates that the energy shifts due to these two factors often occur in the *opposite* directions and thus partially cancel each other out with few exceptions (e.g. $\Lambda = 0$, and $\Lambda = 1$ and 2 with $p = 0$ for $J = 5$ where the shifts occur in the same directions). The value of the splitting for $\Lambda = 1$ is about 1 cm^{-1}, and it is only on the order of ~ 0.1 cm^{-1} for $\Lambda = 2$. For $\Lambda \geq 3$ the splittings are negligible. However, the effect of the Coriolis coupling survives, since energies of all states are still reduced (relative to the symmetric-top rotor approximation) by a non-negligible shift. It varies in

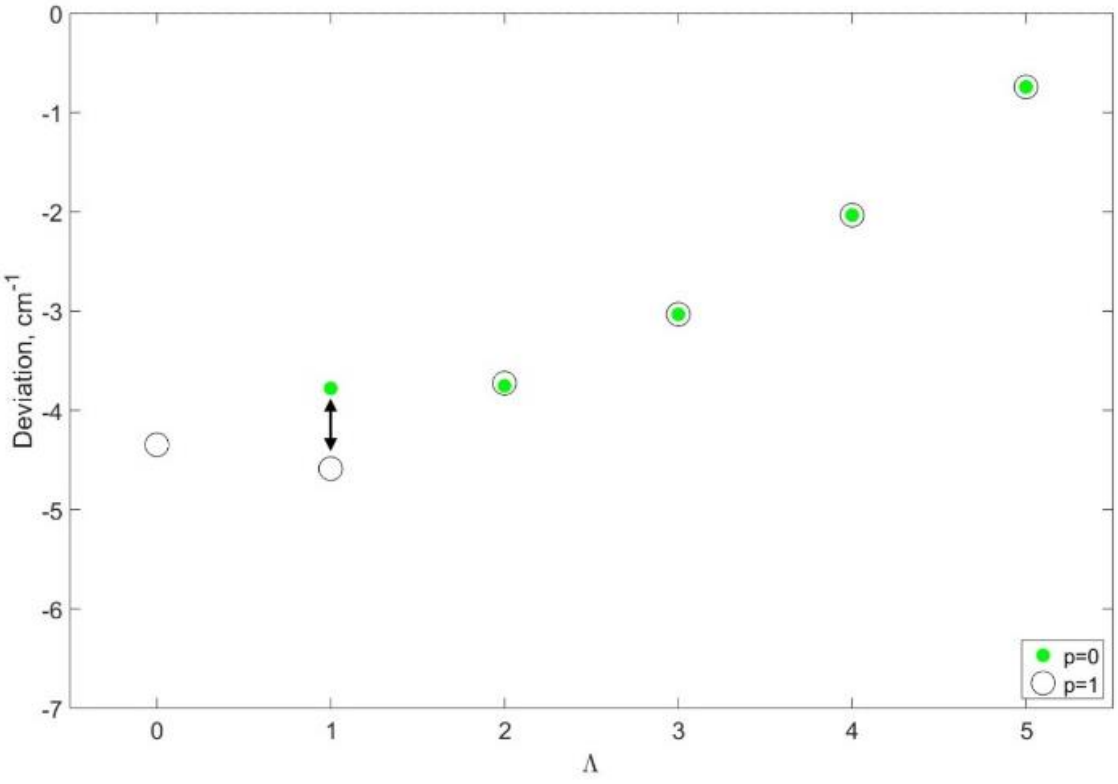

Figure 42. Same as Figures 40 and 41, but for both asymmetric top rotor and Coriolis terms together (exact calculation).

the range between negative 5 cm^{-1} and 1 cm^{-1} as the value of Λ is increased from $\Lambda = 0$ to $\Lambda = 5$.

6.3. Effect of Vibrational Excitations

In this section we explore dependency of Λ-doublings on vibrational excitation of a molecule, on example of singly-substituted ozone isotopologue.

Overall, the spectra we computed and assigned contain up to the 11 quanta of bending motion, 8 quanta of asymmetric stretch and 7 quanta of symmetric stretch. For comparison, in the work of Poirier and co-workers[117] for $J = 5$ the states with no more than 2 quanta of vibrational excitation in one mode were computed. We found that the assignments of the vibrational states in terms of the normal mode quantum numbers (v_1, v_2, v_3) are relatively certain for the lower 100 vibrational states for each set of (J, Λ, p) for both $^{16}O^{18}O^{16}O$ and $^{16}O^{16}O^{18}O$. A complete list of these assignments can be found in Supplementary Information of Refs. 107 and 140.

Figure 43(a) summarizes the progressions of energies for the normal mode overtones, which validates our vibrational assignments, while Figure 43(b) represents the dependence of parity splittings (or Λ-doublings) on the number of quanta in these vibrational progressions. From Figure 43 one can see that the value of splitting monotonically increases for the bending mode progression and monotonically decreases for the symmetric stretching mode progression of ozone. In contrast, for the asymmetric stretching mode progression of ozone, the value of splitting first increases and then slowly decreases, remaining roughly the same through a broad range of vibrational excitations.

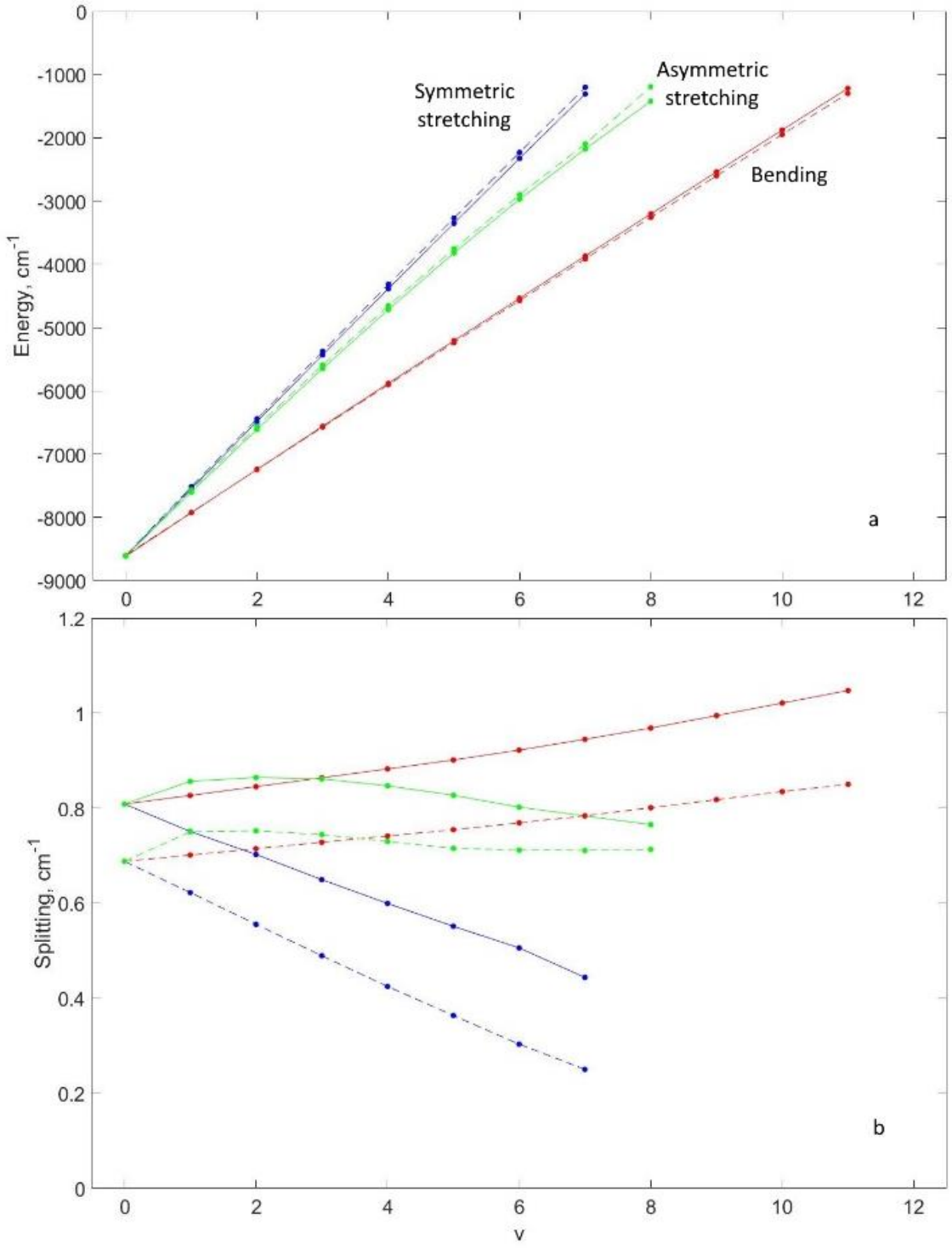

Figure 43. Evolution of energies and parity splittings for $J = 5$ and $\Lambda = 1$ as a function of number of vibrational quanta along the three normal modes of ozone. For each progression, the other two normal modes are not excited ($v = 0$). Solid and dashed lines correspond to symmetric $^{16}O^{18}O^{16}O$ and asymmetric $^{16}O^{16}O^{18}O$ ozone isotopomers, respectively. Progressions in the lower frame have the same colors as those in the upper frame.

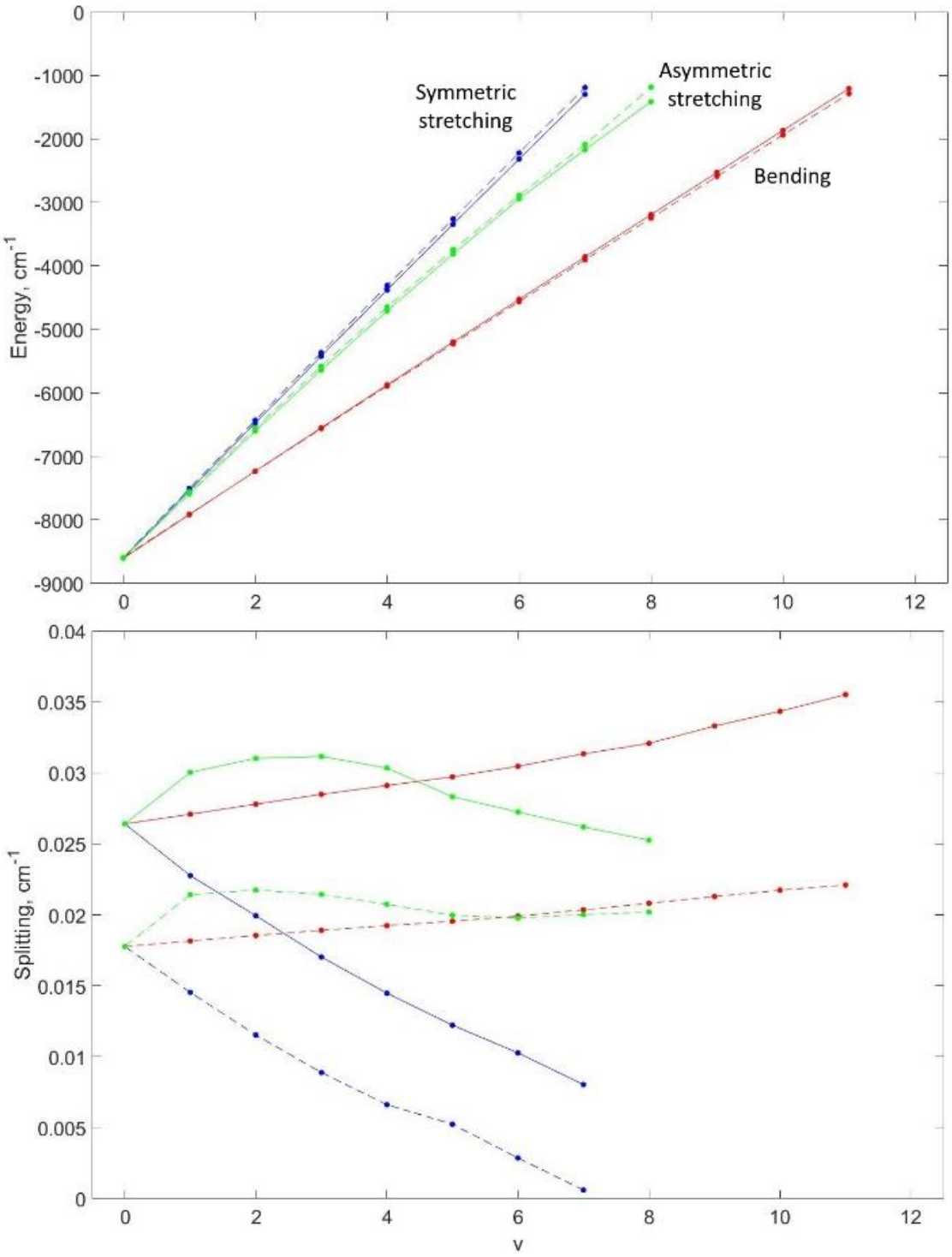

Figure 44. Same as Figure 43, but for $\Lambda = 2$.

When parity changes, the asymmetric top rotor contribution (given by Eq. (39)) in $\Lambda = 1$ block changes sign (due to Eq. (78)), therefore the magnitude of parity splittings is proportional to the magnitude of the asymmetric top rotor term, which, in turn, is proportional to the difference between the rotational constants A and B (degree of asymmetry). As we will see later in this chapter, the changes in the values of parity splittings observed in Figures 43 and 44 indeed correlate with the changes in relative values of rotational constants A and B, which appear due to distortions in molecular geometry, associated with the vibrational excitations.

Similar dependencies for $\Lambda = 2$, where the magnitudes of splittings are much smaller, are shown in Figure 44. Qualitatively, the splittings of the $\Lambda = 2$ states follow the same trends as we can see for $\Lambda = 1$ in Figure 43. Looking at the data in Figures 43 and 44, we can conclude that the values of splittings do not change dramatically through the range of vibrational excitations considered here.

6.4. Fitting and Analysis of Rovibrational Spectra

In order to compare and contrast the spectra of symmetric and asymmetric ozone molecules we fitted their rotational energy levels using the following expression:

$$E_{\mathrm{rot}}(J,\Lambda,p) = E_{\mathrm{vib}} + \frac{A+B}{2}J(J+1) + \left(C - \frac{A+B}{2}\right)\Lambda^2 + (-1)^{J+\Lambda+p}\frac{\Delta W(J,\Lambda)}{2} \quad (129)$$

The first term corresponds to the vibrational energy, the next two terms add rotational energy of the symmetric top rotor (parity-independent), and the last term is responsible for the splitting between the two parities, where the absolute value of the splitting is given by Wang's formula through binomial coefficients:[141,142]

$$\Delta W(J,\Lambda) = 8(C-A)\binom{J+\Lambda}{\Lambda}\binom{J}{\Lambda}\Lambda^2\left(\frac{\beta}{8}\right)^{\Lambda}(1-\beta)^{-1} \quad (130)$$

where

$$\beta = \frac{A-B}{2C-A-B} \quad (131)$$

is used to characterize the degree of asymmetry of a rotor.

First, we tried to fit the rotational spectrum of the ground vibrational state (0,0,0) in each ozone isotopomer by the symmetric-top rotor formula, with the parity splitting neglected, i.e. by setting $\Delta W = 0$ in Eq. (129). The results of such fitting are presented in Table 25. The first row shows the fitted values of the vibrational energy for the ground state of each molecule. The values in parenthesis are given for comparison and correspond to the exact vibrational energies, computed in this chapter. The next two rows report the values of the fitting coefficients $(A+B)/2$ and C for given isotopomers. Experimental data[143] are given in parenthesis for comparison. In all cases the fitted values of $(A+B)/2$ are in perfect agreement with the experimental data, while the fitted values

Table 25. Least squares fitting coefficients (in cm^{-1}) of Eq. (129), where the parity splitting term ΔW is set to 0, computed using all rotational states with $0 \le J \le 5$ of the ground vibrational state for listed ozone isotopomers. The numbers in parenthesis are experimental spectroscopic constants,[143] or, in case of E_{vib}, the accurately computed energies of the ground vibrational state. Energy is defined with respect to the lower dissociation channel of the corresponding isotopomer.

Parameter	$^{16}O^{18}O^{16}O$	$^{16}O^{16}O^{18}O$	$^{18}O^{16}O^{18}O$	$^{18}O^{18}O^{16}O$
E_{vib}	-8629.717 (-8629.724)	-8615.466 (-8615.474)	-8617.638 (-8617.645)	-8632.133 (-8632.140)
$(A+B)/2$	0.418 (0.418)	0.397 (0.397)	0.375 (0.375)	0.395 (0.396)
C	3.300 (3.290)	3.498 (3.488)	3.432 (3.422)	3.235 (3.225)
RMSE	0.123	0.105	0.0954	0.112

of C indicate differences on the order of 0.01 cm^{-1}. The last row gives the root mean square error (RMSE) for a given fit, and all of those values are on the order of 0.1 cm^{-1}.

Next, we fitted the rotational spectrum of the ground vibrational state in each ozone isotopomer using the fully relaxed version of Eq. (129). The values of fitting coefficients for this case are given in Table 26, which is structured in the same way as Table 25. In contrast to the Table 25, these fits correspond to the asymmetric-top rotor molecules and allow one to determine the values of A and B separately, based on the magnitudes of parity splittings. The non-zero difference between A and B also permits us to determine the value of asymmetry parameter β for each isotopomer of ozone, reported in the fifth row of Table 26. Note that when the ΔW parameter in Eq. (129) is relaxed, the values of RMSE are reduced by an order of magnitude, to about 0.01 cm^{-1}, which means that the quality of the fit of the data is significantly improved.

Looking at the values of rotational constants in Table 26, one can see that they are similar in all isotopomers of ozone, roughly equal to $A \approx 0.42\ cm^{-1}$, $B \approx 0.37\ cm^{-1}$ and

Table 26. Same as Table 25, but with relaxed ΔW term.

Parameter	$^{16}O^{18}O^{16}O$	$^{16}O^{16}O^{18}O$	$^{18}O^{16}O^{18}O$	$^{18}O^{18}O^{16}O$
E_{vib}	-8629.717 (-8629.724)	-8615.466 (-8615.474)	-8617.638 (-8617.645)	-8632.133 (-8632.140)
A	0.445 (0.445)	0.420 (0.420)	0.396 (0.396)	0.420 (0.420)
B	0.391 (0.391)	0.374 (0.374)	0.354 (0.354)	0.371 (0.372)
C	3.300 (3.290)	3.498 (3.488)	3.432 (3.422)	3.235 (3.225)
β	9.36×10^{-3} (9.40×10^{-3})	7.40×10^{-3} (7.44×10^{-3})	6.82×10^{-3} (6.87×10^{-3})	8.66×10^{-3} (8.48×10^{-3})
RMSE	0.0128	0.0126	0.0118	0.0118

$C \approx 3.3\ \mathrm{cm}^{-1}$, with differences on the order of ±5% due to isotopic substitutions. These numbers satisfy reasonably well the condition of the symmetric top rotor approximation, $A \approx B \ll C$, which was frequently used in the past to ease calculations but is avoided here, in order to reach the new higher level of accuracy. The fitted values of A and B match the experimental values precisely for all molecules, with the exception of 0.001 cm^{-1} difference for B in the case of $^{18}O^{18}O^{16}O$. The fitted values of C deviate from the corresponding experimental measurements only by 0.01 cm^{-1}. The ground ro-vibrational energies predicted by these fits are also in good agreement with the results of the exact calculations, all higher by only about 0.007 cm^{-1}. This excellent agreement with experimental results serves as another benchmark test for the accuracy of SpectrumSDT.

The values of the asymmetry parameter approach $\beta \approx 0.01$ for all isotopomers of ozone. One can see that in the case of single isotopic substitution, the symmetric ozone molecule $^{16}O^{18}O^{16}O$ has slightly higher value of β than the asymmetric molecule $^{16}O^{16}O^{18}O$. But, in case of the double substitution the behavior is reversed: now the asymmetric molecule $^{18}O^{18}O^{16}O$ demonstrates slightly higher values of β, compared to the symmetric molecule $^{18}O^{16}O^{18}O$.

These trends are further explored in Figure 45, where we collected the values of parity splittings for the cases of $\Lambda = 1$ and $\Lambda = 2$, for each isotopomer of ozone considered here. Roughly, for $\Lambda = 1$ the splittings are on the order of $\Delta W \approx 0.04$ cm^{-1} for $J = 1$, and they are increased tenfold when the rotational excitation is raised to $J = 4$, reaching $\Delta W \approx 0.4$ cm^{-1}. In the case of $\Lambda = 2$, the splittings are about two orders of magnitude smaller, starting from $\Delta W \approx 0.0005$ cm^{-1} for $J = 2$ and reaching about $\Delta W \approx 0.02$ cm^{-1} for $J = 5$. The data presented in Figure 45 are also reported in Tables 27 and

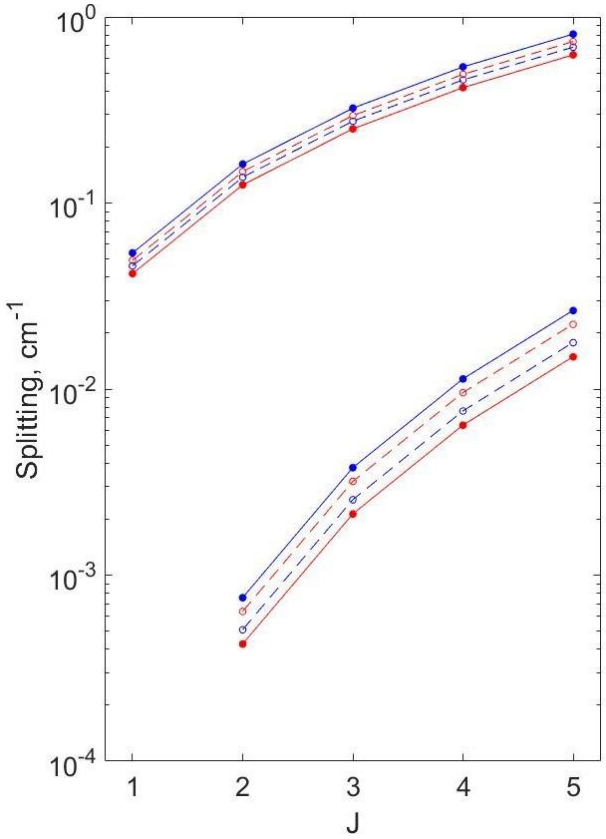

Figure 45. Absolute values of parity splittings in the ground vibrational state of different ozone isotopomers for $\Lambda = 1$ (upper series) and $\Lambda = 2$ (lower series), as a function of J. Filled and empty symbols correspond to the exact values of splittings computed directly from the rovibrational energies for symmetric and asymmetric isotopomers, respectively. Solid and dashed lines show the predictions of the analytic fit of these data by Eq. (130) for symmetric and asymmetric isotopomers, respectively. The blue and red colors correspond to singly and doubly substituted ozone isotopologues, respectively.

28. From this figure and tables, one can clearly see that symmetric and asymmetric ozone molecules behave differently in the cases of singly and doubly substituted ozone. Namely, in the case of single substitution the splitting is larger for the symmetric isotopomer, while in the case of double substitution the splitting is larger for the asymmetric isotopomer.

In order to include the effect of vibrational excitation, we modified Eq. (129) by expressing E_{vib} through the second order Dunham expansion as:

$$E_{\text{vib}}(v_1, v_2, v_3) = E_{\text{elec}} + \sum_{i=1}^{3} \omega_i \left(v_i + \frac{1}{2}\right) + \sum_{i,j=1}^{3} \chi_{ij} \left(v_i + \frac{1}{2}\right)\left(v_j + \frac{1}{2}\right) \quad (132)$$

The first term of Eq. (132) is the lowest energy on the PES, the bottom of the well. The next term adds harmonic contribution from each mode (3 normal modes total in case of ozone) and the last term adds the intra-mode and inter-mode anharmonicities.

Table 27. The values of the splittings $\Delta W(J, \Lambda = 1)$ in cm^{-1} for the ground vibrational state in various ozone isotopomers.

J	$^{16}O^{18}O^{16}O$	$^{16}O^{16}O^{18}O$	$^{18}O^{16}O^{18}O$	$^{18}O^{18}O^{16}O$
$J = 1$	0.0539	0.0459	0.0417	0.0492
$J = 2$	0.162	0.138	0.125	0.148
$J = 3$	0.324	0.275	0.250	0.295
$J = 4$	0.539	0.459	0.417	0.492
$J = 5$	0.809	0.688	0.626	0.737

Table 28. Same as Table 28, but for $\Lambda = 2$.

J	$^{16}O^{18}O^{16}O$	$^{16}O^{16}O^{18}O$	$^{18}O^{6}O^{18}O$	$^{18}O^{18}O^{16}O$
$J = 2$	0.000756	0.000509	0.000427	0.000638
$J = 3$	0.00379	0.00255	0.00213	0.00319
$J = 4$	0.0114	0.00764	0.00640	0.00958
$J = 5$	0.0265	0.0178	0.0149	0.0224

First, we used Eqs. (129)-(132) to fit only the rovibrational states with no more than one quantum of the vibrational excitation in each mode, assuming a harmonic oscillator model, i.e. setting all $\chi_{ij} = 0$. The results of such fitting are presented in Table 29 for all isotopomers of ozone considered here. Now the first row represents electronic energy E_{elec} relative to the dissociation limit. For comparison, the energy values at the minimum energy point on the PES are given in parenthesis (different in the singly and doubly substituted ozone molecules, since the dissociation energy includes zero-point energy of the heaviest diatomic fragment, which is $^{16}O^{18}O$ in the case of the singly substituted ozone but is $^{18}O^{18}O$ in the case of the doubly substituted ozone). The next

Table 29. Least squares fitting coefficients (in cm^{-1}) of Eq. (129) and (132), where the anharmonicity terms χ_{ij} are set to 0, computed using all rotational states with $0 \leq J \leq 5$ and vibrational states with up to 1 quanta of excitation (4 vibrational states total) for different ozone isotopomers. The numbers in parenthesis are experimental spectroscopic constants[143,144] or, in case of E_{elec}, the actual lowest energy of the PES. Energy is defined with respect to the lower dissociation channel of the corresponding isotopomer.

Parameter	$^{16}O^{18}O^{16}O$	$^{16}O^{16}O^{18}O$	$^{18}O^{16}O^{18}O$	$^{18}O^{18}O^{16}O$
E_{elec}	-10015 (-10044)	-10014 (-10044)	-9995 (-10024)	-9995 (-10024)
ω_1	1068 (1074)	1085 (1090)	1066 (1072)	1055 (1061)
ω_2	687.7 (696.3)	679.2 (684.6)	662.8 (668.1)	672.1 (677.5)
ω_3	1015 (1008)	1034 (1028)	1025 (1019)	999.3 (993.9)
A	0.443 (0.445)	0.418 (0.420)	0.394 (0.396)	0.418 (0.420)
B	0.389 (0.391)	0.372 (0.374)	0.352 (0.354)	0.369 (0.372)
C	3.301 (3.290)	3.499 (3.488)	3.432 (3.422)	3.235 (3.225)
RMSE	0.236	0.233	0.236	0.216

three rows of Table 29 report the fitted values of harmonic frequencies ω_1, ω_2 and ω_3. For comparison, experimental values of the fundamental excitation energies[144] are given in parenthesis for each molecule. These data demonstrate a very good agreement between theory and experiment, with differences of only ~6 cm^{-1} in all modes of all isotopomers. The next three rows of Table 29 list the rotational constants A, B and C derived from this rovibrational fit. Their values are similar to the ones given in Tables 25 and 26, but not exactly the same, which indicates that vibrational excitation has some effect on the rotational spectrum.

To explore this question in detail, we carried out the fits of rotational spectra using Eqs. (129)-(131) separately for the first excited vibrational state of each mode: (001), (010) and (100). The resultant fitting parameters are collected in Tables 30-32. Comparing these data with the results of Table 26, one can see that excitation of the bending and asymmetric stretching vibrational modes increases the values of β, while excitation of the symmetric stretching mode decreases it.

The accuracy of the common rovibrational fit, Eqs. (129)-(132), is relatively lower, compared to the purely rotational fits of individual vibrational states, as evidenced by increased values of RMSE. However, such behavior is expected, since the magnitude

of vibrational quanta are much larger than rotational, and the absolute value of RMSE is still small, therefore we conclude that this fit is accurate.

Finally, we used Eq. (132) without restrictions on anharmonicities to fit the rovibrational states with no more than 2 quanta of excitation, cumulatively across all

Table 30. Same as Table 26, but for the first vibrationally excited state in the bending mode (0, 1, 0), second vibrational state overall.

Parameter	$^{16}O^{18}O^{16}O$	$^{16}O^{16}O^{18}O$	$^{18}O^{16}O^{18}O$	$^{18}O^{18}O^{16}O$
E_0	-7942.247	-7936.536	-7955.073	-7960.294
A	0.444	0.419	0.395	0.419
B	0.389	0.372	0.352	0.369
C	3.351	3.549	3.479	3.282
β	9.39×10^{-3}	7.42×10^{-3}	6.84×10^{-3}	8.69×10^{-3}
RMSE	0.0138	0.0136	0.0128	0.0127

Table 31. Same as Table 26, but for the first vibrationally excited state in the asymmetric stretching mode (0, 0, 1), third vibrational state overall.

Parameter	$^{16}O^{18}O^{16}O$	$^{16}O^{16}O^{18}O$	$^{18}O^{16}O^{18}O$	$^{18}O^{18}O^{16}O$
E_0	-7614.874	-7581.576	-7591.836	-7632.546
A	0.441	0.416	0.392	0.416
B	0.384	0.366	0.345	0.364
C	3.253	3.451	3.381	3.193
β	10.1×10^{-3}	8.17×10^{-3}	7.79×10^{-3}	9.31×10^{-3}
RMSE	0.0132	0.0131	0.0122	0.0122

Table 32. Same as Table 26, but for the first vibrationally excited state in the symmetric stretching mode (1, 0, 0), fourth vibrational state overall.

Parameter	$^{16}O^{18}O^{16}O$	$^{16}O^{16}O^{18}O$	$^{18}O^{16}O^{18}O$	$^{18}O^{18}O^{16}O$
E_0	-7561.458	-7530.665	-7551.638	-7576.739
A	0.443	0.418	0.394	0.418
B	0.393	0.376	0.357	0.372
C	3.299	3.498	3.438	3.231
β	8.69×10^{-3}	6.69×10^{-3}	5.97×10^{-3}	8.04×10^{-3}
RMSE	0.0126	0.0127	0.0131	0.0116

modes, which includes overtones and combination bands (10 vibrational states total). The results of this fit are given in Table 33. As one can see, the values of RMSE increase again but not critically, reaching 0.35 cm^{-1} on average for all isotopomers considered here. This number is not large, considering the span of the fitted spectrum of roughly 2000 cm^{-1} which fills about a quarter of the potential energy well in ozone on its way to the dissociation towards $O + O_2$.

The first row in Table 33 shows excellent agreement between the fitted and the actual electronic energies, with the average deviation of about 2 cm^{-1}. The values of harmonic frequencies ω_1, ω_2 and ω_3 in Table 33 should not be mixed with excitation

Table 33. Same as Table 29, but without restriction on the values of χ_{ij} (vibrational anharmonicities).

Parameter	$^{16}O^{18}O^{16}O$	$^{16}O^{16}O^{18}O$	$^{18}O^{16}O^{18}O$	$^{18}O^{18}O^{16}O$
E_{elec}	-10042 (-10044)	-10042 (-10044)	-10021 (-10024)	-10022 (-10024)
ω_1	1094	1112	1090	1082
ω_2	701.5	693.3	676.4	685.4
ω_3	1064	1084	1076	1046
χ_{11}	-2.919	-4.861	-2.484	-4.865
χ_{22}	-1.308	-1.283	-1.210	-1.249
χ_{33}	-12.83	-14.95	-13.82	-13.70
χ_{12}	-7.419	-7.850	-7.140	-7.490
χ_{13}	-33.00	-26.26	-31.30	-25.35
χ_{23}	-14.87	-15.21	-15.26	-14.17
A	0.441 (0.445)	0.416 (0.420)	0.392 (0.396)	0.416 (0.420)
B	0.387 (0.391)	0.370 (0.374)	0.350 (0.354)	0.367 (0.372)
C	3.302 (3.290)	3.500 (3.488)	3.433 (3.422)	3.236 (3.225)
RMSE	0.363	0.361	0.357	0.336

energies, and should not be directly compared to the experimental data given in Table 29, since those numbers do not take into account anharmonicity effects.

Analysis of the intra-mode anharmonicity parameters in Table 33 indicates that the bending mode is the least anharmonic, with $\chi_{22} \approx -1.2$ cm^{-1}, while the asymmetric-stretching mode is the most anharmonic, with more than ten times larger anharmonicity parameter of about $\chi_{33} \approx -14$ cm^{-1}. Both of these characteristics change little across the four isotopic substitutions considered here, indicating similar values for symmetric and asymmetric ozone molecules with single and double isotopic substitutions.

However, we found that the symmetric-stretching mode in ozone has its own interesting property. This mode is less anharmonic in symmetric ozone molecules with $\chi_{11} \approx -2.7$ cm^{-1} and is more anharmonic in asymmetric ozone molecules with $\chi_{11} \approx -4.9$ cm^{-1}, and this large difference is systematically present in both singly and doubly-substituted ozone species. The inter-mode anharmonicity parameters $\chi_{12} \approx -7.5$ cm^{-1} and $\chi_{23} \approx -15$ cm^{-1} remain roughly the same across the four isotopomers, but the value of χ_{13} behaves differently. It is larger in symmetric ozone molecules, $\chi_{13} \approx -32$ cm^{-1}, and is smaller in asymmetric ozone molecules, $\chi_{13} \approx -25$ cm^{-1}, and this appreciable difference is systematically present in both singly and doubly-substituted ozone species. These systematic mass-independent differences might be related to the isotope effects in ozone, η-effect in particular.

6.5. Extrapolation of Parity Splittings

Excellent agreement of the fitted spectroscopic constants with the experimental results, together with the low values of RMSE of the fits in the previous section, permit

us to use Eqs. (129)-(132) to estimate the behavior of the spectrum of ozone molecules at larger values of J that are difficult to calculate explicitly.

Figure 46 shows extrapolation of the parity splittings for the ground vibrational state of the singly substituted ozone isotopomers ($^{16}O^{18}O^{16}O$ and $^{16}O^{16}O^{18}O$) as a function of J for different values of Λ. The fitted data points, available in the range $1 \leq J \leq 5$, are shown by symbols. Solid and dashed lines correspond to the analytic fits of these data for symmetric $^{16}O^{18}O^{16}O$ and asymmetric $^{16}O^{16}O^{18}O$ isotopomers, respectively. The fits are extended to extrapolate up to $J = 50$. The curves corresponding to $1 \leq \Lambda \leq 5$ are labelled explicitly in the picture; the curves for $\Lambda > 5$ can be easily identified using the

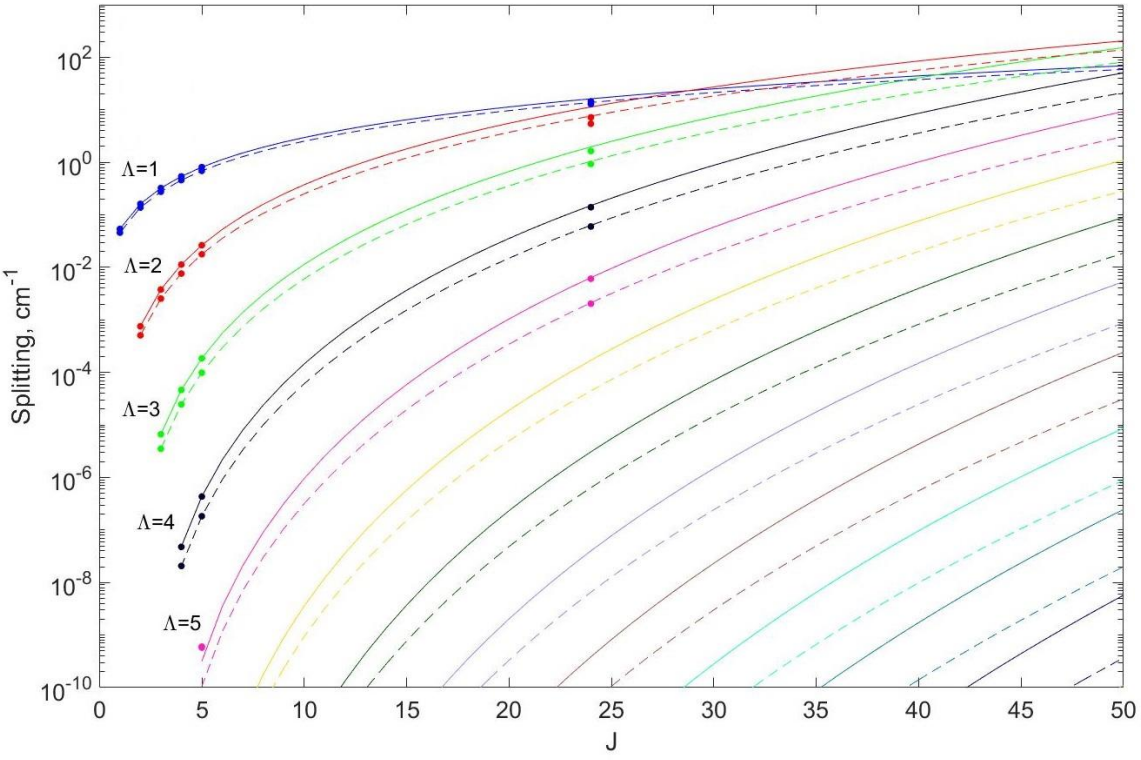

Figure 46. Extrapolation of parity splittings for $^{16}O^{18}O^{16}O$ (solid line) and $^{16}O^{16}O^{18}O$ (dashed line) as a function of J. Symbols mark exact values of splittings calculated in this work. Different values of Λ are shown by different colors. The points at $J = 24$ were computed separately to check the quality of extrapolation and are not included in the fit.

overall trend. Figure 47 shows similar data for the doubly substituted isotopomers, symmetric $^{18}O^{16}O^{18}O$ and asymmetric $^{18}O^{18}O^{16}O$.

From the Figures 46 and 47, and from Eq. (130), one can see that for the low values of J the splittings between different parities decrease exponentially as a function of Λ but they increase as a function of J, as $O(J^{2\Lambda})$. Thus, the curves corresponding to the higher values of Λ start lower, but grow faster and eventually cross the curves corresponding to the lower values of Λ. This is indeed what we can see at $J \approx 30$, where $\Lambda = 1$ crosses the $\Lambda = 2$ curve, and at $J \approx 50$, where the $\Lambda = 2$ curve is crossed by $\Lambda = 3$. The analytical fits allow us to predict that in the region of $J = 50$ the states with $\Lambda = 1$ to 5 are all expected to have splittings above 1 cm^{-1}.

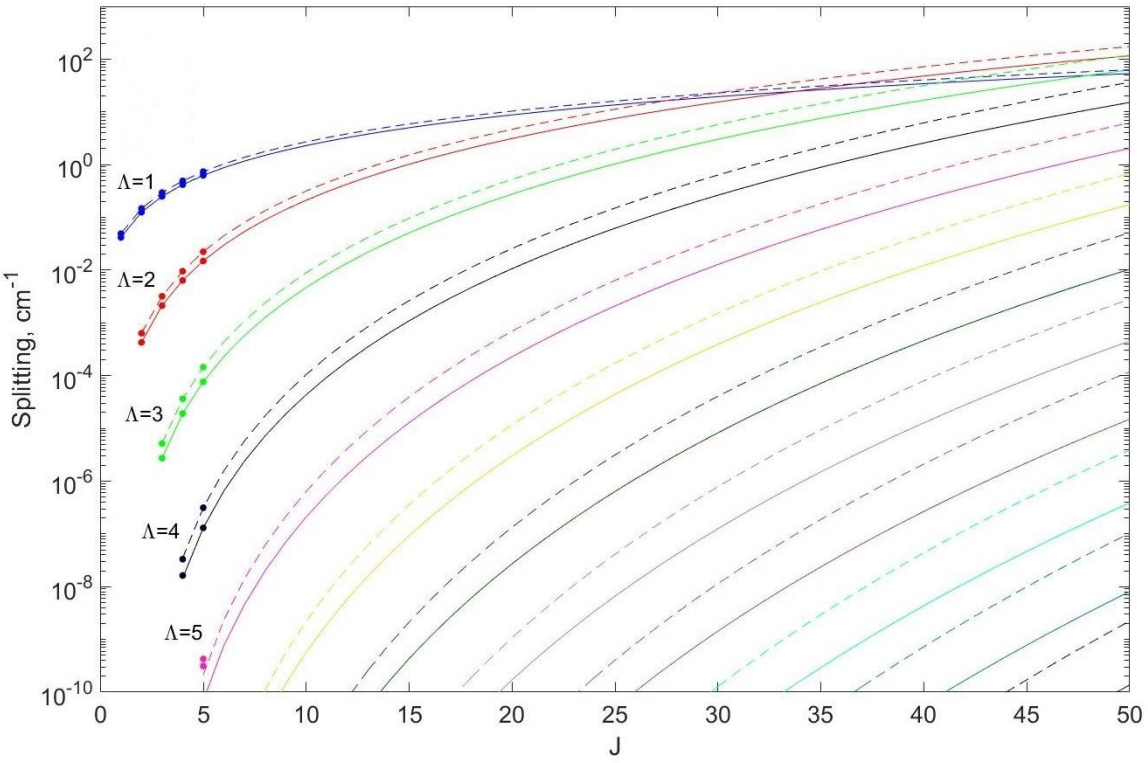

Figure 47. Extrapolation of parity splittings for $^{18}O^{16}O^{18}O$ (solid line) and $^{18}O^{18}O^{16}O$ (dashed line) as a function of J. Symbols mark exact values of splittings calculated in this work. Different values of Λ are shown by different colors.

As for the symmetric vs. asymmetric molecule behavior, the trends reported in Figure 45 for the low values of J are expected to hold for higher values of J as well. Namely, Figures 46 and 47 indicate that the splittings of $^{16}O^{18}O^{16}O$ are greater than those of $^{16}O^{16}O^{18}O$ in the whole range of the considered values of J, while for the doubly substituted isotopomers the behavior is just the opposite, i.e. the splittings for $^{18}O^{18}O^{16}O$ are greater than those of $^{18}O^{16}O^{18}O$. This order is not expected to change for any value of J and Λ due to the way the splittings depend on them in Eq. (130), although the absolute value of difference between the splittings in the symmetric and asymmetric molecules grows as a function of J, which can be clearly seen in the case of $\Lambda = 5$.

6.6. Rovibrational Partition Functions

Extrapolation of the spectra toward large values of J can also be used to compute the rovibrational partition functions Q_{asym} and Q_{sym} for asymmetric and symmetric ozone molecules, as:

$$Q(T) = \sum_{i=1}^{N} (2J_i + 1) \exp\left(-\frac{E_i - E_1}{kT}\right) \tag{133}$$

where the sum is over all ro-vibrational states of the corresponding isotopomer.

The partition functions of Eq. (133) can be used to determine the ratio of the number of states in asymmetric and symmetric ozone molecules, $R = Q_{\text{asym}}/Q_{\text{sym}}$, in the same way as in Chapter 5, which may demonstrate a source of isotope effects, if it deviates from the statistical value of $R = 2$.

Figure 48 summarizes our results for the singly and doubly substituted ozone in the range of temperatures relevant to the stratosphere and the laboratory studies. The solid blue and red lines give the values of $R = Q_{\mathrm{asym}}/Q_{\mathrm{sym}}$ for the singly and doubly substituted ozone molecules respectively (calculated from their extrapolated spectra). In each case the spectrum was fitted with Eqs. (129)-(132), using the rovibrational states with $0 \leq J \leq 5$ and up to 2 quanta of vibrational excitation, and extrapolated up to the energy ~4000 cm^{-1} above the bottom of the potential energy well. One can see that in the singly substituted ozone molecule the ratio of the partition functions deviates from the statistical value of $R = 2$ by about +0.05 (2.5%) in the whole range of the considered

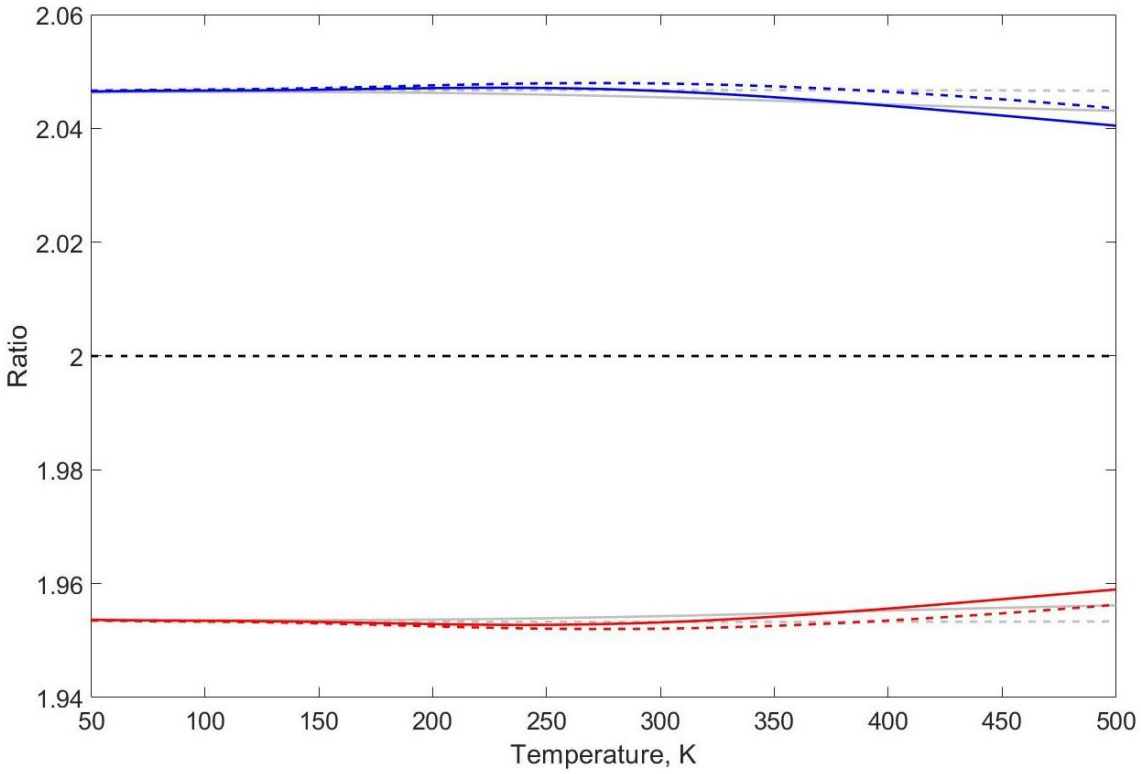

Figure 48. The ratio of partition functions of asymmetric and symmetric isotopomers of ozone. The solid blue (red) color corresponds to the singly (doubly) substituted isotopologues of ozone. The dashed lines correspond to the case when the parity splittings are neglected. The gray lines in the background show analogous result calculated based on purely rotational spectrum, without inclusion of any vibrationally excited states.

temperatures, while in the doubly substituted case the same deviation occurs in the opposite direction, –0.05. Interestingly, the singly-substituted and the doubly-substituted ozone molecules behave differently, and the difference of R values for them is on the order of 0.1, which is a substantial deviation from the statistical value of $R = 2$.

The dashed red and blue lines in Figure 48 are given to demonstrate the effect of parity splittings on the value of the ratio $R = Q_{\mathrm{asym}}/Q_{\mathrm{sym}}$. These dashed lines were obtained using the fits of the spectra by a simplified expression, with fixed $\Delta W = 0$ in Eq. (129). One can see that at low temperatures the effect of parity splittings is negligible, since only the low levels of rotational excitations are accessible, where the values of parity splittings are small. For higher temperatures, the effect of splittings on $R = Q_{\mathrm{asym}}/Q_{\mathrm{sym}}$ becomes visible, but is still relatively small (on the order of 0.005), an order of magnitude smaller than the effect of the single vs. double isotopic substitutions.

The gray lines in the background of Figure 48 were obtained using purely rotational partition functions Q_{asym} and Q_{sym} of the ground vibrational state only, without including any excited vibrational states. These are given to illustrate the effect of vibrational excitation. As before, the dashed gray lines correspond to the case when the parity splittings are neglected. We can see that inclusion of the vibrational excitations has small effect at low temperature, but becomes more important at higher temperatures. Without vibrations, the values of the ratios $R = Q_{\mathrm{asym}}/Q_{\mathrm{sym}}$ remain nearly constant throughout the considered temperature range.

As an experiment, we also tried to use a more relaxed version of the fit, where the rotational constants A, B and C are allowed to have different values for different vibrational states, which was done by carrying out separate fits for all vibrational states in

the considered energy range, similar to the data demonstrated in Tables 30-32. The result of this is presented in Figure 49. This way of calculation has better flexibility, since each vibrational state is allowed to have its own set of rotational constants. However, a single-set approach, considered in Figure 48, already has RMSE low enough to leave this flexibility mostly unused, as one can see by comparing the results of Figure 48 and Figure 49.

6.7. Summary

In this chapter we computed the rotational-vibrational states of singly- and doubly-substituted ozone isotopologues, for the rotational excitations up to $J = 5$. The range of vibrational excitations extends up to 7 quanta of excitations in one mode. To the

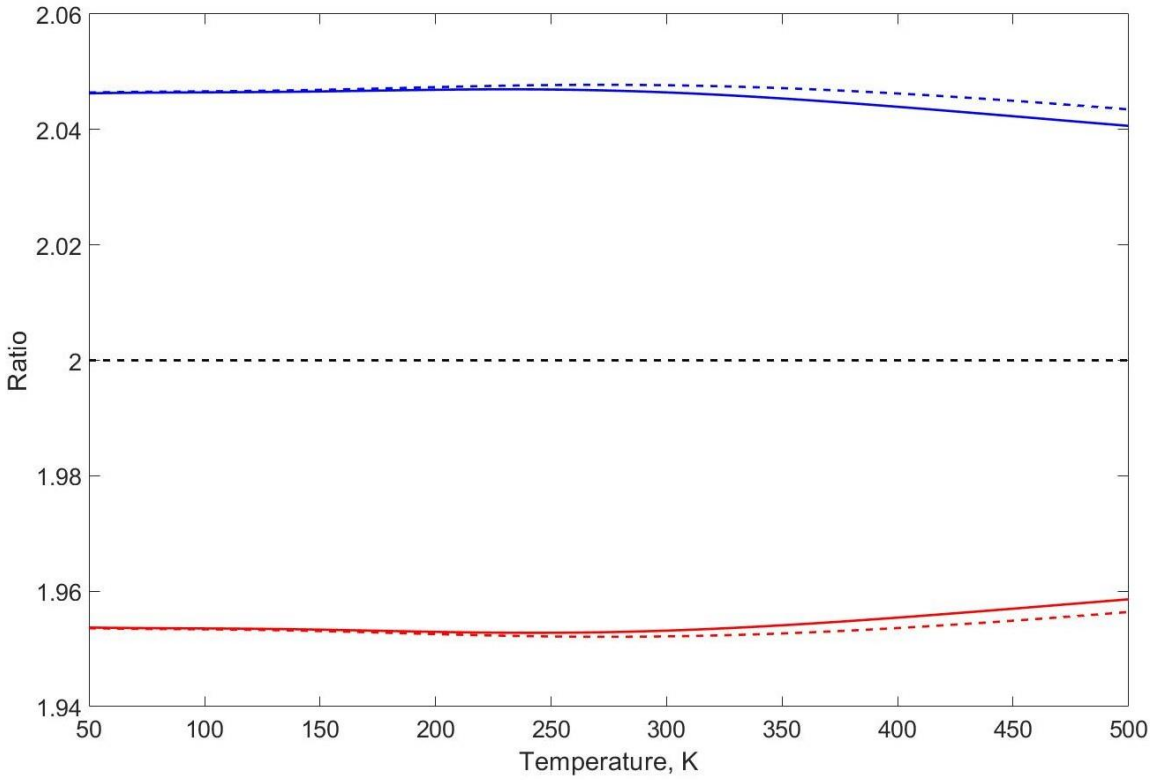

Figure 49. Same as Figure 48, but with a separate set of rotational constants for each vibrational state.

best of our knowledge such calculations have never been reported before for the rotationally excited doubly substituted ozone molecule.

The code (SpectrumSDT) was rigorously tested by comparing the calculated data with the results recently published by Poirier and coworkers[117] and the results of an existing well-tested APH3D program of Kendrick). Excellent agreement was found.

First, we carried out the simplest calculations within the symmetric-top rotor approximation, and then we added the asymmetric-top rotor terms and the Coriolis coupling terms, one at a time, and finally all together. This was done for the methodological reason, in order to illuminate the effect of each term on the spectrum of rotational-vibrational states, and most importantly on the Λ-doubling, which is the splitting of energies for the states of two parities. We showed that for the low values of rotational excitation in ozone, the Coriolis coupling effect is about an order of magnitude stronger than the asymmetric top rotor effect (in terms of shifts from the symmetric top rotor limit). The splittings due to the Coriolis and the asymmetric-top rotor effects, however, were on the same order of magnitude, but occurred in the opposite directions. Overall, in the exact calculations with both effects included, the influence of the two phenomena partially cancels out, leading to relatively small residual splittings (Λ-doublings).

Our new data computed here allows us to do a systematic analysis of isotope effects in the rotational-vibrational spectra of ozone. Namely, we checked whether it is reasonable to expect that, due to the Coriolis coupling effect, the asymmetric ozone isotopomers (singly substituted $^{16}O^{16}O^{18}O$ and doubly substituted $^{18}O^{18}O^{16}O$) would behave similar to each other but different from the symmetric ozone isotopomers (singly

substituted $^{16}O^{18}O^{16}O$ and doubly substituted $^{18}O^{16}O^{18}O$), which in turn would also behave similar to each other. So far, we found no justification for this hypothesis. We found that for ozone the deviations of rotational constants from the standard symmetric-top-rotor behavior is affected by isotopic composition as much as it is affected by the symmetry of the molecule. For example, in the case of single isotopic substitution the value of the rotational asymmetry parameter β appears to be smaller in asymmetric $^{16}O^{16}O^{18}O$ than it is in symmetric $^{16}O^{18}O^{16}O$, but, it is just opposite in the case of double substitution, where the value of the rotational asymmetry parameter β is found to be larger in asymmetric $^{18}O^{18}O^{16}O$ than it is in symmetric $^{18}O^{16}O^{18}O$.

Another relevant feature, that has never been discussed in the literature on ozone before, is the value of parity splitting (Λ-doubling) due to the Coriolis coupling effect. These splittings, accurately captured by our calculations, were determined and examined here for $1 \leq \Lambda \leq 5$, for the four ozone isotopomers considered here. We found that these splittings are affected by isotopic substitutions as much as they are affected by molecular symmetry, namely: in the case of single isotopic substitution the splittings are larger in symmetric ozone $^{16}O^{18}O^{16}O$, but in the case of double isotopic substitution the splittings are larger in asymmetric ozone $^{18}O^{18}O^{16}O$. Again, one cannot claim that symmetry is a determining factor.

Then we checked how a “bulk” energy-averaged characteristic of the molecule, such as its rotational-vibrational partition function, is affected by the Coriolis coupling effect, and how much these partition functions are different in different isotopomers of ozone. Since it is expected that the number of allowed rovibrational states in asymmetric molecules would be twice larger than it is in symmetric molecules, we have chosen to use

the ratio of partition functions for asymmetric and symmetric ozone molecules to serve as a useful metric: $R = Q_{\mathrm{asym}}/Q_{\mathrm{sym}}$. Its value is expected to be close to $R = 2$, therefore any deviation would be considered as an isotope effect. We found, first of all, that for the temperatures below 500 K the effect of parity splittings on the ratio R is very small and thus the role of the Coriolis coupling is negligible. We also found that the accurately computed value of this metric deviates from the expected statistical $R = 2$, but the direction of this deviation depends on the number of isotopic substitutions. Namely, in the singly substituted case the ratio $^{16}O^{16}O^{18}O/^{16}O^{18}O^{16}O$ is larger than expected, while in the doubly substituted case the ratio $^{18}O^{18}O^{16}O/^{18}O^{16}O^{18}O$ is smaller than expected, in both cases by approximately the same amount, ±0.05. Although by itself this is an interesting isotope-related phenomenon, this effect is relatively small, and is driven by masses, not by the symmetry.

The data used in this chapter, including state energies, vibrational symmetries, parities p, isotopomer-specific assignments and the weights of all Λ-components for each ro-vibrational coupled state, are available from the archive file included in the Supplementary Information of Refs. 107 and 140.

CHAPTER 7. THE EFFECT OF ROTATION-VIBRATION COUPLING ON SCATTERING RESONANCES IN OZONE

In this chapter we use the theoretical framework outlined in Chapter 4 to calculate *scattering resonances* above dissociation threshold for four isotopically substituted ozone species: $^{16}O^{18}O^{16}O$, $^{16}O^{16}O^{18}O$, $^{18}O^{16}O^{18}O$ and $^{16}O^{18}O^{18}O$, for all values of the total angular momentum J from 0 to 4. To make these calculations numerically affordable, a modification of the theory in Chapter 4 is developed, which allows to employ one vibrational basis set, optimized for a typical rotational excitation (J, Λ), to run calculations at several desired values of J. In order to quantify the effect of Coriolis coupling, new data are contrasted with those computed using the symmetric-top rotor approximation, where the rotation-vibration coupling terms are neglected.

The effect of rotation-vibration coupling on the *bound* states of ozone (below the dissociation threshold) was studied in great detail, using both a semi-empirical model Hamiltonian,[138,145] and the first-principle calcualtions,[118,146] including the results, presented in Chapter 6.[107,140] There, we concluded that the observed effect of rotation-vibration coupling was not significantly different for symmetric and asymmetric isotopomers of ozone. This, however, might not hold true for the *scattering resonances* (above the dissociation threshold), whose properties are of much greater importance for the recombination reaction of ozone. Thus, in this manuscript we focus specifically on the properties of the scattering resonances.

Both scattering resonances and the effects of rotation-vibration coupling are computationally demanding in their own right, let alone when taken together. For this reason, the previous workers concerned with the scattering resonances in ozone,[50,51,93,147–

[149] did not take the rotation-vibration coupling into account. To the best of our knowledge, the data presented in this chapter is the first data on fully coupled rovibrational spectra of scattering resonances in $^{16}O^{18}O^{16}O$, $^{16}O^{16}O^{18}O$, $^{18}O^{16}O^{18}O$ and $^{16}O^{18}O^{18}O$, obtained entirely from the first-principle calculations. Importantly, in our calculations symmetric and asymmetric isotopomers of ozone (such as $^{16}O^{16}O^{18}O$ and $^{16}O^{18}O^{16}O$ in the case of single isotopic substitution) are addressed simultaneously, as the two isotopomers of the same molecule that can interconvert at high energies.

In the traditional (rotationally-adiabatic) basis approach, described in Chapter 4, one needs to compute a separate vibrational basis set for each Λ, since the basis set is adjusted to a specific rotational potential. Assessing computational cost of such approach, we found that in cases when vibrational basis set is large, which is necessary for calculation of scattering resonances, large portion of the overall cost comes from the necessity to compute a new vibrational basis set for each Λ and even larger portion from necessity to evaluate a new set of vibrational overlaps (Eq. (111)).

Here we present a modification of the original method that helps to carry out these calculations through the range of several values of the total angular momentum J in a more efficient way. A similar idea has been considered by Leforestier, but the theory has only been formulated for the case of Jacobi coordinates.[150] In the case of APH coordinates, another similar approach has been exploited in a context of the coupled-channel calculations of the reactive scattering,[151] but our approach is different and more efficient.

7.1. Rotationally Fixed Basis Method

The general theoretical framework of SpectrumSDT has been covered in detail in Chapter 4, where we considered traditional *rotationally-adiabatic* basis set. In this section we discuss the advantages and disadvantages of this approach, and introduce modifications to make the calculations more efficient for the case of scattering resonances.

Recall from Chapter 4 that the 2D vibrational basis functions $\mathrm{X}^{j}_{\Lambda n}(\theta,\varphi)$ have a dependency on J (implicit index) and Λ, due to the presence of rotational potential term $V^{\Lambda n}_{\mathrm{rot}}$ in Eq. (94). Such choice permits to take into account the effects of rotational excitation and distortion, by adjusting the 2D vibrational basis set $\mathrm{X}^{j}_{\Lambda n}$ adiabatically, to be optimized specifically for each individual rotational state of the symmetric-top rotor (J,Λ). This requires solving the 2D vibrational problem $J+1$ times for each value of J, which by itself is not computationally demanding. The advantage of this elegant traditional approach is that we always operate with the most optimal basis set, which is expected to give the fastest convergence (with respect to the basis set size) and thus produce the smallest Hamiltonian matrix.

The snag, however, is that one also needs to compute the overlap matrixes $\langle \mathrm{X}^{j}_{\Lambda n} | \mathrm{X}^{j'}_{\Lambda' n'} \rangle$ (Eq. (111)) for each such set of solutions. The functions $\mathrm{X}^{j}_{\Lambda n}$ are not analytical, so the overlaps have to be computed by explicit numerical integration and, for accurate calculations of the excited vibrational states or scattering resonances, the size of these matrices can be rather large. We found that in practice the computational cost of this integration far outweighs the advantage of having a slightly smaller Hamiltonian matrix when vibrational basis set is large.

One way to circumvent this issue is to use the same set of 2D vibrational basis functions X_n^j for all values of J and Λ (note that index Λ does not appear anymore since all functions X_n^j have the same value of Λ here). One natural choice is to use basis functions obtained for the non-rotating molecule, $J = 0$ and $\Lambda = 0$, which has a simple physical motivation: the energy of rotational excitation (the "lift" of the potential energy surface (PES) that the molecule experiences as it rotates) is typically smaller than the vibrational energy of the molecule (the depth of the PES itself). Therefore, inclusion of the rotational excitation can be considered as a perturbation to the purely vibrational problem, and the basis set optimized for a non-rotating molecule should in principle be suitable. One downside of this approach is that at large values of J the number of basis functions X_n^j, needed for convergence of results, may be higher compared to the rotationally-adiabatic choice of the basis.

The most straightforward way to define a basis set for non-rotating molecule is to simply move the rotational potential term out of the definition of $\widehat{H}_{2\mathrm{D}}^n$, so that Eq. (94) becomes:

$$\widehat{H}_{2\mathrm{D}}^n = \hat{T}_\theta^n + \hat{T}_\varphi^n + V_{\mathrm{pes}}^n + V_{\mathrm{ext}}^n \tag{134}$$

and Eq. (93) becomes:

$$\begin{aligned}\langle h_n \mathrm{X}_n^j \widetilde{D}_\Lambda \big| \widehat{H} \big| h_{n'} \mathrm{X}_{n'}^{j'} \widetilde{D}_{\Lambda'} \rangle = {} & \langle h_n \big| \hat{T}_\rho \big| h_{n'} \rangle \langle \mathrm{X}_n^j | \mathrm{X}_{n'}^{j'} \rangle \, \tilde{\delta}_{\Lambda\Lambda'} \\ & + \langle \mathrm{X}_n^j \big| \widehat{H}_{2D}^n \big| X_n^{j'} \rangle \, \delta_{nn'} \tilde{\delta}_{\Lambda\Lambda'} + \langle \mathrm{X}_n^j | V_{\mathrm{rot}}^{\Lambda n} | \mathrm{X}_n^{j'} \rangle \, \delta_{nn'} \tilde{\delta}_{\Lambda\Lambda'} \\ & + \langle h_n \mathrm{X}_n^j \widetilde{D}_\Lambda | \hat{T}_{\mathrm{asym}} + \hat{T}_{\mathrm{cor}} | h_{n'} \mathrm{X}_{n'}^{j'} \widetilde{D}_{\Lambda'} \rangle\end{aligned} \tag{135}$$

In a way similar to the derivations in section 4.3.1, one can show that:

$$\langle \mathrm{X}_n^j | V_{\mathrm{rot}}^{\Lambda n} | \mathrm{X}_n^{j'} \rangle = \hbar^2 \left(J(J+1) \langle \mathrm{X}_n^j | \frac{A_n + B_n}{2} | \mathrm{X}_n^{j'} \rangle + \Lambda^2 \langle \mathrm{X}_n^j | C_n - \frac{A_n + B_n}{2} | \mathrm{X}_n^{j'} \rangle \right) \tag{136}$$

Note, that the matrix of Eq. (136) is diagonal in n and Λ due to the $\delta_{nn'}\tilde{\delta}_{\Lambda\Lambda'}$ factor in Eq. (135). The asymmetric-top rotor term $\hat{T}_{\mathrm{asym}}$ and the Coriolis term $\hat{T}_{\mathrm{cor}}$ are treated as before.

The basis set X_n^j of the non-rotating molecule $(J,\Lambda) = (0,0)$ can be efficient and sufficient for the ro-vibrational calculations at small values of J. However, for prediction of thermal reaction rates at room temperature one often has to deal with rotational states up to $J_{\mathrm{max}} \sim 100$. For ozone recombination reaction in particular, the calculations of rotational states up to $J_{\mathrm{max}} \sim 50$ are desirable. If the calculations for all these values of J and Λ are to be carried out with the same basis set, it would certainly make more sense to choose one that corresponds to the values of J and Λ somewhere in the middle of the broad range of rotational excitations.

Let us say that we optimized one basis set X_n^j for a chosen pair of $(J,\Lambda) = (J_{\mathrm{bs}},\Lambda_{\mathrm{bs}})$ ("bs" = "basis set"), picked somewhere in the range $0 \le J_{\mathrm{bs}} \le J_{\mathrm{max}}$ and $0 \le \Lambda_{\mathrm{bs}} \le J_{\mathrm{bs}}$ based on physical intuition, energy considerations, or some kind of a convergence study (note that the values of J_{bs} and Λ_{bs}, selected for the basis functions X_n^j, are in general different from the values of J and Λ for the overall problem). The corresponding value of the vibrating symmetric-top rotor energy $V_{\mathrm{rot}}^{\Lambda_{\mathrm{bs}}}$ will be denoted as $V_{\mathrm{rot}}^{\mathrm{bs}}$.

To achieve the desired effect, we simply add $V_{\mathrm{rot}}^{\mathrm{bs}}$ to Eq. (134) and subtract it from the symmetric-top rotor term in Eq. (135), i.e. Eqs. (134) and (135) become:

$$\hat{H}_{\mathrm{2D}}^n = \hat{T}_\theta^n + \hat{T}_\varphi^n + V_{\mathrm{pes}}^n + V_{\mathrm{ext}}^n + V_{\mathrm{rot}}^{\mathrm{bs},n} \tag{137}$$

and

$$\begin{aligned}\langle h_n \mathrm{X}_n^j \widetilde{D}_\Lambda | \widehat{H} | h_{n'} \mathrm{X}_{n'}^{j'} \widetilde{D}_{\Lambda'} \rangle = {} & \langle h_n | \widehat{T}_\rho | h_{n'} \rangle \langle \mathrm{X}_n^j | \mathrm{X}_{n'}^{j'} \rangle \tilde{\delta}_{\Lambda\Lambda'} \\ & + \langle \mathrm{X}_n^j | \widehat{H}_{2D}^n | \mathrm{X}_n^{j'} \rangle \delta_{nn'} \tilde{\delta}_{\Lambda\Lambda'} \\ & + \langle \mathrm{X}_n^j | V_{\mathrm{rot}}^{\Lambda n} - V_{\mathrm{rot}}^{\mathrm{bs},n} | \mathrm{X}_{n'}^{j'} \rangle \delta_{nn'} \tilde{\delta}_{\Lambda\Lambda'} \\ & + \langle h_n \mathrm{X}_n^j \widetilde{D}_\Lambda | \hat{T}_{\mathrm{asym}} + \hat{T}_{\mathrm{cor}} | h_{n'} \mathrm{X}_{n'}^{j'} \widetilde{D}_{\Lambda'} \rangle \end{aligned} \tag{138}$$

The goal of this swap of terms is to compensate for the centrifugal lift of the chosen basis set, permitting to predict ro-vibrational energies for any rotational excitation J, which can be both smaller ($J < J_{\mathrm{bs}}$) or larger ($J \geq J_{\mathrm{bs}}$) than that of the chosen basis set.

Incorporating these results into the final expression for the Hamiltonian matrix element in terms of the expansion coefficients of 1D (a_{nlm}^i) and 2D (b_{nli}^j) basis functions (as in Eq. (119)) we obtain:

$$\begin{aligned} & \langle h_n \mathrm{X}_n^j \widetilde{D}_\Lambda | \widehat{H} | h_{n'} \mathrm{X}_{n'}^{j'} \widetilde{D}_{\Lambda'} \rangle \\ & = \tilde{\delta}_{\Lambda\Lambda'} \left(\langle h_n | \hat{T}_\rho | h_{n'} \rangle \sum_l^L \sum_m^M O_{nn'lm}^j + \delta_{nn'} \delta_{jj'} \varepsilon_n^j \right) \\ & + \frac{\hbar^2}{4} U_{\Lambda\Lambda'} \delta_{nn'} \sum_l^L (A_{nl} - B_{nl}) \sum_m^M O_{nlm}^j \\ & + (-1)^{\Lambda+s} 2\hbar^2 W_{\Lambda\Lambda'} \delta_{nn'} \sum_l^L B_{nl} \cos\theta_l \sum_m^M m O_{nlm}^j \\ & + \hbar^2 \tilde{\delta}_{\Lambda\Lambda'} \delta_{nn'} \times \left(\left(\frac{J(J+1) - J_{\mathrm{bs}}(J_{\mathrm{bs}}+1)}{2} \right) \sum_l^L (A_{nl} + B_{nl}) \sum_m^M O_{nlm}^j \right. \\ & \left. + (\Lambda^2 - \Lambda_{\mathrm{bs}}^2) \sum_l^L \left(C_{nl} - \frac{A_{nl} + B_{nl}}{2} \right) \sum_m^M O_{nlm}^j \right) \end{aligned} \tag{139}$$

where $O_{nn'lm}^j$ is the same as in Eq. (120), except it does not depend on Λ anymore:

$$O^{j}_{nn'lm} = \left(\sum_{i}^{S_{nl}} b^{j}_{nli} a^{i}_{nlm}\right)\left(\sum_{i'}^{S_{n'l}} b^{j'}_{n'li'} a^{i'}_{n'lm}\right) \tag{140}$$

7.2. Overview of Computed Data

The methodology described in the previous section was utilized to compute all coupled rotational-vibrational states of singly and doubly substituted ozone molecules up to the energy of 1000 cm^{-1} above the dissociation threshold for five values of the total angular momentum $0 \leq J \leq 4$ and with all values of Λ included. The reference basis set X^{j}_{n} was optimized for $J = 4$ and $\Lambda = 2$. Only the states with positive energy (scattering resonances above dissociation threshold) were considered in the following analysis (around 80000 states total). A complex absorbing potential (CAP) in the form suggested by Manolopoulos[152] was used to impose the boundary conditions. The CAP was defined with the minimum absorption energy $E_{\min} = 7$ cm^{-1} and spans the range of ~6 Bohr from the end of the ρ-grid. The optimized DVR-grid for ρ coordinate covered the range of $3 \leq \rho \leq 20$ Bohr and consisted of 94 functions total. An equidistant DVR grid for θ covered the range $0.43 \leq \theta \leq 1.56$ rad with a total of 100 functions. The number of VBR functions for φ coordinate was 200 and the value of basis cut-off energy was set to 6000 cm^{-1}.

For every resonance we computed its energy E_i and width Γ_i, which determines its lifetime through $\tau_i = \hbar/\Gamma_i$, and the decay rate $k_i = \Gamma_i/\hbar$. The states with widths > 50 cm^{-1} as well as the states contributing less than 0.02 to Q (computed by setting $p_i = p_i^{\mathrm{SYM}} + p_i^{\mathrm{ASYM}} + p_i^{\mathrm{VdW(S)}} + p_i^{\mathrm{VdW(A)}} + p_i^{\mathrm{VdW(B)}}$, the total probability) were excluded from the analysis as unphysical artefacts. The meaning of Q and p_i is explained further in this chapter (section 7.4).

It is nearly impossible to converge every individual state above the dissociation threshold. Therefore, our convergence parameters, including position of the CAP, were adjusted to ensure convergence of the overall dynamical partition function of the molecule (Q, as defined further in section 7.4) to within 1%. Convergence of the individual states depends on their properties. Broad resonances with $\Gamma \sim 10$ cm^{-1} are converged to within 1 cm^{-1} or better (both energy and width). Narrower resonances are converged much better. Convergence of broader resonances is not important, since they make negligibly small contributions to the dynamical partition function Q (their weights w_i are close to 1, but their probabilities p_i are close to 0).

Moreover, in order to have more information about the nature of each state, we integrated the modulus squared of its wave function over five specific regions of the PES, indicated by color in Figure 50. The resultant five probabilities are also listed in Table 34 for the case of singly substituted ozone molecule. For the doubly substituted case, the labelling of regions in Figure 50 and Table 34 is analogous and can be obtained simply by changing all ^{16}O isotopes to ^{18}O and vice versa.

Note that VdW(A) is separated from VdW(S) by a potential energy barrier on the PES. The corresponding isomers do not interconvert freely, and therefore should both be defined and included into consideration separately. This is particularly important since one of them is associated with symmetric, while the other one with asymmetric ozone molecule, even though asymptotically they both merge into a single dissociation channel.

Table 34: Definitions of five probabilities computed for each ro-vibrational state of ozone.

Color in Figure 50	Meaning	Probability label
Dark green	Covalently bound symmetric ozone molecule $^{16}O^{18}O^{16}O$	p_i^{SYM}
Violet	Covalently bound asymmetric ozone molecules $^{16}O^{16}O^{18}O$	p_i^{ASYM}
Turquoise	Van der Waals complex in the ^{16}O + $^{16}O^{18}O$ channel, near asymmetric $^{16}O^{16}O^{18}O$	$p_i^{\mathrm{VdW(A)}}$
Light green	Van der Waals complex in the $^{16}O^{18}O$ + ^{16}O channel, near symmetric $^{16}O^{18}O^{16}O$	$p_i^{\mathrm{VdW(S)}}$
Pink	Van der Waals complexes in the $^{16}O^{16}O$ + ^{18}O channel	$p_i^{\mathrm{VdW(B)}}$

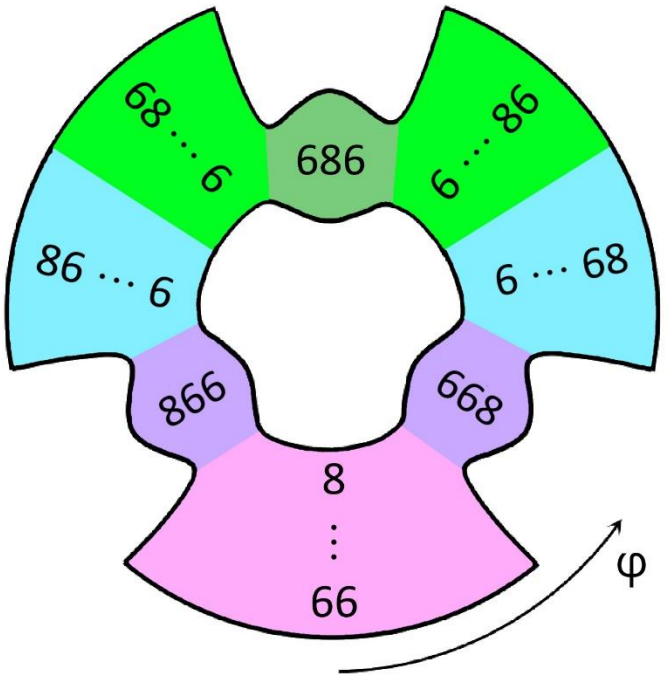

Figure 50. A schematic representation of the PES of ozone in APH coordinates, labelled for the case of a singly substituted molecule. Three tight deep wells correspond to the covalently bound ozone molecules: $^{16}O^{18}O^{16}O$ (single well) and $^{16}O^{16}O^{18}O$ (double well). Five broad and shallow plateaus correspond to the weakly bound van der Waals complexes: $^{16}O^{18}O\cdots{}^{16}O$, $^{16}O^{16}O\cdots{}^{18}O$ and $^{16}O\cdots{}^{16}O^{18}O$ (double-well each). The meaning of colors is summarized in Table 34. The arrow shows direction of change of φ-coordinate.

The exact definitions of the regions in Figure 50 are as follows. The covalent wells of the symmetric and asymmetric molecules are defined as the regions of PES with $120° \leq \varphi \leq 240°$ and $240° \leq \varphi \leq 120°$ respectively, and the values of ρ up to the position of the centrifugal barrier between the covalent and Van der Waals wells, which is generally situated around $\rho = 5.5$ Bohr. The exact position of the barrier was computed accurately based on the analysis of 2D basis functions $\mathrm{X}_n^j(\theta, \varphi)$ and depends on J, Λ and a specific pathway under consideration.

The Van der Waals wells B, A and S are defined as the regions with the values of ρ from the border between the covalent and Van der Waals wells to 11 Bohr and the following values of φ:

- $-60° \leq \varphi \leq 60°$ for VdW B
- $60° \leq \varphi \leq \varphi_{bar}$ or $-\varphi_{bar} \leq \varphi \leq -60°$ for VdW A
- $\varphi_{bar} \leq \varphi \leq 360° - \varphi_{bar}$ for VdW S

The values of barrier position between VdW A and S (φ_{bar}) was found numerically by scanning the PES and are equal to $\varphi_{bar} = 117.65°$ for the singly substituted and $\varphi_{bar} = 122.35°$ for the doubly substituted ozone isotopologues. The area beyond 11 Bohr is considered a fully dissociated molecule and integrated separately from the Van der Waals area.

The complete set of data computed for this chapter can be found in Ref. 153.

7.3. Distribution of State Properties

We found that the complexity of the PES of ozone is responsible for the appearance of a broad distribution of properties of its states. An overview of these properties is presented in Figure 51, where each point corresponds to one computed ro-vibrational state.

The two axes give the total covalent ($p_i^{\mathrm{SYM}} + p_i^{\mathrm{ASYM}}$) and total Van der Waals ($p_i^{\mathrm{VdW(A)}} + p_i^{\mathrm{VdW(B)}} + p_i^{\mathrm{VdW(S)}}$) probabilities. Color reflects the value of Γ_i (on a log scale).

From Figure 51 we can see that both singly and doubly substituted ozone molecules exhibit broad distributions of state properties. The lower right corner of each frame corresponds to mainly covalent states, while the upper left corner corresponds to mainly Van der Waals (VdW) states, and we see that both kinds of resonance states are possible in ozone.

The five probabilities defined in Table 34 and used to plot Figure 51 correspond to contiguous regions on the PES, so, whenever they do not add up to 1, the remaining probability corresponds to the asymptotic part of the PES (dissociation channels). Qualitatively, the more a point deviates from the diagonal in Figure 51, the more probability in the dissociation region it has. In particular, the points near the origin have all their probability in the dissociation region and correspond to the continuum of free particle states, while the points on the diagonal have no probability in the dissociation region and correspond to the bound states.

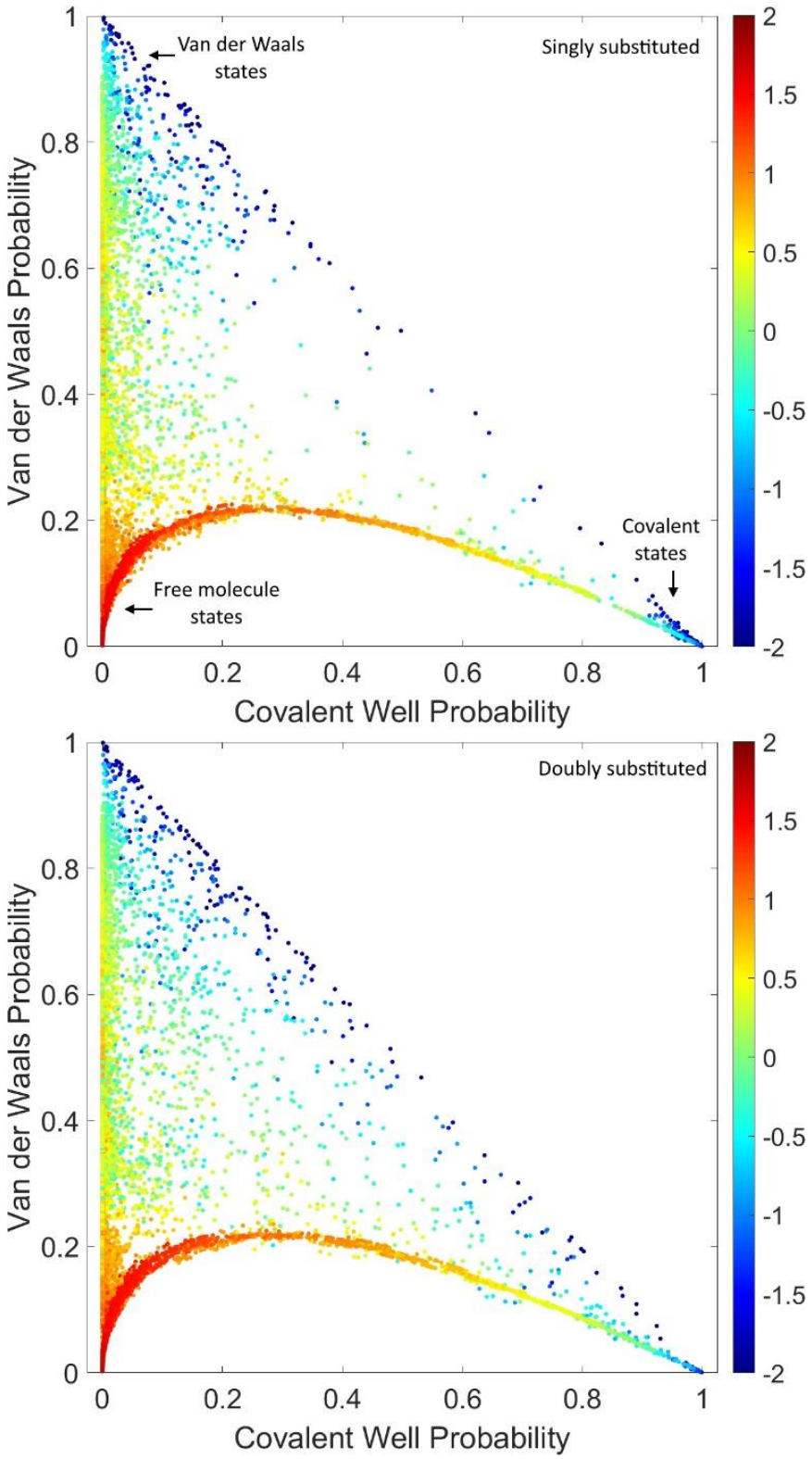

Figure 51. Distribution of the covalent and Van der Waals probabilities for scattering resonances in the singly substituted (upper frame) and doubly substituted (lower frame) molecules of ozone, based on the coupled ro-vibrational calculations up to $J = 4$. Color corresponds to decimal logarithm of the resonance width (Γ_i, in cm^{-1}), as indicated by the color bar.

Finally, note the absence of any states along the horizontal axis in Figure 51. Any hypothetical state there would need to have significant probabilities in the covalent and dissociation regions, while having zero probability in the VdW region. The covalent and dissociation regions are separated by VdW region, so it comes as no surprise that all the actual states that have non-zero probability in covalent and dissociation regions simultaneously, also have non-zero probability in VdW region.

Tracking the points from right to left along the edge of this empty area in the right half of the plot, one can see that any probability "missing" from the covalent region gets redistributed between VdW and dissociation regions rather uniformly, taking into account that the dissociation region is about 60% larger than VdW. The same does not hold true in the left half of the plot, where the points along the edge start having more probability in the dissociation region compared to the VdW region.

The typical values of resonance widths vary through four orders of magnitude range, $10^{-2} \leq \Gamma_i \leq 10^{2}$ cm^{-1}. Narrower (longer lived) states are shown by blue points in Figure 51, and are found mainly in the covalent corner, in the VdW corner, and along the diagonal line that connects them. They correspond to the relatively stable states, not coupled to the asymptotic region of free particle states, which explains their stability. Broader (short lived) states are shown by red points, and are found mainly near the origin, which corresponds to the mostly free-particle states, which also makes sense. Note that the states with substantial VdW probability (around 0.5) appear to be longer-lived (they have smaller gammas) than the states with the same probabilities in the covalent region.

7.4. Average Properties of Scattering Resonances

Since different resonances exhibit rather different properties, it is useful to average those over the distribution, in order to obtain a small set of representative values (which can be used for comparison of different isotopomers of ozone, for example). In order to be meaningful, this should be a weighted average that takes into account the importance of a given scattering resonance in the ozone recombination reaction. Building upon the previous work,[51] we define the weight of each state i in the average as its contribution to the corresponding partition function:

$$Q_i = p_i^{\mathrm{mol}} w_i \exp\left(-\frac{E_i}{kT}\right) \tag{141}$$

In what follows, the average values will be computed separately for the covalent and the VdW states, for symmetric and asymmetric ozone isotopomers, and for the singly and doubly substituted ozone isotopologues. Therefore, the first factor in Eq. (141) is introduced to separate contributions to different molecules and corresponds to the state's probability p_i associated with a given region on the PES, as defined in Table 34.

The second factor in Eq. (141) is a weight w_i, defined as:

$$w_i = \frac{\Gamma_i/\hbar}{\Gamma_i/\hbar + [\mathrm{M}]k_i^{\mathrm{stab}}} \tag{142}$$

This weight is based on the standard Lindeman mechanism of recombination[154] and accounts for state population at a given pressure of bath gas, which lets one to give higher weights to wider states that are naturally more important for the recombination reaction. The lower the pressure, the less restrictive this factor is. For example, in the limit of zero pressure, all states would be equally important regardless of their widths.

For stabilization rate coefficient k_i^{stab}, we use a simple model introduced previously.[51] Namely, the value of k_i^{stab} is calculated as:

$$k_i^{\mathrm{stab}} = \sigma^{\mathrm{stab}} v (p_i^{\mathrm{SYM}} + p_i^{\mathrm{ASYM}}) \tag{143}$$

where σ^{stab} is the stabilization cross-section taken from Ref. 53 as $\sigma^{\mathrm{stab}} = 154.0326\ a_0^2$, and v is the average speed of O_3 + Ar system:

$$v = \sqrt{\frac{8kT}{\pi \mu_{\mathrm{stab}}}} \tag{144}$$

where μ_{stab} is the reduced mass of O_3 + Ar system:

$$\mu_{\mathrm{stab}} = \frac{\mathrm{m}(\mathrm{O_3})\mathrm{m}(\mathrm{Ar})}{\mathrm{m}(\mathrm{O_3}) + \mathrm{m}(\mathrm{Ar})} \tag{145}$$

where $\mathrm{m}(\mathrm{O_3})$ and $\mathrm{m}(\mathrm{Ar})$ are the masses of O_3 and Ar, respectively.

The last thing in Eq. (141) is the Boltzmann factor at given temperature. Here and further in this chapter we assume the conditions that correspond to the experiments of Mauersberger group with $[\mathrm{M}] = 267$ hPa (about 0.3 Bar) and $T = 298\mathrm{K}$.[36,38]

All three factors in Eq. (141) vary between zero and one, so the value of Q_i is also less than one. Importantly, the sum of Q_i over the states of a given molecule represents its *dynamical partition function*:[51]

$$Q = \sum Q_i \tag{146}$$

The "*dynamical*" prefix here is used to stress that it depends on dynamical factors, such as lifetime of the states, as well as on pressure and temperature. It is important to take into account these factors since they play a crucial role in the ozone recombination reactions.

Note that here we report the values of vibrational partition functions Q per rotational state (of a symmetric top rotor, i.e. divided by the number of rotational Λ-blocks in the ro-vibrational calculation). Space degeneracy (factor of $2J+1$) is also not taken into account in order to facilitate comparison between different values of J. Additionally, the values of Q for asymmetric ozone isotopomers are divided by 2, to account for the number of wells and put all partition functions values on the same scale.

The dynamical partition functions Q and other related properties are presented in Tables 35-37. In Table 35, the values of Q were computed for resonances localized in covalent wells, by setting $p_i^{\mathrm{mol}} = p_i^{\mathrm{SYM}}$ for symmetric isotopomers (columns 2 and 4) and $p_i^{\mathrm{mol}} = p_i^{\mathrm{ASYM}}$ for asymmetric isotopomers (columns 3 and 5) in Eq. (141). In Table 36, the values of Q were computed for resonances localized in VdW wells, by using $p_i^{\mathrm{mol}} = p_i^{\mathrm{VdW(B)}}$ for homonuclear dissociation channel (columns 2 and 4) and $p_i^{\mathrm{mol}} = p_i^{\mathrm{VdW(A)}} + p_i^{\mathrm{VdW(S)}}$ for heteronuclear dissociation channel (columns 3 and 5). In Table 37, the values of Q were computed with contributions from both covalent and Van der Waals wells, by setting $p_i^{\mathrm{mol}} = p_i^{\mathrm{SYM}} + p_i^{\mathrm{VdW(S)}}$ for symmetric isotopomers (columns 2 and 4) and $p_i^{\mathrm{mol}} = p_i^{\mathrm{ASYM}} + p_i^{\mathrm{VdW(A)}} + p_i^{\mathrm{VdW(B)}}$ for asymmetric isotopomers (columns 3 and 5).

The first row of these tables lists considered isotopomers, and the main question here is how the symmetric and asymmetric ozone molecules compare and contrast. In the second row we report the weighted average values of the resonance width, computed as:

$$\tilde{\Gamma} = \frac{\sum Q_i \Gamma_i}{\sum Q_i} = \frac{\sum Q_i \Gamma_i}{Q} \tag{147}$$

The corresponding partition functions Q are reported in the third row. Rows 4 to 6 report several other weighted average properties, calculated in a way similar to Eq. (147). Namely, the average wavefunction probability is given by:

Table 35. Average properties of scattering resonances localized over the covalent wells of ozone, computed for various isotopic substitutions based on the coupled ro-vibrational calculations for all J up to $J = 4$. The data in parentheses correspond to the approximate symmetric-top rotor treatment.

	$^{16}O^{18}O^{16}O$	$^{16}O^{16}O^{18}O$	$^{18}O^{16}O^{18}O$	$^{16}O^{18}O^{18}O$
$\tilde{\Gamma}$, cm^{-1}	3.12 (3.19)	3.29 (3.36)	2.06 (2.14)	3.05 (3.16)
Q	4.66 (4.53)	4.54 (4.41)	5.86 (5.65)	5.12 (4.93)
$\tilde{p}$	0.532 (0.552)	0.528 (0.541)	0.575 (0.600)	0.499 (0.522)
$\tilde{Q}_i$	0.230 (0.242)	0.241(0.245)	0.254 (0.266)	0.238 (0.248)
$\tilde{N}$	20.4 (18.9)	18.8 (18.0)	23.1 (21.3)	21.5 (20.0)
η	0.975 (0.974)		0.874 (0.873)	

Table 36. Same as Table 35, but for the scattering resonances localized over Van der Waals plateaus.

	$^{16}O^{16}O\cdots^{18}O$	$^{16}O\cdots^{16}O^{18}O$ and $^{16}O^{18}O\cdots^{16}O$	$^{16}O\cdots^{18}O^{18}O$	$^{16}O^{18}O\cdots^{18}O$ and $^{18}O^{16}O\cdots^{18}O$
$\tilde{\Gamma}$, cm^{-1}	6.01 (6.10)	7.20 (7.25)	7.03 (7.18)	6.12 (6.19)
Q	17.1 (16.7)	17.0 (16.7)	18.2 (17.7)	17.7 (17.4)
$\tilde{p}$	0.458 (0.473)	0.397 (0.408)	0.346 (0.360)	0.427 (0.443)
$\tilde{Q}_i$	0.299 (0.304)	0.270 (0.275)	0.224 (0.230)	0.275 (0.282)
$\tilde{N}$	57 (55.1)	63.4 (61.2)	81.6 (77.6)	64.5 (61.7)

Table 37. Same as Table 35, but for both covalent and VdW regions together.

	$^{16}O^{18}O^{16}O$	$^{16}O^{16}O^{18}O$	$^{18}O^{16}O^{18}O$	$^{16}O^{18}O^{18}O$
$\tilde{\Gamma}$, cm^{-1}	6.24 (6.30)	5.95 (6.02)	5.04 (5.12)	5.83 (5.95)
Q	21.8 (21.3)	21.6 (21.1)	23.2 (22.7)	23.3 (22.6)
$\tilde{p}$	0.328 (0.333)	0.451 (0.455)	0.366 (0.374)	0.430 (0.431)
$\tilde{Q}_i$	0.192 (0.194)	0.278 (0.274)	0.207 (0.210)	0.266 (0.260)
$\tilde{N}$	114 (111)	77.7 (77.0)	112 (109)	(87.1)
η	0.991 (0.992)		1.00 (0.999)	

$$\tilde{p} = \frac{\sum Q_i p_i^{\mathrm{mol}}}{Q} \tag{148}$$

where the values of p_i^{mol} are calculated for different columns as described above.

The average contribution of one resonance to a partition function is given by:

$$\tilde{Q}_i = \frac{\sum Q_i Q_i}{Q} = \frac{\sum Q_i^2}{Q} \tag{149}$$

And the average "number of resonances" is given by:

$$\widetilde{N} = \frac{Q}{\tilde{Q}_i} = \frac{Q^2}{\sum Q_i^2} = \frac{(\sum Q_i)^2}{\sum Q_i^2} \tag{150}$$

Note, that $\widetilde{N}$ is not literally a number of resonances, but rather a factor relating Q and $\tilde{Q}_i$, which can be roughly thought of as a "number of resonances" (and such terminology will be used in this paper), but one should still be careful with its interpretation.

Finally, the last row of Tables 35 and 37 gives the value of η-effect, defined as the ratio between of the values of Q, computed for symmetric and asymmetric isotopomers. Namely:

$$\eta = \frac{Q(^{16}\mathrm{O}^{16}\mathrm{O}^{18}\mathrm{O})}{Q(^{16}\mathrm{O}^{18}\mathrm{O}^{16}\mathrm{O})} \tag{151}$$

for single substitution, and

$$\eta = \frac{Q(^{18}\mathrm{O}^{18}\mathrm{O}^{16}\mathrm{O})}{Q(^{18}\mathrm{O}^{16}\mathrm{O}^{18}\mathrm{O})} \tag{152}$$

for double substitution.

For ozone resonances localized over the covalent well we found that average values $\tilde{\Gamma}$ in asymmetric ozone molecules are larger than those in symmetric ones, by 5.5% in the case of single and by as much as 48% in the case of double substitution (see

Table 35). We attribute it to the fact that the well on the PES that hosts the symmetric ozone molecule (see Figure 50), and the vibrational wave functions that sit in this well, are always symmetric with respect to the well's dissociation channels ($^{16}O + {}^{18}O^{16}O$ and $^{16}O^{18}O + {}^{16}O$ in singly-substituted case), i.e. each such wave function must decay equally into these channels. In contrast, the double-wells on the PES that host asymmetric ozone molecules are slightly tilted, which introduces asymmetry into the vibrational wave functions. Some of these states lean more towards one channel (say $^{16}O + {}^{16}O^{18}O$) and dissociate primarily into it, while other states lean more towards the other channel ($^{16}O^{16}O + {}^{18}O$). Overall, such asymmetric dissociation appears to be more efficient, and this is observed for the states localized over the covalent wells in both singly and doubly substituted molecules. Therefore the "driving force" of this effect is symmetry, not mass.

Interestingly, scattering resonances distributed over the VdW plateau of the PES behave differently. In the case of single substitution, VdW states in the asymmetric channel ($^{16}O + {}^{16}O^{18}O$) exhibit larger values of $\tilde{\Gamma}$ than those in the symmetric channel ($^{16}O^{16}O + {}^{18}O$) by 20%. But in the case of double substitution the picture is reversed and VdW states in the asymmetric channel ($^{16}O^{18}O + {}^{18}O$) exhibit smaller values of $\tilde{\Gamma}$ than those in the symmetric channel ($^{16}O + {}^{18}O^{18}O$) by 13%. Explanation for this "flip" is that the VdW states, located in the channel region of the PES, are primarily influenced by the value of asymptotic vibrational zero-point energy (ZPE) of the channel. In the case of single substitution the asymmetric channel is deeper, because $ZPE(^{16}O^{18}O) < ZPE(^{16}O^{16}O)$, but in the case of double substitution the symmetric channel is deeper, because $ZPE(^{16}O^{18}O) > ZPE(^{18}O^{18}O)$. The decay of resonances into a deeper channel is

always more efficient, and therefore for the VdW states the "driving force" of the effect is mass, rather than symmetry.

Comparing Tables 35 and 36, one notices that the values of $\tilde{\Gamma}$ for VdW states are much larger than those for the covalent states, by a factor of ×2 to ×3. This makes sense, since resonances located in the long-range part of the PES are expected to decay faster. This might seem to contradict the results in Figure 51, but keep in mind that the weight function of Eq. (141) favors certain states more than others, which makes the direct comparison of these quantities from Figure 51 non-trivial. Also from Tables 35 and 36, one can clearly see that the partition functions Q of resonances distributed over the VdW parts of the PES are significantly larger than those of the resonances localized over the covalent wells, by a factor of ×3 to ×4.

At present time it is not entirely clear what is the role of the VdW states of ozone in the recombination process,[120,149,155] but here, as a limiting case, we will compute the average values for resonances of both kinds put together. The results of this are presented in Table 37, where one can clearly see that when the covalent and the VdW resonances are both accounted, the values of partition functions Q for symmetric and asymmetric ozone species equalize (to within less than 1% difference), in both singly and doubly substituted cases. It was not the case when only the covalent well probabilities were included into Q, as one can see from Table 35, where asymmetric ozone molecules exhibited smaller Q than the symmetric ones, by 3% and 13% in the cases of single and double substitutions, respectively.

As for the values of average resonance widths $\tilde{\Gamma}$, the mass-driven pattern, associated with the VdW states (Table 36), dominates over the symmetry-driven pattern,

associated with the covalent states (Table 35), which comes as no surprise, since the values of partition function Q are much larger in the case of the VdW states. Namely, in the singly substituted case, the values of $\tilde{\Gamma}$ for asymmetric molecules are smaller by 5% than those for symmetric molecules, but this is opposite in the doubly substituted case, where the values of $\tilde{\Gamma}$ for asymmetric molecules are larger by 15%.

7.5. Influence of Rotational Excitation

The values presented in Tables 35-37 are computed based on all available values of J ($J \leq 4$). However, it is also instructive to study how these values evolve as function of J in order to understand how much they can change for larger values of J.

In Figures 52, 54 and 56 we reported $Q(J)$ and $\tilde{\Gamma}(J)$ dependencies, obtained in the same way as in Tables 35-37, but for each value of J separately. One can see that in Figures 54 and 56 the values of $Q(J)$ gradually decrease, as expected due to increase in centrifugal barrier that separates the lowest-energy covalent states in the vicinity of the dissociation threshold from the dissociation area, therefore reducing their width-factor w_i (Eq. (141)) and making them contribute less to Q. Looking at the values of $\tilde{\Gamma}(J)$, one can see that the largest change is often observed for going from $J = 0$ to $J = 1$, after which they decrease slower and rather monotonic, for the same reasons as $Q(J)$. Interestingly, these trends are less pronounced in the case of covalent states (Figure 52). The remaining properties are discussed in the following sections.

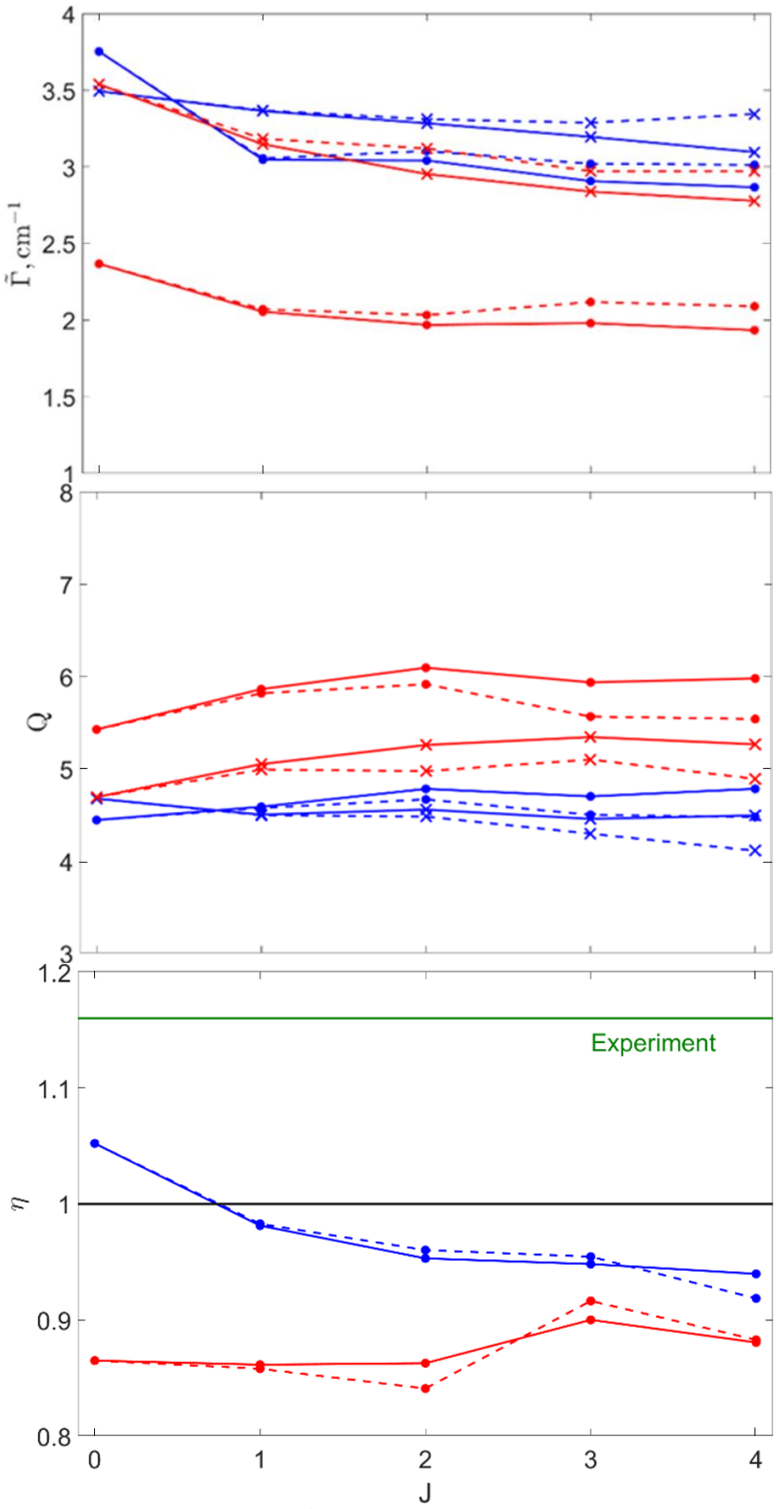

Figure 52. Average resonance width ($\tilde{\Gamma}$), partition function (Q) and η-effect of scattering resonances in ozone as a function of rotational excitation up to $J = 4$, for the states localized over the covalent well (as in Table 35). The blue (red) color corresponds to the singly (doubly) substituted isotopologues of ozone. The dots (x-symbols) correspond to symmetric (asymmetric) isotopomers. The solid (dashed) lines correspond to the exact coupled rotation-vibration (approximate symmetric-top rotor) calculations.

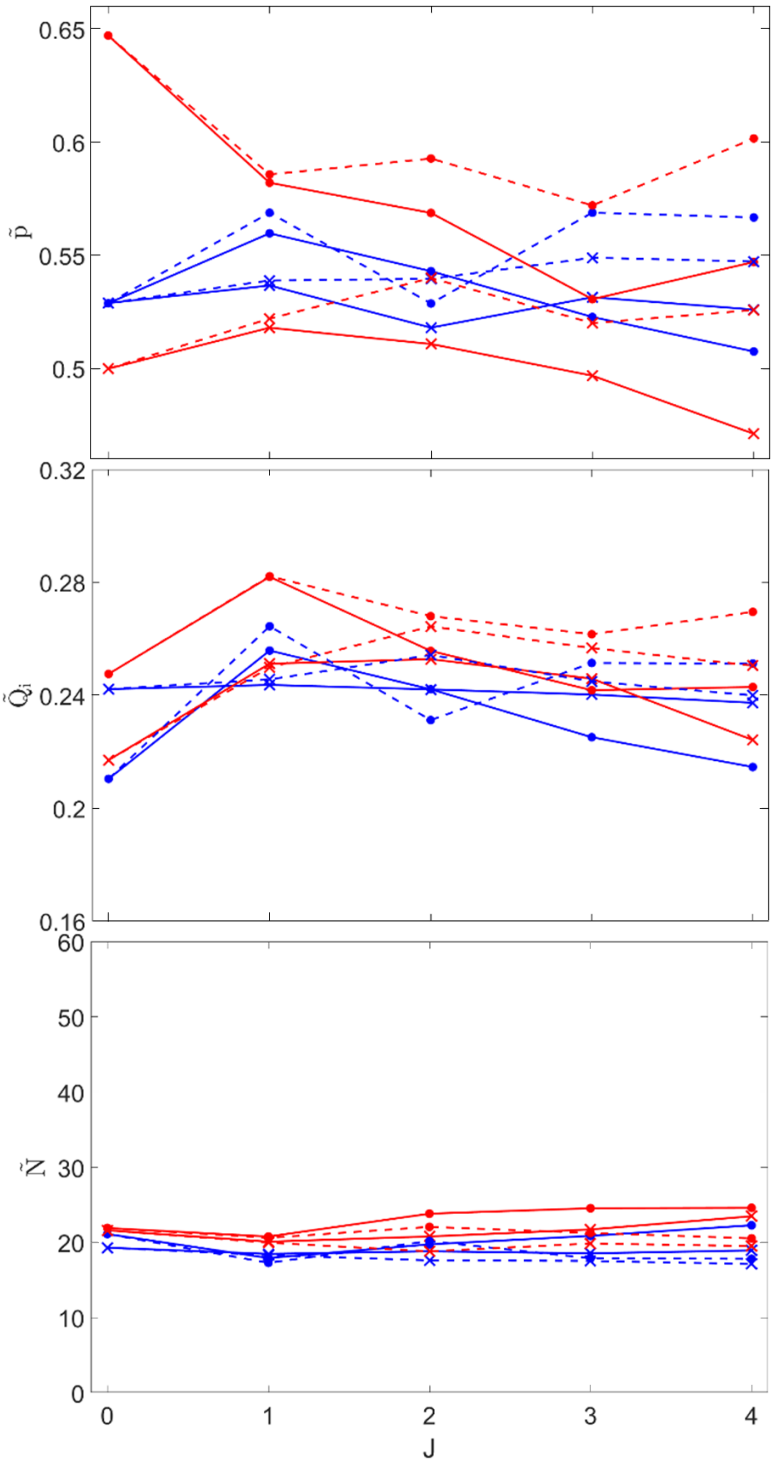

Figure 53. Same as Figure 52, but for the values of $\tilde{p}$, $\tilde{Q}_i$ and $\tilde{N}$.

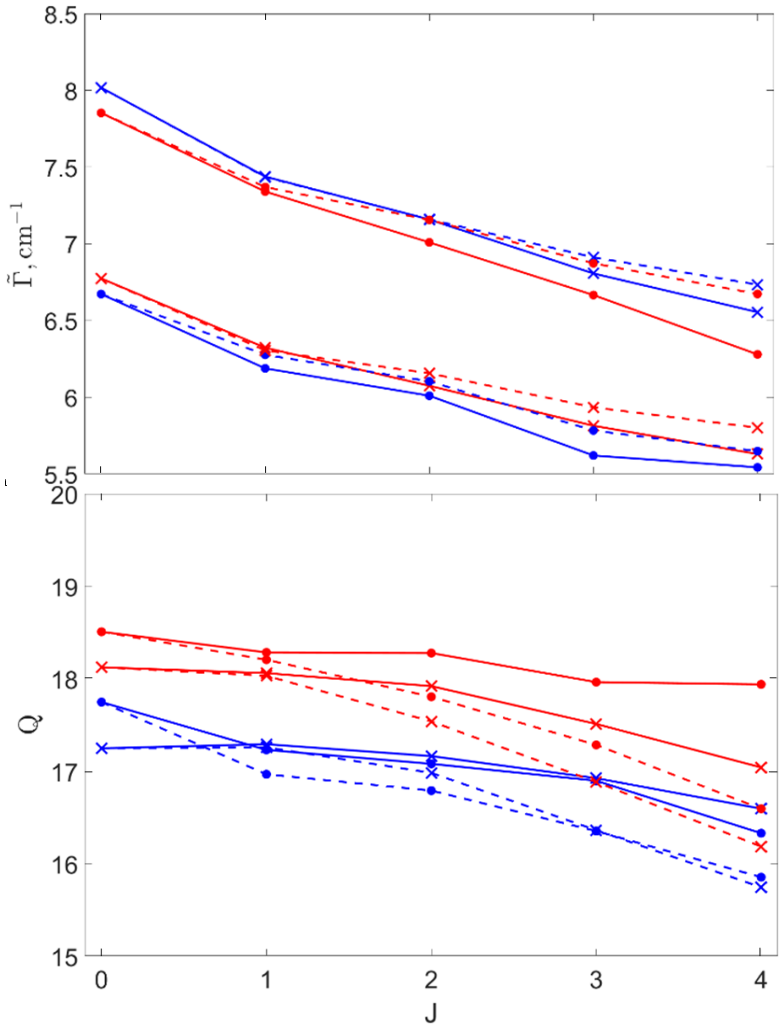

Figure 54. Same as Figure 52, but for the states localized over the VdW plateau (as in Table 36). The dots (x-symbols) correspond to homonuclear (heteronuclear) dissociation channels.

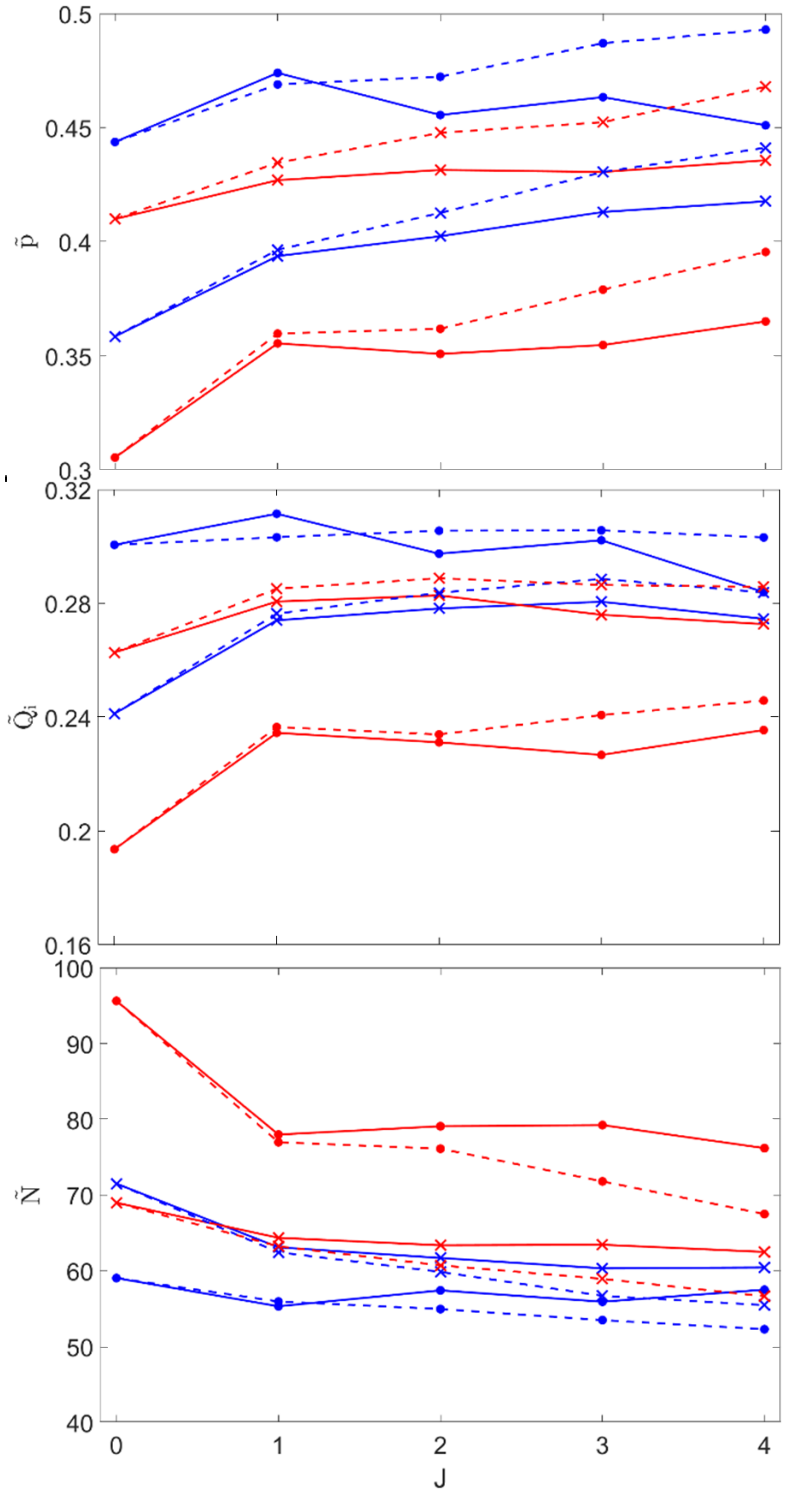

Figure 55. Same as Figure 54, but for the values of $\tilde{p}$, $\tilde{Q}_i$ and $\tilde{N}$.

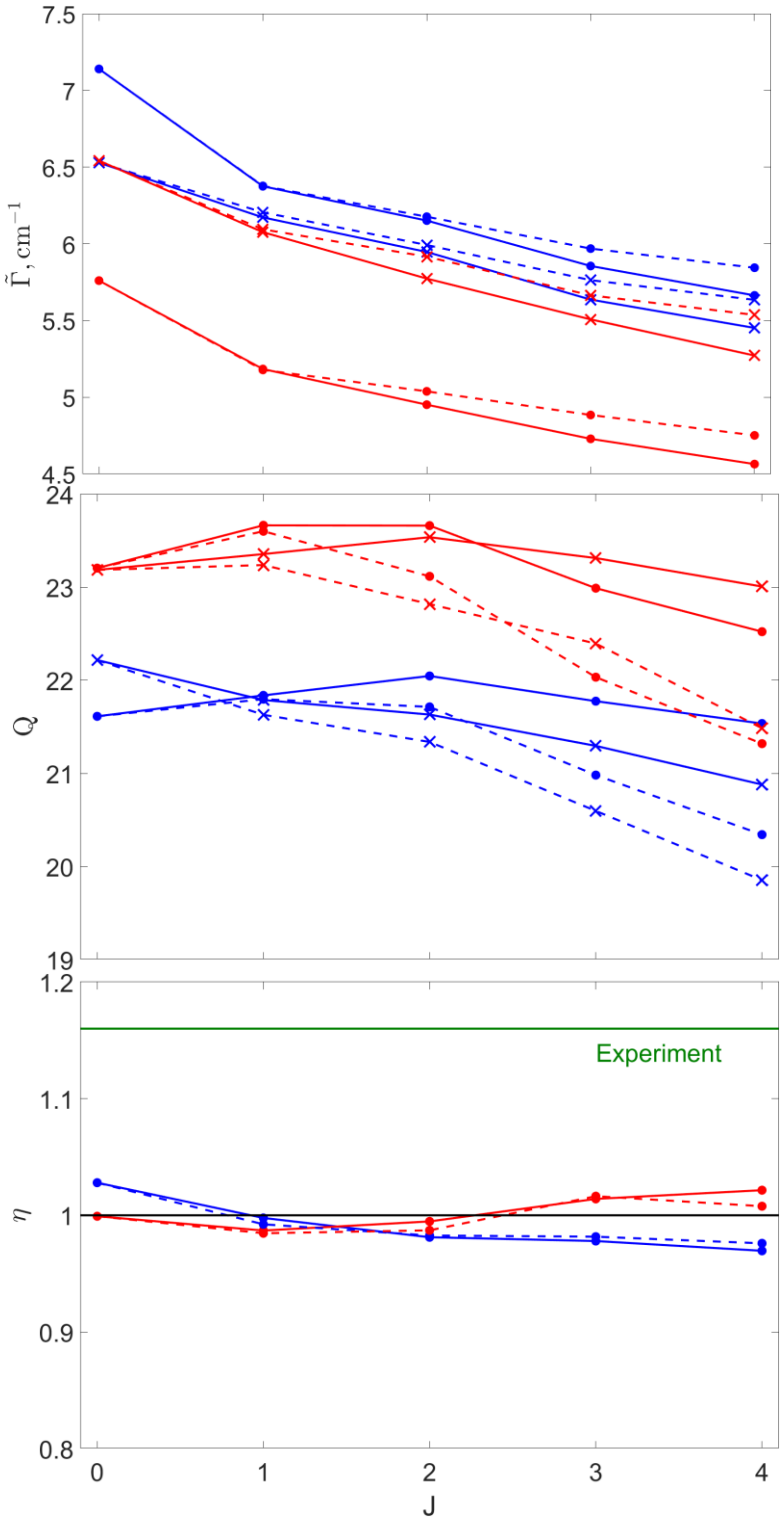

Figure 56. Same as Figure 52, but for both covalent and Van der Waals regions together (as in Table 37).

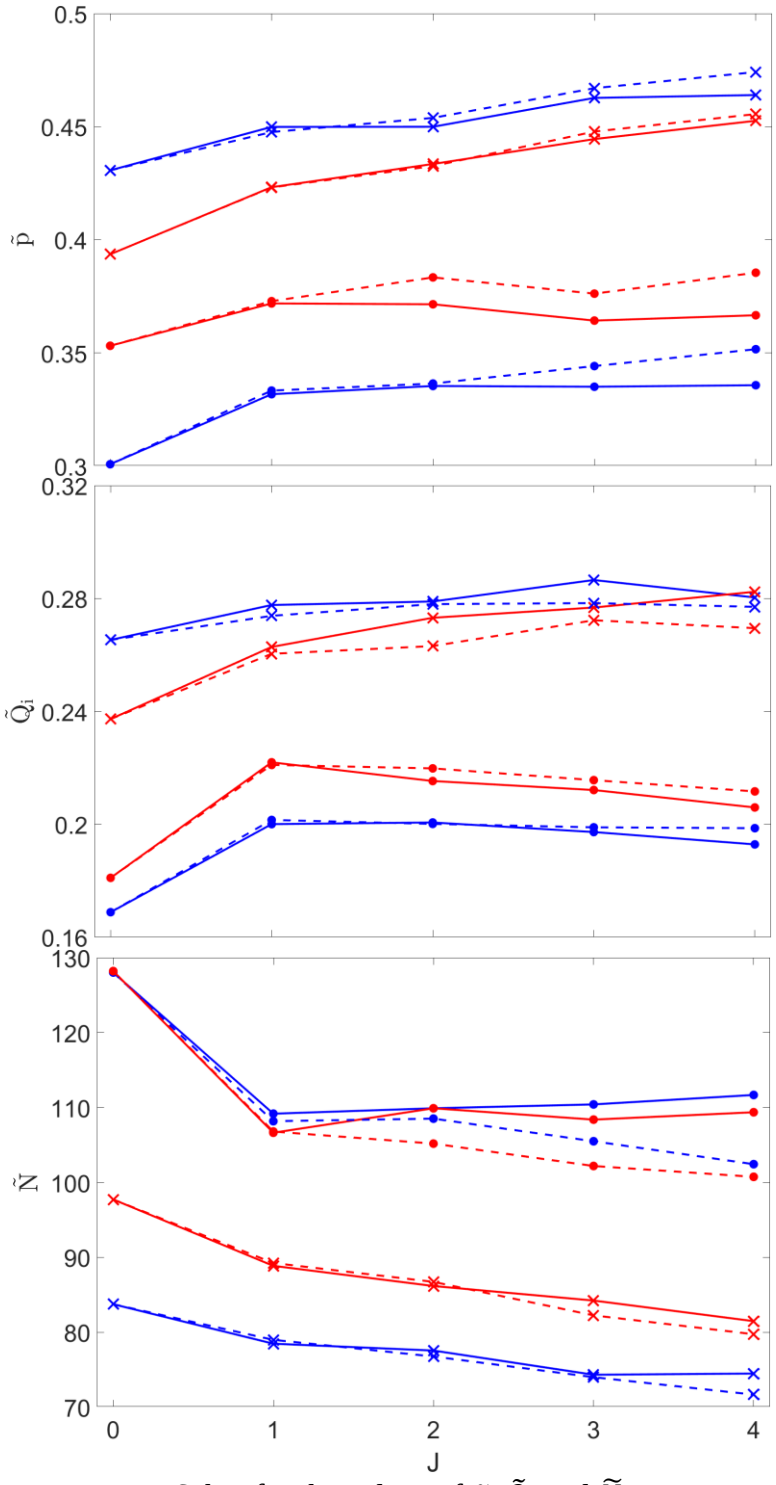

Figure 57. Same as Figure 56, but for the values of $\tilde{p}$, $\tilde{Q}_i$ and $\tilde{N}$.

7.6. Implications for Symmetry-Driven Isotope Effect

As it was stated earlier, recombination reaction that forms ozone exhibits a robust symmetry-driven isotope effect. Namely, in the experiment[38] the asymmetric ozone molecules (such as $^{16}O^{16}O^{18}O$ and $^{16}O^{18}O^{18}O$) are formed at a rate that is about 16% *higher* than the rate of formation of symmetric ozone molecules (such as $^{16}O^{16}O^{16}O$, $^{16}O^{18}O^{16}O$ or $^{18}O\,^{16}O^{18}O$). It is sometimes argued in the literature[156,157] that this effect can be explained if one assumes (and proves) that the symmetric and asymmetric ozone molecules possess different lifetimes. Let us review the data in Tables 35-37 in the light of this hypothesis.

To begin with, one should keep in mind that the rate of ozone recombination is determined by the dynamical partition function of scattering resonances Q, rather than by $\tilde{\Gamma}$ directly. The dependence of Q on the values of Γ_i of individual resonances is given by their weights w_i in Eq. (141) above.

With the choice of $[\mathrm{M}] = 267$ hPa, the value of weight $w_i = 0.5$ corresponds to $\Gamma_i \approx 8 * 10^{-3}$ cm^{-1}, while the values of $w_i = 0.1$ and 0.9 correspond to $\Gamma_i \approx 9 * 10^{-4}$ and $7 * 10^{-2}$ cm^{-1}, respectively. For practical purposes, all resonances with $\Gamma_i > 1$ cm^{-1} can be considered as broad, which means that their weight w_i at a given pressure reached the maximum ($w_i = 1$) and thus it does not depend on the actual value of Γ_i anymore.

With this in mind, let us look at the results of Table 35 first, for resonances localized over the covalent wells. We see that, indeed, the asymmetric ozone molecules $^{16}O^{16}O^{18}O$ and $^{16}O^{18}O^{18}O$ exhibit larger values of $\tilde{\Gamma}$ and one may (erroneously) expect that those would translate into larger values of weights w_i and partition functions Q (and thus higher rates of recombination). However, the values of Q in Table 35 show an

opposite trend, they are smaller for the asymmetric molecules, compared to the symmetric ones. How can that be? Well, notice that the values of average $\tilde{\Gamma}$ reported in the Table 35 are in the range of broad resonances, when the actual values of resonance widths do not affect the recombination process anymore (even if they show some mass-independent symmetry-driven trend). Therefore, a property other than the resonance width Γ_i must be important for explanation of the trends of Q values seen in Table 35.

Let us consider the quantities in rows 4-6 of Tables 35-37. All these quantities are weighted averages, which take into account the contribution Q_i of each state (its importance). From these data it becomes very clear that the values of partition function Q correlate well with the average number of resonances $\tilde{N}$, rather than with the average resonance width $\tilde{\Gamma}$, which means that the main driver of the effect is the number of metastable states in the symmetric and asymmetric ozone molecules (not their lifetimes). It appears that asymmetric ozone molecules have smaller number of effective states $\tilde{N}$, compared to the symmetric ozone molecules, just opposite to what we hoped to find (beyond the factor of 2, applied to the values of Q for asymmetric isotopomers, as stated above).

The symmetry-driven isotope effect itself, can be expressed as a ratio of partition functions for asymmetric and symmetric molecules. In the experiments of Mauersberger group[38] these numbers were found to be on the order of $\eta = 1.16$. The last row of Tables 35 and 37 reports our data for η, based on the calculations for $0 \leq J \leq 4$ combined. The dependence of isotope effect on rotational excitation, $\eta(J)$, is presented in the last frame of Figures 52 and 56. Unfortunately, neither of these data come close to the experimental results. Indeed, in all considered cases we obtain $\eta < 1$, for both singly and doubly

substituted cases, while in the experiment the isotope effect is observed to occur in the opposite direction, $\eta > 1$.

7.7. The Effect of Van der Waals States

Table 36 and Figures 54 and 55 contain the same analysis, but for the scattering resonances distributed over the VdW parts of the PES. Since the partition functions Q of the VdW states are larger than those of the covalent-well states, it is not surprising that many properties listed in Table 37 are dominated by those listed in Table 36. Interestingly, the overall average number of resonances $\widetilde{N}$ in Table 37 is still *smaller* for asymmetric ozone molecules, in both singly and doubly substituted cases. This feature can be (at least partially) explained by the fact that for the highly delocalized states probability in the asymmetric region of PES is expected to be roughly twice as large compared to the symmetric region (see Figure 50). This contributes to higher values of $\tilde{p}$ and $\tilde{Q}_i$ for asymmetric isotopomers and eventually translates to lower values of $\widetilde{N}$.

These differences, although mass-independent, have no influence on the isotope effect, which depends on the values of Q only. Importantly, the isotope effect η vanishes almost entirely when all ozone states are taken together, in both cases of single and double isotopic substitutions (last row in Table 37).

Figure 56 represents evolution of the corresponding isotope effect as a function of total angular momentum J. Here we can see some progressive deviation from the reference value of $\eta = 1$ (which corresponds to no isotope effect), but it is rather small and occurs in the opposite directions for singly and doubly substituted ozone molecules, which is consistent with our earlier findings for the bound states of ozone in Chapters 5

and 6, but is inconsistent with experimental data, where the same value of η is found irrespectively of the number of isotopic substitutions.

It is quite unfortunate, but based on the data obtained here for a limited range of rotational excitations $0 \leq J \leq 4$, we cannot reproduce large and robust η-effect observed in the experiments.

7.8. The Influence of Rotation-Vibration Coupling (Coriolis Effect)

One of the main goals of this paper was to check whether the symmetry-driven isotope effect could be explained by the Coriolis coupling which, according to a recently published hypothesis,[123] may act differently in symmetric and asymmetric ozone molecules. All results presented and discussed so far were obtained using an accurate (basically exact) coupled rotational-vibrational calculations, which include the asymmetric-top rotor term and the Coriolis coupling term in the Hamiltonian. Such calculations are numerically demanding. In addition, we carried out a set of approximate calculations neglecting these rotation-vibration coupling terms, which corresponds to a symmetric-top rotor approximation (where Λ is assumed to be a good quantum number). Such calculations are much cheaper, since different Λ-blocks of the Hamiltonian matrix are uncoupled, and thus can be diagonalized independently. The results of these simplified calculations are also presented in Tables 35-37 (in parenthesis), and Figures 52-57 (dashed-lines).

Without going through comparison of each pair of numbers, let us summarize what we learned about the role of rotation-vibration coupling:

The values of Q, $\tilde{\Gamma}$ and $\widetilde{N}$ are indeed somewhat affected by inclusion of the rotation-vibration coupling, but these changes are almost uniform across isotopomers, so

none of the computed properties change their relative order. Therefore, the value of isotope effect η remains nearly the same for both singly and doubly substituted ozone molecules, in both Table 35 (only resonances localized over the covalent well) and Table 37 (VdW states added to the covalent ones).

The values of Q and $\widetilde{N}$ always increase as the rotation-vibration coupling is included, which indicates that on average the spectrum of the uncoupled ozone states is less dense, as one might expect. In contrast, the values of $\tilde{\Gamma}$ always decrease, which indicates that on average the resonances are made more stable by inclusion of the rotation-vibration coupling, they live longer, decay slower.

The change is slightly larger for resonances localized over the covalent well, than for the VdW states because in the covalent case the number of effective resonances is smaller and thus the values of Q and the average properties are more sensitive to changes in each individual states. Moreover, the stretched VdW complexes are closer to the symmetric-top rotor model, than their compact covalently bound counterparts.

From Figures 52, 54 and 56, we see that at larger values of J the effect of rotation-vibration coupling on the magnitude of the partition function Q grows roughly linearly with J. However, this effect is rather uniform for symmetric and asymmetric isotopomers, therefore we also see that the value of isotope effect η, remains small and mostly unchanged through the range of J considered here.

7.9. Summary

In this chapter we developed a modification of theory presented in Chapter 4 that permits to decrease computational cost in the case of calculation of coupled scattering resonances with large vibrational basis set. Such calculations are required when we want

to predict thermal rate of a reaction, or another property (such as partition function) averaged over a broad distribution of rotational excitations. Traditional approach is to use multiple vibrational basis sets, optimized and truncated for each individual rotational state. This is elegant but is numerically inefficient. We demonstrated here that it is possible to choose one vibrational basis set, optimized for a typical rotational excitation (J, Λ), say somewhere in the middle of the desired range of rotational excitations, to employ it in the coupled rotation-vibration calculations for many values of J, in a relatively broad range.

The goal of this chapter was to reach higher vibrational energies, above the dissociation threshold, to determine how the rotation-vibration coupling influences scattering resonances in ozone. These metastable states participate in the ozone forming reaction and their properties are believed to be responsible for the mass-independent symmetry-driven isotope effect. Not only the states localized in the compact covalent well of ozone, but also the large-amplitude states distributed over a broad VdW interaction plateau of the PES are of interest.

The data computed in this chapter gives us accurate and valuable information about the influence of rotation-vibration coupling (the Coriolis force) on the recombination reaction of ozone, and on the corresponding isotope effect. This was not available in the past.

Namely, analysis of our data indicates that the average properties of scattering resonances, such as their average lifetime $\tilde{\Gamma}$, the average number of such states $\widetilde{N}$, and their cumulative partition function Q, are all affected by the rotation-vibration coupling, and this effect grows as the value of angular momentum J is increased. However, we also

found that various isotopomers and isotopologues of ozone (symmetric and asymmetric ozone molecules with single and double isotopic substitutions) are influenced by the Coriolis effect rather uniformly. When the ratio η of partition functions for asymmetric vs. symmetric ozone molecules is computed, the Coriolis effect largely cancels, and this cancelation seems to occur for all values of J. So far, we were not able to attribute any appreciable mass-independent symmetry-driven isotopic fractionation to the Coriolis coupling effect.

All data computed for this chapter is available in Ref. 153.

CHAPTER 8. EFFICIENT METHOD FOR AN APPROXIMATE TREATMENT OF ROTATION-VIBRATION COUPLING

The conclusions of the previous chapter were based on the results obtained for the values of $J \leq 4$. One can argue that larger values of J (around $J \approx 25$) have larger contribution to the recombination reaction of ozone (as indicated by Ref. 51), and thus need to be taken into account. Unfortunately, even with the optimization developed in Chapter 7, higher values of J remain computationally unaffordable and further approximations need to be developed in order to explore the effect of rotation-vibration coupling on the scattering resonances with large total angular momentum J.

In this chapter we develop an approximate method that enables us to take into account a large portion of rotation-vibration interaction, while keeping the calculations computationally affordable. This method is applied to calculation of scattering resonances in ozone with large values of J in effort to determine whether the effect of rotation-vibration coupling could lead to appearance of symmetry-driven isotope effects.

Exact rotational-vibrational Hamiltonian matrices include up to $J + 1$ Λ-blocks, corresponding to the symmetric-top rotor states (see Figure 23), which makes the them unaffordably large for direct diagonalization, especially when calculation of scattering resonance is concerned, where the presence of a complex absorbing potential (CAP) makes the Hamiltonian matrix non-Hermitian, large vibrational basis, needed to describe delocalized high energy states above the dissociation threshold, increases the size of each Λ-block, and a large number of eigenvalues is required.

For example, in the case of ozone calculation presented below, the size of each Λ-block is about 20000, which results in the full Hamiltonian matrix of the size about

500000×500000 for $J \sim 25$ and about 10% of eigenvalues are needed. Such large eigenproblems are basically impossible to solve even on the fastest computers available to us today.

A well-known straightforward way to make such calculations affordable is to neglect all off-diagonal Λ-blocks in the Hamiltonian matrix (due to $\hat{T}_{\mathrm{cor}}$ and $\hat{T}_{\mathrm{asym}}$ terms of the Hamiltonian operator), in which case the overall matrix splits into the independent diagonal Λ-blocks that can be diagonalized one by one for any value of J. This is called the symmetric top rotor approximation, or the Λ-conserving approximation (since Λ becomes a good quantum number). It has been applied extensively in the past to study many molecules and processes, including the kinetics of ozone recombination reaction.[39,51,93,118,122,124] The effects of neglecting rotation-vibration coupling, and various methods of improving the accuracy of this approximation, have been recently discussed in detail.[158] But what if the contribution of $\hat{T}_{\mathrm{cor}}$ and $\hat{T}_{\mathrm{asym}}$ is expected to be important and cannot be neglected?

For these cases, we developed and tested an approximate method to take into account the effects of rotation-vibration coupling, which remains practical even for large values of J. Let us consider the method.

8.1. Partially Coupled Method

First, recall from Chapter 4 that the rotational structure of the Hamiltonain matrix produced by the last three terms of the Hamiltonian operator ($\hat{T}_{\mathrm{sym}}$, $\hat{T}_{\mathrm{asym}}$ and $\hat{T}_{\mathrm{cor}}$, see Eq. (32)) in the basis of DVR functions in $h_n(\rho)$ (Eq. (88)), optimized hyper-angle functions $\mathrm{X}^{j}_{\Lambda n}(\theta,\varphi)$ (Eq. (97)) and symmetrized Wigner functions $\widetilde{D}_{\Lambda}(\alpha,\beta,\gamma)$ (Eq. (50)), considered in this work, is “block three-diagonal”, as shown in Figure 23.

Namely, $\hat{T}_{\mathrm{sym}}$ only couples basis functions with the same values of Λ (i.e., within the diagonal blocks of the matrix, $\Lambda' = \Lambda$), while $\hat{T}_{\mathrm{cor}}$ and $\hat{T}_{\mathrm{asym}}$ couple functions with the values of Λ different by ± 1 and ± 2, respectively (producing the off-diagonal blocks with $\Lambda' = \Lambda \pm 1$ and $\Lambda' = \Lambda \pm 2$). $\hat{T}_{\mathrm{asym}}$ also contributes to one diagonal block with $\Lambda' = \Lambda = 1$.

The two methods considered before represent two limiting cases, in which either *all* Λ-blocks are included (the full-coupled exact approach) or *one* Λ-blocks is included (symmetric top rotor approximation) in the Hamiltonian matrix. But why not to try an intermediate partially coupled method, in which *some* Λ-blocks of the overall Hamiltonian matrix are included for each Λ? For example, it makes sense to include several nearest blocks in the vicinity of each Λ that are *directly coupled* to it by $\hat{T}_{\mathrm{cor}}$ and $\hat{T}_{\mathrm{asym}}$, namely $\Lambda' = \Lambda \pm 1$ and $\Lambda' = \Lambda \pm 2$. These are expected to be the most important for a given value of Λ. All other more distant values of Λ', linked by *chain coupling* through these blocks, are expected to be less important and therefore can be neglected. Since in this method we include some of the Λ-blocks, but not necessarily all of them, we would like to call this approach a *partially-coupled* method, or a PC-method for short, to complement the well-known coupled-channel (CC), centrifugal-sudden (CS) and infinite-order sudden (IOS) methods.[125,159–161]

Just as in the symmetric top rotor approximation, in our PC-method a series of independent matrix diagonalizations needs to be done for different values of Λ to cover the range of $0 \leq \Lambda \leq J$. Performing these calculations for all values of Λ up to J, one can obtain a complete spectrum of states for that J. Alternatively, it may be more efficient to do calculations for some values of Λ, and then interpolate in between. An example of this

process is shown in Figure 58, where borders of reduced "sub-matrices" considered for every other value of Λ are shown with dashed lines. Note that the maximum number of Λ-blocks included in each calculation is always limited to five, which makes such calculations affordable even for large values of J.

Indeed, the cost of matrix diagonalization grows at least quadratically. Therefore, replacing one diagonalization of a matrix that contains $(J+1)\times(J+1)$ blocks, with a series of $J+1$ independent diagonalizations of the matrices that contain 5×5 blocks at most, one can gain a substantial computational advantage. Interestingly, a similar idea

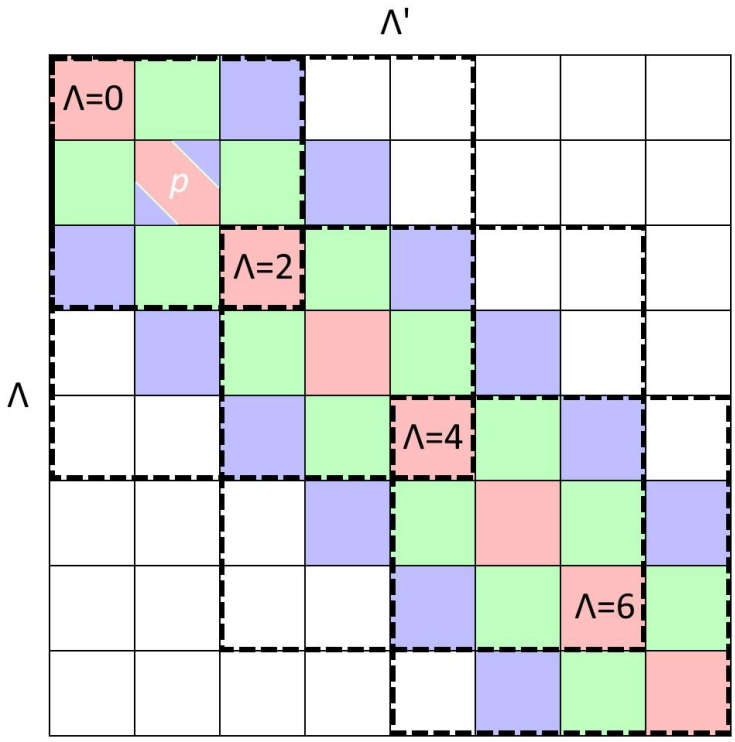

Figure 58. A schematic rotational block structure of the Hamiltonian matrix for J = 7 and p = 1. Individual blocks are labelled by the values of Λ and Λ' of the symmetric top rotor. Each block includes all vibrational basis functions. Red, green, and blue colors show contributions from $\hat{T}_{sym}$, $\hat{T}_{cor}$ and $\hat{T}_{asym}$ terms in the Hamiltonian operator, respectively. The four black dashed squares show the boundaries of "sub-matrixes" in the calculations for $\Lambda = 0$, 2, 4 and 6, up to $\Lambda' = \Lambda \pm 2$ in each case. The white p letter marks the only block, where the values of matrix elements are affected by parity.

was recently developed in the context of a non-reactive inelastic scattering and was found to be both accurate and numerically efficient.[162]

The accuracy of PC-method for each state depends on the distribution of Λ-values in its wave function. Since the range of the Λ-states in the truncated basis set is restricted to only five ($\Lambda' = \Lambda \pm 2$), the wave functions with much broader distributions would not be accurately described. The actual accuracy of the method is expected to be system/problem dependent and should normally be tested, by comparison with the full-coupled calculations, at least for the low values of J, when the full-coupled calculations are possible. This is what we do next.

8.2. Test of Partially-Coupled Method

In this section we test our PC-method by comparing it with the full-coupled calculations (that are considered to be exact) and with the symmetric top rotor (a widely used approximation), using the case of $J = 4$ and positive parity $p = 0$, when all these calculations are numerically affordable. In this test, and in this chapter overall, we are not particularly interested in spectroscopic characteristics of the individual quantum states. Instead, we are looking at scattering resonances above the dissociation threshold that play the role of metastable states (reaction intermediates) in the process of ozone formation.

To compare these three methods, we want to compute the corresponding dynamical partition functions Q, similarly to what we did in Chapter 7. However, one caveat of the partially-coupled approach is that each sub-Hamiltonian includes a range of Λ-values, but only the "central" value of Λ has its direct couplings included, so we need to filter out contributions from the states localized near the ends of the range, where further rovibrational coupling is missing. We cannot assign a definite value of Λ to a

state, since Λ is not a good quantum number, but we can add a weight factor to Q, equal to the probability in the central Λ for each state. With this in mind, the new definition of the dynamical partition function for this chapter is:

$$Q(\Lambda) = \sum_i p_i^{\Lambda} p_i^{\mathrm{mol}} w_i \ \exp\left(-\frac{E_i}{kT}\right) \tag{153}$$

where p_i^{Λ} is the state's localization probability in a given value of Λ (see Eq. (121)) and the meaning of the remaining factors is the same as in Eq. (141). The value of p_i^{mol} in this chapter is defined to include contributions from both covalent and Van der Waals regions, as in Table 37. Pressure and temperature are set to the same values as in Chapter 7 at $P = 267$ hPa (≈ 0.3 Bar) and $T = 298$ K.

The partition functions of Eq. (151), computed with the three methods are shown in Figure 59. We see that all three partition functions decrease as a function of Λ, which is partially due to the Boltzmann factor (energy of states E_i grows quickly when Λ is raised) and partially due to the weight w_i (higher centrifugal barrier hinders the population of resonances), same as what we saw in section 7.5 with respect to J.

Next we see that inclusion of the rotation-vibration coupling (red vs. blue symbols) leads to increase of the dynamical partition function Q for all values of Λ, in this case by about 5% on average, which is a non-negligible effect.

Finally, we see that the results obtained with the partially coupled method (green) are much closer to the results of exact full-coupled method, compared to the data obtained within the symmetric top approximation. For $\Lambda = 2$ the result of partially

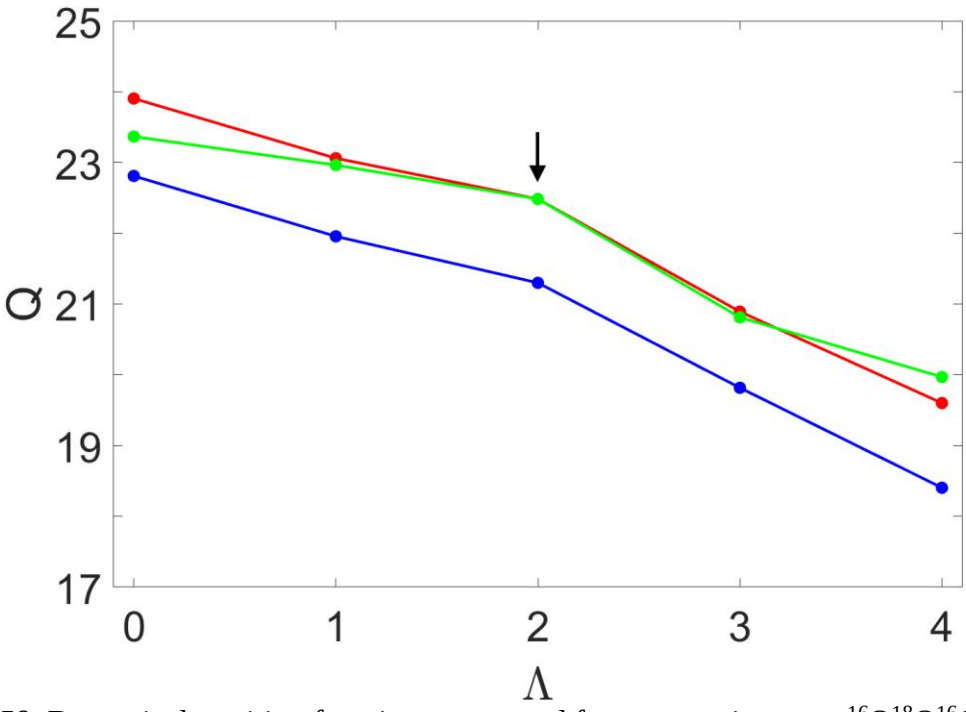

Figure 59. Dynamical partition functions computed for symmetric ozone $^{16}O^{18}O^{16}O$ at J = 4 and p = 0. Calculations with no coupling (symmetric top) are shown in blue, partial coupling in red, and the full coupling (exact) in green. The black arrow shows the point ($\Lambda = 2$), where the partial coupling approach coincides with the exact method.

coupled calculations coincides with the exact result (marked with an arrow), since in this case the "five-block window" of the partially coupled approach happens to cover the whole Hamiltonian matrix. As we move away from $\Lambda = 2$, the fully and partially coupled approaches start to diverge, but still stay close to each other and away from the data of the decoupled symmetric top rotor approximation. The difference is largest for the terminal Λ-values ($\Lambda = 0$ and $\Lambda = 4$). Generally, one should expect that the deviation from the full-coupled method is proportional to the number of missing Λ-blocks in a reduced sub-matrix.

From Figure 59 we conclude that the partially coupled approach behaves as expected and can be used as an approximation for calculation of the coupled rotational-vibrational resonance spectra for large values of J.

8.3. Calculations with Large Total Angular Momentum

In this section we apply the partially coupled method, described in the previous section, to carry out calculation of the resonance spectra in singly substituted ozone isotopomers $^{16}O^{18}O^{16}O$ and $^{16}O^{16}O^{18}O$ and use it to evaluate the corresponding $Q(\Lambda)$ dependencies for $J = 24$ and 28, typical to ozone formation at room temperature,[51] for several representative values of Λ. Since the full-coupled calculations are unaffordable in these cases, only the results for the uncoupled (symmetric top) and for our partially coupled method are presented and discussed. The convergence parameters of these calculations are identical to those reported in section 7.2. The complete dataset, calculated for this chapter, will be made available in a future publication.

The results are presented in Figures 60 and 61. For $\Lambda \geq 1$ the results were averaged over two parities (for $\Lambda = 0$ only positive parity is possible). We see again that,

as Λ is raised, the values of $Q(\Lambda)$ decrease rather monotonically and are expected to vanish around $\Lambda = 20$. One clear trend observed in all these data is that the values of partition function Q are systematically higher in the calculations where the rotation-vibration coupling is included (using our PT-method), compared to the uncoupled (symmetric top rotor) calculations, by up to 17% for $J = 28$, and up to 20% in case of $J = 24$. This is expected since the density of states generally increases with additional couplings.

The solid lines in all frames of Figures 60 and 61 are calculated using the states of allowed symmetry only (see Table 15). As a computational experiment, we also tried to include the states with forbidden symmetry. The dashed lines correspond to the $Q(\Lambda)$ averaged over both allowed and forbidden symmetries. One can see that the inclusion of forbidden symmetry does not significantly alter the results, which tells us that the two ro-vibrational symmetries behave similarly and there are no unexpected/unusual isotope effects associated with the forbidden symmetry.

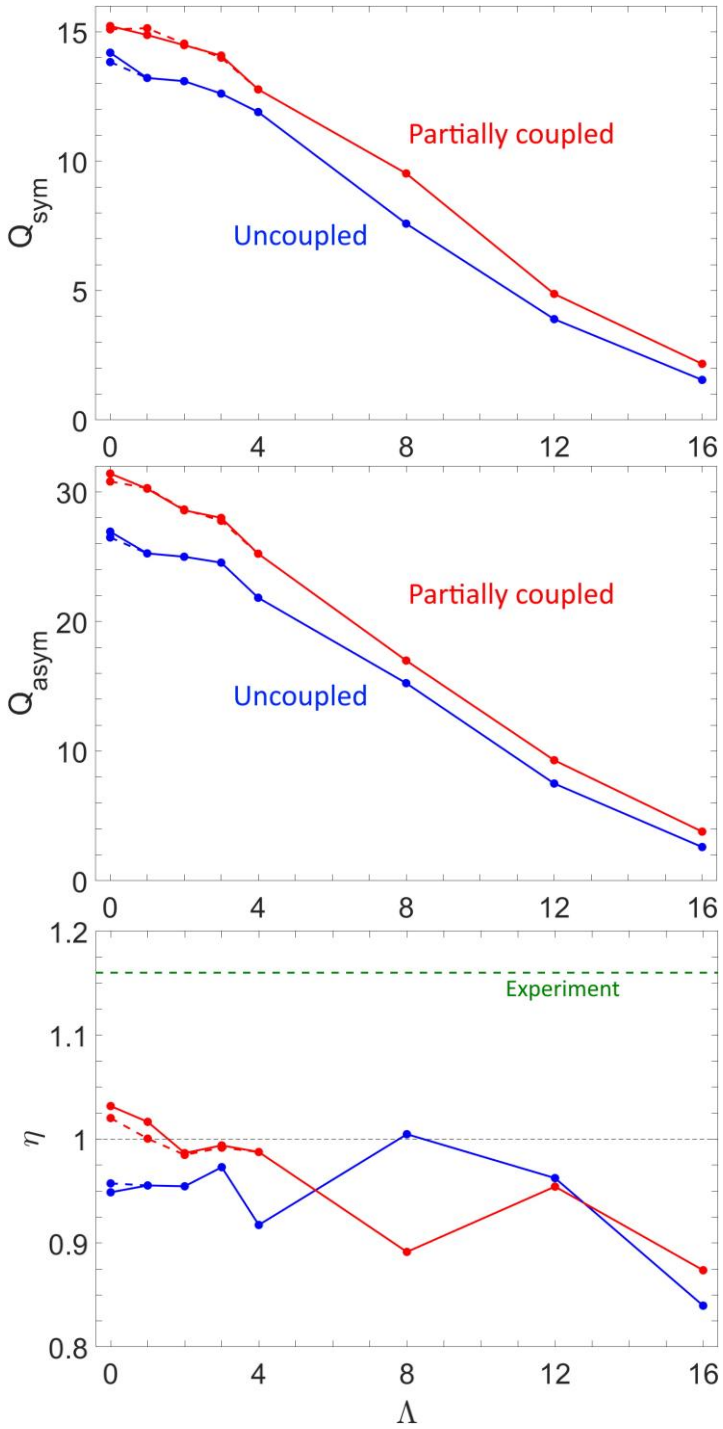

Figure 60. Parity-averaged dynamical partition functions for symmetric ($^{16}O^{18}O^{16}O$, top frame) and asymmetric ($^{16}O^{16}O^{18}O$, middle frame) ozone molecules at $J = 24$, and the resultant η-effect (bottom frame). The blue and red lines correspond to the uncoupled (symmetric top) and partially coupled calculations, respectively. The solid lines are computed using the states of allowed ro-vibrational symmetry only. The dashed lines represent the symmetry-averaged case, when both allowed and forbidden symmetries are included.

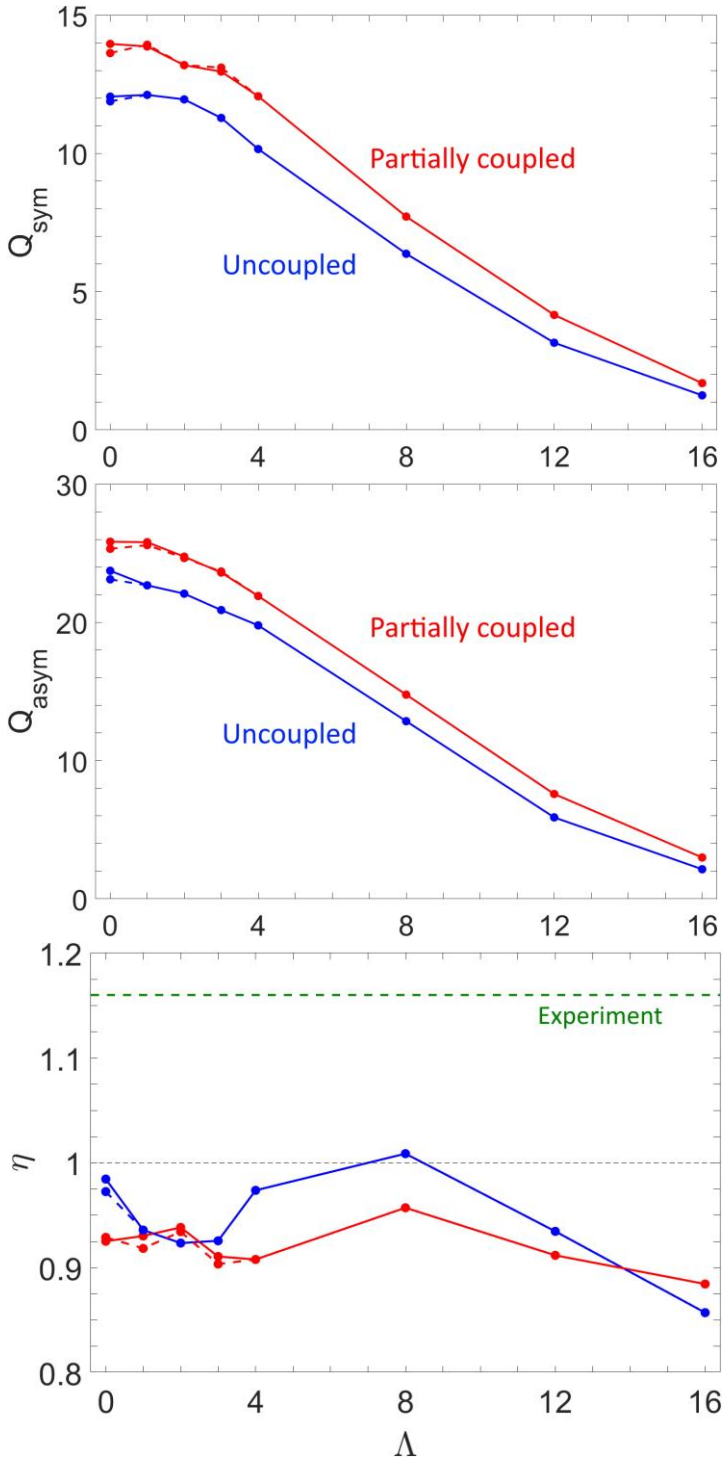

Figure 61. Same as Figure 60, but for $J = 28$.

Recall from Chapter 4, that the only Λ-block non-trivially affected by parity is $(\Lambda, \Lambda') = (1,1)$ (see Figure 58), where the effect is coming from $\tilde{T}_{\text{asym}}$ term or, more specifically, from matrix $U_{\Lambda\Lambda'}$ of Eq. (78). Therefore in the case of uncoupled calculations, where $\hat{T}_{\text{asym}}$ term is neglected, the value of parity has no effect on the Hamiltonian matrix and any properties of its eigenstates. In particular, for $\Lambda \geq 1$ the states of the two parities are degenerate and, although only one vibrational symmetry is allowed for each parity, both vibrational symmetries show up in the spectrum, because they come from different parities (see Table 15). The only exception is $\Lambda = 0$, when only one (positive) parity is possible, and thus only one vibrational symmetry is allowed. Therefore, inclusion of forbidden symmetry only makes difference in the case of $\Lambda = 0$ for uncoupled calculations.

In the full-coupled calculations, the effect of the parity-affected block spreads to all states of the system via chain coupling of consecutive Λ-blocks, but its influence, and the role of parity, becomes weaker for the states dominated by large values of Λ (recall from Figures 46 and 47 that the value of parity splitting drops exponentially as a function of Λ).

In the partially coupled method this chain-coupling is restricted to act within five blocks, $\Lambda' = \Lambda \pm 2$. Therefore, the calculations for $\Lambda \geq 4$ are decoupled from $\Lambda = 0$ and $\Lambda = 1$ and the states of two parities become degenerate again, just as in the uncoupled case. Thus, solid and dashed red lines in Figures 60 and 61 deviate one from another only at $\Lambda \leq 3$.

Looking at the data in Table 15, one can see that the effects of parity of the rotational functions and the symmetry of vibrational functions are closely related and

should be considered together. Our data here indicate that they both are relatively small in the rotationally excited ozone molecules (dashed vs. solid lines of the same color in Figures 60 and 61), compared to the overall effect of the ro-vibrational coupling (red vs. blue lines).

8.4. Implications for Symmetry-Driven Isotope Effect

The bottom frame of Figures 60 and 61 reports the ratio of dynamical partition functions in symmetric and asymmetric ozone molecules, defined as:

$$\eta = \frac{Q^{\mathrm{asym}}}{2Q^{\mathrm{sym}}} \tag{154}$$

This definition is identical to Eq. (151), except the factor of 2 there was incorporated into Q^{asym} directly. The value of η-effect on the order of $\eta = 1.16$ (green in Figures 60 and 61) would permit to interpret mass-independent fractionation as a symmetry-driven isotope effect,[38,163] with asymmetric ozone molecules formed 16% faster than the symmetric ones.

However, the data presented in Figures 60 and 61 for all values of Λ, both uncoupled (blue) and partially coupled (red), exhibit the values of η less than one (with the exception of one blue point where η is just slightly larger than one). We can also see that the addition of partial ro-vibrational coupling (red) did not introduce any systematic bias in the favor of asymmetric isotopomer. On average, the value of η-effect remained similar to the uncoupled case (blue). The same conclusion was made in Chapter 7 with exact calculations of low values of J.

Finally, let us compare the average values of resonance width in symmetric and asymmetric ozone isotopomers (computed with Eq. (147), as before). The results are shown in Figures 62 and 63. From these data one can conclude that, on average, the inclusion of ro-vibrational coupling has little effect on resonance widths, and therefore is not expected to affect the lifetimes of the metastable ozone states. The inclusion of forbidden symmetry, related to the effect of parity, makes even less difference (dashed lines). Resonance widths appear to be more sensitive to the value of Λ, but this effect is

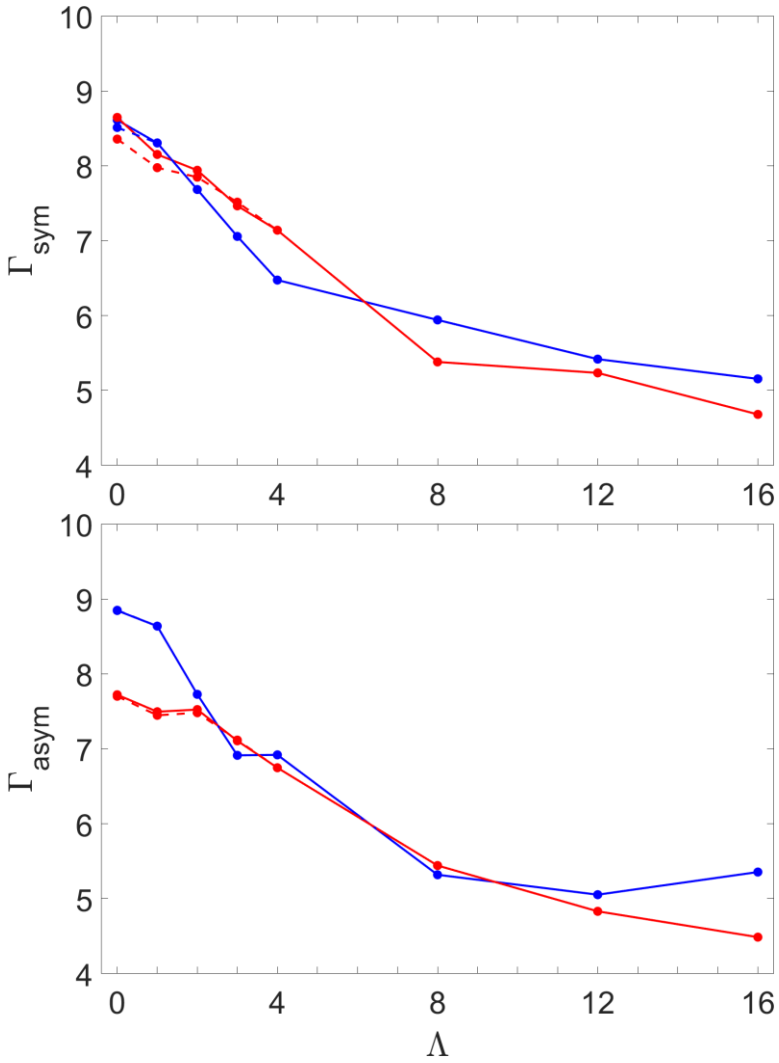

Figure 62. Average values of resonance widths in symmetric (16O18O16O, top frame) and asymmetric (16O16O18O, middle frame) ozone molecules for $J = 24$. The meaning of lines and colors is the same as in Figure 60.

about the same in symmetric and asymmetric ozone molecules. Also, comparison of average resonance widths computed here for $J = 24$ and $J = 28$ with those considered in Figure 56 for $J \leq 4$ shows that they are less sensitive to J and more sensitive to Λ, but again, these dependencies are very similar in symmetric and asymmetric ozone molecules, which does not help us to explain why the asymmetric ozone molecules are formed faster.

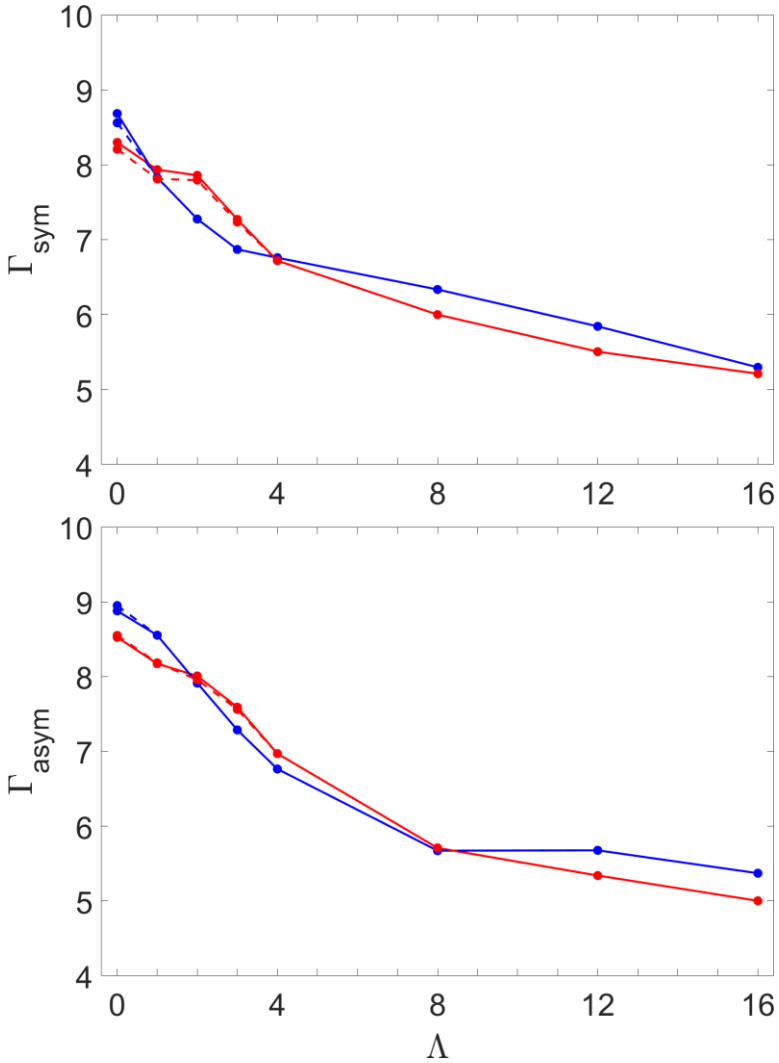

Figure 63. Same as Figure 62, but for $J = 28$.

8.5. Summary

In this chapter we explored the effect of rotation-vibration coupling on resonance spectra of ozone isotopomers with large values of J. In particular, our goal was to determine whether rotation-vibration coupling (Coriolis effect) could introduce a systematic bias in favor of isotopically substituted asymmetric isotopomers of ozone, such as $^{16}O^{16}O^{18}O$. This could help to explain the origin of the mysterious η-effect, responsible for mass-independent fractionation of oxygen isotopes in the atmosphere. Based on the results presented here, we conclude that while the addition of rovibrational coupling appreciably increases the average number of metastable ozone states (given by the dynamical partition function), the changes are rather uniform for both symmetric and asymmetric isotopomers of ozone. The average lifetimes of ozone molecules do not seem to be appreciably affected by the rovibrational coupling and remain similar in both symmetric and asymmetric ozone isotopomers, therefore we cannot conclude that the η-effect is associated with differences in lifetimes.

In order to make the calculations in this chapter numerically feasible, we developed a partially coupled method that permits to capture the major contribution of ro-vibrational coupling terms without diagonalization of the entire Hamiltonian matrix. This method is approximate, but it is general and applicable to many other molecules and processes in the spectroscopic and dynamic context. The number of coupled Λ-blocks does not have to be equal to five, as in this manuscript ($\Lambda' = \Lambda \pm 2$). Instead it can be viewed as a convergence parameter, varied to achieve desired level of accuracy.

As indicated in Ref. 107, if the *z*-axis is chosen perpendicular to the molecular plain, then both $\hat{T}_{\mathrm{asym}}$ and $\hat{T}_{\mathrm{cor}}$ terms contribute to the same Λ-blocks and the resulting

Hamiltonian matrix becomes block two diagonal. In this case the effect of direct coupling, studied here could be achieved using just 3 blocks. This can make the method even more affordable, enabling the coupled rotation-vibration calculations for more complicated systems and processes.

CHAPTER 9. SPECTRUMSDT: A GENERAL PROGRAM FOR CALCULATION OF ROVIBRATIONAL ENERGIES AND LIFETIMES IN TRIATOMIC SYSTEMS

In Chapter 4 we considered a general theory of rotational-vibrational coupling in APH coordinates, and derived necessary equations for the matrix elements. This theory was then implemented in a computer program (SpectrumSDT), which was used to compute the spectra of several ozone isotopomers and analyze them, especially in relation to the isotope effects, in Chapters 5-8. The developed theory is general and can be applied to other three-atomic systems. The program, however, was written specifically for ozone, and lacked the flexibility to handle other systems.

In this chapter we made the program more flexible, and present the first general and user-ready version of SpectrumSDT (v1.0) that can be applied to the triatomic systems other than ozone. Several programs for the rovibrational calculations exist, such as ScalIT,[164,165] Geniush,[111,166,167] DVR3D,[168] BOUND[169] and MOLSCAT,[170] but our code offers unique features.

In particular, SpectrumSDT can find states both below and above the dissociation threshold, with or without ro-vibrational coupling, with or without lifetime information. Moreover, it carries out integration of computed wave functions over user-defined regions of the PES, in order to automatically assign isomers (or isotopomers) and compute channel-specific decay rates of scattering resonances (spontaneous first order process determined by resonance widths). This information is essential for the description of reactions characterized by complicated potential energy landscape with multiple reaction channels, as demonstrated in Chapters 5-8.

Finally, our code offers three options for the treatment of rotation-vibration coupling. In addition to the standard symmetric-top rotor approximation (when the coupling is neglected) and the exact full-coupled calculations (which is numerically demanding), we provide an affordable partially coupled approach (see Chapter 8). In this first release, SpectrumSDT is limited to ABA-type molecules (where two atoms are the same, and one is different, including the AAB and BAA isomers) and is applicable to wave functions that do not extend into the regions of Eckart singularities (equilateral and linear shapes). These limitations will be lifted in future releases.

The program, building instructions and examples of running are available in a GitHub repository.[119]

9.1. Theoretical Considerations

In this section we provide a concise summary of the most relevant theoretical aspects of SpectrumSDT for a lay user. Refer to Chapters 4-8 for more detailed description.

9.1.1. Basis Sets and Sequential Diagonalization Truncation (SDT) Procedure

On the lowest level, SpectrumSDT uses discrete variable representation (DVR) for ρ and θ coordinates (basically, a grid of points) and variational basis representation (VBR) of cosines or sines functions for φ (Eqs. (104)-(105)), which enforces either symmetric or antisymmetric property of wave functions with respect to $\varphi = 0$ and $\varphi = \pi$, required for ABA-molecules in the APH coordinates. The two symmetries are independent, so the calculations are split into two separate runs for each symmetry.

SpectrumSDT constructs a hierarchy of progressively more optimal basis sets through the procedure known as Sequential Diagonalization Truncation (SDT).[109,110] In

short, SDT starts with solving a one-dimensional Schrodinger equation, where all couplings with other coordinates are neglected, in each of the 1D-slices along φ at every combination of grid points in ρ and θ. The obtained 1D-solutions are used as a locally optimal basis set to solve 2D problem in φ and θ, where the some of the previously neglected couplings are taken into account, and the basis set is further optimized (sequential diagonalization). Finally, the 2D solutions are used as a basis set for the overall 3D problem, with all couplings taken into account. Of course keeping all the solutions from 1D and 2D levels would result in unnecessarily large basis, so only the solutions with energies less than a specified convergence parameter E_{cut} are retained in the basis set (truncation).

9.1.2. Eckart Singularities

As stated above, one of the limitations of the current version is its inability to handle wave functions in the regions of Eckart singularities. As one can see from section 4.2, $\hat{T}_{\varphi} \to -\infty$ as $\theta \to 0$ in Eq. (35) and $V_{\mathrm{ext}} \to -\infty$ as $\theta \to 0$ or $\pi/2$ in Eq. (36). These are Eckart singularities, corresponding to the equilateral configuration at $\theta = 0$ and the linear configuration at $\theta = \pi/2$ (see Figure 22). While this problem is in principle solvable within existing framework by using a special basis set,[104] the current release of SpectrumSDT does not implement this feature yet, therefore if a wave function for a particular molecule is allowed to have a significant probability near $\theta = 0$ or $\pi/2$, the solution is not reliable.

Fortunately, in many cases this issue is naturally avoided. First, many covalently bound triatomic molecules with sp^2 hybridization, such as O_3, naturally have a highly repulsive PES in the regions of Eckart singularities, which prevents the vibrational wave

function from reaching there. Second, the rotational potential term $\hat{T}_{\mathrm{sym}}$, given by Eq. (38), approaches $+\infty$ in the same regions due to the B and C terms in Eqs. (42) and (43). This extra potential "shields" Eckart singularities at sufficiently high values of rotational excitation (J, Λ), even if the PES does not. For both of these cases our code is able to give accurate results.

9.1.3. Hamiltonian Matrix Structure

The rotational state of the basis functions used to build the Hamiltonian matrix can be either *fixed* or *adiabatic* (see section 7.1).[153] In the *adiabatic* case, a separate basis set is used for each value of the symmetric top quantum number Λ (projection of total angular momentum onto *z*-axis) that is going to be included in the Hamiltonian matrix for a given value of total angular momentum quantum number *J*. This creates a better suited basis set, since it experiences the same rotational potential as a target wave function. This approach is relatively standard and often found in the literature,[39,51,122] but it requires computing many different basis sets and, most importantly, the corresponding overlaps for all values of *J* and Λ, which can be numerically demanding.

In the alternative *fixed* option, the basis set with one (representative) combination of *J* and Λ is used to describe wave functions with arbitrary values of *J* and Λ. This reduces the computational cost of both *basis* and *overlaps* calculation stages, but creates a less efficient basis set, therefore a higher value of the *cut-off energy* (E_{cut}) may be needed. In Chapter 7 we demonstrated that this approach is more efficient. However, one has to be careful when handling a molecule with wave functions reaching the ends of θ-grid. In this case, using a basis set with high values of *J* and Λ relative to a target wave function, will exclude basis functions near the ends of the θ-grid (due to the effect of

rotational potential), which may result in less accurate representation of the target wave function in that area.

The rotational terms in Eqs. (38)-(40) translate to the Hamiltonian matrix structure shown in Figure 23. In the cases when couplings between different Λ blocks can be neglected, the overall matrix can be split into the diagonal Λ blocks, which significantly simplifies the process of solving the eigenvalue problem. This is known as symmetric-top rotor approximation. As a compromise between speed and accuracy, when the effects of ro-vibrational coupling cannot be neglected, it is also possible to partially take it into account, by including only a certain number of adjacent blocks for each value of Λ. For example, including up to five blocks, within the $\Lambda \pm 2$ range, permits to capture most of the rotational-vibrational interaction, as demonstrated in Chapter 8.

9.1.4. Optimized ρ-Grid (Optional)

One practically relevant aspect of SpectrumSDT that we have not considered so far is the existence of an option to generate an optimized grid of DVR functions for ρ coordinate, which can take into account shape of potential energy surface and place more points in the covalent wells region (where higher accuracy is desired) and less points in the dissociation region, where wave function is smooth and the same amount of points as in covalent wells would be an overkill. Such grid is built as follows:

Suppose we have a 1D potential $V(\rho)$ and we want to place points along ρ-coordinate in an optimal way to represent wave functions. The idea is to make grid spacing in ρ proportional to the local de Broglie wavelength $\lambda(V(\rho))$. This way one can accurately capture wave function oscillations, without placing too many points in the regions where wave periods are large. To achieve this, one can define an auxiliary grid *x*,

where the distance is unitless and a given point $x = t$ corresponds to t oscillations of a wave with total energy E_{max} in the original space (ρ), as measured from a starting point ρ_0.

The points in *x* can be mapped to ρ and vice versa, therefore if one has an equidistant grid in *x*, its mapping onto ρ would be an optimal grid with a fixed number of points per oscillation of the wave. Assuming the step size in *x* is $\alpha/2$, one can derive the following differential equation that relates the two grids:[93,96]

$$\frac{d\rho}{dx} = \frac{\alpha}{2}\lambda\big(V(\rho)\big) = \frac{\alpha}{2}\frac{h}{\sqrt{2\mu(E_{max} - V(\rho))}} \tag{155}$$

where factor of 2 in the denominator is chosen to make $\alpha = 1$ correspond to 2 points per period – the smallest meaningful number. This way the values of α range from 0 to 1 and control the density of the resulting optimal grid (smaller values of α generate denser grids). The exact value of α for a given problem is a convergence parameter. The derivative $d\rho/dx$ in Eq. (155) is further referred to as Jacobian of the grid ρ.

In general, any function smaller than the actual potential can be used as $V(\rho)$ in Eq. (155). Using such potential "envelopes" can be helpful to increase density of points in selected regions or improve integration accuracy if the envelope function is analytical.

9.2. Practical Considerations

9.2.1. General

The workflow of the program is separated into the following stages (runs): `grids`, `potential`, `basis`, `overlaps`, `eigensolve` and `properties`. Using multiple stages allows to utilize processors efficiently by separating computationally expensive sections with different degree of parallelizability. The stages have to be launched sequentially one after another from their respective folders.

The folder structure for each calculation may consist of up to 4 levels (see Figure 64). On the first level, there are subfolders for each value of Λ (referred to as more traditional *"K"* in the code, parameters, file names and further in this chapter), as well as separate folders for each range of *K* that a user wants to consider for calculation of eigenpairs. The range that includes all values of *K* for a given *J* is referred to with a keyword `all`. The next two levels in a *K* range folder identify the values of parity and vibrational symmetry of the basis set corresponding to the calculation within. The folders corresponding to a scalar value of *K* skip the level corresponding to parity since parity only has the effect on calculations involving more than one value of *K*.[140] The last level is divided into folders corresponding to stages from `basis` to `properties`. `Grids` and `potential` stages do not have a folder within a particular calculation folder since they can be shared across multiple calculations. The output files from each stage are stored either in the stage folder itself, or in `out_stagename` subfolder within the stage folder.

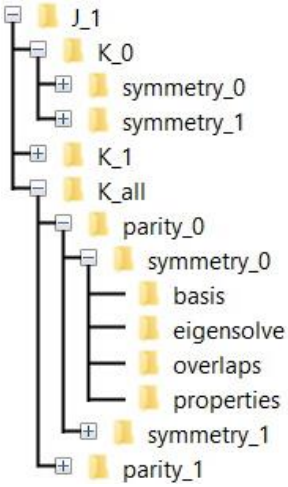

Figure 64. An example of root folder structure for $J = 1$. Inner structure of the folders marked by "+" is not shown for clarity. All folders on the same level of hierarchy have identical inner structures, except *K*-folders corresponding to a singular value of *K* skip the *parity* level.

The stage folders all need to have a copy of a configuration file with the values of K, parity, symmetry, and stage corresponding to a given subfolder. A python script `init_spectrumsdt_folders.py` in `scripts` folder is available to generate the correct folder structure, copy a given template configuration file to all target subfolders and fill out placeholder values corresponding to each folder for a given value of *K*. Run `init_spectrumsdt_folders.py --help` for more details. To keep the parameters consistent between stages, we do not recommend manually changing the configuration files generated by `init_spectrumsdt_folders.py` in the stage subfolders.

The configuration file has to be named `spectrumsdt.config` and has to be present in every stage folder. Each parameter is assigned in the format *key* = *value*. Both keys and values are case-sensitive, and each assignment has to start on a new line and finish on the same line, except for parameter groups. The order of parameters, number of spaces, empty lines, or characters after the comment mark "!" do not matter. In the case of parameter groups, the open parenthesis "(" has to be present on the same line after the assignment character "=", followed by assignment of individual parameters of the group on the following lines and ending with the close parenthesis ")" on a separate line. Some examples of input files can be found in `config_examples` folder.

All stages except `grids` support parallel execution with an arbitrary number of processes, implemented via message passing interface (MPI).

9.2.2. Grids

The purpose of this first stage is to generate grids for all APH coordinates. Even though the basis set for φ is not a DVR, a φ-grid is still generated for numerical

integration of the basis functions in φ. The grids for ρ and θ are described with the parameter groups `grid_rho` and `grid_theta`, which include at least the following parameters (determined by convergence studies):

- `from` – the left border of the grid,
- `to` – the right border of the grid,
- `step` – grid step,
- `num_points` – the total number of points in the specified interval.

Specifying `step` automatically defines `num_points` and vice versa, so these parameters cannot be specified together. All parameters with units are specified in Bohr for `grid_rho` and in degrees for `grid_theta`. The φ-grid is always defined in the range from 0 to 2π, so only the number of points is specified via `num_points_phi` key.

After this stage is completed, the three grid files corresponding to each coordinate are generated. The grid files are written in the following format: the first line specifies the values of `from`, `to`, `step` and `num_points` that were used to generate this grid. The next `num_points` lines specify the coordinate of each point and, in case of ρ-grid, Jacobian value at that point. Jacobians are meaningful only for optimized grids and are always equal to 1 for equidistant grids. All grid points are placed in the centers of their respective intervals. All values with units in the grid files are specified in Bohr for ρ-grid and radians for θ- and φ-grids.

Advanced parameters.

In the calculations of scattering resonances one typically needs to set up a long-range grid in ρ to describe the dissociation region. In these cases, using an equidistant

grid leads to unnecessarily dense points in the dissociative region. One can reduce the cost of such calculations by optimizing the grid step as described in section 9.1.4.

Enabling optimization procedure for ρ-grid requires specifying grid parameter `optimal = 1`, alongside with the necessary information to define Eq. (155), which includes the following grid parameters:

- `envelope_path` – the path to the file defining the envelope function $V(\rho)$. The function is defined by specifying its values at the grid points. Each row contains 2 numbers: ρ in Bohr and $V(\rho)$ in Hartree. The grid on which $V(\rho)$ is defined does not have to be the same as the ρ-grid for the eigenvalue problem, which allows to re-use the same envelope function for any ρ-grid. As a rule of thumb, it is recommended to use minimum energy path (MEP) along ρ in a given PES as the envelope function $V(\rho)$.

A python script `extract_MEP.py` is available in the `scripts` folder to automatically generate minimum energy path along ρ. The script takes no arguments and has to be invoked in the folder with calculated `pes.out` and grid files. The extracted MEP is written to a file named `MEP_rho.dat`. Note that the MEP does not have to be calculated precisely, since precision of MEP does not affect the precision of subsequent calculations. A rough MEP may generate slightly suboptimal grid spacing, but the final grid density is a convergence parameter, controlled by `step`.

In the program, the points specified in the MEP file are used to build a cubic spline for the right branch ($\rho > \rho_0$) of $V(\rho)$, and fit analytical Eckart potential for the left branch ($\rho < \rho_0$).

- `max_energy` – the value of E_{max} in Eq. (155) in wave numbers. This specifies the maximum total energy considered for a particle moving in the specified envelope

potential $V(\rho)$. E_{max} has to be larger than $V(\rho)$ for any value of ρ. Local density of grid points is proportional to $E_{max} - V(\rho)$, therefore E_{max} can be considered as a tool to control balance of points between the covalent well and the dissociation region. In the limiting case when E_{max} is equal to the asymptotic value of $V(\rho)$ in the dissociation region, all the grid points would be placed in the covalent well region and little or none in the dissociation region. For larger values of E_{max}, the difference between $E_{max} - V(\rho)$ in the well and dissociation regions becomes less pronounced and points are generated in a more uniform fashion.

- `solver_steps` – optional, specifies number of steps in Runge-Kutta algorithm used to solve Eq. (155). Typically, does not need to be set explicitly. The default value of 2048 is expected to work well for majority of applications.

Note that when optimized grid is requested, `step` grid parameter controls the step size in the auxiliary equidistant *x*-grid, i.e. `step` sets the value of α in Eq. (155).

In addition to these parameters, the following config parameter has to be specified to calculate the reduced particle mass μ:

- `mass` – the description of masses of atoms in the system under consideration. The masses have to be listed as 3 comma-separated numbers corresponding to masses given in atomic unit of mass (*i.e.*, in masses of an electron, m_e) of atoms in ABA order. Instead of providing an explicit value of mass, it is possible to use a shortcut consisting of an element symbol and its mass number. For example, H1 will be replaced with the mass of hydrogen-1 and O18 will be replaced with the mass of oxygen-18. These shortcuts exist for all stable isotopes of the elements in the first three periods. The exact values of

isotopic masses are taken from Ref. 139 and can be found in `src/base/constants.f90` file.

Note that `mass` is a config parameter, and not a grid parameter, therefore it is not a part of a grid parameter group and should be specified as a top-level parameter. An example of a config file that generates optimized grid for ozone can be found in `config_examples` folder.

9.2.3. Potential

Majority of PESs do not operate in APH coordinates directly, therefore a conversion from APH to a more common coordinate system is likely required. SpectrumSDT offers two ways to alleviate this procedure. One way is to use `output_coordinate_system` key to carry out coordinate conversion at `grids` stage. If used with valid values other than `aph`, `pes.in` file will be created in addition to the grid files, where each row after the header row specifies molecular geometry converted to the chosen coordinate system. In response, user needs to provide a file named `pes.out`, with the values of the PES in Hartree at geometries in `pes.in`. Note that `pes.out` is not expected to have a header line, therefore row numbering is shifted by 1 relative to `pes.in`.

The following values of `output_coordinate_system` are supported:

- `aph` – the default value. `pes.in` file is not generated since it is trivial to simply iterate the values in the grid files.
- `mass jacobi` – mass-scaled version of Jacobi coordinates. See Eqs. (52a)-(52c) in Ref. 100.

- `jacobi` – regular Jacobi coordinates, where *r* (Bohr) is the distance between the terminal A-atoms (in ABA notation); *R* (Bohr) is the distance from the center of mass between the two A atoms (midpoint) to the B atom; and Θ (in radians) is the angle between these two vectors.
- `cartesian` – molecular geometry is described with x- and y- coordinates of atom B and x-coordinate of an atom A. The remaining 6 Cartesian coordinates are fixed to 0. All values are given in Bohr.
- `all bonds` – three pair-wise distances in Bohr between the atoms. Indexes 1 and 3 are assigned to the A atoms and index 2 is assigned to B.
- `internal` – two A-B bond lengths in Bohr and A-B-A angle in radians.

Note that `mass` has to be specified if a value other than `aph` or `mass jacobi` is given to `output_coordinate_system`, since coordinate conversion is mass-dependent. This makes it necessary to re-calculate potential values for different isotopomers even if underlying PES program is the same.

Another way is to directly use `src/base/coordinate_conversion.f90` module in user's PES program to convert coordinates dynamically. In this case the user can set `output_coordinate_system` to `aph` to avoid generating `pes.in` and read the APH-grids directly. The combinations of APH points should be iterated in order ρ, θ, φ (i.e., ρ changes least frequently, φ changes most frequently). An example of a Fortran program that reads the grids and writes ozone potential of Dawes et al.[112] in this way can be found in `PES_examples/ozone/ozone_pes.f90`.

9.2.4. Basis

This stage uses the grids and potential from the previous two stages to solve 1D and 2D problems in the given potential (see section 4.5). The following parameters have to be specified:

- `J` – total angular momentum quantum number for basis functions.
- `K` – projection of total angular momentum onto *z*-axis quantum number for basis functions.
- `basis` – parameter group that includes the following parameters:
  - `num_functions_phi` – number of VBR basis functions to include in the primitive basis set for 1D problem (convergence parameter, see Eqs. (104)-(105)).
  - `symmetry` – "0" for symmetric basis functions (cosines); "1" for antisymmetric functions (sines).
  - `cutoff_energy` – maximum energy of a solution in 1D or 2D problem (convergence parameter, in wavenumbers). Solutions with energies above this are not included in the basis set.
  - `min_solutions` – minimum number of solutions retained in each 1D and 2D problem, even when energies exceed `cutoff_energy`. Typically does not need to be set. The default value of 3 is expected to work well for majority of applications.
- `grid_path` – full path to a folder with APH-grids and `pes.out` files.
- `root_path` – full path to the top-level folder of the current calculation (from where `init_spectrumsdt_folders.py` was executed).

In addition, `stage` has to be set to `basis`, and `mass` has to be specified. The number of 2D solutions kept in basis for each value of ρ is written to

`num_vectors_2d.dat` file. The binary files storing 1D and 2D basis functions are written to `out_basis` folder.

Note that multiple basis calculations with different values of `K` and `symmetry` are required for a single problem in cases when the Hamiltonian matrix consists of multiple *K*-blocks and the *adiabatic* basis set is employed.

The basis set is calculated independently for each value of ρ, which are distributed among the available processors. Therefore the number of points in ρ-grid limits the maximum number of processors that can do useful work at this stage.

9.2.5. Overlaps

This stage uses basis functions from the previous stage (`basis`) to calculate the Hamiltonian matrix elements for the row of blocks with the given value of `K`. In addition to the parameters specified at `basis` stage, the following parameters are required:

- `fixed_basis` – at this stage specifying this parameter group instructs the program to compute additional overlaps necessary for the *fixed* basis mode (see section 9.1.3).
- `use_rovib_coupling` – "0" is for uncoupled symmetric top; specifying "1" instructs the program to compute additional overlaps for the off-diagonal *K*-blocks necessary to build the Hamiltonian matrix with rotational-vibrational coupling terms (see Figure 23).

All output files from this stage are binary and are stored in the `out_overlaps` folder. Calculation of individual matrix elements is independent and distributed among available processors, therefore this stage is expected to scale efficiently with the number of processors.

9.2.6. Eigensolve

This stage uses the matrix elements computed at the previous stage (`overlaps`) to build the Hamiltonian matrix and find its eigenpairs (energies and wave functions). In addition to parameters specified at the `overlaps` stage, the following parameter are required:

- `J` – total angular momentum quantum number for the current problem. Note that this can be different from the value of `J` at the `basis` stage if *fixed* basis mode is employed.
- `parity` – the value of inversion parity of the wave functions, "0" or "1" (see Eq. (50)). Only matters if rotational-vibrational coupling is enabled (`use_rovib_coupling = 1`), $J > 0$ and the block corresponding to $K = 0$ or 1 is included in the Hamiltonian matrix.
- `symmetry` – the symmetry of the vibrational basis set in $K = 0$ block, "0" for symmetric or "1" for antisymmetric basis. The subsequent values of K have to have alternating symmetry, therefore this choice defines symmetry for all values of K included in the Hamiltonian. Note that the symmetry is always defined with respect to $K = 0$ even in cases when there is no block corresponding to $K = 0$ in the Hamiltonian matrix.
- `K` – the values of K to include in the Hamiltonian matrix. Can either be a scalar number for a symmetric top rotor calculation; "all" for a fully coupled rotational-vibrational calculation with all valid values of K for given J and *parity*, from mod(J+*parity*, 2) to J; or a custom K-range in the form $K_1..K_2$ to include only values of $K_1 \leq K \leq K_2$ for a partially coupled calculation. In the case of *adiabatic* basis, the

`basis` and `overlaps` stages of appropriate symmetry have to be finished and available for all values of *K* specified in this parameter.

- `eigensolve` – parameter group with the options for an eigenvalue solver (SLEPc). The options include the following:
    - `num_states` – number of eigenpairs to converge.
    - `ncv` – largest dimension of the working subspace, optional. Typically does not need to be set explicitly, set `mpd` instead. Determined automatically by SLEPc if left unset.
    - `mpd` – maximum projected dimension, optional, used to further restrict the size of projected eigenproblem on certain steps of the algorithm. Determined automatically by SLEPc if left unset. Refer to SLEPc manual for more details on `ncv` and `mpd` parameters.[171] For small number of eigenvalues (< 300) we recommend leaving `mpd` unset. For larger number of eigenvalues one can improve performance by setting `mpd` manually. Too small values of `mpd` lead to quickly increasing solution time, while too large values require too much memory and also worsen running time, although not as quickly as too small values. The optimal value of `mpd` is problem-dependent, but in our experience the values around 0.2*`num_states` is a good starting guess.
    - `max_iterations` – maximum number of iterations the solver is allowed to perform, optional. Typically does not need to be set explicitly. The default value of 10000 is expected to work well for majority of applications.

For calculations in the *fixed* basis mode, one has to describe what rotational state should be used for the basis set. This is done through the `fixed_basis` parameter group, which includes the following parameters:

- `J` – total angular momentum of the basis set functions.
- `K` – projection of the total angular momentum onto *z*-axis of the basis set functions.
- `root_path` – full path to the top-level folder with the `basis` and `overlaps` calculations for the values of `J` and `K` specified in this parameter group.

The lifetimes of the states are computed by adding a complex absorbing potential (CAP) in the form suggested by Manolopoulos.[152] By default CAP is not added. One can choose to add it by specifying parameter group `cap`, which consists of only one parameter:

- `min_absorbed_energy` – minimum energy at which absorption is required, specified in wavenumbers relative to energy of the dissociated molecule in the lowest dissociation channel (i.e. electronic dissociation energy plus zero-point energy). Note that enabling CAP is only meaningful for calculation of scattering resonances above the dissociation threshold.

The computed energies and widths of resonances are printed to file `states.fwc`. The wave functions are saved in binary form in `out_eigensolve` folder. This stage is parallelizable to some extent, but parallelization efficiency is decreasing with the number of processors, therefore a relatively low number of processors (around 32) is advised for efficient utilization, but higher number of processors can also be used if efficiency is not a concern.

9.2.7. Properties (Optional)

At this stage one can characterize the wave functions calculated at the previous stage by analyzing their properties, such as probability distributions over specified *sections* of the overall space and splitting of resonance width between the existing dissociation channels. The boundaries of these sections typically correspond to the edges of covalent or Van der Waals wells, or other objects of interest, which are PES-dependent, therefore it is up to the user to define them for a particular problem. Each section is defined as a new subgroup of a parameter group `wf_sections`, specified by an arbitrary unique key and may include the following parameters:

- `name` – specifies section name for the header row in the output file. Optional, the value of the key, specifying this section, will be used as `name` if this parameter is not explicitly given.
- `K` – specifies the range of the values of K for the current section, optional.
- `rho` – specifies the range of ρ-values for the current section (in Bohr), optional.
- `theta` – specifies the range of θ-values for the current section (in degrees), optional.
- `phi` – specifies the range of φ-values for the current section (in degrees), optional.
- `stat` – determines which statistic is to be calculated for the current section, optional. The possible values are `probability` (default) or `gamma` (resonance width). Specifying `gamma` instructs the program to integrate the wave function probability in a given section, multiplied by CAP, to get a portion of the overall width associated with

this section. This can be useful to calculate channel-specific decay rates of the metastable states.

All ranges are specified in the form *A..B* to include the values from *A* to *B* inclusively. The final shape of the section in the 4D (K,ρ,θ,φ) space is the intersection of the ranges specified for each individual coordinate. Omitting all range parameters defines a trivial section that spans the whole space and has to evaluate to 1 if `stat = probability`, or total resonance width if `stat = gamma`.

The method of section definition implemented here limits their shapes to hyper-rectangles, but hyper-rectangles in the APH coordinates are often what one is looking for and more complicated shapes can be approximated by adding up multiple hyper-rectangles.

The results of this stage are written to `states.fwc` file, where the first two columns duplicate the results of the previous stage, and the next *n* (number of sections) columns add the statistics corresponding to the specified sections. Each processor computes its fraction of the wave functions independently from the other processors (except for the final merge of data for printing to a file), therefore high parallelization efficiency is expected for this stage.

9.3. Application to SO_2

Numerous applications of SpectrumSDT to ozone isotopomers (especially in relation to the isotope effects) were considered in Chapters 5-8, which includes examples of symmetric top rotor calculations, partially coupled and fully coupled rotation-vibration calculations, both for bound states and scattering resonances with their lifetimes. Various checks and comparisons proving the validity of the computed results have been

presented. For example, Figures 33 and 34 provide comparison of computed energies and splittings for $J = 0$ (no rotation) with the previously reported results of Ndengué et al.[115] and Petty et al.,[117] demonstrating an excellent agreement in all cases. Figures 37 and 39 include comparison of fully coupled rotation-vibration energies for the values of J up to 5 with the results of Petty et al.[117] and APH3D program of Kendrick et al.,[104] once again showing an excellent agreement. Spectroscopical constants fitted to the computed spectrum in Tables 25, 26, 29 and 33 show a precise agreement with experimental results as well.[143,144]

In addition to plain energies and lifetimes of scattering resonances, SpectrumSDT can compute localization properties of the wave functions and channel-specific decay rates, which can be used as input for theoretical prediction of reaction rates, as it has been demonstrated in the recent study of ozone recombination reaction $O_2 + O \rightarrow O_3$ and related isotope effects.[39,51,122] The theoretical framework presented there is straightforward to generalize for application to other three-atom systems.

In this section we present a benchmark calculation to demonstrate SpectrumSDT's applicability to molecules other than ozone, on the example of sulfur dioxide (SO_2). SO_2 is an ABA-molecule, whose PES prevents its wave functions from reaching Eckart singularities at the edges of θ-coordinate, therefore it is suitable for calculations with SpectrumSDT. The calculations in this manuscript use KAKPJG MRCI-F12 PES for the singlet ground $\tilde{X}^1A_1$ state of SO_2.[172] In contrast to ozone, which has three covalent wells, SO_2 has only one well, therefore its PES is qualitatively different from ozone.

A comparison of results obtained with SpectrumSDT in this manuscript and those obtained in Klos et al.[172] with ScalIT[164,165] is presented in Figure 65. As one can see, the difference is on the order of 10^{-3} cm^{-1}, same as what we observed for the case of ozone. Therefore, we conclude that the results of SpectrumSDT are accurate and the benchmark test is successful. The exact parameters used for this calculation can be found in `config_examples/so2` folder.

9.4. Summary

In this chapter we presented a first public version of SpectrumSDT: an open-source program for calculation of energies and lifetimes of bound states and scattering resonances of ABA-molecules in APH coordinates. An extensive description of available options and practical recommendations have been provided. The accuracy of the program has been tested and verified on the examples of ozone and sulfur dioxide.

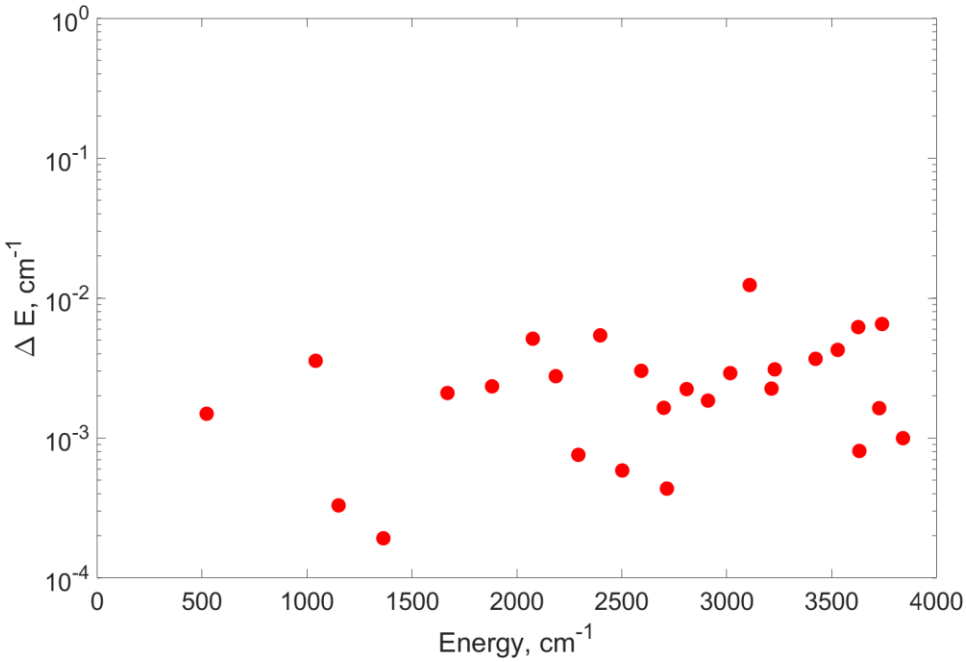

Figure 65. Comparison between the vibrational energies of SO_2 (J = 0), calculated in this manuscript and those reported in Klos et al.[172] The horizontal axis shows energies of states relative to the ground vibrational state. The vertical axis shows the absolute value of difference between the corresponding energy levels in the two sets of data.

The program, building instructions and examples of running are available in a GitHub repository.[119]

Libraries Credit

SpectrumSDT uses the following libraries:

- LAPACK for diagonalization of 1D and 2D Hamiltonians.[95]
- fdict for an implementation of dictionaries in Fortran.[173]
- SLEPc for an implementation of an iterative eigensolver.[174–176]
- PETSc as an underlying library for SLEPc.[177]

CHAPTER 10. OVERALL SUMMARY AND FUTURE WORK

In the Introduction we defined the most important fundamental concepts, such as the isotope effect, isotope fractionation, ζ-effect, and η-effect, explained the difference between mass-dependent and mass-independent fractionations and formulated the goals of this work.

We conducted electronic structure calculations (Chapter 2) for the tetrasulfur molecule to obtain two potential energy surfaces. Our first surface describes the double-well region around the isomerization pathway and is computed at the CCSD(T)-F12a/VTZ-F12 level of theory. The surface includes two degrees of freedom: the dimer-dimer distance *R*, and the gearing motion angle α. The global surface is computed at MRCI/aug-pV(T+d)Z level of theory and features an additional degree of freedom – the second bending angle. This 3D surface can be used to model the recombination reaction of tetrasulfur $S_2 + S_2 \rightarrow S_4$ and obtain vibrational states up to the dissociation threshold. These surfaces are the first ever built for the tetrasulfur molecule.

The 2D PES was used to perform calculations of the vibrational states of tetrasulfur using the custom code I developed from scratch (Chapter 3). The code uses SDT to reduce the size of the Hamiltonian matrix, as well as FFT and mixed VBR/DVR basis set. The normal mode analysis reveals strong mixing of the bending and stretching motions. Despite the simplicity of our model, the obtained results are in qualitative agreement with the experiments and lay the groundwork for future improvements.

However, to describe the recombination reaction one needs vibrational energies up to the dissociation threshold and above it (and lifetimes for scattering resonances), so for the next step in this direction we plan to finalize the 3D MRCI surface, which has a

correct dissociation limit, and carry out calculations of rovibrational spectra. The remaining three degrees of freedom in S_4 (the two double bonds and the torsional motion) are fairly independent and harmonic, therefore they can be taken into account in a statistical fashion.

The vibrational energies and lifetimes computed on such surface can be used as input data to predict the recombination reaction rate constant of tetrasulfur recombination reaction ($S_2 + S_2 \rightarrow S_4$). Note that to estimate the magnitude of the isotope effects (Eqs. (7) and (10) in Introduction) one needs the reaction rate constants not only for the unsubstituted case (all ^{32}S), but also for every isotopic combination under consideration. Three stable rare isotopes of sulfur (^{33}S, ^{34}S, ^{36}S) together with different places for substitutions constitute 6 options for single substitution and 18 options for double substitution (even more for triple and quadruple substitutions, but those cases are rare). Neither of these options has ever been considered by anyone, so they all require calculations, and these opportunities are still open.

Moreover, there are several other recombination reactions in the sulfur polymerization chain (for example, $S_4 + S_4 \rightarrow S_8$) relevant to the atmosphere of the ancient Earth, as it was discussed in the Introduction. Other reactions can contribute to the isotope effects as well, so they have to be taken into account and the same analysis as for the tetrasulfur (including calculation of a PES) needs to be repeated.

Tetrasulfur is not the only species where unusual mass-independent isotope effects are observed. Similar effects have also been observed, for example, in ozone. Considering similarity in the observed effects, it is likely that both tetrasulfur and ozone have a common origin of the isotope effects. However, in contrast to tetrasulfur, ozone is

a much better studied molecule with multiple well-tested potential energy surfaces, several calculations of vibrational and rovibrational spectra, and more available experimental data to compare with. This makes ozone molecule a good candidate for theoretical modelling and initial checking of the properties and hypotheses related to the isotope effects.

One of such hypotheses has been recently proposed by the group of Marcus.[41,123] According to their hypothesis, the coupling between rotational and vibrational degrees of freedom, neglected in the previous work of Teplukhin,[94] might be the reason behind the isotope effects in ozone. Therefore, we decided to check this hypothesis and perform such coupled rovibrational calculations.

However, the previously existing version of theory and code were not suitable to perform such calculations, so we started with derivation of necessary equations for the matrix elements (Chapter 4). The final formulas, expressed directly in terms of the basis expansion coefficients (which is most useful for practical implementations), were derived for the efficient calculations of matrix elements, for construction of the Hamiltonian matrix, for expressing the total ro-vibrational wavefunction, for the assignment of quantum numbers to the computed eigenstates, and finally for the identification of possible isotopomers of the molecule on the global PES (i.e. symmetric vs. asymmetric ozone). The developed theoretical framework was implemented in SpectrumSDT and used to study the effects of rotational-vibrational coupling on spectra of ozone and related isotope effects on multiple levels.

First, we considered the simplest case of calculation of bound vibrational states without overall rotation ($J = 0$, Chapter 5) to check whether the ratio between the

number of bound states in asymmetric and symmetric ozone molecules could by itself introduce a bias in favor of asymmetric molecules (i.e. contribute to η-effect in Eq. (18) in Introduction). Statistically, such ratio is expected to be equal to 2, but the actual accurately computed ratio might be different. The calculations that we carried out here show non-negligible deviations of this ratio from the statistically expected factor of 2. In the upper part of the spectrum, where the stabilization process of the metastable ozone species is the most sensitive, both singly- and doubly-substituted ozone molecules deviate in the same direction as observed in the experiments. This property is likely to contribute to the η-effect.

After this, we considered the effects of rotation-vibration coupling on bound spectra of ozone molecules with $J \leq 5$ (Chapter 6). We studied the individual roles of the asymmetric-top rotor term and the Coriolis coupling term and found that both of them affect the parity splittings, introduced by rovibrational coupling, but in the opposite directions, therefore partially cancelling each other out. We checked whether it is reasonable to expect that the Coriolis effect (rovibrational coupling) behaves differently in asymmetric ozone molecules, compared to the symmetric ones (the hypothesis of Marcus), but we found no justification for this hypothesis. We found that for ozone the deviations of rotational constants from the standard symmetric-top-rotor behavior is affected by isotopic composition as much as it is affected by the symmetry of the molecule.

Another relevant feature, that has never been discussed in the literature on ozone before, is the value of parity splitting (Λ-doubling) due to the Coriolis coupling effect. These splittings, accurately captured by our calculations, were determined and examined

here for $1 \leq \Lambda \leq 5$, for the four ozone isotopomers considered here. We found that these splittings are also affected by isotopic substitutions as much as they are affected by molecular symmetry. Once again we cannot claim that symmetry plays a decisive role here.

We checked how a "bulk" energy-averaged characteristic of the molecule, such as its rotational-vibrational partition function, is affected by the Coriolis coupling effect, and how much these partition functions are different in different isotopomers of ozone. We found, first of all, that for the temperatures below 500 K the effect of parity splittings on the ratio of dynamical partition functions is very small and thus the role of the Coriolis coupling is negligible. We also found that the accurately computed value of this ratio deviates from the expected statistical value of 2, but in opposite directions for the singly and doubly substituted molecules, whereas in the experiment both of these molecules behave in the same way. Although by itself this is an interesting isotope-related phenomenon, this effect is relatively small, and is driven by masses, not by the symmetry.

The conclusion of Chapter 6 are based on properties of bound states only. However, for the recombination reaction of ozone, known to be responsible for the isotope effects, the scattering resonances above the dissociation threshold play much more significant role. Therefore, for the next step (Chapter 7), we considered the effect of rotation-vibration coupling on scattering resonances for $J \leq 4$. For this we developed a modification of theory presented in Chapter 4 that permits to decrease computational cost in the case of calculation of coupled scattering resonances with large vibrational basis set. We demonstrated here that it is possible to choose one vibrational basis set, optimized for a typical rotational excitation (J, Λ) and employ it in the coupled rotation-vibration

calculations for many values of J, which provides substantial savings on basis overlap calculation.

Analysis of the computed data indicates that the average properties of scattering resonances, such as their average lifetime $\tilde{\Gamma}$, the average number of such states $\widetilde{N}$, and their cumulative partition function Q, are all affected by the rotation-vibration coupling, and this effect grows as the value of angular momentum J is increased. However, we also found that various isotopomers and isotopologues of ozone (symmetric and asymmetric ozone molecules with single and double isotopic substitutions) are influenced by the Coriolis effect rather uniformly. When the ratio η of partition functions for asymmetric vs. symmetric ozone molecules is computed, the Coriolis effect largely cancels, and this cancelation seems to occur for all values of J, similarly to what we observed before.

One can still argue that all of these conclusions are made for relatively low values of total angular momentum (J), whereas in an actual experiment at room temperature much higher rotational excitations are energetically accessible, and the effects of rovibrational coupling could be qualitatively different in this regime. Therefore, as a final step in checking the role of rotation-vibration coupling for isotope effects we considered calculations with large values of J in Chapter 8.

Such calculations are impossible to carry out in the exact, fully-coupled, way due to large size of the Hamiltonian matrix. Therefore, in order to make the calculations feasible we developed a partially coupled method that permits to capture the major contribution of ro-vibrational coupling terms without diagonalization of the entire Hamiltonian matrix. This method is approximate, but it is general and applicable to many other molecules and processes in the spectroscopic and dynamic context.

Based on the results of analysis of the resonance spectra and the dynamical partition functions that we computed here, we conclude that while the addition of rovibrational coupling appreciably increases the average number of metastable ozone states (given by the dynamical partition function), the changes are still rather uniform for both symmetric and asymmetric isotopomers of ozone. The average lifetimes of ozone molecules do not seem to be appreciably affected by the rovibrational coupling and remain similar in both symmetric and asymmetric ozone isotopomers, therefore we cannot conclude that the η-effect is associated with differences in lifetimes.

All in all, based on the results presented in Chapters 6-8, we conclude that the hypothesis of Marcus about relevance of rotation-vibration coupling (Coriolis effect) for the isotope effects in ozone does not seem to hold out and other venues need to be explored.

One particularly interesting direction is interaction between the vibrational symmetries in the covalent wells and the dissociation channels. Both even and odd symmetries and allowed in the covalent wells, but only odd symmetries are allowed in the homonuclear dissociation channel. However, in the present version of theory and program (SpectrumSDT), the computed states are required to maintain the same vibrational symmetry in both the covalent well and in the dissociation region, therefore even covalent states dissociate to even O_2 states, which are forbidden. Such behavior is unphysical and can be fixed by taking into account the effect of geometric (Berry's) phase, which makes the wave function to change sign for any closed trajectory around a conical intersection.

Another possible direction involves consideration of alternative potential energy surfaces for ozone. All calculations in this work have been performed on the surface of Dawes et al.[112] However, another surface by Tyuterev et al.[113] also exists. According to a recent study,[146] calculations of the isotope exchange reaction on this surface are in slightly better agreement with the experimental data, therefore it would be interesting to see if differences in PES could translate into η-effect.

Finally, in Chapter 9 we presented a first public version of SpectrumSDT program, which is able to carry out calculations of energies and lifetimes of bound states and scattering resonances of any ABA-molecules (not limited to ozone) and supports all options considered in other chapters for ozone. An extensive description of available options and practical recommendations have been provided. The accuracy of the program has been tested and verified on the examples of ozone and sulfur dioxide.

In this release of the code, SpectrumSDT is limited to ABA/AAB-type molecules with wave functions that do not extend into the regions near Eckart singularities. Both of these limitations need to be lifted to increase the number of systems SpectrumSDT can be applied to. Extension to both AAA- and ABC-type systems can be implemented relatively easily by changing the symmetry of the basis set functions. As discussed in Ref. 104, the problem with Eckart singularities can be solved by using, for example, a special basis set, which analytically cancels out the singularities in the expressions for the Hamiltonian matrix elements.

Another interesting direction for development is an implementation of a mixed coordinate system. The APH coordinates, considered in this work are well-suited for description of the covalent wells region, but are not optimal in the asymptotic

dissociation region due to poor coverage of relevant molecular configurations. One could take a coordinate system better suited for the dissociation region (say, Delves coordinates) and work out a switching strategy between the covalent well coordinates and dissociation coordinates in order to have a good description everywhere.

Several of these ideas will be implemented during my postdoctoral project, supported by MolSSI.

BIBLIOGRAPHY

(1) Muller, É.; Philippot, P.; Rollion-Bard, C.; Cartigny, P. Multiple Sulfur-Isotope Signatures in Archean Sulfates and Their Implications for the Chemistry and Dynamics of the Early Atmosphere. *Proc. Natl. Acad. Sci. U. S. A.* **2016**, *113*, 7432–7437.

(2) Domagal-Goldman, S. D.; Poirier, B.; Wing, B. A. Mass-Independent Fractionation of Sulfur Isotopes: Carriers and Sources; 2011.

(3) Dauphas, N.; Schauble, E. A. Mass Fractionation Laws, Mass-Independent Effects, and Isotopic Anomalies. *Annu. Rev. Earth Planet. Sci.* **2016**, *44*, 709–783.

(4) Johnston, D. T. Multiple Sulfur Isotopes and the Evolution of Earth's Surface Sulfur Cycle. *Earth-Science Rev.* **2011**, *106*, 161–183.

(5) Farquhar, J.; Bao, H.; Thiemens, M. H. Atmospheric Influence of Earth's Earliest Sulfur Cycle. *Science (80-.).* **2000**, *289*, 756–758.

(6) Ono, S.; Eigenbrode, J. L.; Pavlov, A. A.; Kharecha, P.; Rumble, D.; Kasting, J. F.; Freeman, K. H. New Insights into Archean Sulfur Cycle from Mass-Independent Sulfur Isotope Records from the Hamersley Basin, Australia. *Earth Planet. Sci. Lett.* **2003**, *213*, 15–30.

(7) Ono, S.; Kaufman, A. J.; Farquhar, J.; Sumner, D. Y.; Beukes, N. J. Lithofacies Control on Multiple-Sulfur Isotope Records and Neoarchean Sulfur Cycles. *Precambrian Res.* **2009**, *169*, 58–67.

(8) Eiler, J. M.; Bergquist, B.; Bourg, I.; Cartigny, P.; Farquhar, J.; Gagnon, A.; Guo, W.; Halevy, I.; Hofmann, A.; Larson, T. E.; et al. Frontiers of Stable Isotope Geoscience. *Chem. Geol.* **2014**, *372*, 119–143.

(9) Farquhar, J.; Wing, B. A. Multiple Sulfur Isotopes and the Evolution of the Atmosphere. *Earth Planet. Sci. Lett.* **2003**, *213*, 1–13.

(10) Kaufman, A. J.; Johnston, D. T.; Farquhar, J.; Masterson, A. L.; Lyons, T. W.; Bates, S.; Anbar, A. D.; Arnold, G. L.; Garvin, J.; Buick, R. Late Archean Biospheric Oxygenation and Atmospheric Evolution. *Science (80-.).* **2007**, *317*, 1900–1903.

(11) Kasting, J. F. The Rise of Atmospheric Oxygen. *Science (80-.).* **2001**, *293*, 819–820.

(12) Farquhar, J.; Savarino, J.; Airieau, S.; Thiemens, M. H. Observation of Wavelength-Sensitive Mass-Independent Sulfur Isotope Effects during SO_2 Photolysis: Implications for the Early Atmosphere. *J. Geophys. Res. Planets* **2001**, *106*, 32829–32839.

(13) Farquhar, J.; Johnston, D. T.; Wing, B. A.; Habicht, K. S.; Canfield, D. E.; Airieau, S.; Thiemens, M. H. Multiple Sulphur Isotopic Interpretations of Biosynthetic Pathways: Implications for Biological Signatures in the Sulphur Isotope Record. *Geobiology* **2003**, *1*, 27–36.

(14) Rumble, D. A Mineralogical and Geochemical Record of Atmospheric Photochemistry. *Am. Mineral.* **2005**, *90*, 918–930.

(15) Ono, S.; Whitehill, A. R.; Lyons, J. R. Contribution of Isotopologue Self-Shielding to Sulfur Mass-Independent Fractionation during Sulfur Dioxide Photolysis. *J. Geophys. Res. Atmos.* **2013**, *118*, 2444–2454.

(16) Lin, Y.; Sim, M. S.; Ono, S. Multiple-Sulfur Isotope Effects during Photolysis of Carbonyl Sulfide. *Atmos. Chem. Phys.* **2011**, *11*, 10283–10292.

(17) Whitehill, A. R.; Xie, C.; Hu, X.; Xie, D.; Guo, H.; Ono, S. Vibronic Origin of Sulfur Mass-Independent Isotope Effect in Photoexcitation of SO_2 and the Implications to the Early Earth's Atmosphere. *Proc. Natl. Acad. Sci. U. S. A.* **2013**, *110*, 17697–17702.

(18) Whitehill, A. R.; Jiang, B.; Guo, H.; Ono, S. SO_2 Photolysis as a Source for Sulfur Mass-Independent Isotope Signatures in Stratospehric Aerosols. *Atmos. Chem. Phys.* **2015**, *15*, 1843–1864.

(19) Endo, Y.; Ueno, Y.; Aoyama, S.; Danielache, S. O. Sulfur Isotope Fractionation by Broadband UV Radiation to Optically Thin SO_2 under Reducing Atmosphere. *Earth Planet. Sci. Lett.* **2016**, *453*, 9–22.

(20) Tokue, I.; Nanbu, S. Theoretical Studies of Absorption Cross Sections for the $\tilde{C}^1B_2$-$\tilde{X}^1A_1$ System of Sulfur Dioxide and Isotope Effects. *J. Chem. Phys.* **2010**, *132*, 024301.

(21) Xie, C.; Jiang, B.; Kłos, J.; Kumar, P.; Alexander, M. H.; Poirier, B.; Guo, H. Final State Resolved Quantum Predissociation Dynamics of $SO_2(\tilde{C}^1B_2)$ and Its Isotopomers via a Crossing with a Singlet Repulsive State. *J. Phys. Chem. A* **2017**, *121*, 4930–4938.

(22) Babikov, D. Recombination Reactions as a Possible Mechanism of Mass-Independent Fractionation of Sulfur Isotopes in the Archean Atmosphere of Earth. *Proc. Natl. Acad. Sci. U. S. A.* **2017**, *114*, 3062–3067.

(23) Babikov, D.; Semenov, A.; Teplukhin, A. One Possible Source of Mass-Independent Fractionation of Sulfur Isotopes in the Archean Atmosphere of Earth. *Geochim. Cosmochim. Acta* **2017**, *204*, 388–406.

(24) Kumar, M.; Francisco, J. S. Elemental Sulfur Aerosol-Forming Mechanism. *Proc. Natl. Acad. Sci.* **2017**, *114*, 864–869.

(25) Lyons, J. R. An Estimate of the Equilibrium Speciation of Sulfur Vapor over Solid Sulfur and Implications for Planetary Atmospheres. *J. Sulfur Chem.* **2008**, *29*, 269–279.

(26) Pavlov, A. A.; Kasting, J. F. Mass-Independent Fractionation of Sulfur Isotopes in Archean Sediments: Strong Evidence for an Anoxic Archean Atmosphere. *Astrobiology* **2002**, *2*, 27–41.

(27) Claire, M. W.; Kasting, J. F.; Domagal-Goldman, S. D.; Stüeken, E. E.; Buick, R.; Meadows, V. S. Modeling the Signature of Sulfur Mass-Independent Fractionation Produced in the Archean Atmosphere. *Geochim. Cosmochim. Acta* **2014**, *141*, 365–380.

(28) Harman, C. E.; Pavlov, A. A.; Babikov, D.; Kasting, J. F. Chain Formation as a Mechanism for Mass-Independent Fractionation of Sulfur Isotopes in the Archean Atmosphere. *Earth Planet. Sci. Lett.* **2018**, *496*, 238–247.

(29) Thiemens, M. H.; Chakraborty, S.; Dominguez, G. The Physical Chemistry of Mass-Independent Isotope Effects and Their Observation in Nature. *Annu. Rev. Phys. Chem.* **2012**, *63*, 155–177.

(30) Gao, Y. Q.; Marcus, R. A. Strange and Unconventional Isotope Effects in Ozone Formation. *Science (80-.).* **2001**, *293*, 259–263.

(31) Thiemens, M. H. Nonmass-Dependent Isotopic Fractionation Processes: Mechanisms and Recent Observations in Terrestrial and Extraterrestrial Environments. In *Treatise on Geochemistry*; Elsevier, 2007; Vol. 4, pp 1–24.

(32) Thiemens, M. H. Mass-Independent Isotope Effects in Planetary Atmospheres and the Early Solar System. *Science (80-.).* **1999**, *283*, 341–345.

(33) Mauersberger, K.; Erbacher, B.; Krankowsky, D.; Günther, J.; Nickel, R. Ozone Isotope Enrichment: Isotopomer-Specific Rate Coefficients. *Science (80-.).* **1999**, *283*, 370–372.

(34) Mauersberger, K. Measurement of Heavy Ozone in the Stratosphere. *Geophys. Res. Lett.* **1981**, *8*, 935–937.

(35) Thiemens, M. H.; Heidenreich, J. E. The Mass-Independent Fractionation of Oxygen: A Novel Isotope Effect and Its Possible Cosmochemical Implications. *Science (80-.).* **1983**, *219*, 1073–1075.

(36) Morton, J.; Barnes, J.; Schueler, B.; Mauersberger, K. Laboratory Studies of Heavy Ozone. *J. Geophys. Res.* **1990**, *95*, 901.

(37) Lide, D. R. *CRC Handbook of Chemistry and Physics*, 85th ed.; CRC Press, 2004.

(38) Janssen, C.; Guenther, J.; Mauersberger, K.; Krankowsky, D. Kinetic Origin of the

Ozone Isotope Effect: A Critical Analysis of Enrichments and Rate Coefficients. *Phys. Chem. Chem. Phys.* **2001**, *3*, 4718–4721.

(39) Teplukhin, A.; Babikov, D. Several Levels of Theory for Description of Isotope Effects in Ozone: Symmetry Effect and Mass Effect. *J. Phys. Chem. A* **2018**, *122*, 9177–9190.

(40) Hathorn, B. C.; Marcus, R. A. An Intramolecular Theory of the Mass-Independent Isotope Effect for Ozone. II. Numerical Implementation at Low Pressures Using a Loose Transition State. *J. Chem. Phys.* **2000**, *113*, 9497–9509.

(41) Kryvohuz, M.; Marcus, R. A. Coriolis Coupling as a Source of Non-RRKM Effects in Ozone Molecule: Lifetime Statistics of Vibrationally Excited Ozone Molecules. *J. Chem. Phys.* **2010**, *132*, 224305.

(42) Marcus, R. A. Theory of Mass-Independent Fractionation of Isotopes, Phase Space Accessibility, and a Role of Isotopic Symmetry. *Proc. Natl. Acad. Sci.* **2013**, *110*, 17703–17707.

(43) Tuzson, B. Symmetry Specific Study of Ozone Isotopomer Formation, University of Heidelberg, 2005.

(44) Schinke, R.; Grebenshchikov, S. Y.; Ivanov, M. V.; Fleurat-Lessard, P. Dynamical Studies of the Ozone Isotope Effect: A Status Report. *Annu. Rev. Phys. Chem.* **2006**, *57*, 625–661.

(45) Ivanov, M. V.; Grebenshchikov, S. Y.; Schinke, R. Intra- and Intermolecular Energy Transfer in Highly Excited Ozone Complexes. *J. Chem. Phys.* **2004**, *120*, 10015–10024.

(46) Ivanov, M. V.; Schinke, R. Temperature Dependent Energy Transfer in Ar–O_3 Collisions. *J. Chem. Phys.* **2005**, *122*, 234318.

(47) Babikov, D.; Kendrick, B. K.; Walker, R. B.; Pack, R. T.; Fleurat-Lessard, P.; Schinke, R. Metastable States of Ozone Calculated on an Accurate Potential Energy Surface. *J. Chem. Phys.* **2003**, *118*, 6298–6308.

(48) Babikov, D.; Kendrick, B. K.; Walker, R. B.; Pack, R. T.; Fleurat-Lessard, P.; Schinke, R. Formation of Ozone: Metastable States and Anomalous Isotope Effect. *J. Chem. Phys.* **2003**, *119*, 2577–2589.

(49) Babikov, D.; Kendrick, B. K.; Walker, R. B.; Schinke, R.; Pack, R. T. Quantum Origin of an Anomalous Isotope Effect in Ozone Formation. *Chem. Phys. Lett.* **2003**, *372*, 686–691.

(50) Grebenshchikov, S. Y.; Schinke, R. Towards Quantum Mechanical Description of the Unconventional Mass-Dependent Isotope Effect in Ozone: Resonance Recombination in the Strong Collision Approximation. *J. Chem. Phys.* **2009**, *131*,

181103.

(51) Teplukhin, A.; Gayday, I.; Babikov, D. Several Levels of Theory for Description of Isotope Effects in Ozone: Effect of Resonance Lifetimes and Channel Couplings. *J. Chem. Phys.* **2018**, *149*, 164302.

(52) Ivanov, M. V.; Schinke, R. Vibrational Energy Transfer in Ar–O_3 Collisions: Comparison of Rotational Sudden, Breathing Sphere, and Classical Calculations. *Mol. Phys.* **2010**, *108*, 259–268.

(53) Ivanov, M. V.; Babikov, D. On Stabilization of Scattering Resonances in Recombination Reaction That Forms Ozone. *J. Chem. Phys.* **2016**, *144*, 154301.

(54) Adler, T. B.; Knizia, G.; Werner, H.-J. A Simple and Efficient CCSD(T)-F12 Approximation. *J. Chem. Phys.* **2007**, *127*, 221106.

(55) Werner, H.-J.; Knizia, G.; Manby, F. R. Explicitly Correlated Coupled Cluster Methods with Pair-Specific Geminals. *Mol. Phys.* **2011**, *109*, 407–417.

(56) Werner, H.-J.; Knowles, P. J. An Efficient Internally Contracted Multiconfiguration-Reference Configuration Interaction Method. *J. Chem. Phys.* **1988**, *89*, 5803–5814.

(57) Knowles, P. J.; Werner, H. An Efficient Method for the Evaluation of Coupling Coefficients in Configuration Interaction Calculations. *Chem. Phys. Lett.* **1988**, *145*, 514–522.

(58) Shamasundar, K. R.; Knizia, G.; Werner, H.-J. A New Internally Contracted Multi-Reference Configuration Interaction Method. *J. Chem. Phys.* **2011**, *135*, 054101.

(59) Hampel, C.; Peterson, K. A.; Werner, H.-J. A Comparison of the Efficiency and Accuracy of the Quadratic Configuration Interaction (QCISD), Coupled Cluster (CCSD), and Brueckner Coupled Cluster (BCCD) Methods. *Chem. Phys. Lett.* **1992**, *190*, 1–12.

(60) Deegan, M. J. O.; Knowles, P. J. Perturbative Corrections to Account for Triple Excitations in Closed and Open Shell Coupled Cluster Theories. *Chem. Phys. Lett.* **1994**, *227*, 321–326.

(61) Grant, D. J.; Dixon, D. A.; Francisco, J. S. Coupled Cluster Study of the Energetic Properties of S_2^X (X=0,+1,1). *J. Chem. Phys.* **2007**, *126*, 144308.

(62) Francisco, J. S.; Lyons, J. R.; Williams, I. H. High-Level Ab Initio Studies of the Structure, Vibrational Spectra, and Energetics of S_3. *J. Chem. Phys.* **2005**, *123*, 054302.

(63) Peterson, K. A.; Lyons, J. R.; Francisco, J. S. An Ab Initio Study of the Low-

Lying Electronic States of S_3. *J. Chem. Phys.* **2006**, *125*, 084314.

(64) Du, S.; Francisco, J. S.; Shepler, B. C.; Peterson, K. A. Determination of the Rate Constant for Sulfur Recombination by Quasiclassical Trajectory Calculations. *J. Chem. Phys.* **2008**, *128*, 204306.

(65) Du, S.; Germann, T. C.; Francisco, J. S.; Peterson, K. A.; Yu, H.-G.; Lyons, J. R. The Kinetics Study of the $S + S_2 \rightarrow S_3$ Reaction by the Chaperone Mechanism. *J. Chem. Phys.* **2011**, *134*, 154508.

(66) Matus, M. H.; Dixon, D. A.; Peterson, K. A.; Harkless, J. A. W.; Francisco, J. S. Coupled-Cluster Study of the Electronic Structure and Energetics of Tetrasulfur, S_4. *J. Chem. Phys.* **2007**, *127*, 174305.

(67) Eckert, B.; Steudel, R. Molecular Spectra of Sulfur Molecules and Solid Sulfur Allotropes; 2003; pp 31–98.

(68) Ramírez-Solís, A.; Jolibois, F.; Maron, L. Ab Initio Molecular Dynamics Studies of Tetrasulfur. Dynamics Coupling the C_{2v} Open and D_{2h} Closed Forms of S_4. *J. Phys. Chem. A* **2010**, *114*, 12378–12383.

(69) Werner, H.-J.; Knowles, P. J.; Knizia, G.; Manby, F. R.; Schütz, M. Molpro: A General-Purpose Quantum Chemistry Program Package. *Wiley Interdiscip. Rev. Comput. Mol. Sci.* **2012**, *2*, 242–253.

(70) Werner, H.-J.; Knowles, P. J.; Knizia, G.; Manby, F. R.; Schütz, M.; Celani, P.; Györffy, W.; Kats, D.; Korona, T.; Lindh, R.; et al. MOLPRO, Version 2015.1, a Package of Ab Initio Programs.

(71) McCarthy, M. C.; Thorwirth, S.; Gottlieb, C. A.; Thaddeus, P. Tetrasulfur, S4: Rotational Spectrum, Interchange Tunneling, and Geometrical Structure. *J. Chem. Phys.* **2004**, *121*, 632–635.

(72) Thorwirth, S.; McCarthy, M. C.; Gottlieb, C. A.; Thaddeus, P.; Gupta, H.; Stanton, J. F. Rotational Spectroscopy and Equilibrium Structures of S_3 and S_4. *J. Chem. Phys.* **2005**, *123*, 054326.

(73) Knowles, P. J.; Hampel, C.; Werner, H.-J. Coupled Cluster Theory for High Spin, Open Shell Reference Wave Functions. *J. Chem. Phys.* **1993**, *99*, 5219–5227.

(74) Knowles, P. J.; Hampel, C.; Werner, H.-J. Erratum: Coupled Cluster Theory for High Spin, Open Shell Reference Wave Functions. *J. Chem. Phys.* **2000**, *112*, 3106–3107.

(75) Knizia, G.; Adler, T. B.; Werner, H.-J. Simplified CCSD(T)-F12 Methods: Theory and Benchmarks. *J. Chem. Phys.* **2009**, *130*, 054104.

(76) Paukku, Y.; Yang, K. R.; Varga, Z.; Truhlar, D. G. Global Ab Initio Ground-State

Potential Energy Surface of N_4. *J. Chem. Phys.* **2013**, *139*, 044309.

(77) Bender, J. D.; Doraiswamy, S.; Truhlar, D. G.; Candler, G. V. Potential Energy Surface Fitting by a Statistically Localized, Permutationally Invariant, Local Interpolating Moving Least Squares Method for the Many-Body Potential: Method and Application to N_4. *J. Chem. Phys.* **2014**, *140*, 054302.

(78) Braams, B. J.; Bowman, J. M. Permutationally Invariant Potential Energy Surfaces in High Dimensionality. *Int. Rev. Phys. Chem.* **2009**, *28*, 577–606.

(79) Ayouz, M.; Babikov, D. Improved Potential Energy Surface of Ozone Constructed Using the Fitting by Permutationally Invariant Polynomial Function. *Adv. Phys. Chem.* **2012**, *2012*, 1–9.

(80) Ayouz, M.; Babikov, D. Global Permutationally Invariant Potential Energy Surface for Ozone Forming Reaction. *J. Chem. Phys.* **2013**, *138*, 164311.

(81) Ivanov, M. V.; Babikov, D. Mixed Quantum-Classical Theory for the Collisional Energy Transfer and the Rovibrational Energy Flow: Application to Ozone Stabilization. *J. Chem. Phys.* **2011**, *134*, 144107.

(82) Clary, D. C. Quantum Dynamics of the $O(^3P)+CH_4 \rightarrow CH_3+OH$ Reaction. *Phys. Chem. Chem. Phys.* **1999**, *1*, 1173–1179.

(83) Yu, H.-G.; Nyman, G. Quantum Dynamics of the $O(^3P)+CH_4 \rightarrow OH+CH_3$ Reaction: An Application of the Rotating Bond Umbrella Model and Spectral Transform Subspace Iteration. *J. Chem. Phys.* **2000**, *112*, 238–247.

(84) Sun, Q.; Bowman, J. M. Reduced Dimensionality Quantum Reactive Scattering: H_2 +CN→H+HCN. *J. Chem. Phys.* **1990**, *92*, 5201–5210.

(85) de Boor, C. *A Practical Guide to Splines*; Springer: New-York, 1978.

(86) Jiang, J.; Park, G. B.; Field, R. W. The Rotation-Vibration Structure of the SO_2 $\tilde{C}^1B_2$ State Explained by a New Internal Coordinate Force Field. *J. Chem. Phys.* **2016**, *144*, 144312.

(87) Park, G. B.; Jiang, J.; Field, R. W. The Origin of Unequal Bond Lengths in the C^1B_2 State of SO_2: Signatures of High-Lying Potential Energy Surface Crossings in the Low-Lying Vibrational Structure. *J. Chem. Phys.* **2016**, *144*, 144313.

(88) Kumar, P.; Jiang, B.; Guo, H.; Kłos, J.; Alexander, M. H.; Poirier, B. Photoabsorption Assignments for the $\tilde{C}^1B_2 \leftarrow \tilde{X}^1A_1$ Vibronic Transitions of SO_2, Using New Ab Initio Potential Energy and Transition Dipole Surfaces. *J. Phys. Chem. A* **2017**, *121*, 1012–1021.

(89) Gayday, I.; Teplukhin, A.; Babikov, D. Computational Analysis of Vibrational Modes in Tetra-Sulfur Using Dimensionally Reduced Potential Energy Surface.

Mol. Phys. **2019**, *117*, 2546–2558.

(90) Knowles, P. J.; Werner, H.-J. Internally Contracted Multiconfiguration-Reference Configuration Interaction Calculations for Excited States. *Theor. Chim. Acta* **1992**, *84*, 95–103.

(91) Tennyson, J.; van der Avoird, A. Quantum Dynamics of the van Der Waals Molecule $(N_2)_2$: An Ab Initio Treatment. *J. Chem. Phys.* **1982**, *77*, 5664–5681.

(92) Bačić, Z.; Light, J. C. Highly Excited Vibrational Levels of '"Floppy"' Triatomic Molecules: A Discrete Variable Representation—Distributed Gaussian Basis Approach. *J. Chem. Phys.* **1986**, *85*, 4594–4604.

(93) Teplukhin, A.; Babikov, D. Efficient Method for Calculations of Ro-Vibrational States in Triatomic Molecules near Dissociation Threshold: Application to Ozone. *J. Chem. Phys.* **2016**, *145*, 114106.

(94) Teplukhin, A. Theoretical Study of Ozone Forming Recombination Reaction and Anomalous Isotope Effect Associated with It, Marquette University, Milwaukee, 2017.

(95) Anderson, E.; Bai, Z.; Bischof, C.; Blackford, S.; Demmel, J.; Dongarra, J.; Croz, J.; Greenbaum, A.; Hammarling, S.; McKenney, A.; et al. *LAPACK Users' Guide*, 3rd ed.; Society for Industrial and Applied Mathematics: Philadelphia, 1999.

(96) Kokoouline, V.; Dulieu, O.; Kosloff, R.; Masnou-Seeuws, F. Mapped Fourier Methods for Long-Range Molecules: Application to Perturbations in the $Rb_2(0_u^+)$ Photoassociation Spectrum. *J. Chem. Phys.* **1999**, *110*, 9865–9876.

(97) Meyer, R. Trigonometric Interpolation Method for One-Dimensional Quantum-Mechanical Problems. *J. Chem. Phys.* **1970**, *52*, 2053–2059.

(98) Hassanzadeh, P.; Andrews, L. Vibronic Absorption Spectra of Sulfur (S_3 and S_4) in Solid Argon. *J. Phys. Chem.* **1992**, *96*, 6579–6585.

(99) Boumedien, M. S.; Corset, J.; Picquenard, E. Vibrational Study and Molecular Structure of Two S_4 Isomers in Sulphur Vapour. *J. Raman Spectrosc.* **1999**, *30*, 463–472.

(100) Pack, R. T.; Parker, G. A. Quantum Reactive Scattering in Three Dimensions Using Hyperspherical (APH) Coordinates. Theory. *J. Chem. Phys.* **1987**, *87*, 3888–3921.

(101) Teplukhin, A.; Babikov, D. Interactive Tool for Visualization of Adiabatic Adjustment in APH Coordinates for Computational Studies of Vibrational Motion and Chemical Reactions. *Chem. Phys. Lett.* **2014**, *614*, 99–103.

(102) Teplukhin, A.; Babikov, D. Visualization of Potential Energy Function Using an

Isoenergy Approach and 3D Prototyping. *J. Chem. Educ.* **2015**, *92*, 305–309.

(103) Johnson, B. R. The Quantum Dynamics of Three Particles in Hyperspherical Coordinates. *J. Chem. Phys.* **1983**, *79*, 1916–1925.

(104) Kendrick, B. K.; Pack, R. T.; Walker, R. B.; Hayes, E. F. Hyperspherical Surface Functions for Nonzero Total Angular Momentum. I. Eckart Singularities. *J. Chem. Phys.* **1999**, *110*, 6673–6693.

(105) Blandon, J.; Parker, G. A.; Madrid, C. Mapped Grid Methods Applied to the Slow Variable Discretization–Enhanced Renormalized Numerov Approach. *J. Phys. Chem. A* **2016**, *120*, 785–792.

(106) Kokoouline, V.; Greene, C. H. Unified Theoretical Treatment of Dissociative Recombination of D_{3h} Triatomic Ions: Application to H_3^+ and D_3^+. *Phys. Rev. A* **2003**, *68*, 012703.

(107) Gayday, I.; Teplukhin, A.; Kendrick, B. K.; Babikov, D. Theoretical Treatment of the Coriolis Effect Using Hyperspherical Coordinates, with Application to the Ro-Vibrational Spectrum of Ozone. *J. Phys. Chem. A* **2020**, *124*, 2808–2819.

(108) Davydov, A. S. *Quantum Mechanics*; Haar, D. Ter, Ed.; Pergamon Press, 1965.

(109) Bačić, Z.; Whitnell, R. M.; Brown, D.; Light, J. C. Localized Representations for Large Amplitude Molecular Vibrations. *Comput. Phys. Commun.* **1988**, *51*, 35–47.

(110) Light, J. C.; Carrington, T. Discrete-Variable Representations and Their Utilization. In *Advances in Chemical Physics*; Prigogine, I., Rice, S. A., Eds.; John Wiley & Sons, 2000; Vol. 114, pp 263–310.

(111) Fábri, C.; Mátyus, E.; Császár, A. G. Rotating Full- and Reduced-Dimensional Quantum Chemical Models of Molecules. *J. Chem. Phys.* **2011**, *134*, 074105.

(112) Dawes, R.; Lolur, P.; Li, A.; Jiang, B.; Guo, H. Communication: An Accurate Global Potential Energy Surface for the Ground Electronic State of Ozone. *J. Chem. Phys.* **2013**, *139*, 201103.

(113) Tyuterev, V. G.; Kochanov, R. V.; Tashkun, S. A.; Holka, F.; Szalay, P. G. New Analytical Model for the Ozone Electronic Ground State Potential Surface and Accurate Ab Initio Vibrational Predictions at High Energy Range. *J. Chem. Phys.* **2013**, *139*, 134307.

(114) Siebert, R.; Schinke, R.; Bittererová, M. Spectroscopy of Ozone at the Dissociation Threshold: Quantum Calculations of Bound and Resonance States on a New Global Potential Energy Surface. *Phys. Chem. Chem. Phys.* **2001**, *3*, 1795–1798.

(115) Ndengué, S. A.; Dawes, R.; Wang, X.-G.; Carrington, T.; Sun, Z.; Guo, H.

Calculated Vibrational States of Ozone up to Dissociation. *J. Chem. Phys.* **2016**, *144*, 074302.

(116) Lapierre, D.; Alijah, A.; Kochanov, R. V.; Kokoouline, V.; Tyuterev, V. G. Lifetimes and Wave Functions of Ozone Metastable Vibrational States near the Dissociation Limit in a Full-Symmetry Approach. *Phys. Rev. A* **2016**, *94*, 042514.

(117) Petty, C.; Spada, R. F. K.; Machado, F. B. C.; Poirier, B. Accurate Rovibrational Energies of Ozone Isotopologues up to J = 10 Utilizing Artificial Neural Networks. *J. Chem. Phys.* **2018**, *149*, 024307.

(118) Gayday, I.; Teplukhin, A.; Babikov, D. The Ratio of the Number of States in Asymmetric and Symmetric Ozone Molecules Deviates from the Statistical Value of 2. *J. Chem. Phys.* **2019**, *150*, 101104.

(119) SpectrumSDT https://github.com/IgorGayday/SpectrumSDT.

(120) Ivanov, M. V.; Babikov, D. Collisional Stabilization of van Der Waals States of Ozone. *J. Chem. Phys.* **2011**, *134*, 174308.

(121) Hippler, H.; Rahn, R.; Troe, J. Temperature and Pressure Dependence of Ozone Formation Rates in the Range 1–1000 Bar and 90–370 K. *J. Chem. Phys.* **1990**, *93*, 6560–6569.

(122) Teplukhin, A.; Babikov, D. Properties of Feshbach and "Shape"-Resonances in Ozone and Their Role in Recombination Reactions and Anomalous Isotope Effects. *Faraday Discuss.* **2018**, *212*, 259–280.

(123) Kryvohuz, M.; Marcus, R. A. Coriolis Coupling as a Source of Non-RRKM Effects in Triatomic near-Symmetric Top Molecules: Diffusive Intramolecular Energy Exchange between Rotational and Vibrational Degrees of Freedom. *J. Chem. Phys.* **2010**, *132*, 224304.

(124) Teplukhin, A.; Babikov, D. A Full-Dimensional Model of Ozone Forming Reaction: The Absolute Value of the Recombination Rate Coefficient, Its Pressure and Temperature Dependencies. *Phys. Chem. Chem. Phys.* **2016**, *18*, 19194–19206.

(125) Pack, R. T. Space-fixed vs Body-fixed Axes in Atom-diatomic Molecule Scattering. Sudden Approximations. *J. Chem. Phys.* **1974**, *60*, 633–639.

(126) Kumar, P.; Ellis, J.; Poirier, B. Rovibrational Bound States of SO_2 Isotopologues. I: Total Angular Momentum J=0–10. *Chem. Phys.* **2015**, *450–451*, 59–73.

(127) Kumar, P.; Poirier, B. Rovibrational Bound States of SO_2 Isotopologues. II: Total Angular Momentum J=11–20. *Chem. Phys.* **2015**, *461*, 34–46.

(128) Kumar, P.; Poirier, B. Isotope Shifts and Band Progressions in SO_2 Rovibrational

Energy Levels: Using Quantum Theory to Extract Rotational Constants. *Mol. Phys.* **2019**, *117*, 2456–2469.

(129) Herzberg, G. *Molecular Spectra and Molecular Structure II. Infrared and Raman Spectra of Polyatomic Molecules*, 10th ed.; Lancaster Press Inc.: Lancaster, 1962.

(130) Tennyson, J.; Henderson, J. R. Highly Excited Rovibrational States Using a Discrete Variable Representation: The H^+_3 Molecular Ion. *J. Chem. Phys.* **1989**, *91*, 3815–3825.

(131) Tennyson, J.; Sutcliffe, B. T. Variationally Exact Rovibrational Spectra of Nonrigid Triatomics: The HeHF van Der Waals Molecule. *J. Chem. Phys.* **1983**, *79*, 43–51.

(132) Brocks, G.; Tennyson, J. Ab Initio Rovibrational Spectrum of LiNC and LiCN. *J. Mol. Spectrosc.* **1983**, *99*, 263–278.

(133) Miller, S.; Tennyson, J.; Follmeg, B.; Rosmus, P.; Werner, H.-J. Ab Initio Investigation of the Bound Rovibrational States in the Electronic Ground State of HeN^+_2. *J. Chem. Phys.* **1988**, *89*, 2178–2184.

(134) Sarkar, P.; Poulin, N.; Carrington, T. Calculating Rovibrational Energy Levels of a Triatomic Molecule with a Simple Lanczos Method. *J. Chem. Phys.* **1999**, *110*, 10269–10274.

(135) Tarczay, G.; Császár, A. G.; Polyansky, O. L.; Tennyson, J. Ab Initio Rovibrational Spectroscopy of Hydrogen Sulfide. *J. Chem. Phys.* **2001**, *115*, 1229–1242.

(136) Chen, W.; Poirier, B. Quantum Dynamical Calculation of All Rovibrational States of HO_2 for Total Angular Momentum J=0-10. *J. Theor. Comput. Chem.* **2010**, *09*, 435–469.

(137) Brandon, D.; Poirier, B. Accurate Calculations of Bound Rovibrational States for Argon Trimer. *J. Chem. Phys.* **2014**, *141*, 034302.

(138) Barbe, A.; Starikova, E.; De Backer, M. R.; Tyuterev, V. G. Analyses of Infrared FT Spectra of Asymmetric Ozone Isotopologue $^{16}O^{16}O^{18}O$ in the Range 950–3850 Cm^{-1}. *J. Quant. Spectrosc. Radiat. Transf.* **2018**, *218*, 231–247.

(139) Bruno, T. J.; Svoronos, P. D. *CRC Handbook of Chemistry and Physics*, 93rd ed.; 2012.

(140) Gayday, I.; Teplukhin, A.; Kendrick, B. K.; Babikov, D. The Role of Rotation–Vibration Coupling in Symmetric and Asymmetric Isotopomers of Ozone. *J. Chem. Phys.* **2020**, *152*, 144104.

(141) Kivelson, D. A (K+2)Nd Order Formula for Asymmetry Doublets in Rotational

Spectra. *J. Chem. Phys.* **1953**, *21*, 536–538.

(142) Wang, S. C. On the Asymmetrical Top in Quantum Mechanics. *Phys. Rev.* **1929**, *34*, 243–252.

(143) Carney, G. D.; Sprandel, L. L.; Kern, C. W. Variational Approaches to Vibration-Rotation Spectroscopy for Polyatomic Molecules. In *Advances in Chemical Physics*; Prigogine, I., Rice, S. A., Eds.; John Wiley & Sons: New York, 1978; Vol. 37, p 367.

(144) Flaud, J. M.; Bacis, R. The Ozone Molecule: Infrared and Microwave Spectroscopy. *Spectrochim. Acta Part A Mol. Biomol. Spectrosc.* **1998**, *54*, 3–16.

(145) Barbe, A.; Mikhailenko, S.; Starikova, E.; De Backer, M. R.; Tyuterev, V. G.; Mondelain, D.; Kassi, S.; Campargue, A.; Janssen, C.; Tashkun, S. A.; et al. Ozone Spectroscopy in the Electronic Ground State: High-Resolution Spectra Analyses and Update of Line Parameters since 2003. *J. Quant. Spectrosc. Radiat. Transf.* **2013**, *130*, 172–190.

(146) Kokoouline, V.; Lapierre, D.; Alijah, A.; Tyuterev, V. G. Localized and Delocalized Bound States of the Main Isotopologue $^{48}O_3$ and of ^{18}O-Enriched $^{50}O_3$ Isotopomers of the Ozone Molecule near the Dissociation Threshold. *Phys. Chem. Chem. Phys.* **2020**, *22*, 15885–15899.

(147) Charlo, D.; Clary, D. C. Quantum-Mechanical Calculations on Termolecular Association Reactions XY+Z+M→XYZ+M: Application to Ozone Formation. *J. Chem. Phys.* **2002**, *117*, 1660–1672.

(148) Charlo, D.; Clary, D. C. Quantum-Mechanical Calculations on Pressure and Temperature Dependence of Three-Body Recombination Reactions: Application to Ozone Formation Rates. *J. Chem. Phys.* **2004**, *120*, 2700–2707.

(149) Xie, T.; Bowman, J. M. Quantum Inelastic Scattering Study of Isotope Effects in Ozone Stabilization Dynamics. *Chem. Phys. Lett.* **2005**, *412*, 131–134.

(150) Leforestier, C. Grid Representation of Rotating Triatomics. *J. Chem. Phys.* **1991**, *94*, 6388–6397.

(151) Launay, J. M.; Le Dourneuf, M. Hyperspherical Close-Coupling Calculation of Integral Cross Sections for the Reaction $H+H_2 \rightarrow H_2+H$. *Chem. Phys. Lett.* **1989**, *163*, 178–188.

(152) Manolopoulos, D. E. Derivation and Reflection Properties of a Transmission-Free Absorbing Potential. *J. Chem. Phys.* **2002**, *117*, 9552–9559.

(153) Gayday, I.; Grushnikova, E.; Babikov, D. Influence of the Coriolis Effect on the Properties of Scattering Resonances in Symmetric and Asymmetric Isotopomers of Ozone. *Phys. Chem. Chem. Phys.* **2020**, *22*, 27560–27571.

(154) Babikov, D.; Grushnikova, E.; Gayday, I.; Teplukhin, A. Four Isotope-Labeled Recombination Pathways of Ozone Formation. *Molecules* **2021**, *26*, 1289.

(155) Grebenshchikov, S. Y.; Schinke, R.; Fleurat-Lessard, P.; Joyeux, M. Van Der Waals States in Ozone and Their Influence on the Threshold Spectrum of $O_3(X^1A_1)$. I. Bound States. *J. Chem. Phys.* **2003**, *119*, 6512–6523.

(156) Robert, F.; Baraut-Guinet, L.; Cartigny, P.; Reinhardt, P. An Experimental Test for the Mass Independent Isotopic Fractionation Mechanism Proposed for Ozone. *Chem. Phys.* **2019**, *523*, 191–197.

(157) Reinhardt, P.; Robert, F. On the Mass Independent Isotope Fractionation in Ozone. *Chem. Phys.* **2018**, *513*, 287–294.

(158) Sarka, J.; Poirier, B.; Szalay, V.; Császár, A. G. On Neglecting Coriolis and Related Couplings in First-Principles Rovibrational Spectroscopy: Considerations of Symmetry, Accuracy, and Simplicity. II. Case Studies for H_2O Isotopologues, H^+_3, O_3, and NH3. *Spectrochim. Acta Part A Mol. Biomol. Spectrosc.* **2021**, *250*, 119164.

(159) McGuire, P.; Kouri, D. J. Quantum Mechanical Close Coupling Approach to Molecular Collisions. j_z-conserving Coupled States Approximation. *J. Chem. Phys.* **1974**, *60*, 2488–2499.

(160) Parker, G. A.; Pack, R. T. Identification of the Partial Wave Parameter and Simplification of the Differential Cross Section in the j_zCCS Approximation in Molecular Scattering. *J. Chem. Phys.* **1977**, *66*, 2850–2853.

(161) Parker, G. A.; Pack, R. T. Rotationally and Vibrationally Inelastic Scattering in the Rotational IOS Approximation. Ultrasimple Calculation of Total (Differential, Integral, and Transport) Cross Sections for Nonspherical Molecules. *J. Chem. Phys.* **1978**, *68*, 1585–1601.

(162) Yang, D.; Hu, X.; Zhang, D. H.; Xie, D. An Improved Coupled-States Approximation Including the Nearest Neighbor Coriolis Couplings for Diatom-Diatom Inelastic Collision. *J. Chem. Phys.* **2018**, *148*, 084101.

(163) Janssen, C.; Marcus, R. A. Does Symmetry Drive Isotopic Anomalies in Ozone Isotopomer Formation? *Science (80-.).* **2001**, *294*, 951a – 951.

(164) Chen, W.; Poirier, B. Parallel Implementation of Efficient Preconditioned Linear Solver for Grid-Based Applications in Chemical Physics. I: Block Jacobi Diagonalization. *J. Comput. Phys.* **2006**, *219*, 185–197.

(165) Chen, W.; Poirier, B. Parallel Implementation of Efficient Preconditioned Linear Solver for Grid-Based Applications in Chemical Physics. II: QMR Linear Solver. *J. Comput. Phys.* **2006**, *219*, 198–209.

(166) Mátyus, E.; Czakó, G.; Császár, A. G. Toward Black-Box-Type Full- and Reduced-Dimensional Variational (Ro)Vibrational Computations. *J. Chem. Phys.* **2009**, *130*, 134112.

(167) Simkó, I.; Szidarovszky, T.; Császár, A. G. Toward Automated Variational Computation of Rovibrational Resonances, Including a Case Study of the H_2 Dimer. *J. Chem. Theory Comput.* **2019**, *15*, 4156–4169.

(168) Tennyson, J.; Kostin, M. A.; Barletta, P.; Harris, G. J.; Polyansky, O. L.; Ramanlal, J.; Zobov, N. F. DVR3D: A Program Suite for the Calculation of Rotation–Vibration Spectra of Triatomic Molecules. *Comput. Phys. Commun.* **2004**, *163*, 85–116.

(169) Hutson, J. M.; Le Sueur, C. R. BOUND and FIELD: Programs for Calculating Bound States of Interacting Pairs of Atoms and Molecules. *Comput. Phys. Commun.* **2019**, *241*, 1–8.

(170) Hutson, J. M.; Le Sueur, C. R. MOLSCAT: A Program for Non-Reactive Quantum Scattering Calculations on Atomic and Molecular Collisions. *Comput. Phys. Commun.* **2019**, *241*, 9–18.

(171) Roman, J. E.; Campos, C.; Romero, E.; Tomas, A. *SLEPc Users Manual*; 2020.

(172) Kłos, J.; Alexander, M. H.; Kumar, P.; Poirier, B.; Jiang, B.; Guo, H. New Ab Initio Adiabatic Potential Energy Surfaces and Bound State Calculations for the Singlet Ground $\tilde{X}^1A_1$ and Excited $\tilde{C}^1B_2(2^1A')$ States of SO_2. *J. Chem. Phys.* **2016**, *144*, 174301.

(173) fdict https://github.com/zerothi/fdict.

(174) Hernandez, V.; Roman, J. E.; Vidal, V. SLEPc: A Scalable and Flexible Toolkit for the Solution of Eigenvalue Problems. *ACM Trans. Math. Softw.* **2005**, *31*, 351–362.

(175) Hernandez, V.; Roman, J. E.; Vidal, V. SLEPc: Scalable Library for Eigenvalue Problem Computations. In *Lecture Notes in Computer Science*; Springer, 2003; pp 377–391.

(176) Hernandez, V.; Roman, J. E.; Tomas, A. Parallel Arnoldi Eigensolvers with Enhanced Scalability via Global Communications Rearrangement. *Parallel Comput.* **2007**, *33*, 521–540.

(177) PETSc https://www.mcs.anl.gov/petsc.